ISBN 978-82-326-3612-9 (printed ver.)
ISBN 978-82-326-3613-6 (electronic ver.)
ISSN 1503-8181

NTNU
Norwegian University of
Science and Technology

Jost Ruwoldt

Doctoral theses at NTNU, 2018:410

NTNU

Doctoral thesis

**NTNU**
Norwegian University of Science and Technology
Thesis for the Degree of
Philosophiae Doctor
Faculty of Natural Sciences
Department of Chemical Engineering

Doctoral theses at NTNU, 2018:410

Jost Ruwoldt

# Inhibitor-Wax Interactions and Wax Crystallization: New Experimental Approaches and Techniques.

NTNU
Norwegian University of
Science and Technology

Jost Ruwoldt

# Inhibitor-Wax Interactions and Wax Crystallization: New Experimental Approaches and Techniques.

Thesis for the Degree of Philosophiae Doctor

Trondheim, December 2018

Norwegian University of Science and Technology
Faculty of Natural Sciences
Department of Chemical Engineering

NTNU
Norwegian University of
Science and Technology

**NTNU**
Norwegian University of Science and Technology

Thesis for the Degree of Philosophiae Doctor

Faculty of Natural Sciences
Department of Chemical Engineering

ISBN 978-82-326-3612-9 (printed ver.)
ISBN 978-82-326-3613-6 (electronic ver.)
ISSN 1503-8181

Doctoral theses at NTNU,2018:410

Printed by NTNU Grafisk senter

# Preface

This thesis is submitted in partial fulfillment of the doctoral degree at the Norwegian University of Science and Technology (NTNU). It consists of six publications based on work performed at Ugelstad Laboratory, Department of Chemical Engineering, NTNU, under the supervision of Prof. Johan Sjöblom and co-supervision of Prof. Hans-Jörg Oschmann.

The work was carried out as part of *SUBPRO – Subsea Production and Processing*, Research Area C *Separation – Fluid Characterization* from 2015 to 2018. This project was funded by the Norwegian Research Council, NTNU, and industry partners, which include ABB, AkerBP, Aker Solutions, DNV GL, Equinor, Lundin, Neptune Energy, Shell, and VNG Norge.

I graduated with a M.Sc. in Chemical and Bioprocess Engineering in 2015 and a B.Sc. in General Engineering Science in 2013 from Hamburg University of Technology (TUHH). In 2015, I joined Ugelstad Laboratory at NTNU to work on paraffin wax related issues within crude oil production.

*Für Elisabeth*

## Acknowledgements

This thesis benefited from the support of and collaboration with many people, named and unnamed, who have my deepest gratitude.

First and foremost, I would like to express my sincere gratitude to my supervisor Prof. Johan Sjöblom for his guidance, scientific input, support, and encouragement. V*ielen lieben Dank* to my co-supervisor Prof. Hans Oschmann for his help in defining the research objectives, input from his industrial expertise, and constructive discussions.

A special thank you and *merci beaucoup* to Dr. Sebastién Simon for his help, scientific feedback, corrections, and dedication – de facto acting as co-supervisor despite having no official affiliation with me.

Thank you to all the people involved in SUBPRO for the support and the possibility to see the bigger picture of subsea petroleum production. Thank you to Gro and Jon, the management team, PhDs, Postdocs and industry partners – I was very fortunate to be part of this project.

Furthermore, I would like to thank Muh Kurniawan, Geir Humborstad Sørland, Sreedhar Subramanian, and Jens Norrman for their collaboration, contributions and fruitful co-authoring of several publications. Thank you Prof. Paso for the support during the early phase of the project.

Many thanks the staff of Ugelstad Laboratory, in particular Bicheng, May Grete, Camillar, and Jens, for their help, technical advice, and for keeping things smooth and running in the lab.

Thank you dear colleagues, Are, Marcin, Sandra, and Tomas, for the enjoyable time and company on and off work, and for making this experience about more than just science. Thank you to all the regular lunch-attendees for the company and interesting discussions.

*Tusen takk* Elisabeth for your enduring support throughout these years. Without you this thesis would not be what it is today

# Abstract

Issues related to wax crystallization are one of the major challenges faced during crude oil production. Wax inhibitors and pour point depressants (PPD) are in common use for wax prevention, as they can delay gelling and ensure low enough crude oil viscosity even after wax precipitation. Understanding underlying phenomena is therefore paramount for successful wax control. This thesis has consequently been dedicated to (i.) new procedures and techniques for investigating wax crystallization and inhibition, and (ii.) application of these for a better understanding of inhibitor-wax interactions.

A new procedure was developed and tested to compute wax appearance temperature (WAT) from differential scanning calorimetry (DSC) and viscometry data more accurately. In this procedure, WAT is detected once experimental data exceeds a statistical threshold value. Obtained WAT values were discussed among three techniques, various cooling rates, and with respect to thermodynamic solubility of wax.

Isothermal titration calorimetry (ITC) was introduced to study inhibitor-wax interactions. Results showed that PPD additives interact with both dissolved and crystalline wax, but the measured interaction heat was up to 150 times larger with crystalline wax present. Five different wax inhibitors and asphaltenes were tested in ITC and compared with results from DSC, rheometry, and cross-polarized microscopy (CPM). It was concluded that the interaction strength did not correlate with the PPD ability to lower WAT, induce crystal morphology changes, or reduce wax gel strength. Nuclear magnetic resonance (NMR) was introduced to study dissolved wax mobility and inhibitor-wax interactions in liquid phase during crystallization. PPD additives with efficient wax inhibition were shown to suppress secondary peaks in the $T_2$ distribution, suggesting that PPDs can alter interactions of dissolved wax at the solid-liquid interface. In addition, DSC and NMR showed delayed wax precipitation for efficient PPDs, which was confirmed by GC/MS showing that these PPDs could alter compositional changes and promote selective *n*-alkane precipitation.

Moreover, the influence of PPD molecular weight on wax crystallization was studied via two PPD fractionation procedures. It was found that PPD effect on WAT and wax gelation temperature is largely dominated by PPD functional groups and waxy oil composition. PPD molecular weight appeared less crucial, but could in some cases alter efficiency.

The effect of fractionated asphaltenes on wax crystallization was investigated, as these are PPD active substances naturally found in crude oil. Asphaltenes were fractionated by two procedures, yielding fractions with different characteristics. It was concluded that low solubility and mixed functional groups had the most beneficial effect on wax crystallization. Asphaltene-wax interactions were best facilitated by asphaltene molecules with higher polydispersity.

## List of Publications

**Publication I**
Ruwoldt, Jost; Kurniawan, Muh; Oschmann, Hans-Jörg
*Non-linear dependency of wax appearance temperature on cooling rate*
Journal of Petroleum Science and Engineering, 2018. **165**: p. 114-126.

**Publication II**
Ruwoldt, Jost; Simon, Sébastien; Oschmann, Hans-Jörg; Sjöblom, Johan
*Isothermal Titration Calorimetry for Assessing Wax Inhibitors*
Chemistry in the Oil Industry XV: Enabling Efficient Technologies Programme. 2017. Manchester (UK).

**Publication III**
Ruwoldt, Jost; Simon, Sébastien; Norrman, Jens; Oschmann, Hans-Jörg; Sjöblom, Johan
*Wax-Inhibitor Interactions Studied by Isothermal Titration Calorimetry and Effect of Wax Inhibitor on Wax Crystallization*
Energy & Fuels, 2017. **31**(7): p. 6838-6847.

**Publication IV**
Ruwoldt, Jost; Humborstad Sørland, Geir; Simon, Sébastien; Oschmann, Hans-Jörg; Sjöblom, Johan
*Inhibitor-wax interactions and PPD effect on wax crystallization: New approaches for GC/MS and NMR, and comparison with DSC, CPM, and rheometry*
Manuscript submitted to Journal of Petroleum Science and Engineering.

**Publication V**
Ruwoldt, Jost; Kurniawan, Muh; Humborstad Sørland, Geir; Simon, Sébastien; Sjöblom, Johan
*Influence of Wax Inhibitor Molecular Weight: Part 1. Fractionation and Effect on Crystallization of Polydisperse Waxes.*
Manuscript submitted to Journal of Dispersion Science and Technology.

**Publication VI**
Ruwoldt, Jost; Subramanian, Sreedhar; Simon, Sébastien; Oschmann, Hans-Jörg; Sjöblom, Johan
*Asphaltene fractionation based on adsorption onto calcium carbonate: Part 3. Effect of asphaltenes on wax crystallization*
Colloids and Surfaces A: Physicochemical and Engineering Aspects, 2018. **554**: p. 129-141.

## Author Contribution

All experimental work was carried out by me at Ugelstad Laboratory, with few exceptions as specified below. PPD ultrasonic disintegration (Publication V) was conducted by me at Nanolab, NTNU. Pour point tests (Publication VI) were conducted by me at PSL Systemtechnik, Germany. NMR-DOSY measurements (Publication V) were conducted together with Geir Humborstad Sørland at NMR Laboratory, Faculty of Natural Sciences, NTNU. CPM measurements (Publication I), as well as PPD fractionation based on stepwise precipitation and HPLC-SEC measurements (both Publication V) were conducted by Muh Kurniawan at Ugelstad Laboratory. FTIR measurements (Publication VI) were conducted by Sreedhar Subramanian at Ugelstad Laboratory. Elemental analysis (Publication VI) was performed by Laboratory SGS Multilab, France. All in all, the experimental work conducted by individuals other than me amounts to approximately 5 % of the total work.

All manuscripts were written and completed by me. My co-author Muh Kurniawan contributed the CPM method description in Publication I. He also described HPLC-SEC and PPD fractionation by stepwise precipitation in Publication V. My co-author Geir Humborstad Sørland contributed the NMR method description in Publication IV and V. Asphaltene characterization and method description of the asphaltene fractionation in Publication VI was in part contributed by Sreedhar Subramanian.

In addition, contributions were made with regards to experimental planning, data interpretation, manuscript proof-reading, and correction by my supervisors, Prof. Johan Sjöblom and Prof. Hans-Jörg Oschmann, by Dr. Sebastien Simon, and by other individuals as indicated by co-authorship.

## Conference Presentations

*Isothermal Titration Calorimetry for Assessing Wax-Inhibitors*
Oral presentation at the Chemistry in the Oil Industry XV: Enabling Efficient Technologies Programme, Manchester (UK), 2017.

*Calorimetry with Application to Paraffin Wax in Crude Oil Production.*
Poster presentation at the 18th Lähnwitzseminar on Calorimetry, Rostock (Germany), 2018.

# Table of Contents

# Acronyms

| | |
|---|---|
| CPM | cross-polarized microscopy |
| DSC | differential scanning calorimetry |
| DOSY | diffusion ordered spectroscopy |
| EVA | ethylene vinyl-acetate copolymer |
| FTIR | Fourier-transform infrared spectroscopy |
| GC | gas chromatography |
| GC/MS | gas chromatography coupled mass spectrometry |
| HPLC | high pressure liquid chromatography |
| ITC | isothermal titration calorimetry |
| MAC | maleic anhydride amide co-α-olefin |
| MSD | mass spectrometer detector |
| NMR | nuclear magnetic resonance |
| PB | polybutene |
| PE | polyethylene |
| PEP | polyethylene propylene |
| PFG | pulsed field gradient |
| PPD | pour point depressants |
| PS | polystyrene |
| RF | radio frequency |
| SARA | saturates, aromatics, resins, asphaltenes |
| SEC | size-exclusion chromatography |
| WAT | wax appearance temperature |
| WDT | wax dissolution temperature |
| WPC | wax precipitation curve |

# 1. Introduction

In 2015, the world's petroleum production amounted to 95 million barrels per day, satisfying 33 % of the world energy demand[1]. Development and wealth correlate with energy consumption[2, 3], which justifies future prognoses about the world's growing energy demand. Efforts are therefore made to explore unconventional petroleum sources, such as heavy oil, shale oil, and oil sands, as well as harsher environments, e.g. marine deep waters[4]. Especially the latter aggravates issues related to paraffin wax in petroleum. At offshore reservoirs temperatures of 70 - 150 °C and pressures in the range of 55 - 103 MPa ensure high wax solubility[5]. As the oil is transported from subsea wellhead to the production platform, cooling and the loss of light ends lower wax solubility. Wax crystallization can increase fluid viscosity and lead to the formation of a solid-like gel. Possible consequences include reduced production efficiency, pipeline plugging, and restartability issues[6]. Wax management entails significant costs, but production irregularities and loss of equipment are imminent if these issues are not addressed[7-9].

In industry, wax prevention and remediation is part of flow assurance. Different approaches include thermal, mechanical, and chemical techniques[10]. Chemical prevention methods, such as wax inhibitors and pour point depressants (PPD), play an important role due to their ability to alleviate wax related issues at comparably small dosage, thereby vastly improving safety and economics[11]. The effect of wax inhibitors is well understood; the exact inhibition mechanism, however, remains still unknown[11, 12]. The performance of chemical additives can vary greatly between crude oils of different composition and origin. A recent review on wax formation in oil pipelines stated[13]: *"The efficacy of commercially available inhibitors tends to be limited, and has to be evaluated on a case-by-case basis."* Hence, there is a need to better understand the underlying phenomena, which are paraffin wax crystallization and inhibition. Improved inhibitor screening techniques and ultimately the development of better chemical additives for flow assurance can be facilitated with this knowledge.

# 2. Petroleum

The word *petroleum* is derived from the Latin words *petra* and *oleum*, which literally translate to *rock oil*[14]. It refers to hydrocarbon mixtures naturally found in sedimentary rocks, and is an important basis for fuel and chemical feedstock in the modern industry. The words *petroleum* and *crude oil* are often used as synonyms[15].

## 2.1. Origin and Formation

Petroleum is a type of fossil fuel, meaning that it is a remnant of once living organisms that have been embedded in earth's crust[16]. At elevated pressure and temperature, organic matter is transformed as part of diagenesis, catagenesis, and metagenesis[17]. During diagenesis, kerogen is formed, which can further be converted into petroleum and natural gas. However, it is argued whether kerogen poses as an intermediate product or a byproduct during this conversion process[14, 16]. Kerogen is defined as solid, high molecular weight, insoluble matter found in source rocks that yield upon heating[14]. Depending on the composition and biomass origin, it can be grouped into four types[14, 18].

| | |
|---|---|
| Type I kerogen: | Sapropelic kerogen originates from algae, cyanobacteria, and terrestrial plants. It exhibits H/C ratios of above 1.25 and tends to readily produce liquid hydrocarbons. |
| Type II kerogen: | Planktonic kerogen is primarily based on marine organic materials (plankton). Several sub-categories exist, such as exinite (pollen and spores), cutinite (terrestrial plant cuticle), and resinite (terrestrial plants and animal decomposition resins). |
| Type III kerogen: | Humic kerogen is derived from terrestrial plants, such as wood and other lignocellulose materials. The H/C ratio of this type is below 1, yielding a low potential to form liquid hydrocarbons. |
| Type IV kerogen: | Residue kerogen contains mostly decomposed organic matter in the form of polycyclic aromatic compounds. This type has the lowest H/C ratios of below 0.5 and therefore little or no potential to produce hydrocarbons. |

Kerogen undergoes reduction in both H/C and O/C atomic ratios during conversion to coal, petroleum, and natural gas - a process, which is referred to as maturation[19]. Petroleum represents an intermediate state in the maturation process, the so called *oil window*. Petroleum composition is therefore dependent on the degree of maturation and kerogen type[20]. Type I kerogen results in the formation of aliphatic hydrocarbons and few cyclic or aromatic structures[14, 18]. Petroleum derived from type II kerogen is generally rich in NSO-compounds and aromatics. Type III kerogen can produce a paraffinic fluid, but has higher coal- and gas-generating potential[14]. This transformation can be illustrated in a Van Krevelen diagram as shown in Figure 1. At the start of kerogen maturation, each kerogen type is present with the highest H/C and O/C atomic ratios. The maturation process is resembled by moving along the x-axis and y-axis towards the origin.

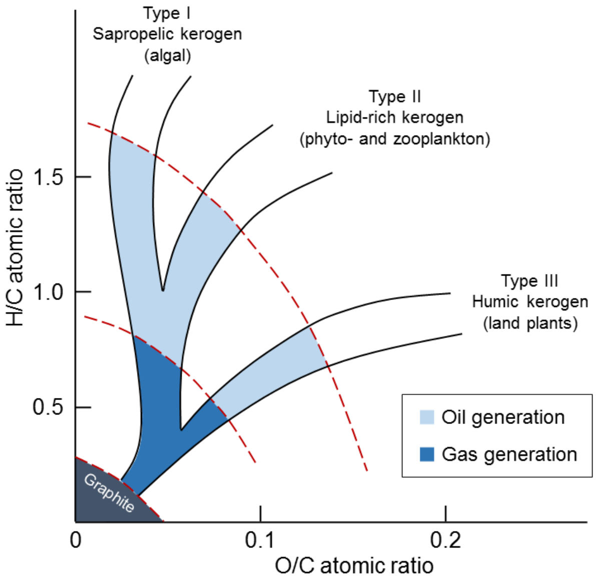

Figure 1. Hypothetical evolutionary pathways (atomic H/C vs. atomic O/C ratios) of kerogen[14].

## 2.2.Petroleum Classification

Petroleum is classified as a liquid hydrocarbon resource that originates from organic sediments[14]. Petroleum can exhibi a wide range of physical properties at similar elementary composition, which makes classification based on elementary analysis difficult. Instead, the amount of saturates and aromatics or the crude oil assay (detailed alkane composition from GC-analysis) can be used for characterization[21]. For example, a crude oil may be classified as paraffinic (saturated, straight chain or branched alkanes), naphthenic (saturated hydrocarbons containing one or more rings), or aromatic (hydrocarbons containing one or more aromatic nuclei)[14]. Also, crude oil can be classified via boiling point distillation, which analyzes the cumulative weight fraction of crude oil with respect to boiling temperature[22]. Moreover, petroleum is referred to as *dead* or *live crude oil*, depending on whether it is sampled during production (live) or after equilibration at ambient conditions (dead). Right after the wellhead, live crude oil is present at elevated pressure and temperature containing a considerable amount of dissolved gasses, which are lost after reaching ambient conditions. Classification based on density and viscosity is frequently used as shown in Figure 2.

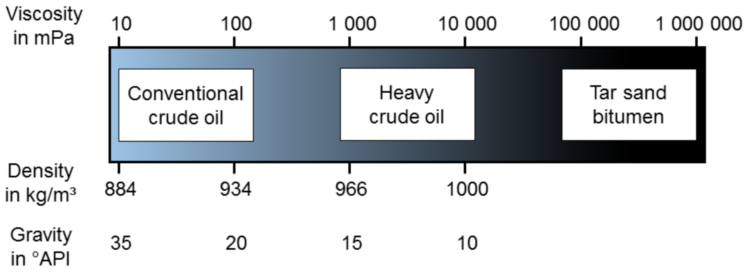

Figure 2. Crude oil classification by viscosity and density[14].

API gravity has become a standard in industry to refer to substances with a lower density than water, in particular petroleum. It is calculated according to Equation (1), where $\rho_{rel}$ refers to the specific gravity of the regarded crude oil[14].

$$API° = \frac{141.5}{\rho_{rel}} - 131.5 \tag{1}$$

API values above 10 indicate that a substance floats in water at ambient conditions, i.e. has a density below 1 kg/m$^3$. Classification of crude oil by API gravity includes light (API > 31.1), medium (22.3 < API < 31.1), and heavy crude oil (API < 22.3). Extra heavy crude oil and bitumen both exhibit API gravity of below 10[23].

## 2.3.Subsea Production and Transportation

Over the years, offshore petroleum production has increased and a growing portion is associated with deep sea production[24]. The transition from onshore to offshore crude oil production is illustrated in Figure 3. Both the number of shallow and deep-water and the maximum water depth of subsea completions per year increased progressively from 1990 to 2000[24]. Despite high investment costs for deep sea operations, the production volume has multiplied since 1995[24, 25].

After reaching the pre-set depth during subsea drilling, the casing pipe is run down the borehole and cemented to prevent collapsing[14]. During well completion, the well is perforated at production depth to enable the flow of oil. A multivalve structure, called Christmas tree, is attached to the top of the well to control the outflow of oil during production. Equipment connected to the Christmas tree can range in complexity from a single satellite well with flowline to several wells on a template or clustered around a manifold[24]. The oil is transported topside through pipelines, which have become an indispensable part of petroleum production[26]. Increasingly high requirements are set for subsea production pipelines, such as resistance to high temperature and pressures[24]. Manufacturers have also looked into enhanced coatings, e.g. wax repellent surfaces[27].

Topside, the pipeline is connected to either a fixed platform, a floating production, storage and offloading unit, or onshore facilities.

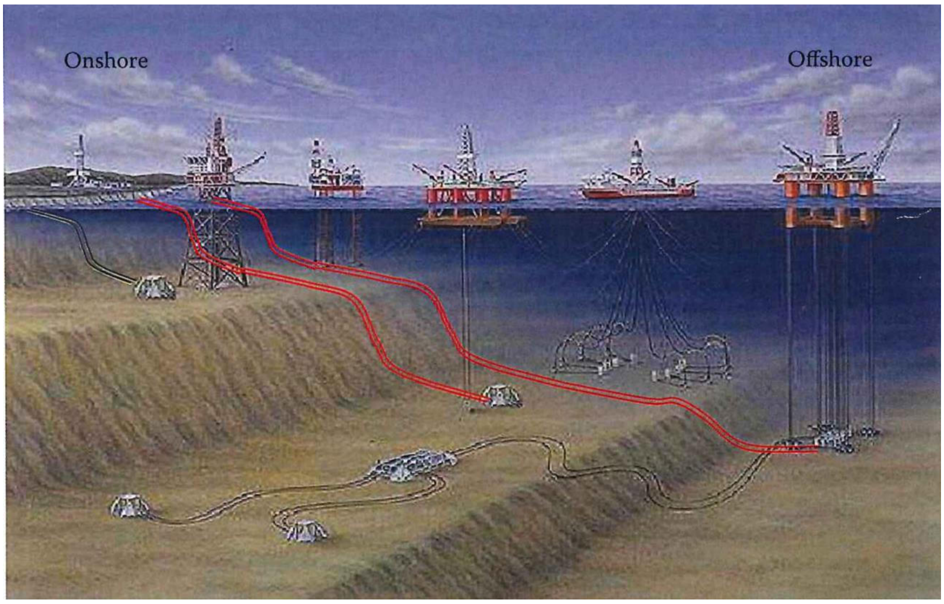

Figure 3. A schematic change from onshore to offshore petroleum production[28].

If the pressure in the oil reservoir is sufficiently high, crude oil will be transported to the surface without further work. This process is referred to as primary production and is often aided by natural gas in the reservoir, which maintains high reservoir pressure[14]. In secondary recovery, various techniques are employed to transport more oil to the surface, e.g. by pumping, and injecting water (water-flooding) or reinjecting natural gas (gas-flooding) into the reservoir. The last step is enhanced oil recovery (tertiary oil recovery), where the oil remaining in pores and cavities of the underground rock is extracted. This can be done via a number of thermal, chemical, and fluidic processes, such as polymer augmented water flooding, micro-emulsion flooding, surfactant flooding, and miscible fluid displacement. Approximately 50 % of the oil is normally left in the reservoir after production.

# 3. Petroleum Composition

In this chapter, the composition of petroleum and component classes of petroleum are discussed. Especially the latter are often used to assess petroleum properties as well as flow assurance issues that might arise during production.

## 3.1. Elementary Composition

Petroleum consists of mostly carbon and hydrogen, with smaller portions of nitrogen, oxygen, sulfur, and trace metals. With a few exceptions, the elemental composition of petroleum is within rather narrow limits (Table 1).

Table 1. Elemental composition of petroleum[14].

| | |
|---|---|
| Carbon | 83.0 – 87.0 % |
| Hydrogen | 10.0 – 14.0 % |
| Nitrogen | 0.1 – 2.0 % |
| Oxygen | 0.05 – 1.5 % |
| Sulfur | 0.05 – 6.0 % |
| Metals (nickel and vanadium) | <1000 ppm |

As pointed out in chapter 2, petroleum composition depends on the biomass origin and the degree of maturation. Petroleum fractionation is often employed to obtain information about the molecular composition.

## 3.2. Petroleum Fractionation

A standard way of analyzing dead crude oils is to perform SARA-analysis[29]. During SARA-fractionation, the crude oil is separated into four fractions: Saturates (S), aromatics (A), resins (R), and asphaltenes (A). Several procedures exist, which utilize differences in solubility and polarity of the fractions. As a first step, asphaltenes are precipitated by dilution with an *n*-alkane solvent of low molecular weight, typically *n*-heptane, *n*-hexane or *n*-pentane[15]. After recovery of the asphaltenes by filtration, the de-asphalted oil, known as maltenes, is further separated by high performance liquid chromatography (HPLC). In a procedure developed by Statoil (now Equinor), maltenes are separated via a chemically bonded silica-$NH_2$ preparative column[30]. First saturates and then aromatics are eluted using *n*-hexane solvent. Resins are subsequently flushed out by back-flushing the column with chloroform.

Even though SARA-analysis is useful to provide a rough description of crude oils, there is no clear chemical designation for individual component, and hence the results can vary depending on the operational procedure[29-31]. Especially the lack of asphaltene structural information impedes the use of SARA as a predictive tool for flow assurance. As a consequence, extended-SARA (E-SARA) was developed, which separates asphaltenes via adsorption on oil-water or oil-solid interfaces[32].

Saturates represent the fraction of saturated alkanes, in particular *n*-, *iso*-, and *cyclo*-alkanes. Paraffins (straight chain and branched alkanes) and naphthenes (containing one or more ring structures) belong to this fraction[14]. Aromatics include benzene derivatives, such as naphthalene, tetralin, and anthracene. They can be grouped into mono-, di- and tri-aromatics, depending on the number of aromatic rings. With increasing molecular weight and polarity, aromatics can also be classified as resins or asphaltenes. As mentioned earlier, the definition of resins and asphaltenes is very much process dependent[15]. One definition for resins is, for example, that these are soluble in *n*-heptane, but insoluble in ethyl acetate[29].

Table 2. Common petroleum products produced from distillation columns[21].

| **Petroleum fraction** | **Hydrocarbon range (approximate)** | **Boiling point range (approximate)** |
|---|---|---|
| Light gases | $C_2$ - $C_4$ | -90 to 1 °C |
| Gasoline | $C_4$ - $C_{10}$ | -1 to 200 °C |
| Naphtha | $C_4$ - $C_{11}$ | -1 to 205 °C |
| Jet fuel | $C_9$ - $C_{14}$ | 150 to 255 °C |
| Kerosene | $C_{11}$ - $C_{14}$ | 205 to 255 °C |
| Diesel fuel | $C_{11}$ - $C_{16}$ | 205 to 290 °C |
| Light gas oil | $C_{14}$ - $C_{18}$ | 255 to 315 °C |
| Heavy gas oil | $C_{18}$ - $C_{28}$ | 315 to 425 °C |
| Wax | $C_{18}$ -$C_{36}$ | 315 to 500 °C |
| Lubricating oil | > $C_{25}$ | > 400 °C |
| Vacuum gas oil | $C_{28}$ - $C_{55}$ | 425 to 600 °C |
| Residuum | > $C_{55}$ | > 600 °C |

Petroleum fractionation also takes places in the refining process, which yields separation according to boiling point ranges. Common products are listed in Table 2 and include gasoline, naphtha, kerosene, diesel fuel, light/heavy gas oil, waxes and lubricating oil[21]. Other fractions than the above mentioned exist and production is for practical reasons adjusted to the market demands[14]. Final products include transportation fuel (gasoline, diesel), aviation fuel (jet fuel, kerosene), and feedstock chemicals (naphtha, wax). SARA-analysis of a crude oil therefore provides not only a measure for the extent of production issues (asphaltenes, resins), but also for readily distilled products (saturates, aromatics).

## 3.3. Paraffin Wax

Paraffin wax is part of the saturate fraction in crude oil. It is composed of mainly straight chain alkanes (*n*-alkanes), but may also contain branched or cyclic structures (*iso*- and *cyclo*-alkanes). Waxes are part of the higher molecular weight components in crude oil, comprising carbon numbers up to $C_{100}$ and higher[33]. Definition of the lower limit can depend on author; some set the limit at $\geq C_{20}$ [34, 35], others at $\geq C_{18}$ [36] or even $\geq C_{16}$ [11].

Depending on the composition, paraffin waxes can be categorized into macrocrystalline and microcrystalline wax[11]. Macrocrystalline wax comprises large portions of low molecular weight *n*-alkanes, typically in the range of $C_{16}$ to $C_{40}$, whereas microcrystalline wax contains mostly higher molecular weight *iso*- and *cyclo-a*lkanes. Macrocrystalline wax is associated with flow problems during crude oil production and transport due to the ability to crystallize in large plate- and needle-shaped geometries, resulting in higher gelling temperatures and gel yield strengths[37]. Microcrystalline wax on the other hand crystallizes to small, amorphous particles with low gel yield strength. Its presence was even shown to weaken gels formed by macrocrystalline wax[38]. Nonetheless, both types of wax can invoke flow assurance issues during crude oil production[7].

## 3.4. Asphaltenes

Asphaltenes constitute the high molecular weight and polarity fraction of petroleum[39]. They are defined as crude oil constituents insoluble in *n*-alkane solvents with low molecular weight (e.g *n*-pentane, *n*-heptane), but soluble in aromatic solvents (e.g. toluene).

Because asphaltenes are defined in terms of solubility parameters, this group can exhibit a high degree of polydispersity. They consist of various polycyclic aromatic hydrocarbons and aliphatic chains, containing heteroatoms such as oxygen, sulfur, and nitrogen, as well as metals such as nickel, vanadium, and iron[36]. Heavy crude oils are often rich in asphaltenes. Asphaltene molecular weight was found to be in the range of 500 to 1000 Da as measured by fluorescence depolarization[40]. Two different structural models have been proposed for asphaltenes (Figure 4)[41]. The continental model has a condensed structure in the center, which can contain polycyclic aromatic hydrocarbons and pendant alkyl chains[42]. The archipelago model represents asphaltenes as systems of several fused rings that are interconnected by alkyl chains and thioether bridges[41].

Asphaltenes do not display classic surfactant-like behavior (amphiphilic character), as they lack well defined hydrophilic heads and hydrophobic tails[36]. Instead, asphaltenes tend to aggregate and form colloidal suspensions. The Yen-Mullins model shows the dominant molecular and colloidal structures for asphaltenes that are present in laboratory solvents and crude oils[43]. In this model, asphaltenes are described as mostly continental type molecules, forming nanoaggregates at concentrations of approximately 100 mg/l, and clusters at for higher concentrations. Several aggregation mechanisms have been proposed, which include π-π stacking, acid-base interactions, hydrogen bonding, and metal coordination complexes[44].

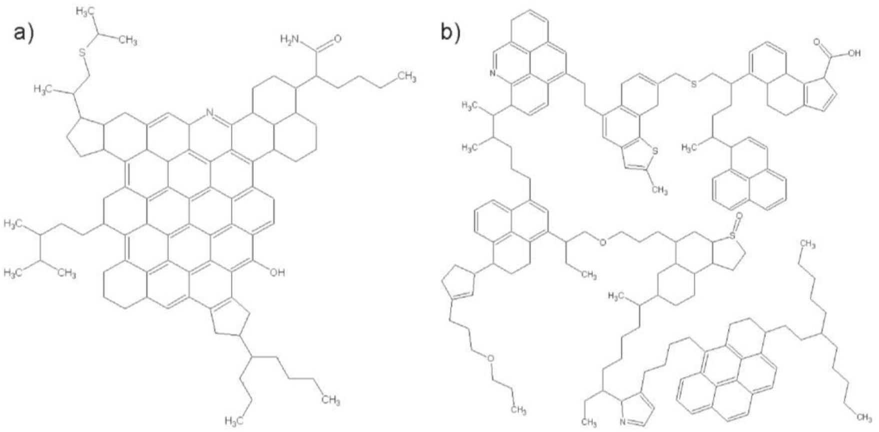

Figure 4. Asphaltene structural models comprising a) continental model and b) archipelago model[41].

## 3.5.Other Petroleum Components

Other components found in crude oil include resins, acids, and bases. Due to their definition, resins exhibit a lower degree of aromaticity and lower molecular weight than asphaltenes[14]. However, because the resin fraction can contain molecules with chemical similarity to asphaltenes, resins play a crucial role in crude oil stability[45]. It has been reported that resins stabilize asphaltenes by dissolving, dispersing, and peptizing[45, 46]. The molecular weight of resins is lower than that of asphaltenes, and resins show less tendency to self-associate[39].

The acidity or basicity of a crude oil can be measured in terms of the total acid number (TAN) or total base number (TBN), which are determined via ASTM D664, D974, or D3339[47-49]. Acids found in crude oil include naphthenic acids and hydrosulfides[14]. Assessment of these is important, as they can cause corrosion in pipeline and subsea equipment. Bases are nitrogen components, more specifically pyridine derivatives[50-52]. However, these are rarely studied compared to their acidic counterparts[53].

# 4. Flow Assurance

Flow assurance is an engineering process used to ensure that hydrocarbon fluids are transported economically from reservoir to end user over the life of a project[24]. In order to assure continuous and profitable flow, this discipline looks into issues that might arise due to both fluid properties and transient states during production and transport.

## 4.1. Arising Issues

Several problematic areas exist, which include paraffin wax, asphaltenes, gas hydrate formation, corrosion and scale formation[24]. In addition, sand is sometimes mentioned in a flow assurance context.

### 4.1.1. Wax Related Issues

Wax related issues include wax deposition during continuous flow, pipeline restart problems due to waxy gelling, increased fluid viscosity, and reduced operational efficiency[36].

Wax deposition imposes flow restrictions, which in the worst case scenario can lead to complete pipeline blockage[7]. For wax deposition to occur, the inner pipeline wall has to be below wax appearance temperature (WAT), inducing a radial temperature gradient within the bulk oil[5]. After an incipient wax layer has formed, the deposition layer grows in thickness while radial transport of wax molecules takes place to the solid-liquid interface and into the deposit. Over time, this transport also yields a change in the deposit composition, increasing solid wax fraction in the deposit as well as the ratio of higher molecular weight alkanes[54]. The deposit layer consequently hardens, which is referred to as aging.

During production stop, quiescent cooling of crude oil can lead to the formation of gels with high yield strength[37, 55, 56]. A solid like gel was reported to form at solid wax contents as low as 1 – 2 %[57]. This can then complicate production restart, which is why flow restart modeling often employs detailed rheological descriptions[58-60].

As wax starts to crystallize, crude oil viscosity increases due to the formed particle dispersion, as well as crystal-crystal interactions and interlocking effects[36]. Due to this, pressure loss along the pipeline is further increased. Moreover, wax particles can stabilize oil-water emulsions and thereby decrease separation efficiency[61, 62].

### 4.1.2. Asphaltene Deposition

Asphaltene deposition is recognized as a significant problem in crude oil production. For this reason, asphaltenes have also been referred to as the 'cholesterol' of petroleum[63]. Asphaltene deposition can take place during primary, secondary, and tertiary petroleum production in both production facilities and oil reservoir[64]. Asphaltenes are destabilized by a number of condition changes, including gas breakout (pressure drop), gas or liquid injection, acid stimulation, and crude mixing[36].

### 4.1.3. Other Issues

Among other issues, gas hydrate formation, scale, and corrosion are commonly addressed problems in flow assurance[36]. Gas hydrates are ice-like solids termed clathrates that can form from water and natural gas at elevated pressures and temperatures slightly below ambient conditions. These crystal structures usually form at the water-gas interface and their growth can result in the formation of hydrate plugs, which in turn can lead to pipeline blockage[65]. Scale is the solids deposition of inorganic salts from aqueous solutions, such as calcium carbonate, sodium chloride, sulfide and sulfate salts[36]. Scale can deposit on almost any surface and cause problems in the reservoir, production equipment, and processing facilities. Corrosion is a process that deteriorates metal piping and equipment due to ion exchange with water. Even though corrosion does not lead to production stop in the same way as wax, asphaltene, or gas hydrate deposits, corrosion has been reported to constitute over 25% of total safety incidents in the oil and gas industry[66].

## 4.2. Wax Management

Wax management can be grouped into prevention and remediation. These can further be subdivided into thermal, chemical, and mechanical measures[67].

### 4.2.1. Thermal Methods

Thermal prevention methods include pipeline insulation and heating to prevent crude oil to cool below WAT[10]. A combination of thermal and chemical remediation measures includes the use of hot solvents or hot water with surfactants to remove deposited wax. Moreover, fused chemical reactions have been reported, which utilize the heat generated by an exothermic reaction in the pipeline for wax deposition removal[68]. Another alternative is provided by cold flow[69, 70]. This technology circumvents the radial temperature gradient that can cause wax deposition on pipeline wall, because oil is first cooled below WAT and then transported as a waxy dispersion.

### 4.2.2. Mechanical Methods

Mechanical removal of wax deposition is predominantly done via pigging[7, 10]. During pigging, a conical or cylindrically formed object (the pig) is pushed through the pipeline, scraping of any deposit from the pipeline wall. Moreover, wireline cutters have been reported for wax removal[10]. Acoustic and sonic treatment were investigated on an experimental basis, but have not been implemented due to limited success[69].

### 4.2.3. Chemical Methods

Chemical prevention methods include the use of wax inhibitors. Among these thermodynamic wax inhibitors, crystal modifiers and pour point depressants, as well as dispersants and surfactants[24] can be mentioned. Thermodynamic inhibitors ensure wax solubility and reduce WAT. Different organic solvents have been used as such, but also blends with gas oil and light distillates[36]. The use of thermodynamic wax inhibitors is considered uneconomical due to the large volumes required. Most pour point depressants act as crystal modifiers, i.e. reducing the pour point via co-crystallization with wax and thereby distortion of crystal morphology[12]. Wax dispersants and surfactants influence particle-particle as well as particle-wall interactions[36]. This effect reduces the ability of wax crystals to stick to the pipeline wall and hence the buildup of a wax deposition layer.

## 4.3.Asphaltene Control

Analogously to wax management via chemical methods, asphaltene stability can be controlled by the use of asphaltene inhibitors, dispersants, and solvents[15]. Asphaltene inhibitors are reported to interact with the aggregates by surface adsorption, which stabilizes these aggregates in the same way as resins[36, 71, 72]. Asphaltene dispersants reduce the size of flocculated asphaltene and stabilizing these as a dispersion[15]. Solvents used for asphaltene removal typically include aromatic solvents such as toluene, xylene, and pyridine, but de-asphalted petroleum has also been considered[36, 73].

## 4.4.Other Phenomena

Gas hydrate can be managed by operating outside the temperature and pressure window for hydrate formation, modifying gas phase composition or removing the water phase, and by the use of production chemicals, such as thermodynamic and kinetic hydrate inhibitors[36]. Scale inhibitors for carbonate and sulfate salts can be based on polymers such as polyphosphates, phosphate esters, polycarboxylates, and polyphosphonates. Methods for corrosion control include water removal, cathodic protection, corrosion resistant alloys, coatings, corrosion inhibitors, as well as oxygen and $H_2S$ scavengers.

# 5. Fundamentals of Wax Crystallization and Related Phenomena

This chapter discusses fundamentals related to wax crystallization from organic solvents and other wax related phenomena within the framework of flow assurance. In addition, theoretical and empirical models are presented, which serve as tools for description and prediction.

## 5.1. Basic Terminology and Definitions

### 5.1.1. Wax Appearance Temperature (WAT)

The *wax appearance temperature* (WAT) is usually the first parameter to consider, when assessing whether wax related issues will occur during petroleum production[7]. The WAT is defined as the highest temperature, at which wax crystallization can be observed. Analogously, the *wax dissolution temperature* (WDT) is defined as the maximum temperature, at which wax can be observed to dissolve[35]. The WAT is also referred to as *cloud point* (ASTM-D2500), where WAT is determined by observing crystal occurrence or cloudiness in a liquid specimen[74]. The WAT is lower than the thermodynamic solubility limit, as a certain portion of wax must crystallize before it can be detected. The sensitivity of WAT detection depends on the wax composition, employed measuring technique, and cooling rate[35, 75, 76]. Different techniques have been developed for WAT determination. These include visual inspection, differential scanning calorimetry (DSC), cross-polarized microscopy (CPM), viscometry, Fourier-transform infrared spectroscopy (FTIR), near-infrared spectroscopy, X-ray computed tomography, filter-plugging, density variation measurements, sonic testing, and nuclear magnetic resonance (NMR)[7, 35, 36, 75, 77-81]. Cloud point measurements by ASTM-D2500 have been discussed critically due to inhomogeneous temperature distributions within the sample, inconsistent cooling gradients, and operator bias during detection[75, 82]. CPM technique also bears the disadvantage of operator bias, but has been acclaimed as the most precise method for WAT determined, since only a small portion of wax has to crystallize for detection[35, 80]. However, studies comparing different techniques have not been conclusive on finding the most sensitive method of detection[35, 76, 80, 83]. It is therefore often recommended to employ a multiple-technique approach when assessing WAT.

### 5.1.2. Wax Precipitation Curve (WPC)

The *wax precipitation curve* (WPC) is defined as the cumulative amount of solid wax precipitated[7]. Alternatively, the WPC can also be given as the relative amount of precipitated wax with respect to the total amount of waxy oil or the total amount of wax. This parameter is of interest, as it can be used to assess the severity of wax crystallization. The WPC can be determined with DSC, where the excess from exothermic wax crystallization is integrated from WAT to low temperatures, at which all wax is assumed to have precipitated[84]. In FTIR, the absorbance band around 735 – 715 cm$^{-1}$ changes with the occurrence of a solid wax phase, which can be utilized for quantification[77]. Proton pulsed NMR has been used for WPC determination also, where the difference in time scale of solid and liquid phase signal decay is exploited[85]. As an alternative or for reference purposes, the total wax content can be determined via precipitation from dilution with petroleum ether and acetone, and subsequent solid phase separation by filtration[86-88].

### 5.1.3. Pour Point

The *pour point* is defined as the temperature at which a liquid loses the ability to flow freely[89]. The pour point has been defined by several ASTM standards including the following:

- ASTM D97 and D5853[89, 90]: The specimen is contained in a cylindrical jar, which is subjected to cooling in a controlled environment. The jar is removed and checked at defined temperature intervals. Pour point is detected as the highest temperature at which movement of the sample can still be observed after tilting the specimen jar.
- ASTM D5949[91]: Controlled bursts of pressured gas are imparted onto the specimen surface, while cooling takes place at a rate of 1.5 °C/min. Specimen movement is monitored at the surface level via optical cameras and the lowest temperature at which movement can be observed is defined as the pour point.
- ASTM D5985[92]: The specimen is contained in a cylindrical cup, which is rotated at 0.1 rpm with a non-rotating piston partially submerged in the specimen. Cooling takes place by maintaining the block temperature approximately 8 °C lower than the specimen temperature. The pour point is detected as the temperature at which viscosity increase causes deflection of the piston.

ASTM D97 and D5853 result in a temperature resolution of 3 °C for pour point. In ASTM D5949, the operator can choose between a resolution of 3 °C or 1 °C. In addition to the standard resolution of 3 °C, the *no-flow point* is defined with a temperature resolution of 0.1 °C in ASTM D5985.

The discussed ASTM standards were designed to subject the sample to as little movement or shearing as possible. Such procedures reflect the conditions present during quiescent cooling in pipeline shut-in. Pour point measurements have therefore been used to not only assess the occurrence of wax related issues, but also to test the efficiency of wax inhibitors[93-96].

The pour point defines an instance after wax crystallization onset and thereby also takes into account the effects of wax crystal growth and agglomeration that lead to gelling. Assuming negligible viscosity change of bulk oil and the presence of similar crystal morphologies, waxy gelling occurs at a specific solids content providing a direct correlation between pour point and wax appearance temperature[97]. This interdependency is shown in Equation (2) for single component *n*-alkane solutions, where $y_{cp}$ refers to the amount of dissolved wax at cloud point $T_{cp}$, and $y_{pp}$ to the amount of dissolved wax at pour point temperature $T_{pp}$.

$$\ln(y_{cp}) - \ln(y_{pp}) = a\left(\frac{1}{T_{cp}} - \frac{1}{T_{pp}}\right) \tag{2}$$

### 5.1.4. Gelation Point

Historically, the gelation point has been defined with regards to polymer crosslinking, where the critical number of connected dimers in a gelled chain is one[98]. Physically, the polymer is said to be at the gelation point if steady state shear viscosity is infinite and equilibrium modulus is zero[99]. A common way of measuring this state is by the use of oscillatory rheology measurements, where the gelation point is defined as the intersection of storage modulus G' and loss modulus G" [100], as shown in Figure 5.

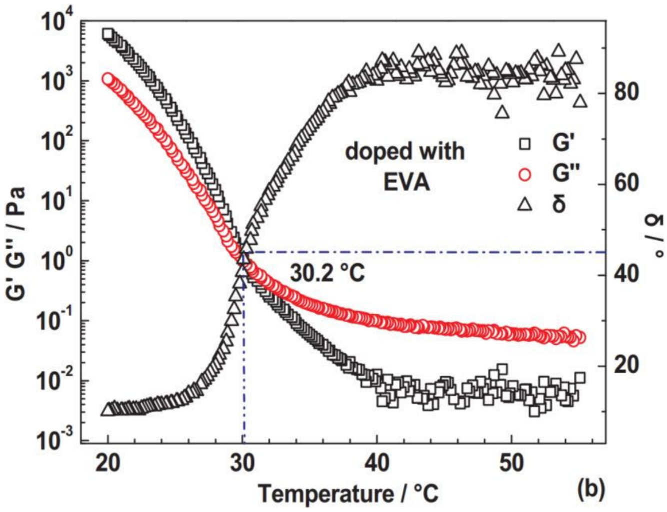

Figure 5. Determination of gelation temperature of a waxy oil using rheology, where G' is the storage modulus and G" is the loss modulus[101].

Imposed oscillation during gelation affects the gelation point measurement. As a result, increasing the applied stress amplitude during waxy gelation has been reported to lower the observed gelation temperature[100]. Moreover, the strain amplitude has been pointed out as an important parameter, since exceeding the linear viscoelastic regime will result in G' and G" to lose their physical meaning[102]. Gelation point measurements have been used to study the properties of waxy gelling, but also to quantify the effect of petroleum derived substances on wax crystallization[103-106]. An alternative to oscillatory measurements has been suggested, in which the waxy oil is subjected to constant shear stress and the gelation point is defined as the temperature at which the shear rate reaches zero[107].

### 5.1.5. Gel Yield Strength

Upon shearing, waxy gels display an initial Hookean response, which is followed by gel breakage, degradation, and various other effects[55]. A graph of the process is shown in Figure 6. After gel breakage, gel degradation processes lead to a decrease in observed shear stress or apparent viscosity, respectively. The gel yield strength, also referred to as gel breakage strength, is defined to quantify the stress necessary to overcome the initial region of high yield stress and induce gel degradation. However, authors have disagreed on the actual definition of gel yield strength[13]. Wardhaug et al. for example defined gel yield stress at the upper end of the initial linear region[108]. Barnes argued that no real yield stress exists, because Bingham fluids continue to flow or creep even below an apparent yield stress[109]. The author noted, however, that yield stress is a concept that can be useful for describing rheology within a limited range of conditions. In this thesis, the convention made by Zhao et al. is be used, which defines gel yield strength as the maximum shear stress recorded during gel breakage[110]. If the shear rate during gel breakage is sufficiently low (0.0001 – 0.1 $s^{-1}$), according procedures have shown good reproducibility[56, 110].

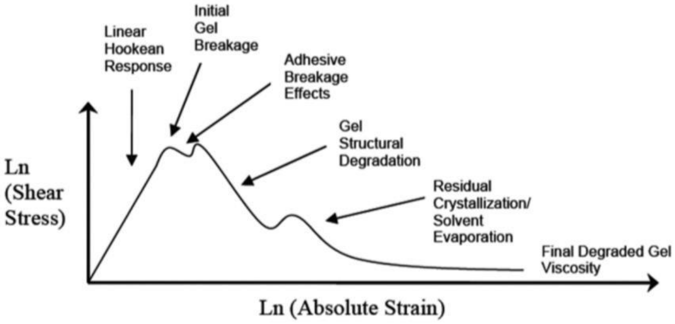

Figure 6. Schematic stress-strain diagram of a waxy gel undergoing continuous shearing with various contributing effects[55].

## 5.2. Thermodynamic Modeling of Wax Solubility

Thermodynamic modeling based on compositional analysis is a tool for predicting the onset and extent of wax precipitation[111]. Wax solubility predictions also provide an input for simulation of more extensive phenomena, such as wax deposition in crude oil pipelines[112-114].

A simple approach is given by the van't Hoff solubility theory, which assumes ideal solubility behaviour and negligible heat capacity change upon crystallization[67]. This theory has been used for binary organic solutions[115-117], but application has also been done to polydisperse waxes[118]. As stated in Equation (3), the mole fraction $x$ of maximum solubility in the liquid phase is related to temperature $T$ via dissolution enthalpy $\Delta H_{diss}$ and entropy $\Delta S_{diss}$, as well as idea gas constant $R$.

$$\ln\left(\frac{1}{x}\right) = \frac{\Delta H_{diss}}{RT} - \frac{\Delta S_{diss}}{R} \tag{3}$$

In thermodynamic modeling, equilibrium of component $i$ is reflected by equal fugacity in liquid ($f_i^L$) and solid phase ($f_i^S$), as shown in Equation (4) [119].

$$f_i^L = f_i^S \tag{4}$$

The distribution coefficient $K_i$, also referred to as partition coefficient, is shown in Equation (5), which is defined as the ratio of concentrations of a compound in a mixture of two immiscible phases at equilibrium[119, 120]. Here, $x_i^L$ and $x_i^S$ refer to the mole fractions of component $i$ in the liquid and solid phase, respectively. The definition of fugacity has been used to extend Equation (5), where $\gamma_i^L$ and $\gamma_i^S$ refer to the activity coefficients, $f_i^{L_0}$ and $f_i^{S_0}$ to the standard state fugacities, and $\bar{v}_i^L$ and $\bar{v}_i^S$ to the molar volumes.

$$K_i = \frac{x_i^S}{x_i^L} = \left(\frac{\gamma_i^L}{\gamma_i^S}\right)\left(\frac{f_i^{L_0}}{f_i^{S_0}}\right)\exp\int_{P_0}^{P}\frac{\bar{v}_i^L - \bar{v}_i^S}{RT}dP \tag{5}$$

This framework has been developed into more detailed descriptions of solid-liquid equilibrium for alkane mixtures. The model of Won introduced simplifications by neglecting the variation of heat capacity and assuming equal temperatures for melting and solid-solid transition[120, 121]. Further development includes the work of Pedersen et al.[119], Ungerer et al.[122], and Coutinho et al.[123]. Moreover, models based on descriptions for excess Gibbs energy $g^E$ have been introduced, such as NRTL and UNIQUAC[124]. Excess Gibbs energy can be related to activity coefficients via Equation (6) and (7), where $n_i$ refers to the moles in component $i$ [125].

$$g^E = RT\sum_i x_i \ln(\gamma_i) \tag{6}$$

$$\left(\frac{\partial n_T g^E}{\partial n_i}\right)_{T,P,n_j} = RTln(\gamma_i) \tag{7}$$

In UNIQUAC, excess Gibbs energy is calculated as sum of a combinatorial and a residual term, which are modeled individually using pure-component molecular-structure constants and component interaction parameters[125]. According descriptions have been used to successfully model e.g. carbon number distributions in wax deposits[126], as well as wax solubility in PPD beneficiated model oils[127].

## 5.3. Wax Nucleation

When considering wax nucleation, it is important to distinguish between primary (no crystals present) and secondary nucleation (induced by crystals)[128]. Primary nucleation is further subdivided into homogeneous nucleation, occurring spontaneously, and heterogeneous nucleation, which is induced by foreign particles or surfaces. In classical nucleation theory, supersaturation is viewed as a local minimum of free energy (metastable state)[129]. The supersaturation ratio $\beta$ is defined as the ratio of actual concentration $c$ divided by the equilibrium concentration $c_{eq}$ as shown in Equation (8) [128].

$$\beta = \frac{c}{c_{eq}} \tag{8}$$

Homogeneous nucleation is achieved via thermal fluctuations leading to the formation of a new phase called nucleus. This represents a global minimum of free energy. The decrease in free energy due to transfer of molecules from liquid to solid state can be described via the difference in chemical potential $\Delta\mu$ [130]. The activation energy $\Delta G^*$ necessary to form a nucleus of critical size is shown in Equation (9), where $\gamma$ refers to the surface free energy of the solid-liquid interface, and $k_B$ is the Boltzmann factor[130, 131]. The assumption of spherical particles was furthermore made.

$$\Delta G^* = \frac{16\pi\gamma^3\Delta\mu^2}{3[k_B T \ln\beta]^2} \tag{9}$$

As supersaturation ratio $\beta$ increases, activation energy $\Delta G^*$ becomes as low as that spontaneous and rapid nucleation occurs. The rate of nucleation J can be expressed as Arrhenius type reaction with pre-exponential factor $J^*$ as given in Equation (10) [128, 130].

$$J = J^* \exp\left(-\frac{\Delta G^*}{k_B T}\right) \tag{10}$$

Homogeneous nucleation theory has been applied to paraffin nucleation by various authors [105, 131-135]. Paso et al. used this framework to derive Equation (11), which relates cooling rate $\dot{T}_{cool}$ with the temperature difference at nucleation $\Delta T_{nuc}$ or more specifically the temperature lag of wax crystallization behind thermal equilibrium[105]. Here, term $A$ is the collision factor, $B$ is a material constant, and $\rho^*$ was introduced as the critical nuclei density, which is defined as the nuclei number density at nucleation onset.

$$\dot{T}_{cool} = \left(\frac{A}{\rho^*}\right)\Delta T_{nuc}\left[\exp\left(-\frac{B}{\Delta T_{nuc}^2}\right) - \frac{\sqrt{B\pi}}{\Delta T_{nuc}}erfc\left(\frac{\sqrt{B}}{\Delta T_{nuc}}\right)\right] \tag{11}$$

By using the terms $A/\rho^*$ as well as $B$ as regression parameters, Equation (11) allowed modeling of WAT differences that arose from variations in cooling rate during DSC measurements. A follow up was made by Mota et al. who used the Nývlt law under the assumption that the metastable zone is not too large, implying that saturation and supersaturation lines are linear and parallel[132]. The description is given in Equation (12), where $c^*$ is the supersaturation concentration and $n$ is the nucleation order with according crystallization rate constant $k_n$ [136].

$$\log(\Delta T_{nuc}) = \frac{1-n}{n}\log\left(\frac{dc^*}{dT}\right) - \frac{1}{n}\log(k_n) + \frac{1}{n}\log\left(\dot{T}_{cool}\right) \qquad (12)$$

The advantage of Equation (12) is that information about nucleation rate and kinetics can be readily obtained by linearization of experimental data[132]. It has to be mentioned, however, that descriptions provided in this section assume homogeneous nucleation, which can be viewed as a simplifying assumption. In real systems, it is difficult to eliminate the influence of both contamination by particles and the fact that a sample is rarely suspended without wall effects[128]. Heterogeneous nucleation would therefore appear closer to the real case, but it would also entail more complicated model descriptions.

## 5.4. Wax Crystallization and Gelling

Wax crystallization is reported to take place in three steps, which are nucleation, growth, and agglomeration[137]. As described in section 5.3, wax nucleation occurs at a temperature lag with respect to the thermal equilibrium. Furthermore, nucleation and growth have been observed to occur in three distinct regimes, which are nucleation lag, supersaturation growth, and equilibrium growth[105]. An example of these regimes from DSC measurements is shown in Figure 7.

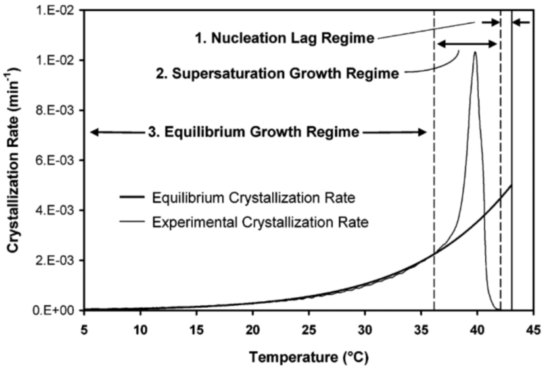

Figure 7. Crystallization rate of 4 wt% $n$-$C_{36}$ in Coray-15 measured by DSC at a cooling rate of 1 °C/min[105].

During crystal growth, more paraffin molecules are added to the initial nucleus, spawning crystal morphologies such as plates, needles, and malcrystalline masses[138]. Plate-like crystals are composed of a parallel alignment of *n*-alkanes, where surface (001) consists of methyl groups at the end of alkane molecules and surface (010), (101), and (111) comprise mainly methylene groups as shown in Figure 8[139].

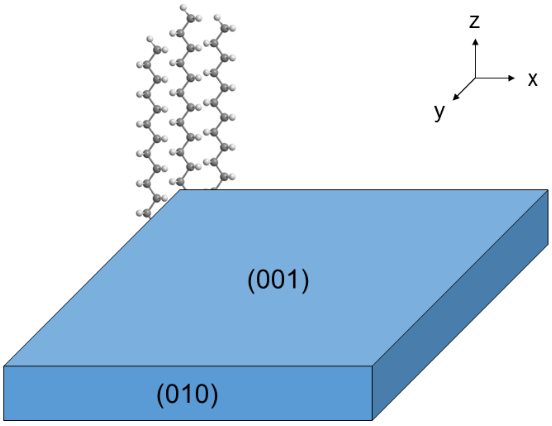

Figure 8. The calculated morphology of a paraffin crystal[139].

As growth continues, wax crystals can reach dimensions large enough for crystals to interlock and form volume spanning networks, as illustrated in Figure 9. This process is referred to as agglomeration and the resulting crystal network can exhibit solid-like flow properties. A significant fraction of liquid oil is occluded within this volume-spanning crystal matrix[54]. Waxy gelling is reported to occur at a solid wax content of 1 – 2 wt%, but it has been shown that a gel can form at wax contents as low as 0.5 wt% [57, 105].

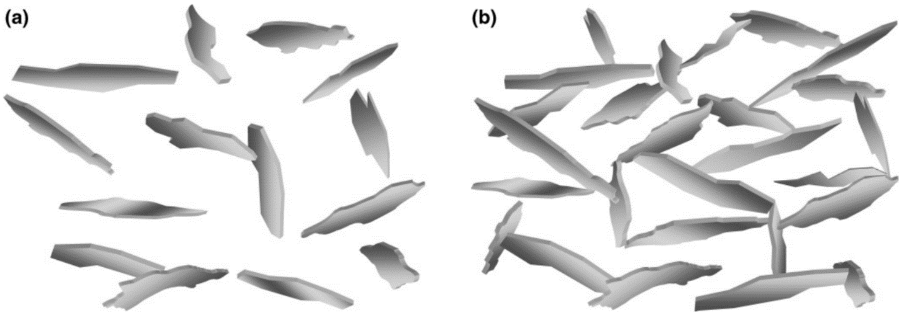

Figure 9. Schematic of plate-like wax crystals that are (a) a free flowing dispersion and (b) in a volume-spanning crystal interaction network[105]

Crystal agglomeration is strongly affected by the crystal morphology. Co-crystallization of alkanes with a higher degree of branching (i.e. *iso*-alkanes) can lead to distortion of plate or needle shaped wax crystals, forming dendrite-like and distorted crystal masses[12, 38]. Gelling of such waxes is consequently delayed, as a higher amount of crystallized solids is required due to lower spatial dimensions of individual crystals. Moreover, the effect on the crude oil viscosity is less pronounced, because distorted crystal masses tend to exhibit lower hydrodynamic radii.

Since crystal morphology is composition-dependent, macrocrystalline and microcrystalline wax are distinguished. The latter contains large amounts of higher molecular weight *iso*-alkanes (see section 3.3). Macrocrystalline wax leads to the formation of strong gels, whereas microcrystalline wax forms weaker gels[37]. The pour point of single component wax ($C_{36}$) was observed to be lowered after addition of lower molecular weight *n*-alkanes ($C_{32}$ and $C_{28}$), which implied a weakening of the formed structures by including inhomogenities[140]. On the other hand, polydispersity has been reported to faclitate gelling due to nanoscale surface roughness of crystals, which provides contact mesh points for crystal interlocking[93]. Waxy gel structure and strength are therefore highly composition dependent.

After the gelation onset, continued wax precipitation induces further crystal growth, leading to enhanced crystal interlocking and an overall stronger crystal network. The dependency between solid wax content $\Phi$ and gel yield strength $\tau_y$ was reported to follow an exponential function as shown in Equation (13) [141], where $\Phi_c$ is a constant, and $a$, $b$ and n are model parameters.

$$\tau_y = \exp(a + b(\Phi - \Phi_c)^n) \tag{13}$$

Other factors that influence waxy gelling are thermal and shear history[142]. High shear rate or stress during wax crystallization can result in the formation of gels with lower yield strength[110]. Moreover, increasing the cooling rate can weaken the crystal network, as this prevents the crystals from growing to larger structures[142, 143]. The resulting yield stress of waxy gels is consequently higher at lower cooling rates[144].

## 5.5.Wax Inhibition

Wax inhibitors and PPDs are widely applied to alleviate issues related to paraffin wax during crude oil production[11]. Different inhibitor chemistries exist as part of wax prevention, which in turn can act beneficially on wax via one or more mechanisms of action.

### 5.5.1. Wax Inhibitors

Wax inhibitors can be grouped into four categories when considering how wax crystallization is affected[10, 24]:

- Thermodynamic wax inhibitors
- Pour point depressants
- Crystal modifiers
- Dispersants and surfactants

Thermodynamic wax inhibitors act by lowering the WAT. This usually entails injection or re-circulating of petroleum or solvent[10], which consequently reduces the relative amount of wax in oil and thereby improves wax solubility. However, re-circulated petroleum, petroleum condensates, and solvents such as benzene, tolene, xylenes, carbon disulphide or chlorinated hydrocarbons are more common for wax removal rather than wax prevention[36]. In wax prevention, thermodynamic wax inhibitors have been stated to be uneconomical, due to the high volume required[24].

PPDs induce pour point beneficiation, hence the name pour point depressants (PPD). This is most commonly achieved by PPDs acting as crystal modifiers, which affect crystal growth and agglomeration, and therefore the structure of the waxy gel[12]. In the ideal case, the resulting crystal morphologies are small and compact with low hydrodynamic radius. The ability of wax crystals to interlock and form a three-dimensional structures is thereby reduced, which reduces pour point and ensures low viscosity of the waxy dispersion[11, 145]. Three main classes of PPDs and crystal modifiers have been distinguished in literature[11, 13, 36], which are ethylene polymers and copolymers, comb polymers, and nanoparticle composites. Ethylene copolymers comprise polyethylene (PE) as crystalline groups and amorphous moieties, such as polybutene (PB) or polyethylene propylene (PEP). The most common and well known ethylene copolymer is ethylene vinyl-acetate copolymer (EVA)[36]. Comb polymers often consist of PE or EVA backbones, which carry pendant alkyl chains. These facilitate interactions with the wax, resulting in on average better wax inhibition as compared to copolymers[11, 36, 146]. Comb polymers are usually synthesized from either (meth)acrylic acid, maleic anhydride or both, resulting in polyacrylate (PA) or poly(maleic anhydride amide co-α-olefin) (MAC) based PPDs[36, 145]. Nanoparticles in combination with polymeric PPDs can be used to enhance effectiveness of the latter. According technologies are still being researched, but chemistries such as poly((octadecyl acrylate) on nanosilica, EVA on nanosilica, and EVA on polymethylsilsesquioxane microsphere have shown promising results[101, 147-149].

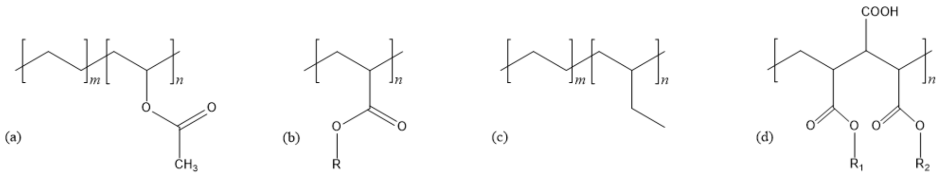

Figure 10. Chemical structure of (a) EVA, (b) PA ester , (c) PE-PEB, and (d) monoester of maleic anhydride acrylate ester copolymer

Dispersants and surfactants coat wax particle surfaces as well as pipeline wall, reducing particle-particle interactions as well as particle adhesion to the wall[24]. For example, Groffe et al. developed a wax dispersant targeted to interfere with the wax crystal growth and agglomeration process, to reduce the overall dimensions of appearing wax crystals, and to adsorb onto metal surfaces rendering them oleophobic[150]. Moreover, synergies may arise from using wax dispersants in combination with pour point depressants[36]. Typical wax dispersants include alkyl sulfonates, alkyl aryl sulfonates, fatty amine ethoxylates, and other alkoxylated products.

### 5.5.2. Inhibition Mechanisms

While the action mechanism of thermodynamic wax inhibitors (improved wax solubility) and wax dispersants (reduced particle adhesion) is straight forward, the precise reaction mechanism of PPDs is still not evident[11]. The common perception is that PPDs react with wax via co-crystallization, and by affecting wax nucleation and wax solubility.

Adsorption of PPD molecules on wax crystals has been studied by molecular dynamics[139, 151-154]. Authors concluded that the PE backbone or pendant alkyl chains of comb polymers adsorb onto the (010) crystal lattice, causing disruption and a decrease in growth rate for further paraffin layers added on top of the PPD[151, 153]. Moreover, it was pointed out that side chain carbon numbers of comb polymers should be close to the average carbon number of crude oil waxes in order to facilitate interaction and co-precipitation[154]. Co-crystallization of PPD polymer with wax has been demonstrated in model waxy solutions, leading to wax crystal distortion and reductions in gel yield strength[155-158].

Above WAT, PE-PEP was shown to self-assemble into micelle-like aggregates, which exhibited a crystalline core with surrounding brushes composed of single alkane chains[159, 160]. Such arrangements can facilitate wax nucleation, creating a larger number of subcritical size wax nuclei, so called polynucleation, which furthermore yields the formation of smaller and more abundant wax crystals[11, 155, 161]. Nanoparticle-PPD composites on the other hand were stated to also act as wax nucleation sites, leading to the formation of larger aggregates that are more compact and amorphous in structure[148, 162].

PPD beneficiation has been reported by many authors to lead to decreased WAT and in some cases also a lower total amount of precipitated wax[96, 155, 161, 163-167]. It has to be mentioned that in addition to decreasing WAT, some additives showed an increase in WDT as well[167]. This indicates that WAT reduction could be the result of kinetic and not thermodynamic effects. However, some authors argue that WAT depression is the result of favorable van der Waals interactions between paraffin chains and long alkyl moieties, leading to improved wax solubilization[11, 168, 169].

### 5.5.3. Petroleum Components with Wax Alleviating Effect

Asphaltenes have been classified as PPD active substance that are naturally occurring in crude oil[95, 103, 106, 166, 170-175]. Asphaltenes were reported to co-crystallize with wax, altering crystal morphology to smaller and distorted crystals, which improved crude oil flowability[106, 171, 176, 177]. Moreover, asphaltene aggregates can serve as nucleation sites for wax crystals, leading to improved rheology due to more finely dispersed wax crystals on the one hand[95, 106], but increasing WAT on the other hand[178]. Some authors state no synergistic interactions between asphaltenes and wax[179], while others report asphaltenes to aggravate issues related to wax[178, 180]. Whether or not asphaltenes have a beneficial effect on wax crystallization has therefore been discussed contradictorily[176]. These contradictions do not come as a surprise when considering the polydisperse nature of asphaltenes. It has been reported that mainly the aliphatic part of asphaltenes is responsible for asphaltene-wax interactions[171, 177, 181]. Experiments featuring fractionated asphaltenes concluded that low polarity and the abundance of alkyl chains accounted for better pour point depression[103, 106, 171, 182].

Nonpolar moieties of polymeric PPDs facilitate interactions with wax, while polar moieties are reported to interact with asphaltenes[11, 183]. Such interactions are complex and the presence of asphaltenes has been reported to both diminish as well as enhance the effect of polymeric PPDs[95, 180]. Synergies beneficial to alleviating wax related challenges were reported for example between asphaltenes and MAC or asphaltenes and EVA[166, 175, 184].

Resins and naphthenic acids were also reported to influence wax crystallization and pour point[95, 177 185]. Possible synergies between indigenous components were pointed out by some of the authors. However, asphaltenes have been the focus of PPD related research among these.

## 5.6.Pipeline Restart Modeling

Shut-in of pipeline flow can lead to waxy gelling, which requires enhanced pressure during restart for breakage and removal of the gelled crude oil. Accurate predictions of pressure and time requirements are therefore necessary for field architecture design, risk abatement, remediation selection, and emergency intervention planning[55].

Three different startup scenarios can be distinguished depending on the elastic-limit yield stress and the static yield stress[186]. Start-up without delay occurs if the pressure applied is high enough for the shear wall stress to be larger than static yield stress. The flow will start immediately with a flow area, a creep area, and an elastic deformation area at the cross-section of the pipeline. The second scenario is given by the shear wall stress being lower than the static yield stress, but higher than the elastic-limit yield stress. In this case, flow will start after a time-period needed for initial shear degradation of the gel. Unsuccessful restart is given by the third scenario, if shear wall stress is lower than the elastic-limit yield stress.

Pipeline start-up and flow cam be modeled based on the finite volume method and according conservation Equations, which are solved in a numerical procedure[58, 187-189]. A simple approach for describing waxy gel degradation is given by first order kinetics in Equation (14) [190], which relates shear stress $\tau$ with time $t$ via initial shear stress $\tau_0$, equilibrium shear stress $\tau_\infty$ and characteristic time constant $t_r$.

$$\tau = \tau_\infty + (\tau_0 - \tau_\infty)e^{-\left(\frac{t}{t_r}\right)} \tag{14}$$

Extensive rheological descriptions are usually encompassed in such modeling approaches. Descriptions can be based on thixotropic, pseudo-plastic, Bingham, and lambda models[55]. The latter for example involves a structural parameter $\lambda$, which is ascribed to the fraction of unbroken linkages in the gel state. It can be used to model decay following a kinetic of order $n$ as shown in Equation (15), where $k$ is the rate constant and $\lambda_e$ is the equilibrium value.

$$\lambda = -k(\lambda - \lambda_e)^n \tag{15}$$

This expression was further used by Zhao et al. to derive a generalized shear stress relationship following third order degradation kinetics as provided in Equation (16)[110, 143]. Here, $\gamma$ is the absolute strain, $h$ is the Hookean constant, and $\lambda_0$ is the initial intact crystal-crystal bond fraction.

$$\tau = \left[\frac{1}{(n-1)k\gamma + \frac{1}{(\lambda_0 - \lambda_e)^{n-1}}}\right]^{\frac{n}{n-1}} \left[h\gamma - \frac{\tau_\infty}{(\lambda_0 - \lambda_e)^n}\right] + \tau_\infty \tag{16}$$

A unified approach is given for example by simplification of the DeKee and Turcotte model in combination with Bingham description as shown in Equations (17), (18), and (19) [55, 191]. This model uses yield stress $\tau_y$, maximum yield stress $\tau_{y,m}$, residual stress $\tau_r$, shear rate $\dot{\gamma}$, critical strain $\gamma_c$, viscosity $\eta$, maximum viscosity $\eta_m$, residual viscosity $\eta_r$, and breakdown rate constant $a$.

$$\dot{\gamma} = \frac{\tau - \tau_y(\gamma)}{\eta(\gamma)} \tag{17}$$

$$\tau_y = \tau_r + \tau_{y,m}\left[\left(1 - \frac{\tau_r}{\tau_{y,m}}\right)^{1-n} + a(\gamma - \gamma_c)\right]^{\frac{1}{1-n}} \tag{18}$$

$$\eta = \eta_r + \eta_m\left[\left(1 - \frac{\eta_r}{\eta_m}\right)^{1-n} + a(\gamma - \gamma_c)\right]^{\frac{1}{1-n}} \tag{19}$$

Complete rheological description during pipeline restart is provided by Equations (17), (18), and (19), which includes the domains low deformation yielding, initial breakdown with deformation, mid-range and mid-to-high strain degradation, and residual slurry Bingham behavior[55].

## 5.7. Wax Deposition Phenomena and Modeling

Simulation of wax deposition build-up and growth is based on equations derived from the finite volume method in computational fluid dynamics. Depending on the model formulation, these comprise one to three transport phenomena domains, i.e. conservation of heat, mass, and momentum[192-194]. The main mechanisms associated with wax deposition include the following[7]:

- *Molecular diffusion* of dissolved wax molecules towards the pipeline wall and into the wax deposit drives deposit build-up and growth.
- *Shear dispersion* of precipitated wax particles leads to the adhesion of these on the wax deposit or pipeline wall.
- *Brownian diffusion* of wax particles can also facilitate wax deposition growth.
- *Gravity settling* will result in the settling of precipitated wax particles at the bottom of the pipeline.

It is generally agreed that molecular diffusion is the dominant mechanism for wax deposition[7, 13, 195]. In addition, shear dispersion and shear stripping reduction are included in some wax deposition simulators[196]. Other mechanisms reported comprise Sorret diffusion, thermophoresis, Saffman effect, and turbophoresis[195, 197].

Aging is commonly modeled as continued diffusion of wax into the deposit layer[5, 198-200]. Ostwald ripening has been reported as an additional effect to contribute to aging[201]. Turbulent flow of waxy crude oil in the pipeline can be described using dimensionless number correlations. Correlations based on Seider and Tate, Dittus-Boelter or the Colburn analogy have been used to calculate the laminar boundary layer, as well as turbulent heat and mass transfer coefficients[7, 192].

Wax deposition modeling usually results in a system of non-linear differential Equations, which are then iteratively solved using numerical integration procedure[192, 199, 202, 203]. Currently available commercial software packages include OLGA wax, FlowWax, WAX® and Michigan Wax Predictor[7]. OLGA wax is a steady state compositional pipeline simulator, which uses diffusion as the major transport mechanism of wax molecules to the pipeline wall[204]. Later versions of OLGA also include shear dispersion and shear stripping reduction[196]. The Michigan Wax Predictor considers diffusion of wax only, but incorporates aging and precipitation kinetics during simulation[192]. DepoWax is based on research done by Lindeloff and Krejbjerg[196, 205]. The according modeling approach also uses a steady-state compositional pipeline simulator with turbulent transfer correlations. WAX®, alternatively referred to as TUHWAX, uses pseudo-steady state to compute one-dimensional flow on the four consecutive steps of hydrodynamics, heat transfer, thermodynamic and deposition rate[9]. Molecular diffusion is also the dominant deposition mechanism. All mentioned simulation packages have the option of multiphase use[7].

# 6. Experimental Techniques – Theories and Principles

DSC, rheometry, and CPM are fundamental in studies of characteristics such as WAT, WPC, wax crystal morphology, and gel yield strength. In addition, techniques such as ITC, GC/MS, and NMR were used in this work to investigate PPD inhibitor-wax interactions on a more fundamental basis.

## 6.1. Wax Preconditioning Protocol

As has been pointed out in section 5.4, wax crystallization is highly influenced by thermal and shear history. Rheometry experiments therefore often encompass accurate shear conditions during wax crystal formation and gelling, such as constant shear rate, shear stress, or quiescent conditions[107, 142, 206]. Thermal history is usually removed by heating to sufficiently high temperature $T_1$ for time interval $t_1$, as illustrated in Figure 11. Solvent evaporation has to be considered during the preconditioning segment if the system is not hermetically sealed. After resetting the thermal history, defined cooling takes place at constant cooling rate $\dot{T}_{cool}$. During cooling, measurements of WAT, WPC, and gelation point can be conducted. The pour point is defined with respect to a constant cooling rate (1.5 °C/min) in ASTM D5949 [91], but other pour point procedures can impose nonlinear cooling gradients. Gel yield strength is usually measured at isothermal conditions $T_2$ after an equilibration segment $t_2$ [55, 101, 207].

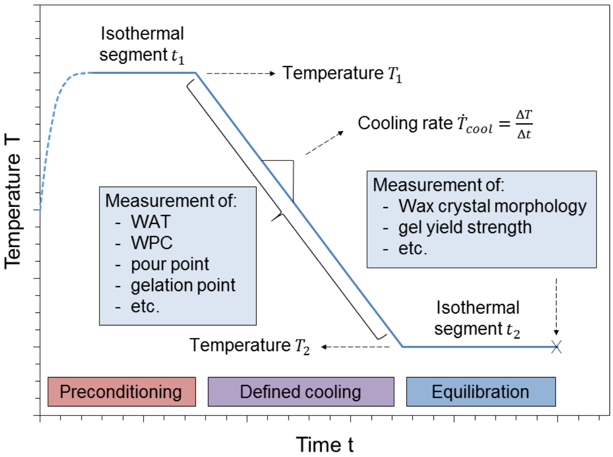

Figure 11. Heating protocol for wax crystallization experiments.

## 6.2. Differential Scanning Calorimetry (DSC)

Differential scanning calorimetry (DSC) is a thermo-analytical technique, which investigates the heat released or taken up by a sample. The setup consists of two sockets in a chamber, which is approximately adiabatic. As shown in Figure 12, sample pan and empty reference pan are placed on designated disks.

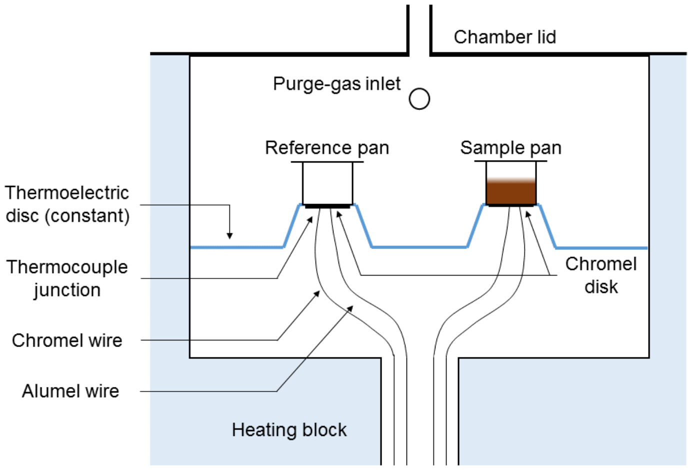

Figure 12. DSC schematic[208]

The chamber is continuously flushed with gas to provide an inert atmosphere. The difference in heat flow of sample and reference socket is measured during data acquisition. A temperature program is applied during experimentation, which typically consists of a series of linear or modulated temperature changes, as well as isothermal segments. This allows for the study of exothermic and endothermic effects that can occur over time or as the temperature changes. Instrument calibration is done by measuring the temperature and heat of melting pure metal, e.g. indium, zinc, tin or gallium, or pure *n*-alkanes. Common applications of DSC include material science, food research, pharmaceutical applications, and petroleum related research[86, 209-211]. In particular, for the study of transition states in metal alloys and phase transition of polymers, DSC is still a very contemporary method[212-215]. In petroleum related research, DSC is predominantly used to study the precipitation of waxes[35, 76, 83, 216]. WAT can be determined due to the exothermic character of wax crystallization, but procedures have also been published on estimating the total wax content[86] as well as the composition of wax in DSC[84]. Linear temperature gradients are commonly used to measure WAT, but the applicability of modulated DSC has also been shown[217].

## 6.3.Rheometry

Rheology is the study of deformation and flow of matter. This discipline seeks to provide quantitative parameters that define how a material will deform as a function of force, time, and space[218]. Application areas include food processing, biofluids, paper and pulp suspensions, polymers, drilling muds, asphalt, paint, and cement industry[219]. Rotational shear rheometers are most commonly used to study according fluids. These can be equipped with concentric cylinder, double gap cylinder, cone-plate, double cone-plate,

plate-plate, and cone-cone type geometries. A schematic of cone-plate geometry, as used in a rotational shear rheometer, is shown in Figure 13.

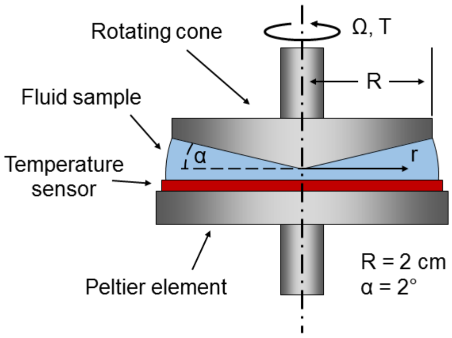

Figure 13. Schematic of cone and plate geometry for rotary rheometers

The advantage of a cone-plate geometry is a uniform shear rate distribution along the radius, which accounts for a comparably simple evaluation of measurement data. At small cone angels ($\alpha < 3$ °), shear rate $\dot{\gamma}$, shear stress $\tau$, and viscosity $\eta$ can be calculated in terms of angular velocity $\Omega$, torque $M$, and geometry radius $R$ using Equations (20), (21), and (22).

$$\dot{\gamma} = \frac{\Omega}{\alpha} \tag{20}$$

$$\tau = \frac{3M}{2\pi R^3} \tag{21}$$

$$\eta = \frac{3\alpha M}{2R^3} \tag{22}$$

The in comparison small gaps used by cone-plate geometry are advantageous for accurate temperature control, which is essential when researching paraffin wax crystallization. In addition to the Peltier element controlling temperature of the bottom plate, a temperature-controlled hood is often used to enclose the top part of the geometry.

A constant shear rate is imposed during viscometry, which can be used to determine WAT as the result of particle induced changes in apparent viscosity[35, 76, 216]. Imposed oscillatory strain or stress can be used to determine the gelation point temperature, which is usually defined as the intersection of storage and loss modulus[100, 101]. Alternatively, non-oscillatory procedures impose a constant shear stress and define gelation as the temperature at which the shear rate reaches zero[38, 107]. Gel yielding is measured after isothermal equilibration and has been used to provide input data for pipeline restart modeling[55, 58, 60, 108, 186].

## 6.4. Cross-polarized Microscopy (CPM)

CPM technique employs optical microscopy coupled with cross-polarization filters. As illustrated in Figure 14, light is polarized in one plane before entering the sample and a subsequent polarization filter with 90° orientation in respect to the first filter.[7] The presence of crystalline structures can rotate the plane of polarization, thereby enabling light to pass the second filter.

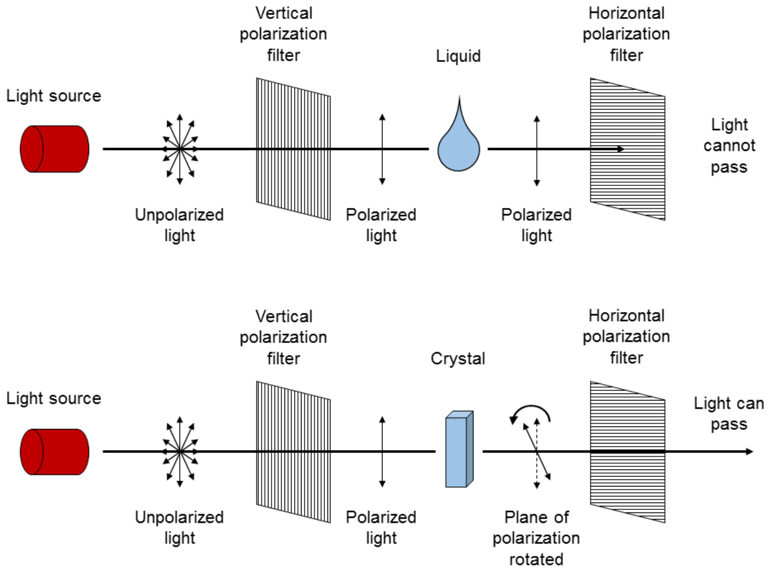

Figure 14. CPM imaging illustrated by effect of a) homogeneous liquid and b) crystalline material on polarized light[7]

An advantage of this technique is that structures can be observed, which are otherwise less or not at all visible in the surrounding liquid medium. One of the most common applications of CPM in flow assurance is the determination of WAT[35, 76, 80, 82, 83, 111]. Moreover, this technique allows viewing of wax crystal morphologies, which has been instrumental in researching crystallization mechanisms and evaluating effect and performance of wax inhibitors[140, 146, 149, 220-223]. For example, CPM imaging has been used for kinetic modeling of wax crystallization, where the amount of light transmitted was assumed to be proportional to the amount of crystalline wax[224]. Moreover, image analysis tools have been used on CPM images to study aspect ratio and size distribution of wax crystals[225].

## 6.5. Isothermal Titration Calorimetry (ITC)

ITC is a technique employed to measure the heat released or taken up by a solution during titration. ITC is built with a sample and a reference cell, both enclosed by an adiabatic chamber. As shown in Figure 15, a syringe is inserted into the sample chamber, which is used for both stirring and titration.

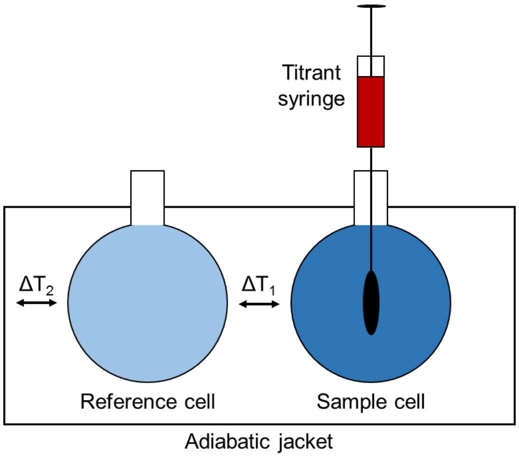

Figure 15. ITC setup schematic

During an experiment, the heat flow required to keep both reference and sample cell at isothermal conditions is recorded. Heat changes due to titration can thus be measured and used to compute the reaction heat between titrant and analyte. ITC is a technique predominantly used to study proteins, ligand binding and interactions with proteins, as well as RNA folding[226, 227]. ITC was first applied to petroleum related systems by Merino-Garcia et al., who investigated the nature of asphaltene-resin and asphaltene-nonylphenol interactions[228, 229]. Furthermore, Wei et al. studied self-association of asphaltene model compounds, aggregation of tetrameric acid, as well as interactions between asphaltenes and tetrameric acid or asphaltene inhibitors.[230-233] This research was continued by Subramanian et al., who measured self-association properties of asphaltenes that had previously been fractionated via solids adsorption or stepwise precipitation[234].

In order to measure the interaction heat between inhibitor and wax, contributions from both inhibitor and wax dilution have to be accounted for as well. Three different types of experiments are therefore conducted in accordance with the procedure developed by Wei et al[233]. The interaction heat $\Delta H_{int}$ is then calculated by subtracting the heat of titrating inhibitor into blank solvent $\Delta H_{PPD}$ and titrating blank solvent into waxy solvent $\Delta H_{wax}$ from the combined heat of titrating inhibitor into waxy solvent $\Delta H_{tot}$ as shown in Equation (23).

$$\Delta H_{int} = \Delta H_{tot} - (\Delta H_{PPD} + \Delta H_{wax}) \tag{23}$$

## 6.6.Proton Nuclear Magnetic Resonance (NMR) Spectroscopy

NMR principle is based on observing the spin of atomic nuclei in presence of magnetic fields. Hydrogen atoms have been studied from the emergence of NMR spectroscopy due to their high receptivity[235]. The spin is a type of angular momentum used in quantum mechanics to describe intrinsic properties of an atomic nucleus. With a spin quantum number of $I = 1/2$, hydrogen can take up two orientations in a magnetic field. The energy difference $\Delta E$ between these two states is given by Equation (24), where $h$ is Planck's constant, $\gamma$ is the gyromagnetic ratio, and $B_0$ the magnetic field strength.

$$\Delta E = \frac{h\gamma B_0}{2\pi} \tag{24}$$

In NMR technique as used in this thesis, a homogeneous magnetic field leads to alignment of the nuclear magnetic moment along the direction of this field. An oscillating magnetic field (RF-field) is then imposed, transverse to the external magnetic field, leading to transitions between the two energy levels[236]. When the RF-field is switched off, the system will align with the external field again, which induces changes in the magnetic flux that are recorded by the same RF-coil used to excite the system. A schematic of the technique is shown in Figure 16.

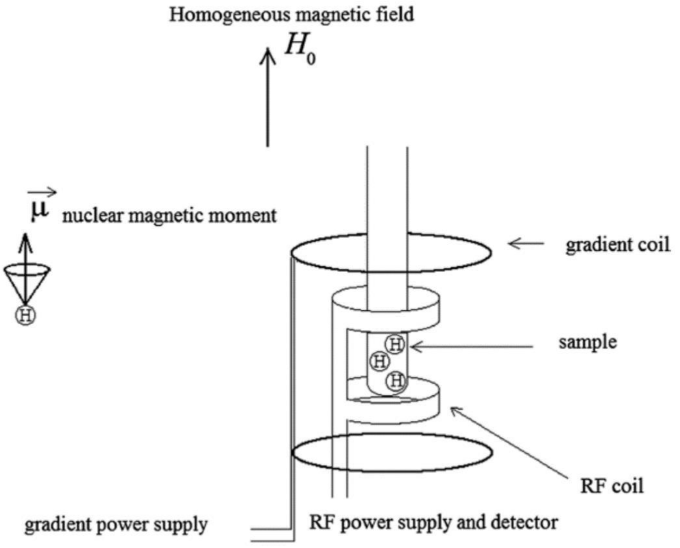

Figure 16. Schematic of PFG-NMR technique[236]

The pulsed field gradient (PFG) NMR method is a well-established technique for studying molecular motion without disturbing the system under investigation, which utilizes hydrogen atoms shifting between the two orientations in a magnetic field[236]. While NMR is a powerful technique for investigating structure and dynamics of various molecules, PFG-NMR has extended to study systems such as dispersions and emulsions[236, 237]. Molecular translation can be studied via diffusion ordered spectroscopy (DOSY), yielding the diffusion coefficient[238]. Using Stokes-Einstein relation given in Equation (25) [239], diffusion coefficient $D$ and Boltzmann constant $k_B$ can further be used to compute the hydrodynamic radius $R_H$.

$$R_H = \frac{k_B T}{6\pi\eta D} \tag{25}$$

NMR-DOSY has for example been applied to study the hydrodynamic radius of asphaltene aggregates in organic solvent[234]. Classical NMR has been used to quantify the solid wax content by relating the signal obtained 10 µs (solid signal contribution) and 70 µs (liquid signal contribution) after the 90° excitation pulse[85]. This method exploits the mobility difference of hydrogen atoms between the two aggregate states. A similar approach for quantifying solid wax uses deuterated solvent, where the liquid phase signal reflects the amount of dissolved components[163].

## 6.7. Gas Chromatography coupled Mass Spectrometry (GC/MS)

Gas chromatography (GC) is an analytical technique used for separating components. The general objective is to find out which components are contained in a particular sample and in what quantity. As the name suggests, GC operates on substances in gaseous phase, so being able to vaporize a sample is a prerequisite for this technique. During analysis, the sample is introduced via the inlet into a column, from which components are eluted and measured in the detector.

Most samples analyzed by gas chromatography are liquids, so an essential function of the inlet is to vaporize the sample and introduce a representative portion as a narrow band on the column[240]. This is commonly realized using split/splitless inlets, where sample is injected by a needle into a heated liner, which is continuously flushed with carrier gas. Either a defined fraction of this carrier gas (split mode) or all carrier gas (splitless mode) is diverted onto the column. Other injector types include on column injection, where the liquid sample is directly injected into the column, or temperature programmed evaporation. High requirements are imposed onto carrier gas purity, as impurities can skew the measurement and cause damage to inlet and column. Capillary columns commonly used in GC are wall-coated open-tubular columns, which are coated with a liquid polymer film, and porous-layer open-tubular columns that are covered with a solid porous-layer having large adsorbing surface[241]. Separation in the column is based on the principle of retention, which implies that dissimilar components are eluted after different retention times. Differences in retention can be caused by differences in solute mobility and solute adsorption on the stationary phase, which can be the cause for a solute migration velocity that is lower than the velocity of the mobile phase (carrier gas).

Detectors are operated at the column outlet to quantify the amount of eluted components. Typical techniques include flame ionization detector, electron capture detector, and mass spectrometer detector (MSD)[240].

The advantage of GC coupled with MSD is that the mass spectrum of an elution peak contains additional information that can be used for component identification. Upon entry of eluent into MSD, the molecules are ionized by an ion source. Ions are then accelerated in an electrical field and separation is achieved on the basis of ion mass over charge value (m/z). Soft and hard ionization can be distinguished, where the latter produces a spectrum of different ion fragments that is component characteristic. MSDs differ mainly in the construction of the analyzer as a beam or ion storage instrument[242]. Typical analyzers include magnetic sector analyzer, quadrupole analyzer, and ion trap analyzer.

# 7. Main Results

The main results obtained from all publications in this thesis are summarized in this chapter. Publications were rearranged in an order that allows for a logical structure, but not a chronological one.

For cross-comparison between the different publications, an overview of PPD additives and their use is provided in Table 3. Further information is listed in the according publications. To test PPD effect on wax crystallization, model systems were mostly based on 5 – 10 wt% macrocrystalline wax in organic solvent.

Table 3. Overview of polymeric PPD additives used throughout the publications

| **Publication** | **PPD alias** | **Concentration (Technique)** | **Chemistry based on** | **Active content** |
|---|---|---|---|---|
| I | PPD | 1000 ppm (DSC, CPM, rheometry) | PA, EVA | 50 % |
| II | PPD 1 | 1000 ppm (DSC, CPM), 2000 ppm (rheometry), 1 wt% (ITC) | Polycarboxylate | 80 % |
| | PPD 2 | | Polycarboxylate, maleic acid | 70 % |
| | PPD 3 | | PA, EVA | 50 % |
| | PPD 4 | | EVA, 25 % Vinyl Acetate | 100 % |
| | PPD 5 | | Modified EVA | 100 % |
| III | PPD $1_P$ | 1000 ppm (DSC, CPM, rheometry), 2 wt% (ITC) | Polycarboxylate (purified) | ~100 % |
| IV | PPD A | 1000 ppm (DSC, CPM, rheometry, NMR, GC/MS) | Polycarboxylate (purified) | ~100 % |
| | PPD B | | Modified EVA (purified) | ~100 % |
| | PPD C | | EVA, 40 % Vinyl Acetate | 100 % |
| V | PPD α | 500 ppm (DSC, CPM, rheometry) | Polycarboxylate (purified) | ~100 % |
| | PPD β | | Modified EVA (purified) | ~100 % |
| | PPD τ | | PS-block-poly(ethylene-ran-butylene)-block-PS | 100 % |
| | PPD Ω | | EVA, 25 % Vinyl Acetate | 100 % |

## 7.1.Publication I

*Nonlinear dependency of wax appearance temperature on cooling rate*

The subject of this study was to introduce improvements to existing procedures for WAT determination and discuss the results with respect to the theoretical WAT, in particular the thermodynamic solubility limit of wax in organic solvents.

In DSC, the prevailing method for WAT determination is by intersection of tangent lines fitted to both baseline before WAT and inflection point of the wax crystallization peak[7]. As shown in Figure 17, this procedure can lead to underestimation of the actual WAT, as baseline deviation usually occurs already before the intersection point.

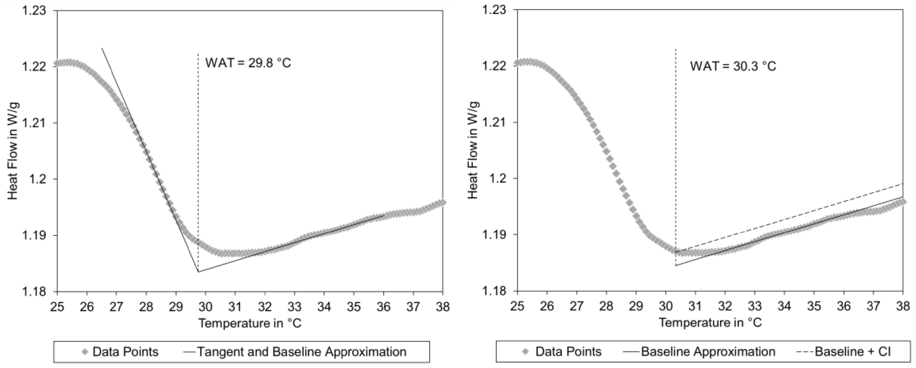

Figure 17. WAT determination using the tangent procedure (left) and a confidence interval (right). The data was recorded via DSC using a light crude oil at a cooling rate of 2 °C/min.

To anticipate improved WAT detection, previous authors have therefore defined WAT based on exceeding the thermal noise of the sample[83]. This approach was further refined into a statistical method, which is also displayed in Figure 17. A confidence interval $CI$ is computed as shown in Equation (26), where $\overline{H}_i$ is the linear baseline fit of data $H_i$ on the temperature interval $\left[T_j, \dots, T_n\right]$.

$$CI = ci \cdot \sigma = ci \sqrt{\frac{1}{n-j}\sum_{i=j}^{n}\left(\overline{H}_i(T_i) - H_i\right)^2} \tag{26}$$

WAT detection is further defined as the highest temperature, below which three consecutive points are outside the confidence interval $CI_{n+k} + \overline{H}_{n+k}(T_{n+k})$ with $k = 1,2,3$. Assuming normal distribution of the thermal noise, the term $ci$ allows for a statistical interpretation of the error. Choosing e.g. $ci = 1.960$ or $ci = 3.291$ implies that less than 5 % or 0.1 %, respectively, of data points outside the confidence interval account for random noise. The term $ci$ therefore allows tuning of the procedure to detect WAT either with higher sensitivity (low $ci$) or with lower statistical error (high $ci$).

The procedure was furthermore adapted to work with viscometry data. To be able to apply the same linear baseline regression, viscometry data was linearized by assuming Arrhenius type viscosity-temperature dependency. Corresponding linearized function is shown in Equation (27), where $\mu$ is the viscosity, $\mu_0$ is the pre-exponential factor, $E_A$ is the activation energy, $R$ the ideal gas constant, and $T$ the temperature.

$$\mu = \mu_0 e^{\frac{E_A}{RT}} \quad \Leftrightarrow \quad \ln(\mu) = \frac{E_A}{R}\frac{1}{T} + \ln(\mu_0) \qquad (27)$$

Initial testing was done with DSC data of solutions with different amounts of macro- or microcrystalline wax in toluene or $n$-dodecane solvent. It showed that the developed procedure was precise if the onset of wax crystallization yielded a pronounced signal change. Low wax concentrations as well as low cooling rates increased the noise contribution, which could result in delayed WAT detection, increased scattering, or no detection of WAT. However, all tested model solutions with more than 5 wt% wax in solvent showed significant WAT detection at cooling rates as low as 0.5 °C/min.

A method comparison of DSC, CPM, and viscometry was conducted on three model waxy solutions and three crude oils. The results are plotted in Figure 18. Data was reproducible within a certain margin of error, and data scattering was the most pronounced for CPM technique. A possible explanation for this is that CPM monitors only a small portion of the sample in contrast to DSC and viscometry, where the sum of effects over the entire sample volume is measured. Overall, no method showed to be the most sensitive for all samples tested, which is in agreement with the reports of other authors[80, 83, 111, 216]. For light crude oil, and macrocrystalline wax in dodecane, either CPM or DSC measured the highest WAT on the entire range of cooling rates. In case of octacosane in dodecane, as well as medium crude oil, DSC technique measured the highest WAT at cooling rates 3 °C/min and above, but viscometry measured the highest WAT at the lowest cooling rate. It was therefore concluded, that more than one technique and a range of representative cooling rates should be tested when assessing WAT.

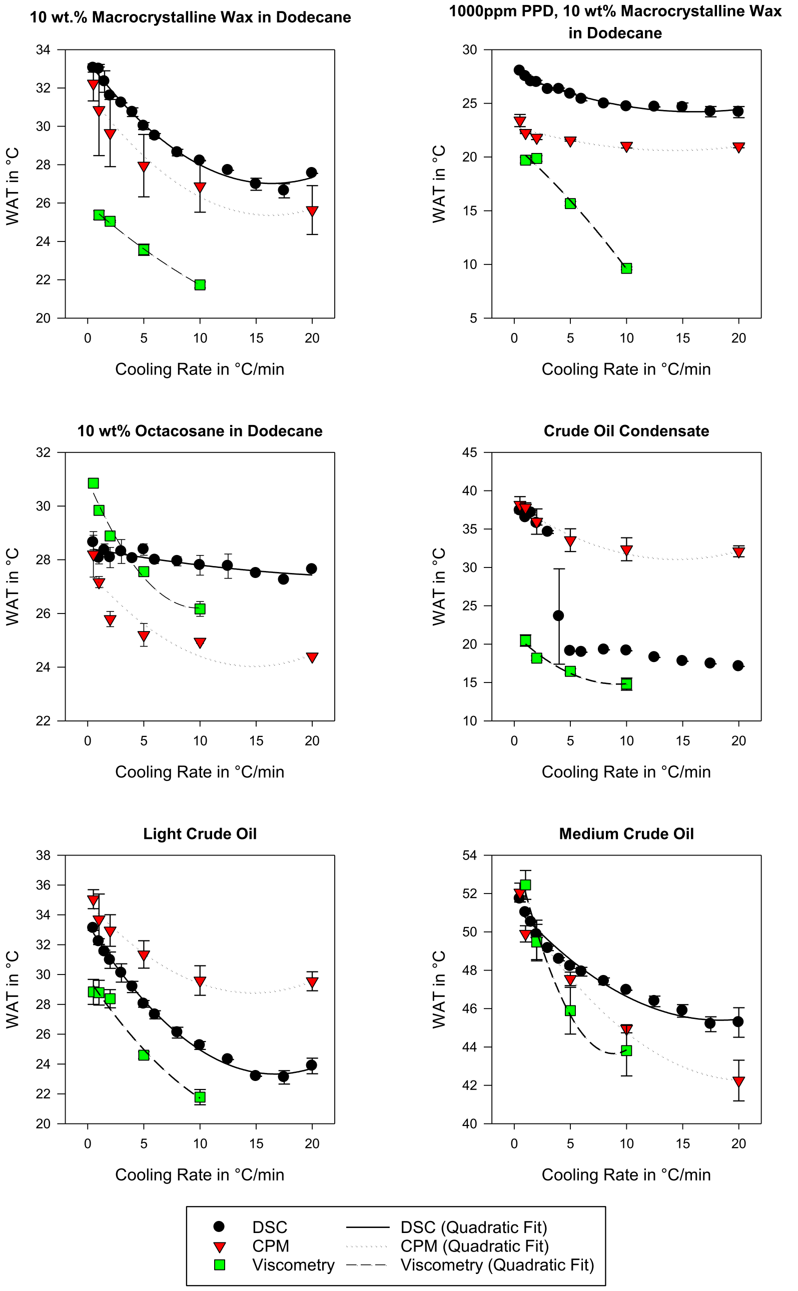

Figure 18. DSC, CPM, and viscometry results: Development of WAT in dependence of cooling rate tested for three model waxy oils and three crude oil samples. Each point represents the average of two to four measurements with according standard deviation. Data series were fitted with a quadratic regression equation.

Measurements in Figure 18 predominantly showed a non-linear progression of WAT with cooling rate. To model the experimental data, the description derived from homogeneous nucleation theory by Paso et al. in Equation (11) was used. The paraffin solubility limit was calculated via the van't Hoff relationship in Equation (3). Under the assumption of one pseudo component, which contributes to the first precipitating fraction, this description could also be extended to polydisperse paraffin waxes. A good model fit was obtained as shown in Figure 19.

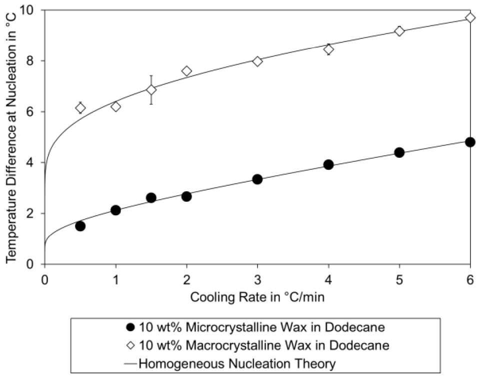

Figure 19. Temperature difference at nucleation in relation to cooling rate for polydisperse paraffin waxes in dodecane. Each value is the average of three measurements, where error bars represent the according standard deviation. The solid lines represent fittings made via homogeneous nucleation theory.

The presented data was also discussed in terms of extrapolation to zero cooling rate. In theory, such an extrapolation could provide a simple approach for obtaining the thermodynamic solubility limit of a given sample. Other authors had previously performed such a linear extrapolation from data with cooling rates ranging from 2 to 20 °C/min[141, 243]. As illustrated in Figure 18, linearity between WAT and cooling rate is only not always the case. Descriptions based on second degree polynomials resulted in a better fit of the measured data, but extrapolation with polynomials is not recommended as long as the equations are not based on relevant physics. Under consideration of equations derived from homogeneous nucleation theory, such an extrapolation could be made via logarithmic or exponential equations. However, under consideration of the experimental data, a strong change in function value would be required when approaching zero cooling rate, which is a region not well defined by the data. Experimental data showed an approximately linear region from 0.5 to 2 °C/min, which could be utilized for linear extrapolation instead. It was concluded that such extrapolation underestimated the actual solubility limit, but that this procedure provided a more accurate estimate than measuring at a fixed cooling rate.

## 7.2. Publication II

*Isothermal Titration Calorimetry for Assessing Wax-Inhibitors*

In this study ITC investigations were performed at two distinct temperatures to distinguish PPD-wax interactions taking place with either dissolved or crystallized wax. The study focused on wax interactions with one selected PPD and asphaltenes.

ITC interaction heat was measured by injecting 2 wt% active PPD or asphaltene solution in xylene isomer blend. Experiments were carried out at 20 °C and 35 °C using 10 wt% macrocrystalline wax in xylenes. Since corresponding WAT is approximately 27 °C, interactions at 20 °C took place with crystalline and dissolved wax, whereas interactions at 35 °C took place with dissolved wax only. Results for PPD $1_P$ are illustrated in Figure 20.

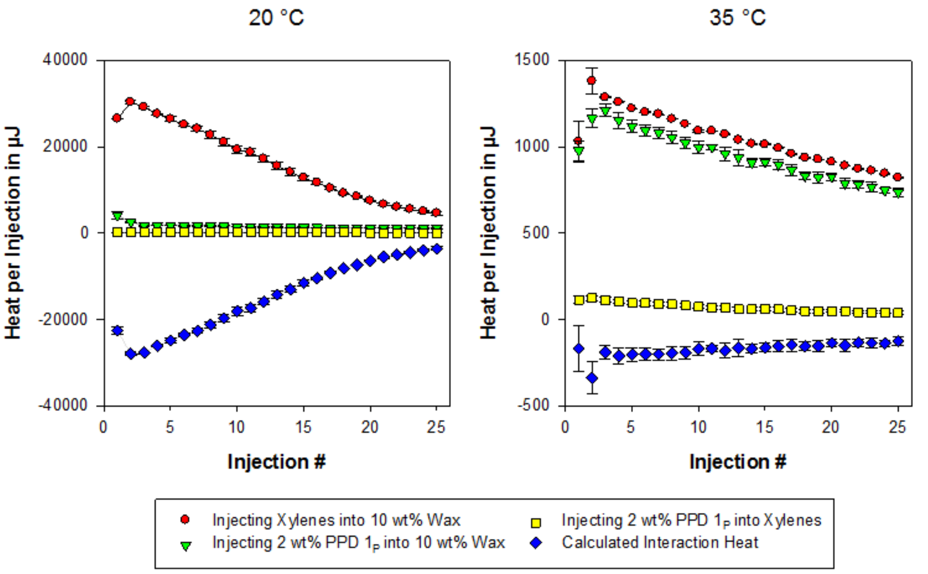

Figure 20. ITC results: Heat per injection for determining the interaction heat of 2 wt% PPD $1_P$ in xylenes with 10 wt% wax in xylenes at temperatures 35 °C and 20 °C. Experiments consist of 25 injections of 10 µl substance into 1 ml sample cell with xylene isomer mixture as bulk solvent. Each measurement represents the average of two to four measurements with according standard deviation.

The dilution heat of PPD $1_P$ is approximately equal at both temperatures and constitutes the lowest contribution to the interaction heat. Overall, injections of blank solvent into wax solution or dispersion show the largest heat contribution. At 35 °C, combined heat of injecting PPD $1_P$ into wax dispersion is almost equal to the wax dilution heat. At 20 °C, this combined heat is low compared to pure solvent injections into wax, which implies exothermic effects cancelling out with endothermic dilution and re-dissolution of wax. The interaction heat consequently is two magnitudes higher at 20 °C than at 35 °C.

For experiments taking place with wax solutions only, the interaction heat was computed with respect to the molar ratio of injected PPD or asphaltenes divided by wax in the sample cell. For this, the average molecular weight of wax was calculated as molar average according to the composition provided in literature[244]. Asphaltene molecular weight was approximated by 750 g/mol, a value reported from fluorescence depolarization[40]. A rough approximation of 150 g/mol as monomer weight was assumed for PPD $1_P$.

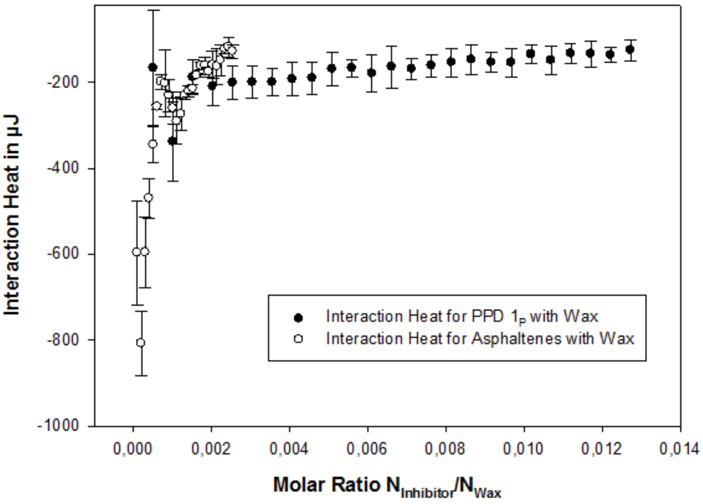

Figure 21. Interaction heat measured at 35 °C and related to molar ratio in the titration cell

The decreasing trend in asphaltene-wax interaction heat shows a depletion of binding sites. In case of PPD $1_P$, there appears to be excess wax molecules, as the interaction heat is decreasing at a much lower rate than for asphaltenes. Overall, the developed procedures enabled quantification of PPD-wax interactions featuring both dissolved and crystalline wax. It was shown that interactions of PPD $1_P$ with crystalline wax were stronger by a factor of up to 150 than interactions with dissolved wax only. The greater interaction heat could be explained by co-crystallization of the PPD. All in all, it was concluded that PPD additives can interact with both dissolved and crystallized wax.

## 7.3.Publication III

*Wax-Inhibitor Interactions Studied by Isothermal Titration Calorimetry and Effect of Wax Inhibitor on Wax Crystallization*

The subject of this study was to use ITC to measure PPD-wax interactions and compare the results to performance characteristics, such as lowering WAT, gel yield strength, or altering wax crystal morphology. Five different PPDs listed in Table 3, as well as asphaltenes were tested in a model waxy oil made of macrocrystalline wax in toluene.

First, PPDs were characterized in terms of molecular weight (HPLC) and precipitation in pure toluene (DSC). Size-exclusion chromatography (SEC) showed a polydisperse molecular weight distribution for all PPDs. The average molecular weight of PPD 4 was highest, and the average molecular weight of PPD 2 lowest. The polydisperse character of PPD 1, 2, and 3 was also reflected by two local maxima occurring in the DSC heat flow. At concentrations of 5 wt% in toluene, PPD 3 showed the lowest and PPD 4 the highest precipitation onset temperature.

Additive performance was evaluated using DSC, CPM, and rheometry. Addition of PPD 1 to the model waxy oil showed the largest WAT decrease in both DSC and viscometry. Other PPDs accounted for approximately 2 – 3 °C WAT decrease compared to the additive free sample, while asphaltenes showed smaller effect. CPM imaging revealed a morphology change from to larger plate-like crystals to small and finely dispersed wax crystals after addition of PPD 1 and 2. PPD 3 and asphaltenes induced the growth of slightly larger but compact crystals. PPD 5 caused little change in crystal morphology. The sample containing PPD 4 exhibited two kinds of crystal types, i.e. small and dispersed crystals, and large crystal aggregates with the largest dimensions observed in this study. CPM imaging corresponded with rheometry measurements at the same temperature. PPD 1 and 2 prevented gelling at 4 °C completely, PPD 3 and asphaltenes showed a large reduction of gel yield strength, and PPD 4 and 5 induced little to no change to gel yield strength.

PPD-wax interaction heat was measured by ITC at 20 °C. Injections were made with 1 wt% active PPD in toluene in the injection syringe and 10 wt% macrocrystalline wax in toluene in the sample chamber. PPD blank injections showed negligible heat contribution due to dilution of PPD 4 and 5, changing exothermic and endothermic character of PPD 1, 2, and 3 dilution. Endothermic asphaltene de-aggregation was found, similar to a previous study[232]. At 20 °C, wax was present in the sample chamber in both solid and dissolved state. As a result, injections made into this wax dispersion were of predominantly endothermic character, because re-dissolution of wax exhibited the largest heat contribution. The only exception was injecting PPD 4 into the wax dispersion, which yielded an exothermic signal. The calculated interaction heat was consequently largest for PPD 4, as shown in Figure 22. PPD 1, 2, and 5 resulted in average and almost identical interaction heat. PPD 3 showed lower interaction heat during the first seven injections and asphaltenes accounted for the lowest interaction heat.

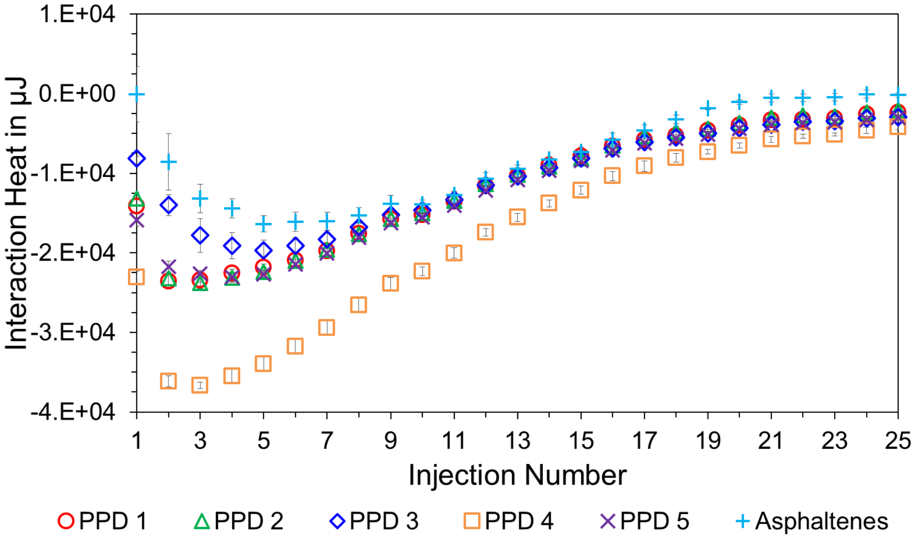

Figure 22. Resulting interaction heat for 1 wt.% active PPD or asphaltenes with 10 wt.% macrocrystalline wax dispersion in toluene at 20 °C. Each injection accounts for 10 µl of titrant being added to 1 ml of wax dispersion. Error bars represent the standard deviation from the average of each measurement.

An additional result of ITC investigations is that asphaltenes showed considerable interaction heat. Corresponding values were lower than for PPD additives, but still these results indicate asphaltene-wax interactions and possible co-crystallization mechanism, which disputes reports stating contradicting effects or no synergistic interactions with wax[176, 179].

ITC maximum interaction heat and additive performance are summarized and compared in Table 4. Overall, PPD 1 and 2 accounted for the best wax inhibition, while displaying average interaction heat. PPD 5 on the other hand showed similar interaction heat as PPD 1 and 2, but exhibited poor wax inhibition performance. The highest interaction heat was measured for PPD 4, which ranks among the last three when ranking performance. It was therefore concluded, that interaction heat and chemical additive effect on alleviating wax related issues show no distinct relation. The ability of PPDs to co-crystallize with wax appears to be a necessity, but other characteristics are important as well, such as changing wax crystal morphology to smaller crystals with less propensity to interlock.

Table 4. Comparison of additive performance with maximum interaction heat

| | **No PPD** | **PPD 1** | **PPD 2** | **PPD 3** | **PPD 4** | **PPD 5** | **Asphaltenes** |
|---|---|---|---|---|---|---|---|
| ITC, maximum interaction heat [mJ] | | -23.6 | -23.8 | -19.7 | -36.6 | -23.0 | -16.4 |
| WAT, DSC, 5 °C/min [°C] | 20.1 | 14.6 | 17.6 | 17.7 | 18.7 | 17.8 | 18.8 |
| WAT, Viscometry, 5 °C/min [°C] | 22.6 | 19.1 | 20.7 | 20.9 | 20.8 | 21.3 | 22.3 |
| Gel-breakage strength [Pa] | 401 | No Gel | No Gel | 120 | 295 | 362 | 71 |
| CPM, crystal morphology | Needle and plate shape | Small, compact | Small, compact | Compact, round | Small and compact or big flakes | Needle and plate shape | Distorted, dendrite like |

## 7.4. Publication IV

*Inhibitor-wax interactions and PPD effect on wax crystallization: New approaches for GC/MS and NMR, and comparison with DSC, CPM, and rheometry*

The subject of this article was to study PPD-wax interactions in liquid phase by the use of NMR and GC/MS compositional analysis. The results were further compared to the PPD effect on WPC depression (DSC) and wax crystallization, i.e. effect on waxy gel strength (rheometry), apparent viscosity during wax crystallization (viscometry), and wax crystal morphology (CPM).

Four different additives, PPD A based on polycarboxylate, PPD B based on PA and EVA, and PPD C based on EVA with 40 wt% vinyl acetate content, as well as asphaltenes were selected for experimentation. The model waxy oil was composed of 5 wt% macrocrystalline wax in toluene with and without the addition of 1000 ppm PPD. All experiments used a cooling rate of 0.2 °C/min to ensure comparability among the results.

Before investigating additive-wax interactions in liquid phase, additive effect on wax crystallization was investigated. The results allowed for a performance ranking as listed in Table 5.

Table 5. Additive performance ranking and effect on wax crystallization

| Additive | Performance | Effect on wax crystallization |
|---|---|---|
| PPD A | Best | Wax crystal distortion to small and finely dispersed particles. Fluid remains free flowing during continuous shearing and after quiescently cooling to -2 °C. |
| PPD B | Good | Wax crystal distortion to round and compact aggregates. Significant increase in apparent viscosity, but fluid also remains free flowing during continuous shearing and after quiescently cooling to -2 °C. |
| PPD C | Poor | Wax crystals are smaller and more finely dispersed, but still exhibit needle or plate shaped geometries. Apparent viscosity was lower than the additive free case during continuous shearing, but gel yield strength increased significantly after quiescent cooling. |
| Asphaltenes | Fair | Wax crystallizes in smaller and more dispersed crystals. Gel yield strength is decreased significantly as compared to the case without additive. Apparent viscosity is lower than the additive free case for the largest part of temperatures tested. |

DSC experiments showed a reduction in WAT for all tested additives. The effect of additive on WPC depression could vary. As shown in Figure 23, asphaltene accounted for no measureable reduction in amount of precipitated wax with temperature. The temperature, below which significant WPC depression was measured, the same trend as the PPD performance ranking. In other words, PPD A addition reduced the total amount of precipitated wax already at WAT, whereas PPD B addition lead to noticeable reduction below 15 °C and PPD C at even lower temperatures.

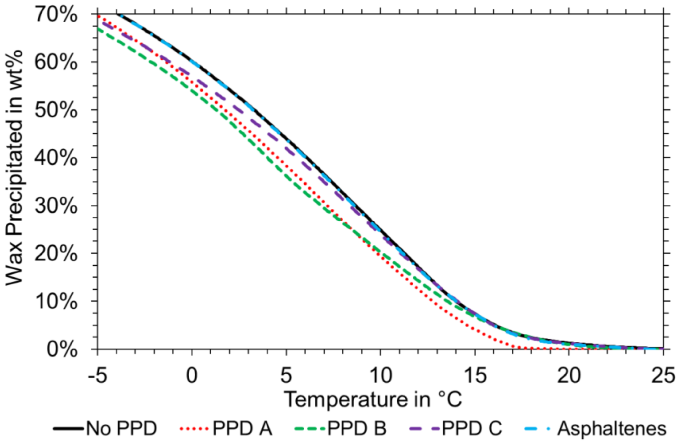

Figure 23. DSC Wax precipitation curve (WPC) for 1000 ppm PPD or asphaltenes and 5 wt% wax in toluene. Percentages were calculated with respect to the total amount of precipitated wax. Lower temperatures were omitted from the plot for better overview.

The apparent solid wax measured by NMR technique showed similar trends as in DSC. In addition, $T_2$-distributions obtained by NMR contained qualitative information. The data in raw form is plotted in Figure 24. Recorded signal intensity is due to hydrogen atoms of dissolved wax, since deuterated toluene was used as bulk solvent. Artifacts and solid phase contributions are visible below $T_2$ of $10^{-3}$ s, but were more pronounced when wax had precipitated or after PPD addition. The hexadecane calibration sample exhibits a shift towards shorter $T_2$ with decreasing temperature, which is caused by the decrease in viscosity and thereby mobility of the dissolved wax. Wax crystallization showed the occurrence of two secondary peaks in addition to the main peak: One around $T_2$ of $10^{-2}$ s and one between $10^0$ – $10^1$ s. The secondary peak at shorter $T_2$ can be explained by the dissolved wax molecules with reduced mobility due to proximity to solid wax crystals. Chemical additives appeared to greatly influence these secondary peaks. PPDs with good performance showed a suppression of either the secondary peak at low $T_2$ (PPD A) or at higher $T_2$ (PPD B). PPD C and asphaltenes in contrast both led to an increase of the secondary peak at low $T_2$. PPD C in particular showed broadening of the $T_2$-distribution and overlapping with signal contributions from the solid phase. Chemical additives therefore appear to influence interactions at the solid-liquid interface, which affects the mobility of dissolved wax molecules.

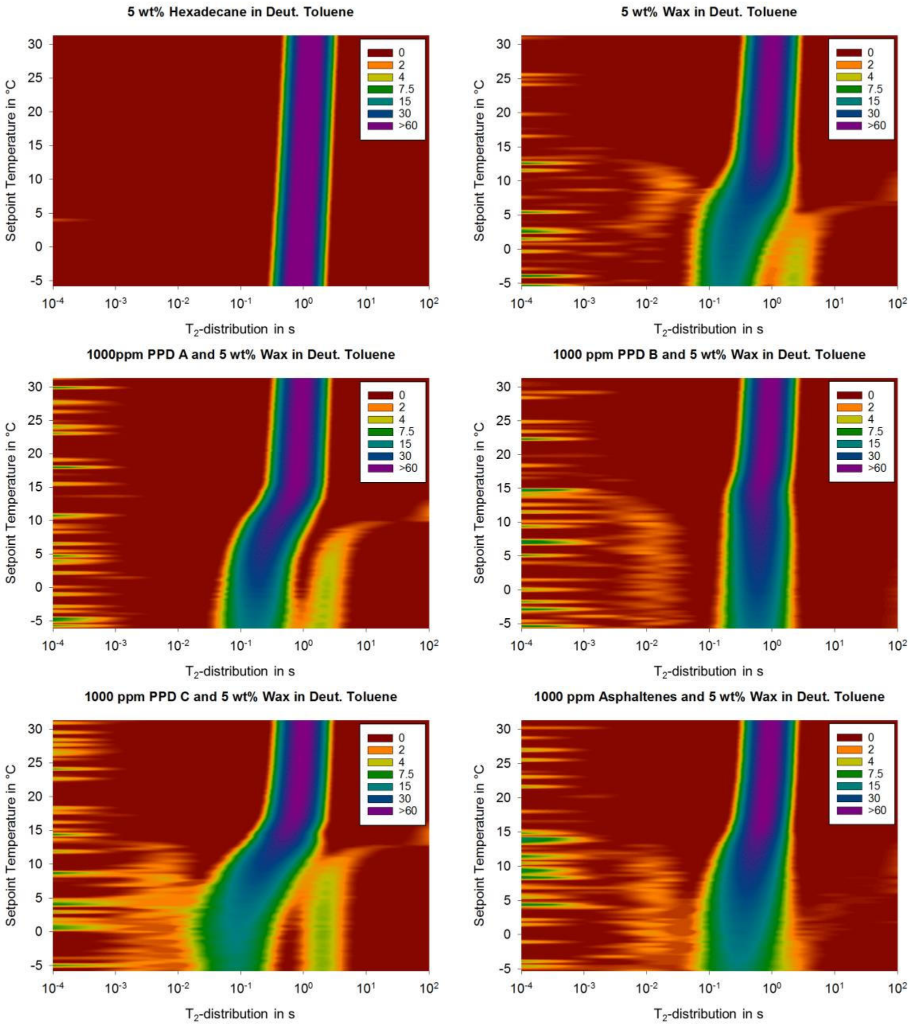

Figure 24. NMR $T_2$-distribution in dependence of (uncorrected) setpoint temperature. Each measurement was made on 3 g solution of 5 wt% alkanes in deuterated toluene with and without 1000 ppm PPD.

GC/MS experiments investigated liquid phase composition of samples taken at specific temperature intervals during wax crystallization, where the solid phase had been removed by filtration. The analysis focused on *n*-alkanes with carbon numbers in the range of $C_{20}$ to $C_{40}$, making up 84.6 wt% of the total wax sample. Data was assessed in terms of the concentration decrease per component and sampling interval. Results of the additive free sample, PPD A, and PPD B are plotted in Figure 25. All samples show similar trends, according to which wax crystallization can be categorized into three steps. Right after the onset of wax crystallization, step (i) is marked by *n*-alkane depletion on a broad range of molecular weight. As the sampling temperature is further decreased, in step (ii) the affected molecular weight range is shifted to a narrower region, which is approximately bell shaped. At even lower temperatures, this bell shaped curve is progressively shifted towards lower molecular weight regimes during step (iii). The effect of PPD addition could induced a delay of step (i) or (ii). This is shown for example in reduced wax precipitation for PPD A between 18 °C and 14 °C. In case of PPD B, *n*-alkane depletion on a broad range of step (i) was extended from 18 °C down to 14 °C.

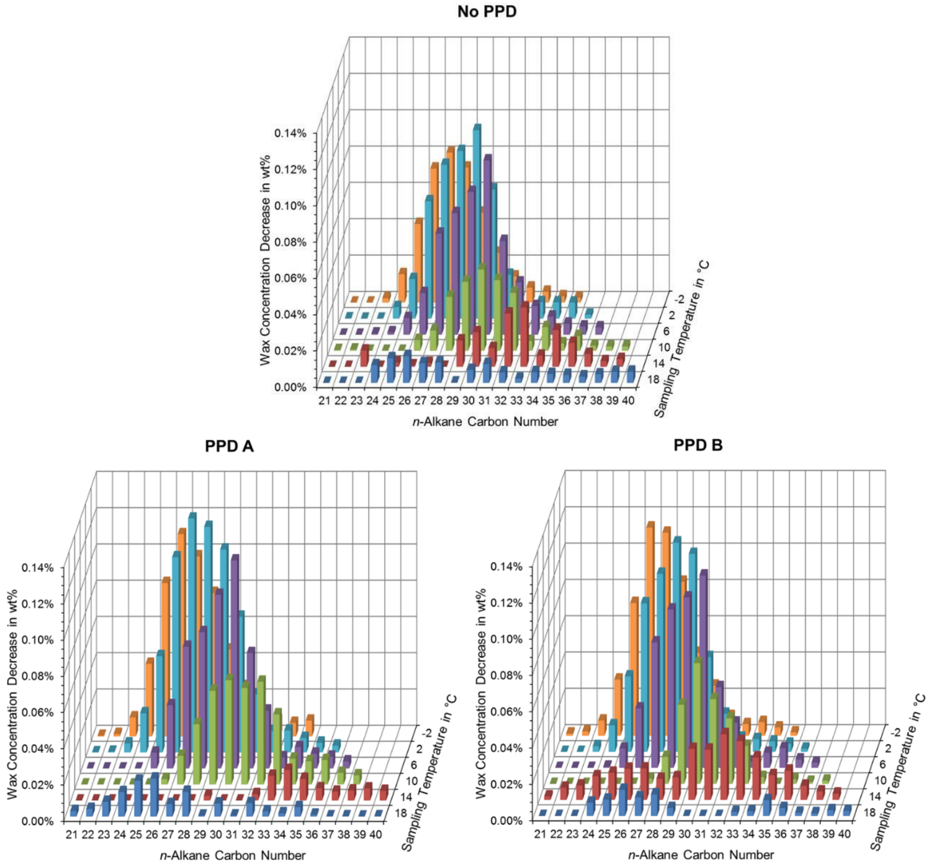

**No PPD**

**PPD A**

**PPD B**

Figure 25. Changes of n-alkane content in liquid phase as measured by GC/MS. Each sample consisted of 1000 ppm PPD and 5 wt% wax in toluene. The wax concentration decrease was computed by subtracting each alkane concentration from the next higher temperature concentration.

In addition to qualitative considerations of the alkane depletion spectrum, the sum over all components was calculated to estimate the relative *n*-alkane decrease. This was put in perspective with the additive ability to depress WPC, more specifically delay precipitation of all wax components. It showed that PPDs with good inhibition performance selectively favored *n*-alkane precipitation. Such an observation makes sense from the viewpoint that comb polymers often carry pendant alkane chains that are tailored to match the average carbon number of the wax[11, 154].

A comparison of WPCs estimated by different techniques is plotted in Figure 26. No PPD and PPD A were selected to represent the base case and one additive with pronounced effect on wax precipitation. As can be seen, the techniques do not superimpose, but depicted trends are similar. NMR shows and earlier onset temperature of wax precipitation than DSC, but a lower total solids content at lower temperatures. GC/MS results are naturally different from DSC and NMR, as only 84.6 wt% of the total wax was considered. The differences between NMR and DSC can be cause by the individual measuring technique, but also by the procedure for calculating the solid wax content. For example, the baseline fitting of DSC data was conducted with a polynomial function, which might not fully represent the involved physics. Moreover, the temperature correction function for NMR did not take into account the heat contribution from exothermic wax crystallization. Moreover, NMR experiments were conducted with deuterated toluene, which has a dissimilar molecular weight than toluene used with other techniques.

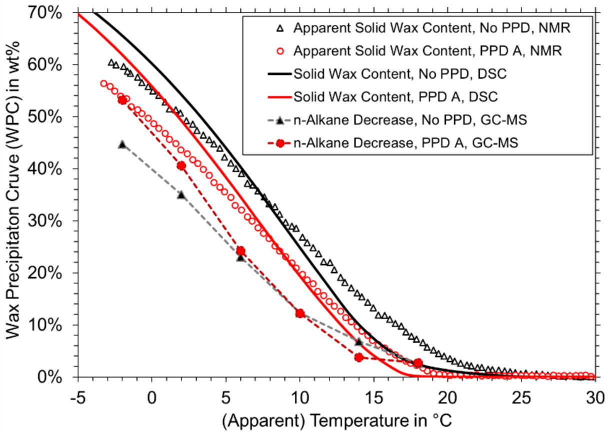

Figure 26. Comparison of WPC determined by different techniques for samples of 5 wt% wax in toluene with and without 1000 ppm PPD A.

In conclusion, it was illustrated that PPD additives interact with paraffin wax in a number of different ways. Co-crystallization might be the main effect responsible for pour point depression, but reducing the overall amount of precipitated wax is contributing to delay gelling as well. Moreover, it was shown that additives can delay certain stages in compositional change during wax precipitation, and affect interactions of dissolved wax at the solid-liquid interface.

## 7.5. Publication V

*Influence of Wax Inhibitor Molecular Weight: Part 1. Fractionation and Effect on Crystallization of Polydisperse Waxes.*

The subject of this study was to fractionate four PPD additives into groups with different molecular weight and investigate the effect of PPD fraction onto wax crystallization.

Two polydisperse PPDs based on polycarboxylate (PPD α) and polyacrylate/EVA (PPD β) were fractionated via stepwise precipitation from *n*-dodecane, separation and purification of both supernatant and precipitate. Two PPDs based on PS-block-poly(ethylene-ran-butylene)-block-PS (PPD τ) and EVA with 25 wt% VA (PPD Ω) were reduced in molecular weight via ultrasonic disintegration in *p*-xylene solvent.

Original and fractionated PPDs were characterized in terms of PS-equivalent molecular weight (HPLC-SEC), hydrodynamic radius (NMR DOSY), and precipitation from n-octane (DSC). Results of HPLC-SEC are plotted in Figure 27. As can be seen, fractionation of PPD α and PPD β resulted in narrower molecular weight distributions for according sub-fractions. In both cases, one fraction with distinctly lower and one with higher molecular weight could be isolated. Ultrasonic disintegration reduced the average molecular weight, while increasing polydispersity.

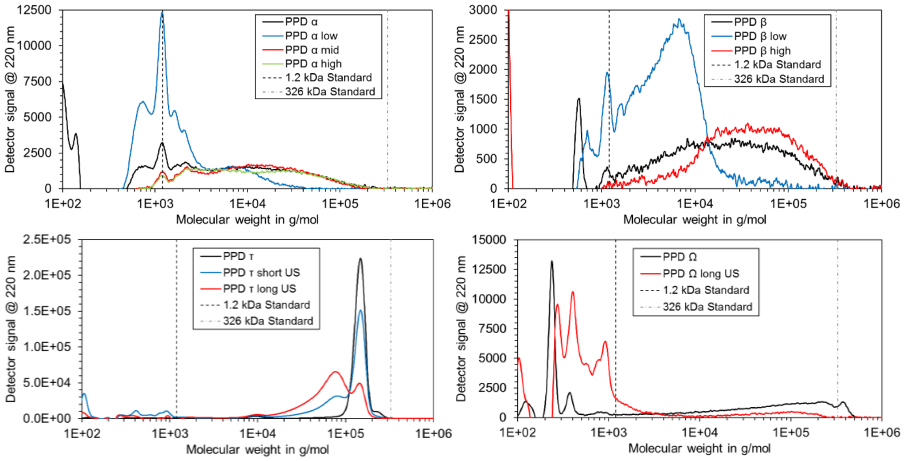

Figure 27. Molecular weight distribution in PS equivalent

The hydrodynamic radius of PPD τ was lowered after ultrasonic treatment, but remained constant in case of PPD Ω and its sub-fraction. The hydrodynamic radius showed an evolution from a broader distribution of PPD α and PPD β towards narrower curves of their respective sub-fractions. Individual trends of these sub-fractions were similar as to HPLC molecular weight distributions.

As can be seen in Figure 28, PPD precipitation from *n*-octane underwent characteristic changes after PPD fractionation. The precipitation profile of PPD τ and PPD Ω was changed little, with slightly increased precipitation temperature after ultrasonic disintegration. Both PPD α and PPD β exhibit multiple crystallization peaks, where the peaks observed at lower temperature would be amplified in case of the lowest molecular weight fraction. The largest peak of either PPD α or PPD β, which is associated with the largest functional portion of each PPD, did not change significantly in precipitation temperature for the highest molecular weight sub-fraction.

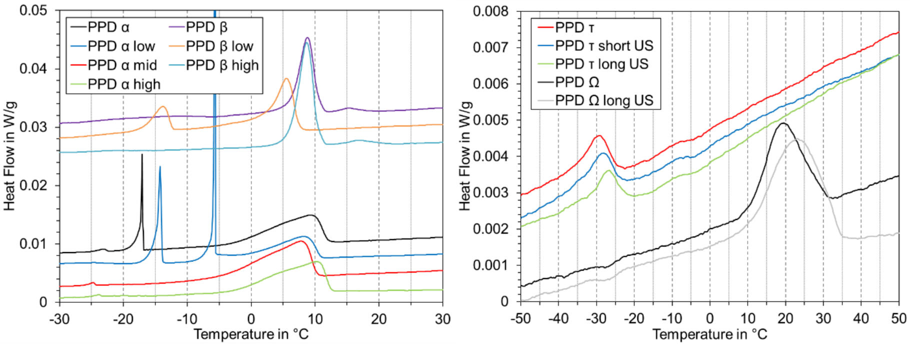

Figure 28. DSC heat flow of 5 wt% PPD in *n*-octane. Each graph represents the average of in total four measurements for improved signal to noise ratio. Graphs were shifted on the y-axis for better overview.

To characterize the effect of each PPD with respective sub-fractions on wax crystallization, DSC and rheology experiments were conducted. Good PPD performance was attributed with the ability to lower WAT or gelation point temperature. Trends in WAT and gelation point depression were similar for different PPD chemistries.

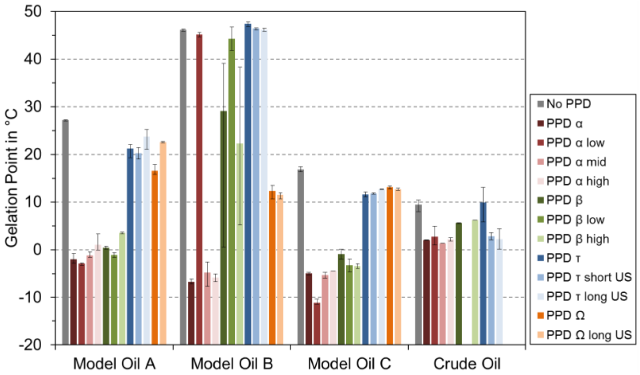

Figure 29. Gelation point computed as average over at least four rheology measurements of 500 ppm PPD in different waxy oils. Error bars mark the minimum and maximum gelation point temperature recorded for each sample. Measurements not displayed indicate that the gelation point was not reached at -20 °C and above.

The results of gelation point measurements are plotted in Figure 29. Overall, PPD τ had the lowest efficiency, PPD α and PPD β were the most effective additives in model oil A and model oil C, and PPD Ω was the most effective in crude oil. Fractionation of PPD τ by ultrasonic disintegration could both aggravate (model oil C) and improve (crude oil) PPD performance. Fractionation by stepwise precipitation exhibited a general trend by the lowest molecular weight fraction (PPD α low and PPD β low) having reduced performance in model oil B and improved performance in model oil A and model oil C. It appeared that removing the high molecular weight fraction of a PPD also reduced the ability of this PPD to act on high molecular weight wax contained in model oil B. These results were also confirmed by CPM imaging, as illustrated in Figure 30. In the presence of PPD α, wax crystallized to compact and amorphous particles with low degree of three dimensional interlocking. In presence of PPD α low, a dense crystal network was formed with little crystal distortion and a high degree of crystal interlocking.

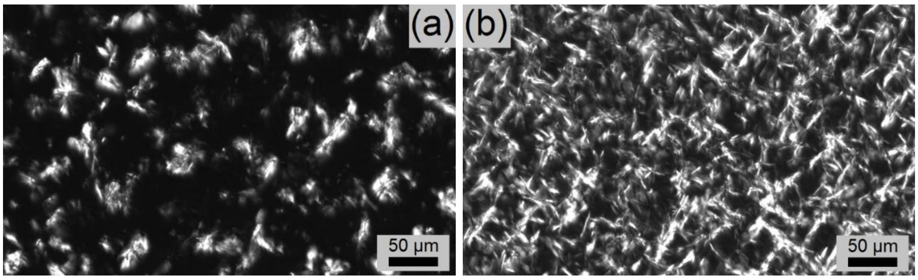

Figure 30. CPM images taken after isothermal equilibration at 20 °C of (a) PPD α in model oil B, and (b) PPD α low in model oil B

In conclusion, PPD molecular weight is one of the parameters that are influencing the additive effect on wax crystallization. Tailoring PPD molecular weight to a particular waxy crude oil can further depress gelation temperature, whereas PPD efficiency can be diminished if molecular weight is not adjusted right. However, effect on wax crystallization and performance of a particular PPD is largely determined by the type of PPD and functional groups. Developing effective wax inhibitors for flow assurance, the molecular weight is therefore a parameter that can be optimized during a later stage of additive development.

## 7.6.Publication VI

*Asphaltene fractionation based on adsorption onto calcium carbonate: Part 3. Effect of asphaltenes on wax crystallization*

The subject of this study was to test the wax alleviating effect of asphaltene fractions with different characteristics. Asphaltenes were fractionated by either adsorption and desorption on calcium carbonate or via stepwise precipitation. Asphaltene effect on wax crystallization was investigated by DSC, rheometry, and pour point tests in a model waxy oil composed of 10 wt% macrocrystalline wax in xylene.

The first procedure was based on stepwise addition of *n*-hexane to heavy crude oil and extraction of the precipitated asphaltenes[234]. Asphaltene fractions *3.5V* (18.2 wt%), *3.5V-6V* (34.3 wt%), and *6V-40V* (47.5 wt%) were obtained, where the prefix indicates the amount of *n*-hexane in ml per mass of crude oil in g. The obtained fractions contained asphaltenes with similar functional groups, but increasingly better solubility in alkane solvent. Elemental analysis revealed similar composition, but an increased oxygen content of *3.5V* asphaltenes.

The second procedure introduced improvements to the previously published batch-method[245], by using a fixed bed column of calcium carbonate. *Whole* asphaltenes were extracted by 40 ml/g *n*-hexane dilution of heavy crude oil. These were then dissolved in toluene and brought in contact with the calcium carbonate. Part of the asphaltenes did not adsorb (*bulk* asphaltenes, 38.8 wt%), which were collected by flushing calcium carbonate with toluene. Subsequent flushing with chloroform yielded the *adsorbed* asphaltene fraction (42.7 wt%). After that, calcium carbonate was dissolved with hydrochloric acid, asphaltenes were extracted with chloroform and dichloromethane and collected as *irreversibly adsorbed* asphaltenes (12.4 wt%). Elemental analysis revealed a progressive increase in H/C ratio and oxygen content that are lowest for *bulk* asphaltenes and highest for *irreversibly adsorbed* asphaltenes. FTIR spectroscopy showed abundance of similar alkyl groups for all fractions, but increased amounts of carbonyl, carboxylic or derivative groups for *irreversibly adsorbed* asphaltenes.

Increasing the concentration of *whole* asphaltenes revealed a progressive reduction in gel yield strength. No-flow point and WAT would also decrease with increased asphaltene concentration, but could increase again once a certain concentration was reached. CPM imaging revealed a change in wax crystal morphology to more compact and branched structures with increasing asphaltene concentration. These results indicate that *whole* asphaltenes act as PPD and crystal modifier.

Asphaltene fractions were tested as 1500 ppm asphaltenes and 10 wt% macrocrystalline wax in xylene. Results showed different effects on waxy gel strength and $WAT_0$ extrapolated to zero cooling rate, as illustrated in Figure 31. *Bulk* asphaltenes had the greatest effect on $WAT_0$, but showed less reduction of waxy gel strength than *whole* asphaltenes. *Irreversibly adsorbed* asphaltenes induced the lowest reduction in $WAT_0$ and gel yield strength. The largest effect on gel yield strength was made by *3.5V* and *3.5V-6V* asphaltenes, which suggests that low asphaltene solubility can help to alleviate waxy gelling.

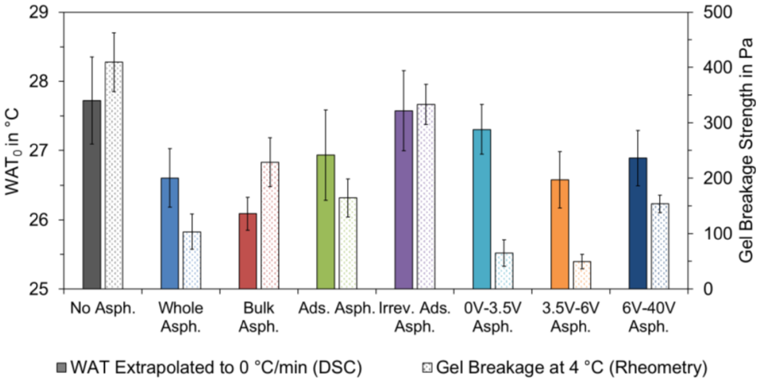

Figure 31. Influence of different asphaltene fractions on $WAT_0$ and gel breakage. Measurements were done with 1500 ppm asphaltenes and 10 wt% macrocrystalline wax in xylene isomer blend. The $WAT_0$ was obtained via linear extrapolation from cooling rates between 0.5 °C/min and 2 °C/min with four measurements per cooling rate, yielding 16 measurements per $WAT_0$. Gel breakage strength was calculated as the maximum yield stress recorded during gel breakage with four to six measurements per sample. Error bars represent the standard deviation of each value.

Similar trends as in Figure 31 were observed by pour point tests. *Bulk*, *3.5V*, and *6V-40V* asphaltenes induced pour point depression larger than that of *whole* asphaltenes. *Irreversibly adsorbed* asphaltenes showed the lowest effect on pour point. CPM imaging showed that *irreversibly adsorbed* asphaltenes induced the largest changes to wax crystal morphology. As depicted in Figure 32, the addition of *irreversibly adsorbed* asphaltenes led to the formation of smaller and more disperse wax crystals. However, the crystal network appears to be denser, which could explain the higher gel yield strength. *3.5V* and *3.5V-6V* asphaltenes both induced a higher degree of crystal branching as compared to *whole* asphaltenes. Addition of *bulk* asphaltenes showed less effect of wax crystal morphology.

It appears that *bulk* asphaltenes, displaying a high solubility and a higher degree of aromaticity, worked best at improving wax solubility and delaying waxy gelation. Reduction of waxy gel strength was achieved the most by *3.5V* and *3.5V-6V* asphaltenes, which exhibited mixed functional groups and lower solubility. High polarity, as found in *irreversibly adsorbed* asphaltenes, had the least beneficial effect on wax crystallization, which is in agreement with the findings of other autors[103, 171, 246].

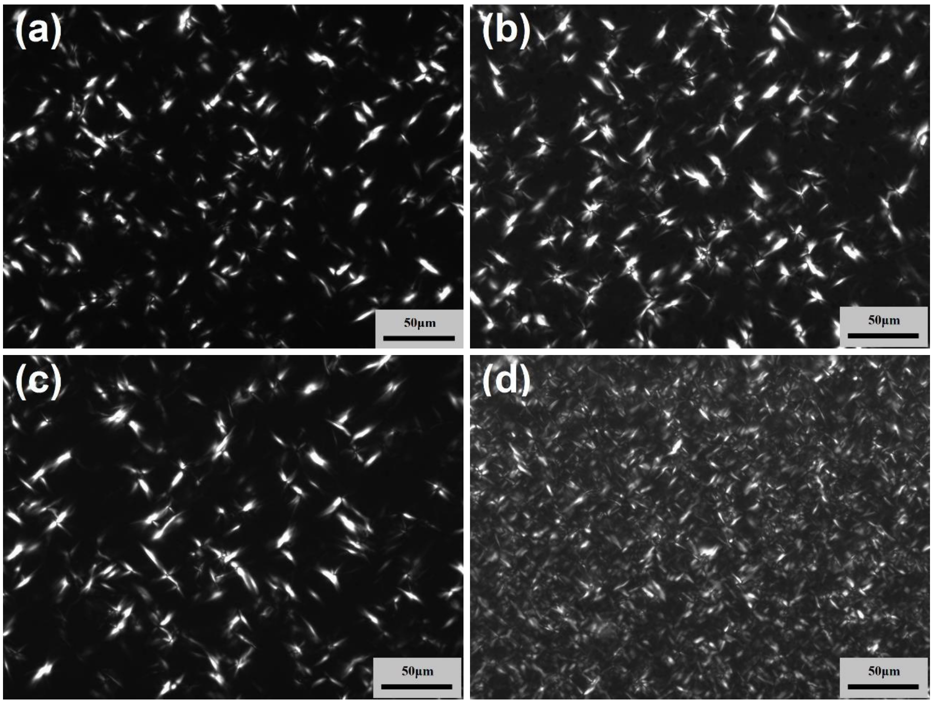

Figure 32. CPM images of 10 wt% macrocrystalline wax in xylene isomer blend with (a) 1500 ppm *whole* asphaltenes, (b) 1500 ppm *3.5V-6V* asphalenes, (c) 1500 ppm *bulk* asphaltenes, and (d) 1500 ppm *irreversibly adsorbed* asphaltenes

ITC was furthermore used to study the interactions of macrocrystalline wax with three selected asphaltene fractions. W*hole* asphaltenes, *bulk* asphaltenes, and *irreversibly adsorbed* asphaltenes were tested to include the fraction with the highest and lowest polarity from fractionation on calcium carbonate, as well as the original material. At 35 °C, interactions of asphaltenes with dissolved wax yielded similar interaction heat. From injection 2 until the last injection, the interaction heat followed an asymptotically decreasing trend, which is a typical pattern for progressive depletion of interaction sites in the bulk wax. Asphaltene interactions with crystalline wax were measured at 20 °C and are plotted in Figure 33. In this case, the interaction heat increases in magnitude until a local extrema is reached between injection 8 and 10, and the interaction heat subsequently decreases. *Whole* asphaltenes showed larger interaction heat than *bulk* and *irreversibly adsorbed* asphaltenes.

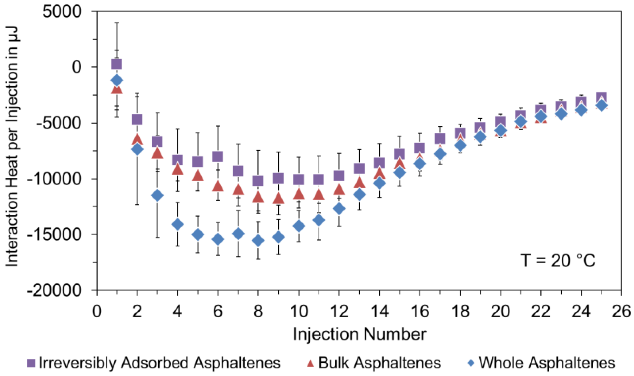

Figure 33. Interaction heat for 2 wt% asphaltenes with 10 wt% macrocrystalline wax in xylene isomer blend at 20 °C. The wax is partially crystallized, as $WAT_0$ = 27.7 °C. Error bars represent the standard deviation.

Overall, asphaltene fractionation did not yield a product equivalent to polymeric wax inhibitors. Inhibition performance tended to be best for asphaltene fractions with low solubility and a mixed range of functional groups. Also, asphaltene interactions with crystalline wax were greater for *whole* asphaltenes than for asphaltene fractions with more distinct properties (*bulk* and *irreversibly adsorbed*). It was therefore concluded that wax crystallization is influenced by an ensemble of asphaltenes with different properties. It was suggested that asphaltenes may form synergies when acting on wax crystallization, which could be explained by bi-functional colloids: Less polar asphaltenes facilitate interaction with wax, i.e. by co-precipitation, whereas more polar asphaltenes impose spatial obstacles for continues wax crystal growth. Still, additional data is needed to support this hypothesis, e.g. the precise structure and composition of individual asphaltene molecules.

# 8. Summary and Conclusion

In this thesis, results were presented with focus on wax crystallization and inhibition. The outcome can be summarized by the following two accomplishments.

(i.) Introduction of new procedures and techniques for investigating wax crystallization and inhibition.
(ii.) Application of (i.) to study inhibitor-wax interactions and improve knowledge and understanding of wax inhibition.

Research was largely conducted on model oils containing only additive and wax in an organic solvent. This approach has the advantage of investigating PPD-wax interactions without the influence of other crude oil constituents. Simplified systems, however, do not fully resemble the real application. Crude oil samples were therefore used in some cases to compare or validate results and procedures.

In publication I, a new algorithm for determining WAT from experimental data was introduced. This algorithm was tested on DSC and viscometry data and compared with CPM measurements featuring multiple model and crude oils. The dependency of WAT with cooling rate was found to be predominantly non-linear, with an approximately linear regime within 0.5 – 2 °C/min. Linear extrapolation to zero cooling rate was found to be a possible measure for comparing samples, even though this does not estimate thermodynamic equilibrium.

In publication II and III, isothermal titration calorimetry (ITC) was introduced to study inhibitor-wax interactions. It was found that the interaction heat of inhibitor with crystalline wax was up to 150 times greater than with dissolved wax. Asphaltene-wax interactions took place on the same order of magnitude, suggesting co-crystallization mechanism of asphaltenes with crystalline wax. Testing multiple inhibitor chemistries showed no correlation between interaction strength and inhibitor effect on wax crystallization, such as reducing WAT or gel yield strength. It was therefore concluded that inhibitor co-crystallization is a necessity for wax inhibition, but not the deciding factor. For efficient wax inhibition, additives are required to induce favorable morphology changes in wax crystals, which can delay gelation and reduce gel yield strength.

In publication IV, NMR and GC/MS were introduced to measure inhibitor effect on the liquid wax phase during wax crystallization. NMR showed that wax inhibitors greatly influence dissolved wax mobility during wax crystallization. Inhibitors with effective wax inhibition could suppress secondary peaks in the $T_2$ distribution, suggesting that the additives alter interactions of dissolved wax at the solid-liquid interface. Liquid phase composition, as measured by GC/MS, was also affected by the inhibitor addition. Effective wax inhibitors could delay certain stages during *n*-alkane depletion, and accounted for more selective *n*-alkane precipitation. Reduction in the amount of precipitated wax for effective additives was also detected in DSC and NMR.

In publication V, the influence of wax inhibitor molecular weight on wax crystallization was studied. Inhibitors were fractionated by stepwise precipitation, which led to fractions with lower polydispersity index, or ultrasonic disintegration, which reduced the molecular weight and increased polydispersity. The lowest molecular weight fraction from stepwise precipitation showed diminished efficiency for high molecular weight wax, whereas performance for low molecular weight waxy model oils was improved. Overall, the effect on WAT and gelation temperature was predominantly determined by the type of inhibitor functional groups. It was therefore concluded that inhibitor molecular weight is a parameter that can be optimized for tailoring this additive to a particular waxy oil, but only after the best-working inhibitor type has been determined.

In publication VI, asphaltenes were fractionated into groups with distinct characteristics, and the effect of each fraction on wax crystallization was studied in a model waxy oil. On average, the best wax inhibition was achieved by *3.5V* and *3.5V-6V* asphaltenes, which exhibited mixed functional groups and low solubility. *Bulk* asphaltenes had the lowest polarity and the highest degree of aromaticity, yielding the best WAT and pour point depression. *Irreversibly adsorbed* asphaltenes were highest in polarity and had the overall worst wax inhibition efficiency. Interaction heat of unfractionated *whole* asphaltenes with crystalline wax was greater than for *bulk* or *irreversibly adsorbed* asphaltenes. It was therefore concluded, that the asphaltene-wax interactions and desirable effects on wax crystallization were facilitated by asphaltene molecules with higher polydispersity.

In summary, methodologies were introduced or improved that enable (1.) more accurate assessment of WAT from experimental data, (2) expanding research on inhibitor-wax interactions, and (3.) fractionation of asphaltenes or wax inhibitors. Results indicate that ITC is suitable for qualitative studies only, but NMR and GC/MS could reflect inhibitor efficiency to some extent. The effect of asphaltene or inhibitor characteristics on wax crystallization was studied via fractionation procedures, but corresponding procedures could also be used for other applications.

The fundamental question is: What defines a good working inhibitor and how does it differ from additives with poor performance? A short answer would be that an efficient wax inhibitor reduces pour point, thereby ensuring crude oil flow-ability. The results in this thesis match the common perception that inhibitors act by affecting wax nucleation, wax crystal morphology, and wax solubility. In addition, wax inhibitors were shown to differ in interaction strength and to influence wax precipitation, compositional changes, and liquid wax mobility. In conclusion, there is a multitude of aspects that can be considered when probing wax inhibitors and their action.

# 9. Scope for Future Work

Experiments conducted in this work predominantly focused on model waxy oils, as well as industrial wax inhibitors, whose chemical makeup was largely proprietary. These choices represent a compromise to study well-defined wax systems on the one hand, but still remain close to the technical application on the other hand. Future work could therefore continue both in the direction of more fundamental research and in the direction of more applied systems.

To facilitate more fundamental research on wax inhibition and inhibitor-wax interactions, future work could extend the introduced procedures and techniques to:

- Better defined model oil mixtures, e.g. single component waxes in organic solvent.
- Wax inhibitor chemistries of known composition, e.g. polyethylene (PE), poly(ethylene-butene) (PEB), polyacrylate (PA) with defined pendant alkyl chain length, etc.
- Resin-wax interactions in analogy to similar research conducted on asphaltenes.

To support research that resembles contemporary technical applications more closely, investigations could be made on:

- Compositional changes during wax crystallization of real crude oil, and the effect of chemical additives thereon.
- NMR measurements to cross-reference the influence of asphaltenes, resins, and wax inhibitors on dissolved wax mobility during wax crystallization.

# References

1. International Energy Outlook 2017 [press release]. www.eia.gov/ieo: U.S. Energy Information Administration, September 14 2017.
2. Arto I, Capellán-Pérez I, Lago R, Bueno G, Bermejo R. The energy requirements of a developed world. Energy for Sustainable Development. 2016;33:1-13.
3. Sorrell S. Reducing energy demand: A review of issues, challenges and approaches. Renewable and Sustainable Energy Reviews. 2015;47:74-82.
4. Zou C, Zhai G, Zhang G, Wang H, Zhang G, Li J, et al. Formation, distribution, potential and prediction of global conventional and unconventional hydrocarbon resources. Petroleum Exploration and Development. 2015;42(1):14-28.
5. Singh PV, Ramachandran; Fogler, H. Scott; Nagarajan, Nagi. Formation and aging of incipient thin film wax-oil gels. AIChE Journal 2000;45(5):1059-74.
6. Kelland MA. Wax (Paraffin) Control. Production Chemicals for the Oil and Gas Industry: CRC Press; 2009.
7. Huang Z, Zheng S, Fogler HS. Wax Deposition: Experimental Characterizations, Theoretical Modeling, and Field Practices. Boca Raton (FL), USA: CRC Press; 2015.
8. Venkatesan R. The deposition and rheology of organic gels [Doctoral Thesis]: University of Michigan; 2004.
9. Sarica C, Volk M. Tulsa University Paraffin Deposition Projects. The University of Tulsa (US); 2004.
10. Al-Yaari M. Paraffin Wax Deposition: Mitigation and Removal Techniques. 2011/1/1/. SPE: Society of Petroleum Engineers; 2011.
11. Yang F, Zhao Y, Sjöblom J, Li C, Paso KG. Polymeric Wax Inhibitors and Pour Point Depressants for Waxy Crude Oils: A Critical Review. Journal of Dispersion Science and Technology. 2015;36(2):213-25.
12. Oschmann H-J. Das Kristallisationsverhalten von Paraffinen in Abhängigkeit von ihrer Zusammensetzung sowie seine Beeinflussung durch Paraffininhibitoren [PhD Thesis]. Papierflieger: Technische Universität Clausthal; 1998.
13. Aiyejina A, Chakrabarti DP, Pilgrim A, Sastry MKS. Wax formation in oil pipelines: A critical review. International Journal of Multiphase Flow. 2011;37(7):671-94.
14. Speight JG. The chemistry and technology of petroleum. 5th ed. ed. Boca Raton, Fla: CRC Press; 2014.
15. Subramanian S. Mitigation and remediation of asphaltene precipitation, deposition and plug formation : importance of asphaltene sub-fractions. Trondheim: Norwegian University of Science and Technology, Faculty of Natural Sciences and Technology, Department of Chemical Engineering; 2017.
16. Formation of fossil fuels. In: Schobert H, editor. Chemistry of Fossil Fuels and Biofuels. Cambridge Series in Chemical Engineering. Cambridge: Cambridge University Press; 2013. p. 103-31.
17. Engel MH. Organic Geochemistry : Principles and Applications: Springer US : Imprint: Springer; 1993.
18. Tissot BP, Welte DH. From Kerogen to Petroleum. In: Tissot BP, Welte DH, editors. Petroleum Formation and Occurrence. Berlin, Heidelberg: Springer Berlin Heidelberg; 1984. p. 160-98.
19. Tissot BP. Recent Advances in Petroleum Geochemistry Applied to Hydrocarbon Exploration. The American Association of Petroleum Geologists Bulletin. 1984;68(5):19.

20. Vandenbroucke M, Largeau C. Kerogen origin, evolution and structure. Organic Geochemistry. 2007;38(5):719-833.

21. Riazi M. Characterization and properties of petroleum fractions: ASTM international West Conshohocken, PA; 2005.

22. Behrenbruch P, Dedigama T. Classification and characterisation of crude oils based on distillation properties. Journal of Petroleum Science and Engineering. 2007;57(1):166-80.

23. Conaway CF. The petroleum industry: a nontechnical guide: Pennwell Books; 1999.

24. Bai Y, Bai Q. Subsea engineering handbook. Waltham (MA), USA: Gulf Professional Publishing (Elsevier); 2012.

25. Lehmkoester J, Schröder T, Lange E, Petersen S, Rüpke L, Söding E, et al. World Ocean Review 3: Marine Resources—Opportunities and Risks. Hamburg, Germany: maribus GmbH. 2014.

26. Fink J. Petroleum Engineer's Guide to Oil Field Chemicals and Fluids. First Edition ed: Gulf Professional Publishing; 2011.

27. Paso K, Kompalla T, Aske N, Rønningsen HP, Øye G, Sjöblom J. Novel Surfaces with Applicability for Preventing Wax Deposition: A Review. Journal of Dispersion Science and Technology. 2009;30(6):757-81.

28. Huang Z, Senra M, Kapoor R, Fogler HS. Wax deposition modeling of oil/water stratified channel flow. AIChE Journal. 2011;57(4):841-51.

29. Mullins OC, Sheu EY, Hammami A, Marshall AG. Asphaltenes, heavy oils, and petroleomics: Springer Science & Business Media; 2007.

30. Aske N, Kallevik H, Sjöblom J. Determination of Saturate, Aromatic, Resin, and Asphaltenic (SARA) Components in Crude Oils by Means of Infrared and Near-Infrared Spectroscopy. Energy & Fuels. 2001;15(5):1304-12.

31. Lundanes E, Greibrokk T. Separation of fuels, heavy fractions, and crude oils into compound classes: A review. Journal of High Resolution Chromatography. 1994;17(4):197-202.

32. Qiao P, Harbottle D, Tchoukov P, Masliyah J, Sjoblom J, Liu Q, et al. Fractionation of Asphaltenes in Understanding Their Role in Petroleum Emulsion Stability and Fouling. Energy & Fuels. 2017;31(4):3330-7.

33. Oliveira LMSL, Nunes RCP, Melo IC, Ribeiro YLL, Reis LG, Dias JCM, et al. Evaluation of the correlation between wax type and structure/behavior of the pour point depressant. Fuel Processing Technology. 2016;149:268-74.

34. Lee HS. Computational and rheological study of wax deposition and gelation in subsea pipelines: ProQuest; 2008.

35. Roenningsen HP, Bjoerndal B, Baltzer Hansen A, Batsberg Pedersen W. Wax precipitation from North Sea crude oils: 1. Crystallization and dissolution temperatures, and Newtonian and non-Newtonian flow properties. Energy & Fuels. 1991;5(6):895-908.

36. Kelland MA. Production chemicals for the oil and gas industry. second ed. Boca Raton: CRC press; 2014.

37. Zhao Y. Shut in and Restart of Waxy Crude Oil Pipelines: Gelation, Rheology Model Development, and Application of Polymer/Ionic Liquid Based Additive [PhD Thesis]. Tondheim, Norway: Norges teknisk-naturvitenskapelige universitet (NTNU); 2013.

38. Kurniawan M, Subramanian S, Norrman J, Paso K. Influence of Microcrystalline Wax on the Properties of Model Wax-Oil Gels. Energy & Fuels. 2018;32(5):5857-67.

39. Speight JG. Petroleum Asphaltenes - Part 1: Asphaltenes, Resins and the Structure of Petroleum. Oil & Gas Science and Technology - Rev IFP. 2004;59(5):467-77.

40. Groenzin H, Mullins OC. Molecular Size and Structure of Asphaltenes from Various Sources. Energy & Fuels. 2000;14(3):677-84.

41. Durand E, Clemancey M, Lancelin J-M, Verstraete J, Espinat D, Quoineaud A-A. Effect of Chemical Composition on Asphaltenes Aggregation. Energy & Fuels. 2010;24(2):1051-62.

42. Groenzin H, Mullins OC. Asphaltene Molecular Size and Structure. The Journal of Physical Chemistry A. 1999;103(50):11237-45.

43. Mullins OC, Sabbah H, Eyssautier J, Pomerantz AE, Barré L, Andrews AB, et al. Advances in Asphaltene Science and the Yen–Mullins Model. Energy & Fuels. 2012;26(7):3986-4003.

44. Gray MR, Tykwinski RR, Stryker JM, Tan X. Supramolecular Assembly Model for Aggregation of Petroleum Asphaltenes. Energy & Fuels. 2011;25(7):3125-34.

45. Andersen SI, Speight JG. PETROLEUM RESINS: SEPARATION, CHARACTER, AND ROLE IN PETROLEUM. Petroleum Science and Technology. 2001;19(1-2):1-34.

46. Spiecker PM, Gawrys KL, Trail CB, Kilpatrick PK. Effects of petroleum resins on asphaltene aggregation and water-in-oil emulsion formation. Colloids and Surfaces A: Physicochemical and Engineering Aspects. 2003;220(1):9-27.

47. Standard Test Method for Acid Number of Petroleum Products by Semi-Micro Color Indicator Titration. D3339: ASTM International; 2017.

48. Standard Test Method for Acid Number of Petroleum Products by Potentiometric Titration. D664: ASTM International; 2018.

49. Standard Test Method for Acid and Base Number by Color-Indicator Titration. D974: ASTM International; 2016.

50. von Mühlen C, de Oliveira EC, Zini CA, Caramão EB, Marriott PJ. Characterization of Nitrogen-Containing Compounds in Heavy Gas Oil Petroleum Fractions Using Comprehensive Two-Dimensional Gas Chromatography Coupled to Time-of-Flight Mass Spectrometry. Energy & Fuels. 2010;24(6):3572-80.

51. Yamamoto M, Taguchi K, Sasaki K. Basic nitrogen compounds in bitumen and crude oils. Chemical Geology. 1991;93(1):193-206.

52. Aksenov VS, Titov VI, Kam'yanov VF. Nitrogen compounds of petroleum oils (review). Chemistry of Heterocyclic Compounds. 1979;15(2):119-35.

53. Bertheussen A. Naphthenic acid solubility in produced water and their interactions with divalent cations [Doctoral Thesis]: Norwegian University of Science and Technology (NTNU); 2018.

54. Paso KG, Fogler HS. Bulk Stabilization in Wax Deposition Systems. Energy & Fuels. 2004;18(4):1005-13.

55. Paso KG. Comprehensive treatise on shut-in and restart of waxy oil pipelines. Journal of Dispersion Science and Technology. 2014;35(8):1060-85.

56. Paso K, Kompalla T, Oschmann HJ, Sjöblom J. Rheological Degradation of Model Wax-Oil Gels. Journal of Dispersion Science and Technology. 2009;30(4):472-80.

57. Kané M, Djabourov M, Volle J-L, Lechaire J-P, Frebourg G. Morphology of paraffin crystals in waxy crude oils cooled in quiescent conditions and under flow. Fuel. 2003;82(2):127-35.

58. Skjæraasen O, Oschmann H-J, Paso K, Sjöblom J. Accurate Assessment of Pipeline Restart Behavior at Subsea Conditions for a Highly Waxy Crude Oil Employing Advanced Computational Pressure Wave Modeling. Industrial & Engineering Chemistry Research. 2015;54(16):4429-40.

59. Kumar L, Paso K, Sjöblom J. Numerical study of flow restart in the pipeline filled with weakly compressible waxy crude oil in non-isothermal condition. Journal of Non-Newtonian Fluid Mechanics. 2015;223:9-19.

60. Zhao Y, Paso K, Sariman MZB, Sjöblom J. Strain-Dependent Rheological Model and Pressure Wave Prediction for Shut in and Restart of Waxy Oil Pipelines. Journal of Dispersion Science and Technology. 2014;35(7):960-9.
61. Kokal SL. Crude Oil Emulsions: A State-Of-The-Art Review. SPE-77497-PA. 2005;20(01):5-13.
62. Lee RF. Agents Which Promote and Stabilize Water-in-Oil Emulsions. Spill Science & Technology Bulletin. 1999;5(2):117-26.
63. Kokal SL, Sayegh SG. Asphaltenes: The Cholesterol Of Petroleum. Middle East Oil Show; 1995; Bahrain. SPE: Society of Petroleum Engineers; 1995.
64. Leontaritis KJ, Mansoori GA. Asphaltene deposition: a survey of field experiences and research approaches. Journal of Petroleum Science and Engineering. 1988;1(3):229-39.
65. Sloan ED. Natural gas hydrates in flow assurance: Gulf Professional Publishing; 2010.
66. Nwachukwu IB. Corrosion Measurement in Oil and Gas Pipeline: A Mathematical Model Approach. SPE Nigeria Annual International Conference and Exhibition; 2018/8/6/; Lagos, Nigeria. SPE: Society of Petroleum Engineers; 2018. p. 16.
67. Paso KG. Paraffin gelation kinetics: University of Michigan.; 2005.
68. Singh P, Fogler HS. Fused Chemical Reactions: The Use of Dispersion To Delay Reaction Time in Tubular Reactors. Industrial & Engineering Chemistry Research. 1998;37(6):2203-7.
69. Jemmett MR. Rheology and deposition of heterogeneous organic mixtures: An expansion of “cold flow” research: The University of Utah; 2012.
70. Bidmus HO, Mehrotra AK. Solids deposition during “cold flow” of wax− solvent mixtures in a flow-loop apparatus with heat transfer. Energy & Fuels. 2009;23(6):3184-94.
71. Rogel E, León O. Study of the Adsorption of Alkyl-Benzene-Derived Amphiphiles on an Asphaltene Surface Using Molecular Dynamics Simulations. Energy & Fuels. 2001;15(5):1077-86.
72. León O, Rogel E, Urbina A, Andújar A, Lucas A. Study of the Adsorption of Alkyl Benzene-Derived Amphiphiles on Asphaltene Particles. Langmuir. 1999;15(22):7653-7.
73. Kabir CS, Jamaluddin AKM. Asphaltene Characterization and Mitigation in South Kuwait's Marrat Reservoir. Middle East Oil Show and Conference; 1999/1/1/; Bahrain. SPE: Society of Petroleum Engineers; 1999. p. 9.
74. Standard Test Method for Cloud Point of Petroleum Products and Liquid Fuels. ASTM D2500: ASTM International; 2017.
75. Kruka VR, Cadena ER, Long TE. Cloud-Point Determination for Crude Oils. 1995.
76. Japper-Jaafar A, Bhaskoro PT, Mior ZS. A new perspective on the measurements of wax appearance temperature: Comparison between DSC, thermomicroscopy and rheometry and the cooling rate effects. Journal of Petroleum Science and Engineering. 2016;147:672-81.
77. Roehner RM, Hanson FV. Determination of Wax Precipitation Temperature and Amount of Precipitated Solid Wax versus Temperature for Crude Oils Using FT-IR Spectroscopy. Energy & Fuels. 2001;15(3):756-63.
78. Paso K, Kallevik H, Sjoblom J. Measurement of wax appearance temperature using near-infrared (NIR) scattering. Energy & Fuels. 2009;23(10):4988-94.
79. Karacan CÖ, Demiral MRB, Kök MV. Application of X-ray CT Imaging as an Alternative Tool for Cloud Point Determination. Petroleum Science and Technology. 2000;18(7-8):835-49.
80. Monger-McClure TG, Tackett JE, Merrill LS. Comparisons of Cloud Point Measurement and Paraffin Prediction Methods. 1999.
81. Becker JR. Paraffin-Crystal-Modifier Studies in Field and Laboratory. 2001. SPE: Society of Petroleum Engineers; 2001.

82. Coutinho JAP, Daridon J-L. The Limitations of the Cloud Point Measurement Techniques and the Influence of the Oil Composition on Its Detection. Petroleum Science and Technology. 2005;23(9-10):1113-28.
83. Kok MV, Létoffé J-M, Claudy P, Martin D, Garcin M, Volle J-L. Comparison of wax appearance temperatures of crude oils by differential scanning calorimetry, thermomicroscopy and viscometry. Fuel. 1996;75(7):787-90.
84. Coto B, Martos C, Espada JJ, Robustillo MD, Peña JL. Analysis of paraffin precipitation from petroleum mixtures by means of DSC: Iterative procedure considering solid–liquid equilibrium equations. Fuel. 2010;89(5):1087-94.
85. Batsberg Pedersen W, Baltzer Hansen A, Larsen E, Nielsen AB, Roenningsen HP. Wax precipitation from North Sea crude oils. 2. Solid-phase content as function of temperature determined by pulsed NMR. Energy & fuels. 1991;5(6):908-13.
86. Chen J, Zhang J, Li H. Determining the wax content of crude oils by using differential scanning calorimetry. Thermochimica Acta. 2004;410(1–2):23-6.
87. Elsharkawy AM, Al-Sahhaf TA, Fahim MA. Wax deposition from Middle East crudes. Fuel. 2000;79(9):1047-55.
88. Burger ED, Perkins TK, Striegler JH. Studies of Wax Deposition in the Trans Alaska Pipeline. Journal of Petroleum Technology. 1981;33(06):1075-86.
89. Standard Test Method for Pour Point of Petroleum Products. D97. ASTM International2017.
90. Standard Test Method for Pour Point of Crude Oils. D5853: ASTM International; 2016.
91. Standard Test Method for Pour Point of Petroleum Products (Automatic Pressure Pulsing Method). D5949: ASTM International; 2016.
92. Standard Test Method for Pour Point of Petroleum Products (Rotational Method). D5985: ASTM International; 2014.
93. Paso KG, Krückert KK, Oschmann H-J, Ali H, Sjöblom J. PPD architecture development via polymer–crystal interaction assessment. Journal of Petroleum Science and Engineering. 2014;115:38-49.
94. Taraneh JB, Rahmatollah G, Hassan A, Alireza D. Effect of wax inhibitors on pour point and rheological properties of Iranian waxy crude oil. Fuel Processing Technology. 2008;89(10):973-7.
95. Oliveira GE, Mansur CRE, Lucas EF, González G, de Souza WF. The Effect of Asphaltenes, Naphthenic Acids, and Polymeric Inhibitors on the Pour Point of Paraffins Solutions. Journal of Dispersion Science and Technology. 2007;28(3):349-56.
96. Pedersen KS, Rønningsen HP. Influence of Wax Inhibitors on Wax Appearance Temperature, Pour Point, and Viscosity of Waxy Crude Oils. Energy & Fuels. 2003;17(2):321-8.
97. Rahimian I, Laux H, Oschmann H-J. Trübungs-und Stockpunktabhängigkeiten in Erdölen. Erdöl, Erdgas, Kohle. 1997;113(2):80-3.
98. Shaw MT. Introduction to Polymer Rheology. Hoboken, United States: John Wiley & Sons, Incorporated; 2012.
99. Winter HH, Chambon F. Analysis of Linear Viscoelasticity of a Crosslinking Polymer at the Gel Point. Journal of Rheology. 1986;30(2):367-82.
100. Venkatesan R, Singh P, Fogler HS. Delineating the Pour Point and Gelation Temperature of Waxy Crude Oils. 2004.
101. Yao B, Li C, Zhang X, Yang F, Sun G, Zhao Y. Performance improvement of the ethylene-vinyl acetate copolymer (EVA) pour point depressant by small dosage of the amino-functionalized polymethylsilsesquioxane (PAMSQ) microsphere. Fuel. 2018;220:167-76.

102. Bossard F, Moan M, Aubry T. Linear and nonlinear viscoelastic behavior of very concentrated plate-like kaolin suspensions. Journal of Rheology. 2007;51(6):1253-70.
103. Li Y, Han S, Lu Y, Zhang J. Influence of Asphaltene Polarity on Crystallization and Gelation of Waxy Oils. Energy & Fuels. 2018;32(2):1491-7.
104. Tinsley JF, Jahnke JP, Dettman HD, Prud'home RK. Waxy Gels with Asphaltenes 1: Characterization of Precipitation, Gelation, Yield Stress, and Morphology. Energy & Fuels. 2009;23(4):2056-64.
105. Paso K, Senra M, Yi Y, Sastry AM, Fogler HS. Paraffin Polydispersity Facilitates Mechanical Gelation. Industrial & Engineering Chemistry Research. 2005;44(18):7242-54.
106. Venkatesan R, Östlund J-A, Chawla H, Wattana P, Nydén M, Fogler HS. The Effect of Asphaltenes on the Gelation of Waxy Oils. Energy & Fuels. 2003;17(6):1630-40.
107. Zhao Y, Paso K, Kumar L, Safieva J, Sariman MZB, Sjöblom J. Controlled Shear Stress and Controlled Shear Rate Nonoscillatory Rheological Methodologies for Gelation Point Determination. Energy & Fuels. 2013;27(4):2025-32.
108. Wardhaugh LT, Boger DV. The measurement and description of the yielding behavior of waxy crude oil. Journal of Rheology. 1991;35(6):1121-56.
109. Barnes HA. The yield stress—a review or 'παντα ρει'—everything flows? Journal of Non-Newtonian Fluid Mechanics. 1999;81(1):133-78.
110. Zhao Y, Kumar L, Paso K, Ali H, Safieva J, Sjöblom J. Gelation and Breakage Behavior of Model Wax–Oil Systems: Rheological Properties and Model Development. Industrial & Engineering Chemistry Research. 2012;51(23):8123-33.
111. Erickson DD, Niesen VG, Brown TS. Thermodynamic Measurement and Prediction of Paraffin Precipitation in Crude Oil. 1993/1/1/. SPE: Society of Petroleum Engineers; 1993.
112. Oliveira ECL, Neto ELB, Pereira CG. Modeling and simulation of paraffin solubility in circular pipes in laminar regime flow. Journal of Petroleum Science and Engineering. 2016;141:70-81.
113. Edmonds B, Moorwood T, Szczepanski R, Zhang X. Simulating wax deposition in pipelines for flow assurance. Energy and Fuels. 2008;22(2):729-41.
114. Kok MV, Saracoglu RO. Mathematical Modelling of Wax Deposition in Crude Oil Pipelines (Comparative Study). Petroleum Science and Technology. 2000;18(9-10):1121-45.
115. Brecevic L, Garside J. Solubilities of tetracosane in hydrocarbon solvents. Journal of Chemical & Engineering Data. 1993;38(4):598-601.
116. Beiny DHM, Mullin JW. Solubilities of higher normal alkanes in m-xylene. Journal of Chemical & Engineering Data. 1987;32(1):9-10.
117. Madsen HEL, Boistelle R. Solubility of octacosane and hexatriacontane in different n-alkane solvents. Journal of the Chemical Society, Faraday Transactions 1: Physical Chemistry in Condensed Phases. 1979;75:1254-8.
118. Paso K, Kompalla T, Aske N, Sjöblom J. A Quartz Crystal Microbalance Characterization of Metal-Oil Interfaces and Interactions with Wax Molecules. Journal of Dispersion Science and Technology. 2008;29(5):775-82.
119. Schou Pedersen K, Skovborg P, Roenningsen HP. Wax precipitation from North Sea crude oils. 4. Thermodynamic modeling. Energy & Fuels. 1991;5(6):924-32.
120. Pauly J, Dauphin C, Daridon JL. Liquid–solid equilibria in a decane+multi-paraffins system. Fluid Phase Equilibria. 1998;149(1):191-207.
121. Won KW. Thermodynamic calculation of cloud point temperatures and wax phase compositions of refined hydrocarbon mixtures. Fluid Phase Equilibria. 1989;53:377-96.

122. Ungerer P, Faissat B, Leibovici C, Zhou H, Behar E, Moracchini G, et al. High pressure-high temperature reservoir fluids: investigation of synthetic condensate gases containing a solid hydrocarbon. Fluid Phase Equilibria. 1995;111(2):287-311.
123. Coutinho JAP, Andersen SI, Stenby EH. Evaluation of activity coefficient models in prediction of alkane solid-liquid equilibria. Fluid Phase Equilibria. 1995;103(1):23-39.
124. Coutinho JAP. Predictive local composition models: NRTL and UNIQUAC and their application to model solid–liquid equilibrium of n-alkanes. Fluid Phase Equilibria. 1999;158-160:447-57.
125. Anderson TF, Prausnitz JM. Application of the UNIQUAC Equation to Calculation of Multicomponent Phase Equilibria. 1. Vapor-Liquid Equilibria. Industrial & Engineering Chemistry Process Design and Development. 1978;17(4):552-61.
126. Probjot S, Arm Y, Scott FH. Existence of a critical carbon number in the aging of a wax-oil gel. AIChE Journal. 2001;47(9):2111-24.
127. Chen WH, Zhang XD, Zhao ZC, Yin CY. UNIQUAC model for wax solution with pour point depressant. Fluid Phase Equilibria. 2009;280(1):9-15.
128. Mullin JW. 5. Nucleation. Crystallization (4th Edition): Elsevier; 2001.
129. Kalikmanov VI. Nucleation Theory: Springer Netherlands; 2013.
130. Auer S, Frenkel D. Suppression of crystal nucleation in polydisperse colloids due to increase of the surface free energy. Nature. 2001;413:711.
131. Maroto-Centeno JA, Pérez-Gutiérrez T, Quesada-Pérez M. Theoretical approach to a better understanding of gelation in the framework of petroleum industry: role played by different parameters. Materialwissenschaft und Werkstofftechnik. 2013;44(5):403-9.
132. Mota FL, Teychéne S, Biscans B. Measurement of the Nucleation and Growth Kinetics of Some Middle Distillate Fuels and Their Blends with a Model Biodiesel Fuel. Industrial & Engineering Chemistry Research. 2014;53(7):2811-9.
133. Kraack H, Sirota EB, Deutsch M. Measurements of homogeneous nucleation in normal-alkanes. The Journal of Chemical Physics. 2000;112(15):6873-85.
134. Kraack H, Deutsch M, Sirota EB. n-Alkane Homogeneous Nucleation: Crossover to Polymer Behavior. Macromolecules. 2000;33(16):6174-84.
135. Turnbull D, Cormia RL. Kinetics of Crystal Nucleation in Some Normal Alkane Liquids. The Journal of Chemical Physics. 1961;34(3):820-31.
136. Nývlt J. Nucleation and growth rate in mass crystallization. Progress in Crystal Growth and Characterization. 1984;9(3):335-70.
137. Machado ALdC, Lucas EF. Poly(Ethylene-co-Vinyl Acetate) (EVA) Copolymers as Modifiers of Oil Wax Crystallization. Petroleum Science and Technology. 1999;17(9-10):1029-41.
138. Clarke EW. Crystal Types of Pure Hydrocarbons in the Paraffin Wax Range. Industrial & Engineering Chemistry. 1951;43(11):2526-35.
139. Wu C, Zhang J-l, Li W, Wu N. Molecular dynamics simulation guiding the improvement of EVA-type pour point depressant. Fuel. 2005;84(16):2039-47.
140. Senra M, Scholand T, Maxey C, Fogler HS. Role of Polydispersity and Cocrystallization on the Gelation of Long-Chained n-Alkanes in Solution. Energy & Fuels. 2009;23(12):5947-57.
141. Zhao Y, Paso K, Sjöblom J. Thermal behavior and solid fraction dependent gel strength model of waxy oils. J Therm Anal Calorim. 2014;117(1):403-11.
142. Venkatesan R, Nagarajan NR, Paso K, Yi YB, Sastry AM, Fogler HS. The strength of paraffin gels formed under static and flow conditions. Chemical Engineering Science. 2005;60(13):3587-98.

143. Zhao Y, Kumar L, Paso K, Safieva J, Sariman MZB, Sjöblom J. Gelation Behavior of Model Wax–Oil and Crude Oil Systems and Yield Stress Model Development. Energy & Fuels. 2012;26(10):6323-31.

144. Cheng C, Boger DV, Nguyen QD. Influence of Thermal History on the Waxy Structure of Statically Cooled Waxy Crude Oil. SPE Journal. 2000;5(02):148-57.

145. Wei B. Recent advances on mitigating wax problem using polymeric wax crystal modifier. Journal of Petroleum Exploration and Production Technology. 2015;5(4):391-401.

146. Wu Y, Ni G, Yang F, Li C, Dong G. Modified Maleic Anhydride Co-polymers as Pour-Point Depressants and Their Effects on Waxy Crude Oil Rheology. Energy & Fuels. 2012;26(2):995-1001.

147. Jing G, Sun Z, Tu Z, Bian X, Liang Y. Influence of Different Vinyl Acetate Contents on the Properties of the Copolymer of Ethylene and Vinyl Acetate/Modified Nano-SiO2 Composite Pour-Point Depressant. Energy & Fuels. 2017;31(6):5854-9.

148. Norrman J, Solberg A, Sjöblom J, Paso K. Nanoparticles for Waxy Crudes: Effect of Polymer Coverage and the Effect on Wax Crystallization. Energy & Fuels. 2016;30(6):5108-14.

149. Yang F, Paso K, Norrman J, Li C, Oschmann H, Sjöblom J. Hydrophilic nanoparticles facilitate wax inhibition. Energy & Fuels. 2015;29(3):1368-74.

150. Groffe D, Groffe P, Takhar S, Andersen SI, Stenby EH, Lindeloff N, et al. A Wax Inhibition Solution to Problematic Fields: A Cchemical Remediation Process. Petroleum Science and Technology. 2001;19(1-2):205-17.

151. Zhang J, Zhang M, Wan J, Li W. Theoretical Study of the Prohibited Mechanism for Ethylene/Vinyl Acetate Co-polymers to the Wax Crystal Growth. The Journal of Physical Chemistry B. 2008;112(1):36-43.

152. Zhang J, Wu C, Li W, Wang Y, Cao H. DFT and MM calculation: the performance mechanism of pour point depressants study. Fuel. 2004;83(3):315-26.

153. Duffy D, Rodger P. Wax inhibition with poly (octadecyl acrylate). Physical Chemistry Chemical Physics. 2002;4(2):328-34.

154. Chen Z, Wang X, Zhang H, Yang C, Shan H. A Study on the Interaction of Crude Oil Waxes With Polyacrylate Pour Point Depressants by Monte Carlo Simulation. Petroleum Science and Technology. 2014;32(17):2151-7.

155. Radulescu A, Schwahn D, Monkenbusch M, Fetters LJ, Richter D. Structural study of the influence of partially crystalline poly(ethylene butene) random copolymers on paraffin crystallization in dilute solutions. Journal of Polymer Science Part B: Polymer Physics. 2004;42(17):3113-32.

156. Hennessy A, Neville A, Roberts KJ. In-Situ SAXS/WAXS and Turbidity Studies of the Structure and Composition of Multihomologous n-Alkane Waxes Crystallized in the Absence and Presence of Flow Improving Additive Species. Crystal Growth & Design. 2004;4(5):1069-78.

157. Zhang J, Wu C, Li W, Wang Y, Han Z. Study on performance mechanism of pour point depressants with differential scanning calorimeter and X-ray diffraction methods☆. Fuel. 2003;82(11):1419-26.

158. Ashbaugh HS, Radulescu A, Prud'homme RK, Schwahn D, Richter D, Fetters LJ. Interaction of Paraffin Wax Gels with Random Crystalline/Amorphous Hydrocarbon Copolymers. Macromolecules. 2002;35(18):7044-53.

159. Monkenbusch M, Schneiders D, Richter D, Willner L, Leube W, Fetters LJ, et al. Aggregation behaviour of PE–PEP copolymers and the winterization of diesel fuel. Physica B: Condensed Matter. 2000;276-278:941-3.

160. Leube W, Monkenbusch M, Schneiders D, Richter D, Adamson D, Fetters L, et al. Wax-Crystal Modification for Fuel Oils by Self-Aggregating Partially Crystallizable Hydrocarbon Block Copolymers. Energy & Fuels. 2000;14(2):419-30.
161. Ashbaugh HS, Guo X, Schwahn D, Prud'homme RK, Richter D, Fetters LJ. Interaction of Paraffin Wax Gels with Ethylene/Vinyl Acetate Co-polymers. Energy & Fuels. 2005;19(1):138-44.
162. Yao B, Li C, Yang F, Sjöblom J, Zhang Y, Norrman J, et al. Organically modified nano-clay facilitates pour point depressing activity of polyoctadecylacrylate. Fuel. 2016;166:96-105.
163. Zhao Y, Paso K, Norrman J, Ali H, Sørland G, Sjöblom J. Utilization of DSC, NIR, and NMR for wax appearance temperature and chemical additive performance characterization. J Therm Anal Calorim. 2015;120(2):1427-33.
164. Li L, Xu J, Tinsley J, Adamson DH, Pethica BA, Huang JS, et al. Improvement of oil flowability by assembly of comb-type copolymers with paraffin and asphaltene. AIChE Journal. 2012;58(7):2254-61.
165. Chen W, Zhao Z, Yin C. The interaction of waxes with pour point depressants. Fuel. 2010;89(5):1127-32.
166. Tinsley JF, Jahnke JP, Adamson DH, Guo X, Amin D, Kriegel R, et al. Waxy Gels with Asphaltenes 2: Use of Wax Control Polymers. Energy & Fuels. 2009;23(4):2065-74.
167. Wang K-S, Wu C-H, Creek JL, Shuler PJ, Tang Y. Evaluation of Effects of Selected Wax Inhibitors on Wax Appearance and Disappearance Temperatures. Petroleum Science and Technology. 2003;21(3-4):359-68.
168. Soliman EA, Elkatory MR, Hashem AI, Ibrahim HS. Synthesis and performance of maleic anhydride copolymers with alkyl linoleate or tetra-esters as pour point depressants for waxy crude oil. Fuel. 2018;211:535-47.
169. Ridzuan N, Adam F, Yaacob Z. Evaluation of the inhibitor selection on wax deposition for Malaysian crude oil. Petroleum Science and Technology. 2016;34(4):366-71.
170. Oh K, Deo M. Characteristics of Wax Gel Formation in the Presence of Asphaltenes. Energy & Fuels. 2009;23(3):1289-93.
171. Alcazar-Vara LA, Garcia-Martinez JA, Buenrostro-Gonzalez E. Effect of asphaltenes on equilibrium and rheological properties of waxy model systems. Fuel. 2012;93:200-12.
172. Lei Y, Han S, Zhang J. Effect of the dispersion degree of asphaltene on wax deposition in crude oil under static conditions. Fuel Processing Technology. 2016;146:20-8.
173. Rogel E, Ovalles C, Vien J, Moir M. Asphaltene characterization of paraffinic crude oils. Fuel. 2016;178(Supplement C):71-6.
174. Song X, Yin H, Feng Y, Zhang S, Wang Y. Effect of SiO2 Nanoparticles on Wax Crystallization and Flow Behavior of Model Crude Oil. Industrial & Engineering Chemistry Research. 2016;55(23):6563-8.
175. Yao B, Li C, Yang F, Zhang X, Mu Z, Sun G, et al. Ethylene–Vinyl Acetate Copolymer and Resin-Stabilized Asphaltenes Synergistically Improve the Flow Behavior of Model Waxy Oils. 2. Effect of Asphaltene Content. Energy & Fuels. 2018.
176. Ariza-León E, Molina-Velasco D-R, Chaves-Guerrero A. Review of Studies on Asphaltene - Wax Interaction and the Effect thereof on Crystallization. CT&F - Ciencia, Tecnología y Futuro. 2014;5:39-53.
177. Kriz P, Andersen SI. Effect of Asphaltenes on Crude Oil Wax Crystallization. Energy & Fuels. 2005;19(3):948-53.
178. García MdC. Crude Oil Wax Crystallization. The Effect of Heavy n-Paraffins and Flocculated Asphaltenes. Energy & Fuels. 2000;14(5):1043-8.

179. Yang X, Kilpatrick P. Asphaltenes and Waxes Do Not Interact Synergistically and Coprecipitate in Solid Organic Deposits. Energy & Fuels. 2005;19(4):1360-75.
180. García MdC, Carbognani L. Asphaltene−Paraffin Structural Interactions. Effect on Crude Oil Stability. Energy & Fuels. 2001;15(5):1021-7.
181. Orea M, Ranaudo MA, Lugo P, López L. Retention of Alkane Compounds on Asphaltenes. Insights About the Nature of Asphaltene–Alkane Interactions. Energy & Fuels. 2016;30(10):8098-113.
182. Prahl U. Isolierung erdölstämmiger Pour Point Depressants und Untersuchung ihrer Wirkungsweise in paraffinhaltigen Fluiden. Papierflieger: Technische Universität Clausthal; 2001.
183. Xu J, Xing S, Qian H, Chen S, Wei X, Zhang R, et al. Effect of polar/nonpolar groups in comb-type copolymers on cold flowability and paraffin crystallization of waxy oils. Fuel. 2013;103:600-5.
184. Yao B, Li C, Yang F, Zhang X, Mu Z, Sun G, et al. Ethylene–Vinyl Acetate Copolymer and Resin-Stabilized Asphaltenes Synergistically Improve the Flow Behavior of Model Waxy Oils. 1. Effect of Wax Content and the Synergistic Mechanism. Energy & Fuels. 2018;32(2):1567-78.
185. Smith PB, Ramsden RMJ. The Prediction Of Oil Gelation In Submarine Pipelines And The Pressure Required For Restarting Flow. SPE European Petroleum Conference; 1978/1/1/; London, United Kingdom. SPE: Society of Petroleum Engineers; 1978.
186. Chang C, Nguyen QD, Rønningsen HP. Isothermal start-up of pipeline transporting waxy crude oil. Journal of Non-Newtonian Fluid Mechanics. 1999;87(2):127-54.
187. Kumar L, Zhao, Y., Paso, K., Grimes, B., Sjöblom, J. and Lawrence, C. Numerical study of pipeline restart of weakly compressible irreversibly thixotropic waxy crude oils. AIChE J. 2015;61:2657-71.
188. Vinay G, Wachs A, Frigaard I. Start-up transients and efficient computation of isothermal waxy crude oil flows. Journal of Non-Newtonian Fluid Mechanics. 2007;143(2):141-56.
189. Frigaard I, Vinay G, Wachs A. Compressible displacement of waxy crude oils in long pipeline startup flows. Journal of Non-Newtonian Fluid Mechanics. 2007;147(1):45-64.
190. Jones SP, Tyson JK. The rheology of a lubricating oil at temperatures below the pour point. Journal of Colloid Science. 1952;7(3):272-83.
191. De Kee D, Code RK, Turcotte G. Flow Properties of Time-Dependent Foodstuffs. Journal of Rheology. 1983;27(6):581-604.
192. Huang Z, Lee HS, Senra M, Scott Fogler H. A fundamental model of wax deposition in subsea oil pipelines. AIChE Journal. 2011;57(11):2955-64.
193. Mehrotra AK, Bhat NV. Modeling the Effect of Shear Stress on Deposition from “Waxy” Mixtures under Laminar Flow with Heat Transfer. Energy & Fuels. 2007;21(3):1277-86.
194. Ramirez-Jaramillo E, Lira-Galeana C, Manero O. Modeling Wax Deposition in Pipelines. Petroleum Science and Technology. 2004;22(7-8):821-61.
195. Azevedo LFA, Teixeira AM. A Critical Review of the Modeling of Wax Deposition Mechanisms. Petroleum Science and Technology. 2003;21(3-4):393-408.
196. Bagatin R, Carniani C, Correra S, Margarone M, Busto C. Wax Modeling: There is Need for Alternatives. 2008/1/1/. SPE: Society of Petroleum Engineers; 2008.
197. Merino-Garcia D, Margarone M, Correra S. Kinetics of Waxy Gel Formation from Batch Experiments. Energy & Fuels. 2007;21(3):1287-95.
198. Hoteit H, Banki R, Firoozabadi A. Wax deposition and aging in flowlines from irreversible thermodynamics. Energy & Fuels. 2008;22(4):2693-706.

199. Singh P, Venkatesan R, Fogler HS, Nagarajan NR. Morphological evolution of thick wax deposits during aging. AIChE Journal. 2001;47(1):6-18.
200. Svendsen JA. Mathematical modeling of wax deposition in oil pipeline systems. AIChE Journal. 1993;39(8):1377-88.
201. Coutinho JAP, Lopes da Silva JA, Ferreira A, Rosário Soares M, Daridon J-L. Evidence for the Aging of Wax Deposits in Crude Oils by Ostwald Ripening. Petroleum Science and Technology. 2003;21(3-4):381-91.
202. Eskin D, Ratulowski J, Akbarzadeh K. Modelling wax deposition in oil transport pipelines. The Canadian Journal of Chemical Engineering. 2014;92(6):973-88.
203. Ramírez-Jaramillo E, Lira-Galeana C, Manero O. Numerical Simulation of Wax Deposition in Oil Pipeline Systems. Petroleum Science and Technology. 2001;19(1-2):143-56.
204. Labes-Carrier C, Rønningsen HP, Kolnes J, Leporcher E. Wax Deposition in North Sea Gas Condensate and Oil Systems: Comparison Between Operational Experience and Model Prediction. 2002/1/1/. SPE: Society of Petroleum Engineers.
205. Lindeloff N, Krejbjerg K. A compositional model simulating wax deposition in pipeline systems. Energy and Fuels. 2002;16(4):887-91.
206. Geri M, Venkatesan R, Sambath K, McKinley GH. Thermokinematic memory and the thixotropic elasto-viscoplasticity of waxy crude oils. Journal of Rheology. 2017;61(3):427-54.
207. Marinho TO, Barbato CN, Freitas GB, Duncke AC, de Oliveira MCK, Nele M. Interaction Effects of Predominantly Linear and Branched Waxes on Yield Stress and Elastic Modulus of Waxy Oils. Energy & Fuels. 2018;32(8):8057-68.
208. Kodre KV, Attarde, S.R., Yendhe, P.R., Patil, R.Y., Barge, V.U. Differential Scanning Calorimetry: A Review. Research and Reviews: Journal of Pharmaceutical Analysis. 2014;3(3):12.
209. Coleman NJ, Craig DQM. Modulated temperature differential scanning calorimetry: A novel approach to pharmaceutical thermal analysis. International Journal of Pharmaceutics. 1996;135(1):13-29.
210. Biliaderis CG. Differential scanning calorimetry in food research—A review. Food Chemistry. 1983;10(4):239-65.
211. Prime RB. Differential scanning calorimetry of the epoxy cure reaction. Polymer Engineering & Science. 1973;13(5):365-71.
212. Wang B, Menyhard A, Alfonso GC, Müller AJ, Cavallo D. Differential scanning calorimetry study of cross-nucleation between polymorphs in isotactic poly(1-butene). Polymer International. 2018.
213. Kemsies RH, Milkereit B, Wenner S, Holmestad R, Kessler O. In situ DSC investigation into the kinetics and microstructure of dispersoid formation in Al-Mn-Fe-Si(-Mg) alloys. Materials & Design. 2018;146:96-107.
214. Frey M, Busch R, Possart W, Gallino I. On the thermodynamics, kinetics, and sub-Tg relaxations of Mg-based bulk metallic glasses. Acta Materialia. 2018;155:117-27.
215. Schick C, Androsch R, Schmelzer JWP. Homogeneous crystal nucleation in polymers. Journal of Physics: Condensed Matter. 2017;29(45):453002.
216. Kök MV, Letoffe JM, Claudy P. DSC and Rheometry Investigations of Crude Oils. J Therm Anal Calorim. 1999;56(2):959-65.
217. Jiang Z, Hutchinson JM, Imrie CT. Measurement of the wax appearance temperatures of crude oils by temperature modulated differential scanning calorimetry. Fuel. 2001;80(3):367-71.
218. Janmey PA, Schliwa M. Rheology. Current Biology. 2008;18(15):R639-R41.

219. Larson RG. 1.1 Complex Fluids versus Classical Solids and Liquids. Structure and Rheology of Complex Fluids: Oxford University Press; 1999.
220. Li M, Sun M, Lu Y, Zhang J. Experimental Study on the Strength of Original Samples of Wax Deposits from Pipelines in the Field. Energy & Fuels. 2017.
221. Fang L, Zhang X, Ma J, Zhang B. Investigation into a Pour Point Depressant for Shengli Crude Oil. Industrial & Engineering Chemistry Research. 2012;51(36):11605-12.
222. Yi S, Zhang J. Relationship between Waxy Crude Oil Composition and Change in the Morphology and Structure of Wax Crystals Induced by Pour-Point-Depressant Beneficiation. Energy & Fuels. 2011;25(4):1686-96.
223. Létoffé JM, Claudy P, Kok MV, Garcin M, Volle JL. Crude oils: characterization of waxes precipitated on cooling by d.s.c. and thermomicroscopy. Fuel. 1995;74(6):810-7.
224. Zougari MI, Sopkow T. Introduction to Crude Oil Wax Crystallization Kinetics: Process Modeling. Industrial & Engineering Chemistry Research. 2007;46(4):1360-8.
225. Soedarmo AA, Daraboina N, Lee HS, Sarica C. Microscopic Study of Wax Precipitation—Static Conditions. Energy & Fuels. 2016;30(2):954-61.
226. Feig AL. Applications of isothermal titration calorimetry in RNA biochemistry and biophysics. Biopolymers. 2007;87(5-6):293-301.
227. Saboury AA. A review on the ligand binding studies by isothermal titration calorimetry. Journal of the Iranian Chemical Society. 2006;3(1):1-21.
228. Merino-Garcia D, Andersen SI. Interaction of Asphaltenes with Nonylphenol by Microcalorimetry. Langmuir. 2004;20(4):1473-80.
229. Merino-Garcia D, Andersen SI. Thermodynamic Characterization of Asphaltene−Resin Interaction by Microcalorimetry. Langmuir. 2004;20(11):4559-65.
230. Wei D, Simon S, Barriet M, Sjöblom J. An ITC study of interaction and complexation of asphaltene model compounds in apolar solvent II: Interactions with asphaltene inhibitors. Colloids and Surfaces A: Physicochemical and Engineering Aspects. 2016;495:87-99.
231. Simon S, Wei D, Barriet M, Sjöblom J. An ITC and NMR study of interaction and complexation of asphaltene model compounds in apolar solvent I: Self-association pattern. Colloids and Surfaces A: Physicochemical and Engineering Aspects. 2016;494:108-15.
232. Wei D, Orlandi E, Simon S, Sjöblom J, Suurkuusk M. Interactions between asphaltenes and alkylbenzene-derived inhibitors investigated by isothermal titration calorimetry. J Therm Anal Calorim. 2015;120(3):1835-46.
233. Wei D, Orlandi E, Barriet M, Simon S, Sjöblom J. Aggregation of tetrameric acid in xylene and its interaction with asphaltenes by isothermal titration calorimetry. J Therm Anal Calorim. 2015;122(1):463-71.
234. Subramanian S, Sørland GH, Simon S, Xu Z, Sjöblom J. Asphaltene fractionation based on adsorption onto calcium carbonate: Part 2. Self-association and aggregation properties. Colloids and Surfaces A: Physicochemical and Engineering Aspects. 2017;514:79-90.
235. Akitt JW, Mann BE. NMR and Chemistry: An introduction to modern NMR spectroscopy: Crc Press; 2000.
236. Sørland GH. Dynamic Pulsed-field-gradient NMR: Springer; 2014.
237. Hore PJ. NMR Principles. In: Lindon JC, editor. Encyclopedia of Spectroscopy and Spectrometry (Second Edition). Oxford: Academic Press; 1999. p. 1833-40.
238. Sebastião RCO, Pacheco CN, Braga JP, Piló-Veloso D. Diffusion coefficient distribution from NMR-DOSY experiments using Hopfield neural network. Journal of Magnetic Resonance. 2006;182(1):22-8.

239. Einstein A. Über die von der molekularkinetischen Theorie der Wärme geforderte Bewegung von in ruhenden Flüssigkeiten suspendierten Teilchen. Annalen der Physik. 1905;322(8):549-60.
240. Bedson P, Prichard E, Royal Society of Chemistry S. Gas Chromatography. Cambridge, United Kingdom: Royal Society of Chemistry; 2003.
241. Poole C. Gas Chromatography : Gas Chromatography. Saint Louis, UNITED STATES: Elsevier; 2012.
242. Hübschmann H-J. Handbook of GC-MS: fundamentals and applications: John Wiley & Sons; 2015.
243. LI Chuan-Xian ZC-G, SUN De-Jun, SUN Jie. Physicochemical Research on Effect of Pour Point Depressant on Wax Precipitation and Dissolution of Waxy Oil. Chemical Journal of Chinese Universities. 2003;24(8):1451-5.
244. Birdi K. Handbook of surface and colloid chemistry: CRC Press; 2015.
245. Subramanian S, Simon S, Gao B, Sjöblom J. Asphaltene fractionation based on adsorption onto calcium carbonate: Part 1. Characterization of sub-fractions and QCM-D measurements. Colloids and Surfaces A: Physicochemical and Engineering Aspects. 2016;495:136-48.
246. Prahl U. Einfluss von Asphaltenen auf die Kristallisation von Paraffinen. Institut für Erdöl- und Erdgasforschung Clausthal-Zellerfeld: Technische Universität Clausthal; 1998.

# Publication I

## Non-linear dependency of wax appearance temperature on cooling rate

Journal of Petroleum Science and Engineering 165 (2018) 114–126

Contents lists available at ScienceDirect

Journal of Petroleum Science and Engineering

journal homepage: www.elsevier.com/locate/petrol

# Non-linear dependency of wax appearance temperature on cooling rate

Jost Ruwoldt [a,*], Muh Kurniawan [a,b], Hans-Jörg Oschmann [a]

[a] *Ugelstad Laboratory, Department of Chemical Engineering, NTNU, N-7491 Trondheim, Norway*
[b] *Research and Development Center for Oil and Gas "LEMIGAS", Jakarta 12230, Indonesia*

ARTICLE INFO

*Keywords:*
Paraffin wax
Wax appearance temperature
Cooling rate
Wax deposition
Flow assurance
Crude oil production

ABSTRACT

The Wax Appearance Temperature (WAT) is usually the first parameter to consider, when assessing whether paraffin wax contained in the crude oil can become an issue during production. As such, correct determination of the WAT is crucial. Changes in cooling rate can cause large differences in the measured WAT. This article therefore investigates the relationship between WAT and cooling rate in detail. A new algorithm is devised to determine the WAT from experimental data more accurately. This algorithm is tested with waxy model solutions and crude oil, and the results are compared between established techniques such as differential scanning calorimetry (DSC), cross-polarized microscopy (CPM), and viscometry. The data is in good agreement with modelling from homogeneous nucleation theory. Contrary to the general belief, the results show a predominantly non-linear dependency of WAT on cooling rate within the tested range of 20 °C/min to 0.5 °C/min. The assumption of linearity is therefore an oversimplification. Linear extrapolation to a zero cooling rate should only be done for cooling rates between 0.5 °C/min and 2 °C/min, as this range showed to be approximately linear. However, large gaps can exist between the theoretical solubility limit and the measured or extrapolated WAT. Moreover, for some samples one technique could be more sensitive at high cooling rates, whereas another technique could be more sensitive at lower cooling rates. It is therefore concluded that when assessing WAT, testing a representative range of cooling rates in addition to testing multiple instruments could be helpful in determining the worst-case-scenario.

## 1. Introduction

Current trends in subsea crude oil production are towards higher depths and harsher climates, which facilitates challenges imposed by paraffin wax contained in the crude oil. As the crude oil is transported through the pipeline, temperature and pressure decrease and the solubility limit of paraffin wax can be exceeded. Crystallized wax may then lead to a number of problems, which include increased fluid viscosity, flow reduction or plugging of the pipeline due to wax deposition, and restartability issues after pipeline shut-in (Kelland, 2014). To assess, whether or not wax related problems are imminent, the Wax Appearance Temperature (WAT) is usually taken as a first indicator (Huang et al., 2015). The WAT is defined as the temperature, at which the onset of wax crystallization can be observed, and is also referred to as cloud point or wax precipitation temperature. Severe costs are associated with wax related issues, such as downtime, wax deposition removal, the loss of equipment, or in an extreme case abandonment of a production site (Singh et al., 2000; Venkatesan, 2004). Correct determination of the WAT is therefore crucial. This article focusses on measuring WAT of several crude oils and model waxy oils to show the dependency between WAT and cooling rate. A new algorithm is presented to determine the WAT from experimental data more accurately. This algorithm is tested on crude oils and waxy model oils of different concentration, and the results are compared between cross-polarized microscopy (CPM), differential scanning calorimetry (DSC), and viscometry. Modelling via homogeneous nucleation theory is conducted, and the results are also discussed in terms of extrapolation to a zero cooling rate.

Wax crystallization has been reported to take place in three steps, which are nucleation, growth, and agglomeration (Machado and Lucas, 1999). During agglomeration, the wax crystals interlock three dimensionally and can form a Bingham-like gel with high yield strength (Emanuele et al., 2005). Different wax crystal shapes have been described, which include plate shaped crystals, needle shaped crystals, and malcrystalline waxes (Clarke, 1951). Based on wax crystal morphology, paraffin waxes can be grouped into macrocrystalline and microcrystalline wax. Consisting of primarily low molecular weight *n*-alkanes, macrocrystalline wax crystallizes to plate and needle shapes, whereas microcrystalline contains large ratios of high molecular weight

---

[*] Corresponding author.
*E-mail address:* jost.ruwoldt@ntnu.no (J. Ruwoldt).

https://doi.org/10.1016/j.petrol.2018.02.011
Received 24 October 2017; Received in revised form 4 January 2018; Accepted 5 February 2018

**Table 1**
Methods and techniques for measuring wax appearance temperatures.

| Method | Measuring Principle | Reference |
|---|---|---|
| Visual Inspection | The appearance of cloudiness in the sample is observed visually. | (Huang et al., 2015; Kelland, 2014) |
| Differential scanning calorimetry (DSC) | An exothermic change in heat flow during cooling accounts for wax crystallization. | (Huang et al., 2015; Kelland, 2014) |
| Cross-polarized microscopy (CPM) | Polarized light is depolarized by appearing wax crystals, making light pass the second filter of two perpendicular Nicol prisms. | (Huang et al., 2015; Kelland, 2014) |
| Viscometry | The appearance of solid crystals changes the viscosity of the sample. | (Huang et al., 2015; Kelland, 2014) |
| Fourier-transform infrared spectroscopy (FT-IR) | The intensity of IR absorbance of solid wax is higher than that of dissolved wax. | (Roehner and Hanson, 2001) |
| Near-infrared (NIR) scattering | Solid wax crystals lead to scattering of NIR light. | (Paso et al., 2009b) |
| X-ray computed tomography (CT) | The density of solid wax crystals is higher than that of the liquid bulk. | (Karacan et al., 2000) |
| Filter-plugging | Waxy crude oil is filtered continuously, where the formation of wax crystals leads to an increase in differential pressure over the filter. | (Monger-McClure et al., 1999) |
| Density variation measurements | Volumetric shrinkage of wax during solidification is detected. | (Kruka et al., 1995) |
| Sonic testing | The velocity, at which sound is transmitted through a medium, changes with the appearance of wax crystals. | (Becker, 2001) |
| Nuclear magnetic resonance (NMR) | Excited hydrogen nuclei in the solid phase have different relaxation time constants than in the liquid phase. | (Roenningsen et al., 1991) |

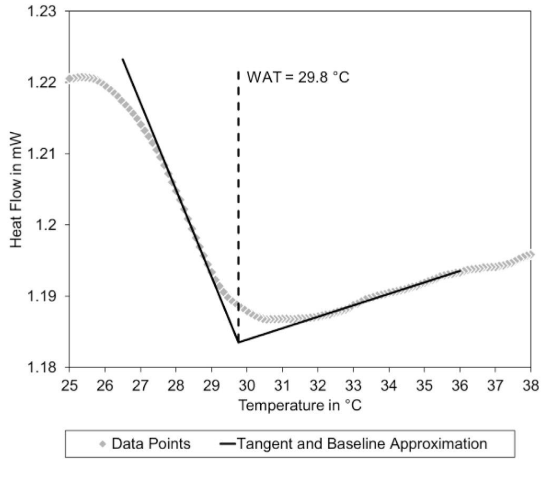

**Fig. 1.** WAT determination using the tangent procedure from DSC data of light crude oil at a cooling rate of 2 °C/min.

*iso-* and *cyclo*-alkanes, which cause it to crystallize to amorphous particles of in comparison smaller dimensions (Yang et al., 2015). Wax inhibitors most commonly act as crystal modifiers, which can change the wax crystal morphology via co-precipitation. The desired effect is that particles are formed, which have a lower hydrodynamic radius and a lower propensity for three dimensional interlocking (Oschmann, 1998). This will result in lower viscosity fluids, gels of lower yield strength, and a decreased pour-point, hence also the name pour point depressant (PPD) for this type of wax inhibitor. Another mechanism described is the formation of solute complexes, which delays wax crystallization and therefore WAT (Claudy et al., 1993).

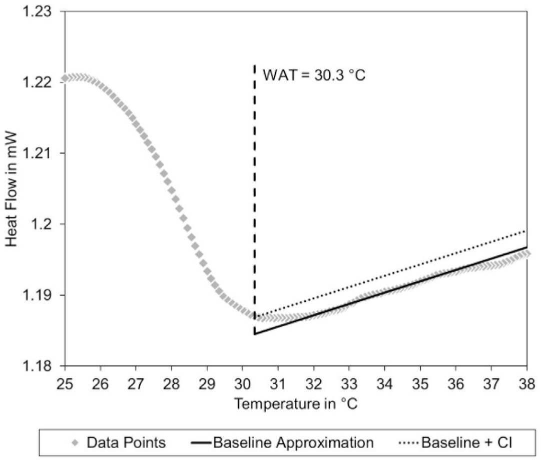

**Fig. 2.** WAT determination from DSC data of light crude oil at a cooling rate of 2 °C/min. A confidence interval with factor ci = 3.291 and temperature interval $T_{int} = 15$ °C was used as input parameters.

A number of methods and techniques have been developed for measuring WAT, which are summarized in Table 1. Kruka grouped WAT measuring techniques according to the utilized physical principle into four categories (Kruka et al., 1995), which are (i) visual detection methods (CPM, NIR), (ii) thermal methods (DSC), (iii) density variation methods, and (iv) viscosity measurements (viscometry). An expansion of this list is provided by (v) mechanical methods (filter-plugging, sonic testing), (vi) radiation methods (x-ray CT), and (vii) electromagnetic methods (NMR). A number of studies have been published on reliability and accuracy of individual methods, and method comparisons (Alcazar-Vara and Buenrostro-Gonzalez, 2011; Amadi et al., 2005; Coutinho and Daridon, 2005; Japper-Jaafar et al., 2016; Kok et al., 1996; Kök et al., 1999; Kruka et al., 1995; Létoffé et al., 1995; Monger-McClure et al., 1999; Roenningsen et al., 1991). Cloud point measurements via ASTM-D2500 or ASTM-D3117 have been critically discussed due to imperfections in temperature homogeneity within the sample, inconsistent cooling gradients, and the operator bias during visual detection (Coutinho and Daridon, 2005; Kruka et al., 1995). Cross polarized microscopy (CPM) is regarded as the most accurate method for predicting the WAT, but also bears the disadvantage of subjectivity when the operator judges the first appearance of wax crystals (Monger-McClure et al., 1999; Roenningsen et al., 1991). In contrast to this, Japper-Jaafar studied three WAT measuring techniques and concluded on micro-DSC and rheometry to provide a better sensitivity than CPM (Japper-Jaafar et al., 2016). Kök et al. compared DSC, CPM, and viscometry by measuring WAT for 15 different crude oils (Kok et al., 1996). The author concluded that there is good agreement between the techniques, if the crude oil shows a significant precipitation rate at crystallization onset. Moreover, the author showed that there can be differences of up to 10 °C and more in WAT, and that none of the methods were superior to another. It was therefore advised to use more than one technique when measuring WAT. Monger-McClure et al. also recommended the use of multiple techniques after comparing WAT measured by DSC, CPM, filter-plugging, and FT-IR (Monger-McClure et al., 1999). In addition, the usefulness of model predictions based on crude oil composition has been mentioned. Erickson et al. used thermodynamic modelling to predict the WAT from

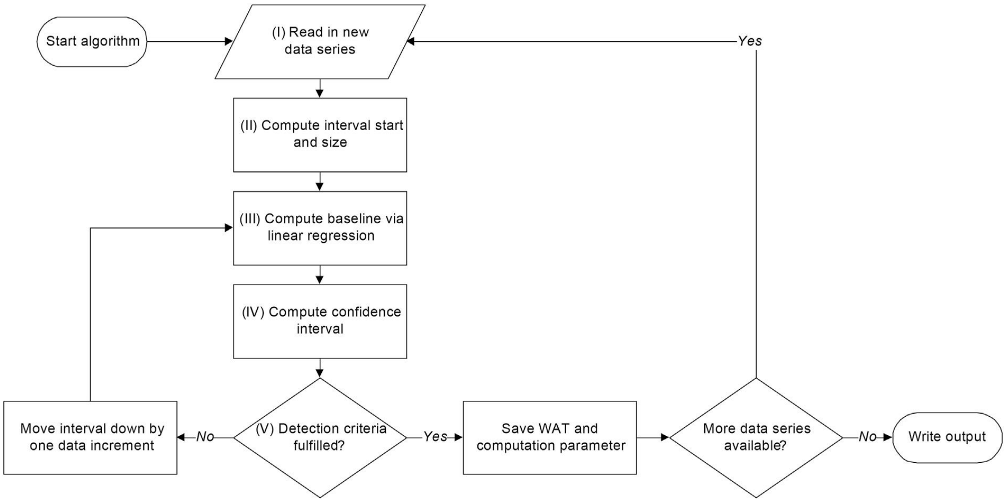

**Fig. 3.** WAT detection algorithm.

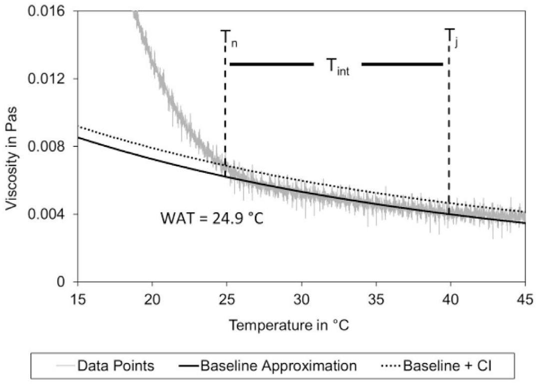

**Fig. 4.** WAT determination using $T_{int} = 15\,°C$ and $ci = 1.960$ for viscometry data of a light crude oil at a cooling rate of 5 °C/min.

compositional analysis, which were in good agreement with measurements from DSC, viscometry, and CPM (Erickson et al., 1993). The cooling or heating rate has a considerable influence on WAT due to super-cooling and -heating effects (Coutinho and Daridon, 2005), which is why some authors have introduced a correction factor at high cooling rates (Monger-McClure et al., 1999). A general criticism for all types of measurements is that a certain amount of wax needs to precipitate before it can be detected, which ultimately leads to a sensitivity that is instrument dependent (Roenningsen et al., 1991).

## 2. WAT-detection algorithm

Using DSC techniques, the WAT is typically obtained as the intersection of baseline and a tangent that is fitted to the inflection point (Huang et al., 2015), as depicted in Fig. 1. A discrepancy arises from the fact that the heat signal is departing from the baseline already before detection of the WAT, which therefore is an underestimate of the actual onset temperature. In addition to that, the interval borders for baseline and tangent computation are usually set manually, which can cause different operators to obtain different values.

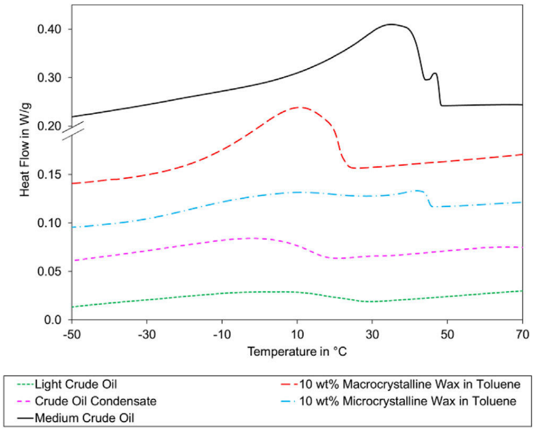

**Fig. 5.** DSC thermal profile of different crude oils and waxy solutions at a cooling rate of 5 °C/min. Data was shifted on the y-axis for better overview.

To improve WAT detection, a new algorithm was developed in this work. As opposed to the tangent procedure, this algorithm is based on the principle of detecting a thermal signal as early as it is statistically significant. In short, the algorithm computes a confidence interval based on the noise of the signal, and detects the WAT as exceeding this threshold value. Similar approaches have been taken by other authors in the past (Kok et al., 1996; Létoffé et al., 1995), and first application has been demonstrated in a preceding publication (Ruwoldt et al., 2017). An illustration is shown in Fig. 2, which also points out the improved sensitivity as the detected WAT is 0.5 °C higher than using the tangent procedure for the same data in Fig. 1. An additional advantage is a lower degree of operator bias, because the algorithm works fully automated after being provided a set of input parameters.

A flowchart of the algorithm is provided in Fig. 3. The individual steps are described more in detail below, where each point is referring to an activity of the flowchart in Fig. 3.

**Table 2**
Calculated wax content of different crude oil and model waxy solutions. Each value is the average with standard deviation of four measurements in case of a crude oil, and two measurements in case of a model waxy solution.

| Sample | Wax Content |
|---|---|
| | *wt%* |
| Light Crude Oil | 2.88 ± 0.02 |
| Crude Oil Condensate | 3.46 ± 0.01 |
| Medium Crude Oil | 44.70 ± 0.05 |
| 10 wt% Macrocrystalline Wax in Toluene | 13.89 ± 0.03 |
| 5 wt% Macrocrystalline Wax in Toluene | 6.00 ± 0.04 |
| 10 wt% Microcrystalline Wax in Toluene | 8.45 ± 0.05 |
| 5 wt% Microcrystalline Wax in Toluene | 3.39 ± 0.02 |

(I) A data series accounting for a single measurement run is extracted from the experimental data. The data series is defined as a two dimensional array of length $m$ with temperature points $\{T_1, \ldots, T_m\}$ and signal values $\{H_1, \ldots, H_m\}$. Corresponding to a constant cooling rate, the temperature is assumed to be continuously decreasing and to follow a constant decrease with each data increment.

(II) For subsequent computations, a data interval $\{T_j, \ldots, T_n\}$ is allocated within the data series $\{T_1, \ldots, T_m\}$ based on the input parameters $T_{int}$ and $T_{start}$. The interval is bound by the highest values for $T_j$ and $T_n$ that satisfy the inequalities $T_j < T_{start}$ and $T_n < T_{start} - T_{int}$.

(III) Using equation (1), linear regression via least squares is performed on the entries within the data interval $\{T_j, \ldots, T_n\}$ to obtain the mean signal values $\overline{H}_i$, also referred to as baseline.

$$\min \sum_{i=j}^{n} \left(\overline{H}_i - H_i\right)^2 \tag{1}$$

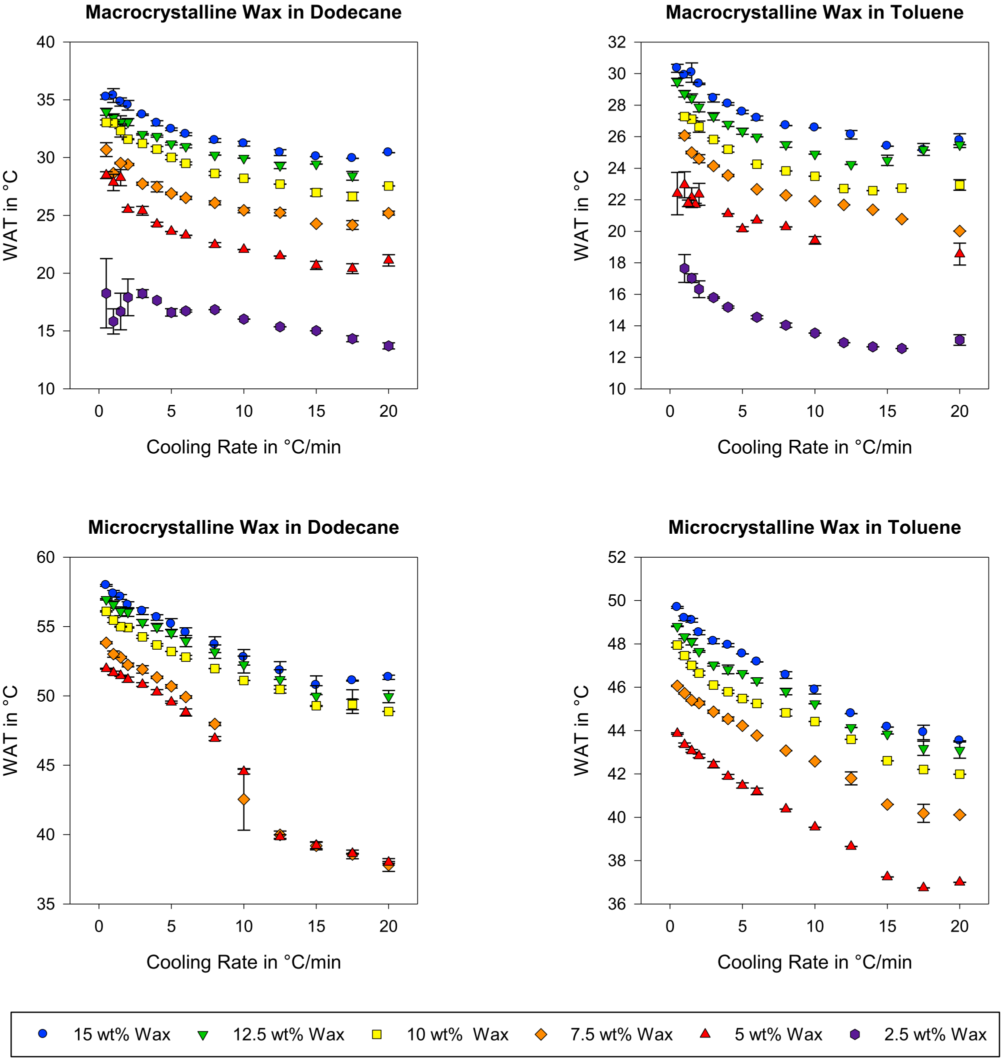

**Fig. 6.** DSC results: Progression of WAT with changing cooling rate tested for concentrations of 2.5–15 wt% wax in two different solvents. Each point represents the average of three measurements with according standard deviation.

(IV) Using equation (2), the confidence interval *CI* is calculated for $\{T_j, \ldots, T_n\}$ as the product of input parameter *ci* and standard deviation $\sigma$.

$$CI = ci \cdot \sigma = ci \sqrt{\frac{1}{n-j} \sum_{i=j}^{n} \left(\overline{H}_i - H_i\right)^2} \tag{2}$$

(V) The detection criteria is checked, which states that the three consecutive values below the lowest interval point $H_n$ have to be outside the confidence interval as stated in equation (3). If the criteria is not fulfilled, then the data interval $\{T_j, \ldots, T_n\}$ is shifted down by one increment, i.e. $j=j+1$ and $n=n+1$, and the algorithm returns to (III). If the criteria is fulfilled, then the WAT is saved as the temperature at $T_{n+1}$.

$$H_{n+k} > \left|\overline{H}_{n+k} + CI\right|, \tag{3}$$

where $k = 1, 2, 3$

For the algorithm to work, the input parameter $T_{int}$ has to be large enough for the straight line approximation to be robust. Testing has shown that values of 10–15 °C produce good results. The input parameter $T_{start}$ needs to be well above the WAT for correct detection, which also imposes requirements on experimental design as the data recording should start at least 20 °C above suspected WAT. Computing the confidence interval, the factor *ci* is not chosen arbitrarily. The assumption of normal distributed noise constitutes for a statistical interpretation of the possible error. Values for *ci* of 1.960 and 3.291 for example imply that less than 5% and 0.1%, respectively, of points outside the confidence interval account for random noise. Choosing a high *ci* therefore causes a less noisy WAT detection, but essentially lowers the sensitivity of the algorithm.

The algorithm is not limited to DSC data and can be extended to a number of different applications. For processing viscometry results in this publication, the data is first linearized under the assumption of Arrhenius type viscosity-temperature dependency of equation (3), where $\mu$ is the viscosity, $\mu_0$ is the pre-exponential factor, $E_A$ is the activation energy, $R$ the ideal gas constant, and $T$ the temperature.

$$\mu = \mu_0 e^{\frac{E_A}{RT}} \quad \Leftrightarrow \quad \ln(\mu) = \frac{E_A}{R}\frac{1}{T} + \ln(\mu_0) \tag{4}$$

Using this linearization, the same linear baseline approximation can be used in the algorithm, which simplifies computational efforts. However, it turned out to be advantageous to transform the value for *CI* back to be checked with the original experiment data. Testing showed a better sensitivity and accuracy for this procedure as opposed to performing thresholding in transformed form. Moreover, working as close to the original data as possible has the advantage of removing any bias that might occur due to data transformation. An example of WAT detection using viscometry data is given in Fig. 4. It has to be noted that Arrhenius type equations are a good approximation for viscosity-temperature dependencies in crude oil, but more accurate descriptions have been devised involving additional parameters (Al-Zahrani and Al-Fariss, 1998; Ronningsen, 1995). However, the viscosity description was not extended, to favor simplicity of the algorithm.

## 3. Experimental section

### 3.1. Materials

Organic solvents were obtained as toluene (≥99.9%, HPLC-grade, VWR Norway), and dodecane (≥99%, reagent grad, Sigmaaldrich Norway). Single component waxes were purchased as n-tetracosane (99% purity, Alfa Caesar, VWR Norway), octacosane (99%, Sigmaaldrich Norway), and hexatriacontane (98%, Sigmaaldrich Norway). Polydisperse waxes were obtained as 5405 (macrocrystalline) wax, and 3971 (microcrystalline) wax from Sasol Wax, Germany. The macrocrystalline wax consists of predominantly *n*-alkanes with carbon numbers around $C_{20}$ to $C_{40}$, whereas the microcrystalline wax consists of majorly *iso*-alkanes with carbon numbers around $C_{36}$ to $C_{75}$ and more. More detailed information about composition and properties is available in literature (Paso et al., 2009a, 2008, 2009c). A PPD based on polyacrylate and poly(ethylene-vinyl acetate) with 50% active content was provided by BASF, Germany. A light crude oil and a crude oil condensate were used, both originating from the Norwegian continental shelf. Properties and composition of the light crude oil are available in a previous publication of our group, where it is referred to as crude oil B (Dudek et al., 2017). Additionally, a medium waxy crude oil from onshore of Sumatra, Indonesia, was obtained.

### 3.2. Sample preparation

Waxy solutions, also referred to as model waxy, were prepared by first weighing the solids and then adding the required amount of solvent. Prior to sampling and usage, the wax was fully dissolved in solvent by heating to at least 20 °C above WAT and keeping at that temperature for a duration of at least 30 min. Also, all model waxy oils were prepared on the day of use and stored in closed vials, to avoid the influence of solvent evaporation. Crude oil samples were heated to at least 20 °C above WAT for a duration of 30–60 min and shaken thoroughly prior to sampling, to

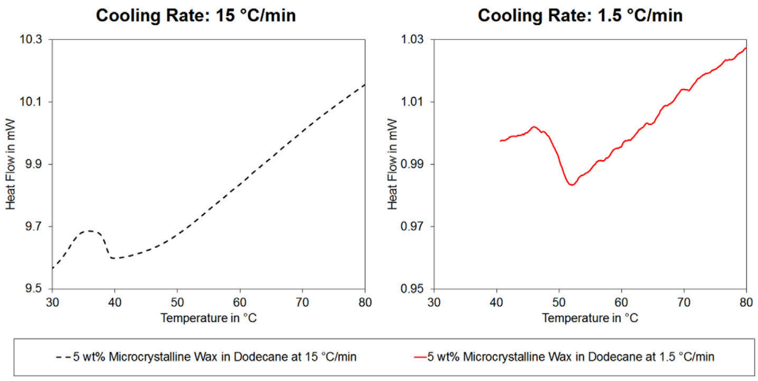

**Fig. 7.** DSC heat profiles for 5 wt% microcrystalline wax in dodecane at cooling rates 15 °C/min and 1.5 °C/min. The heat flow for a cooling rate of 1.5 °C/min was multiplied by a factor of 10 for better comparison.

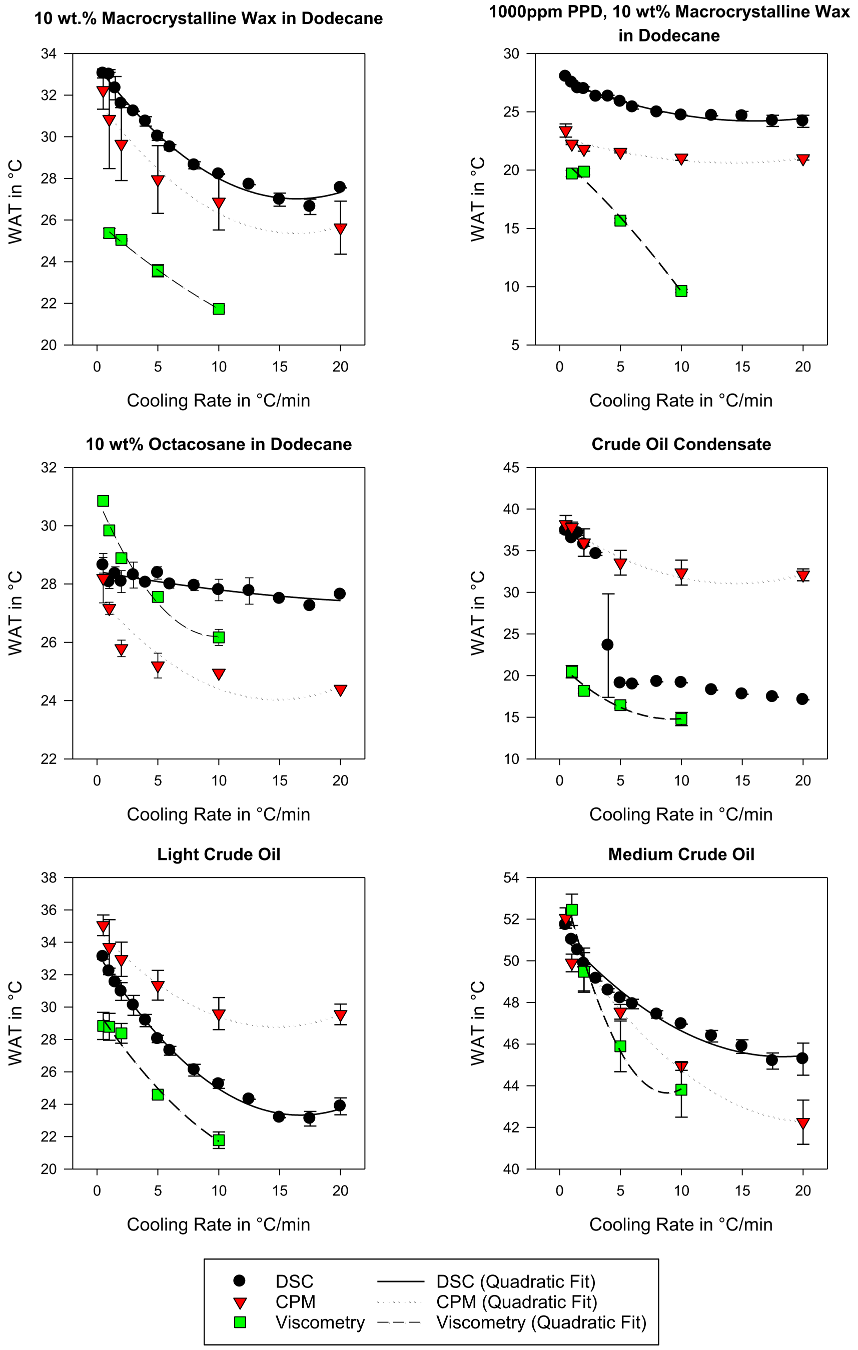

**Fig. 8.** DSC, CPM, and viscometry results: Development of WAT in dependence of cooling rate tested for three model waxy oils and three crude oil samples. Each point represents the average of two to four measurements with according standard deviation. Data series were fitted with a quadratic regression equation.

ensure a homogeneous sample. Longer heating periods were avoided, if possible, to minimize the effects of oxidation in the crude oil.

### 3.3. *Differential scanning calorimetry (DSC)*

DSC experiments were conducted on a Q2000 from TA Instruments using Tzero Hermetic Pans. Calibration of the instrument was done by measuring the heat and temperature of melting pure indium. The sample pan was loaded with 10–20 mg of sample and sealed hermetically. As a result of preliminary screening, no differences in WAT were observed for varying the sample mass between 10 and 25 mg. Experiments were conducted as multiple runs of a single sample loading. During each experiment, a series of cooling rates was applied, going from higher to lower cooling rates. The series was repeated two times to obtain three measurements for each cooling rate in total. Before each measurement, the wax was re-dissolved by heating the sample to more than 40 °C above WAT and keeping isothermal for at least 2 min. No effects of thermal history, such as a drift in WAT, were observed following this heating protocol. The sample pans were weighed before and after the experiment, to ensure that no loss of sample had occurred. Data collection was set to 0.1 s per data point.

### 3.4. *Cross polarized microscopy (CPM)*

A Nikon Eclipse microscope ME600 in cross polarization mode was used for observing the wax crystal visual appearance. A combination of 10X/22 ocular lens and ELWD 10X/0.4 objective lens gave magnification of 100X. VitroTube rectangular capillaries sized 1 mm wide and 0.05 mm deep from VitroCom were used to contain the wax sample. Both ends of the capillary were sealed with 3M Scotch cyanoacrylate base glue, where an air bubble was left each time between the glue and the sample to prevent contamination. Temperature controlling was done by a Linkam LTS120 temperature control stage. Initial temperature was set to more than 20 °C above WAT for 10 min to ensure that the wax crystals were dissolved and to remove any thermal history. A quick cooling of 10 °C/min was applied to bring the temperature down to approximately 15 °C above WAT. The cooling then set at the designated rate until the image capturing was finished. A CoolSnap-Pro monochrome digital camera from Media Cybernetics was used to periodically capture the images. Image capturing was started approximately 5 °C above the suspected WAT, and was designed to give a resolution of greater than 0.1 °C per image. The image series were reviewed manually to observe the earliest wax crystal appearance.

### 3.5. *Viscometry*

Rheological experiments were conducted on an Anton Paar Physica 301. The rheometer was equipped with a 4 cm in diameter 2° cone and plate geometry, which had been sandblasted to provide additional roughness and to prevent slippage. A gap size of 170 mm was used. Each experiment consisted of injecting the hot sample into the rheometer geometry, which had been heated to at least 20 °C above WAT. A defined cooling rate was subsequently applied and the measurement commenced. New sample was used for each measurement. A shear rate of 25 $s^{-1}$ was applied for continuously measuring the viscosity of the sample. Data was recorded every 0.1 s.

## 4. Results and discussion

### 4.1. *Paraffin wax composition and crude oil wax content*

To obtain qualitative and quantitative information about paraffin wax in the crude oil samples, DSC experiments were conducted. The thermal profiles are shown in Fig. 5 and compared with model waxy solutions. Peak height and onset temperature vary, which indicates differences in wax content and molecular weight distribution. The medium crude oil

**Table 3**
WAT method comparison for DSC, CPM, and viscometry. Each value is the average of two to four measurements.

| Sample | Method | | Cooling Rate in °C/min | | | | | | | | | | | | | |
|---|---|---|---|---|---|---|---|---|---|---|---|---|---|---|---|---|
| | | | 20 | 17.5 | 15 | 12.5 | 10 | 8 | 6 | 5 | 4 | 3 | 2 | 1.5 | 1 | 0.5 |
| 10 wt% Macrocrystaline Wax in Dodecane | DSC | **Wax Appearance Temperature in °C** | 27.55 | 26.63 | 26.98 | 27.70 | 28.20 | 28.63 | 29.50 | 30.01 | 30.74 | 31.22 | 31.59 | 32.33 | 32.99 | 33.04 |
| | CPM | | 32.23 | | | | 25.63 | | | 26.88 | | | 27.95 | | 29.65 | 30.85 |
| | Viscometry | | | | | | 21.73 | | | 23.56 | | | 25.05 | | 25.37 | |
| 1000 ppm PPD, 10 wt% Macrocrystaline Wax in Dodecane | DSC | | 24.18 | 24.22 | 24.63 | 24.66 | 24.69 | 24.96 | 25.39 | 25.87 | 26.31 | 26.30 | 26.95 | 27.02 | 27.51 | 28.01 |
| | CPM | | 23.40 | | | | 21.00 | | | 21.05 | | | 21.55 | | 21.80 | 22.25 |
| | Viscometry | | | | | | 9.63 | | | 15.67 | | | 19.86 | | 19.71 | |
| 10 wt% Octacosane in Dodecane | DSC | | 27.64 | 27.24 | 27.49 | 27.76 | 27.79 | 27.94 | 27.99 | 28.38 | 28.05 | 28.30 | 28.08 | 28.35 | 28.07 | 28.64 |
| | CPM | | 28.20 | | | | 24.40 | | | 24.95 | | | 25.20 | | 25.79 | 27.17 |
| | Viscometry | | | | | | 26.17 | | | 27.56 | | | 28.89 | | 29.84 | 30.85 |
| Crude Oil Condensate | DSC | | 17.09 | 17.43 | 17.76 | 18.27 | 19.13 | 19.26 | 18.95 | 19.08 | 23.61 | 34.60 | 35.76 | 37.13 | 36.49 | 37.41 |
| | CPM | | 38.17 | | | | 32.10 | | | 32.37 | | | 33.55 | | 35.98 | 37.80 |
| | Viscometry | | | | | | 14.79 | | | 16.45 | | | 18.18 | | 20.47 | |
| Light Crude Oil | DSC | | 45.28 | 45.19 | 45.88 | 46.38 | 46.96 | 47.42 | 47.92 | 48.20 | 48.58 | 49.14 | 49.87 | 50.51 | 51.01 | 51.72 |
| | CPM | | 29.55 | | | | 29.60 | | | 31.35 | | | 32.95 | | 33.70 | 35.05 |
| | Viscometry | | | | | | 21.78 | | | 24.59 | | | 28.38 | | 28.78 | 28.84 |
| Medium Crude Oil | DSC | | 45.28 | 45.19 | 45.88 | 46.38 | 46.96 | 47.42 | 47.92 | 48.20 | 48.58 | 49.14 | 49.87 | 50.51 | 51.01 | 51.72 |
| | CPM | | | | | | 43.81 | | | 45.89 | | | 49.48 | | 52.45 | |
| | Viscometry | | 49.90 | | | | 49.55 | | | 47.55 | | | 44.95 | | 42.25 | 52.05 |

appears to have both the highest amount and the highest average molecular weight of paraffin wax among the crude oils tested, since the according thermal profile accounts for the largest peak area and the highest crystallization temperature. The heat flows of the medium crude oil and the microcrystalline wax show two local maxima each, which could be due to a bimodal distribution in paraffin molecular weight. The main peak of the crude oil condensate is located approximately 10 °C lower than the main peak of the light crude oil. This indicates a lower average molecular weight, as the total amount of wax in the crude oil condensate appears to be higher due to a greater peak area. Both the medium crude oil and the macrocrystalline wax have more compact peaks as compared to the other crude oils and model wax solutions, which indicates more narrow distribution in molecular weight of the paraffin wax.

The paraffin wax content was determined according to the procedure published by Chen et al. (2004). In this procedure, the DSC heat signal at 5 °C/min is integrated from WAT to −20 °C, and the resulting heat is used to compute the wax content using equation (5), where $c_{wax}$ is the wax content in wt%, and $Q_{oil}$ is the integrated DSC signal as thermal effect of wax precipitation in J/g.

$$c_{wax} = 0.73Q_{oil} + 0.74 \tag{5}$$

The calculated wax contents are listed in Table 2. Testing the procedure on waxy solutions of known composition showed that the calculated wax content deviated from the actual content by a factor between 0.65 and 1.4, depending on wax type and concentration. The computed wax percentages of the crude oil samples therefore only represent the order of magnitude and are not to be taken as absolute values.

### 4.2. Model waxy oils

The WAT-detection algorithm described in chapter 2 was first tested on DSC data of model waxy oils. Different paraffin wax ratios were prepared in dodecane and toluene to include one aliphatic and one aromatic solvent. Type 5405 macrocrystalline wax and type 3971 microcrystalline wax from Sasol Germany were selected as representative wax samples, because these cover essentially different molecular weight distributions. The results are plotted in Fig. 6. The dependency of WAT on cooling rate follows a realistic trend, as increasing wax content and decreasing cooling rate each yield an increase in WAT. The development of WAT with cooling rate can predominantly be described as a quadratic parabola. An exception is made by 5 wt% and 7.5 wt% microcrystalline wax in dodecane, where the progression of WAT with cooling rate resembles a cubic parabola with an inflection point at approximately 10 °C/min. The reason for this deviating curve shape is slow precipitation kinetics of high molecular weight paraffin contained in the microcrystalline wax. An according example is shown in Fig. 7, which illustrates excessive front tailing of the onset peak at 15 °C/min and an in comparison pronounced crystallization onset at 1.5 °C/min. After a sufficient decrease in cooling rate, the precipitation kinetics appear to be no longer the limiting factor, which in turn results in a comparably large increase of 10 °C in WAT between 12.5 °C/min and 8 °C/min. Experiments that were conducted with 2.5 wt% microcrystalline wax in dodecane or toluene are not displayed in Fig. 6, because the results yielded either no or ambiguous WAT values. The microcrystalline wax crystallizes over a broad temperature range, which consequently has a low signal to noise ratio.

Fig. 6 also shows an increase in standard deviation towards slower cooling rates, which is the result of the decrease in signal to noise ratio. Moreover, for a number of measurements the detected WAT at 20 °C/min is higher than that at 17.5 °C/min or 15 °C/min. There is general consensus that high cooling rates will lead to increased temperature lag in the sample, as well as a greater nucleation lag within the sample (Coutinho and Daridon, 2005). Both effects would lead to a decrease in WAT at increasing cooling rate, which is not seen for all measurements with cooling rates above 15 °C/min in Fig. 6. An explanation for this contradiction could be made by the data recording interval, which is time finite. As the cooling rated increases, the resolution of data points per temperature unit decreases and thus the measurement becomes less accurate. Screening at cooling rates above 20 °C/min showed that data became more scattered. Moreover, the instrument had a maximum cooling rate of 30 °C/min at given experiment conditions. Higher cooling rates could not be maintained over the entire operating window. Operating close to maximum conditions could therefore introduce thermal gradients in the instrument, which could skew the temperature measurement and result in the detection of higher WAT values.

It can be concluded that the new WAT-detection algorithm works for a range of paraffin wax concentrations and cooling rates, given there are

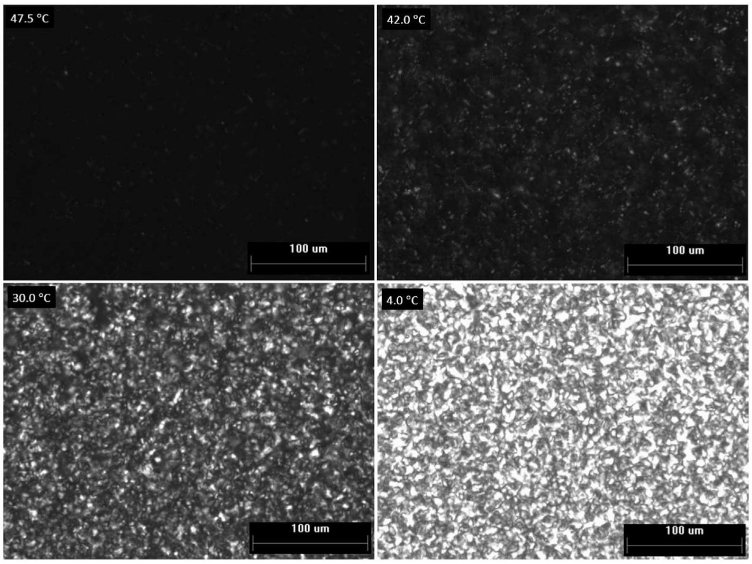

**Fig. 9.** CPM image series of medium crude oil at different temperatures. A cooling rate of 1 °C/min was applied and the detected WAT is 49.7 °C.

not instrument limitations and that the measurement provides a good signal to noise ratio with a pronounced signal change at crystallization onset. Poorly pronounced peaks may produce delayed WAT-detection or no detection at all. A decrease in *ci* can improve sensitivity, but at an increased noise level. Heuristic tuning has shown that for DSC experiments conducted in this work, a confidence interval with a factor of $ci = 3.291$ represents the best trade-off between detection sensitivity and noise level.

### 4.3. Method comparison

To compare the development of WAT with cooling rate among different techniques, measurements were done using DSC, CPM, and viscometry. The results are plotted in Fig. 8 together with regression lines made by fitting second degree polynomials, and the number values are also listed in Table 3. Reproducibility of data in Fig. 8 was given within a certain margin of error. The largest data scattering was observed for CPM. In CPM, the procedure of capturing an image series turned out to be the most accurate, because the operator can review frame by frame to determine the first appearance of wax crystals. An explanation for the comparably higher data scattering may be found in the fact that contrary to DSC and viscometry, CPM views only a fraction of the sample. Crystallization may therefore already take place in the sample, but is not detected due to the limited view. Examples for CPM imaging are

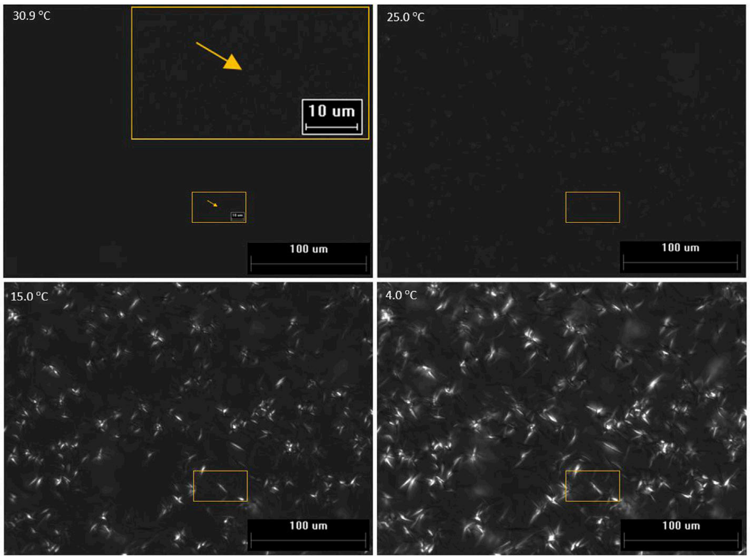

**Fig. 10.** CPM image series of 10 wt% macrocrystallien wax in dodecane at different temperatures. A cooling rate of 1 °C/min was applied and the detected WAT is 30.9 °C.

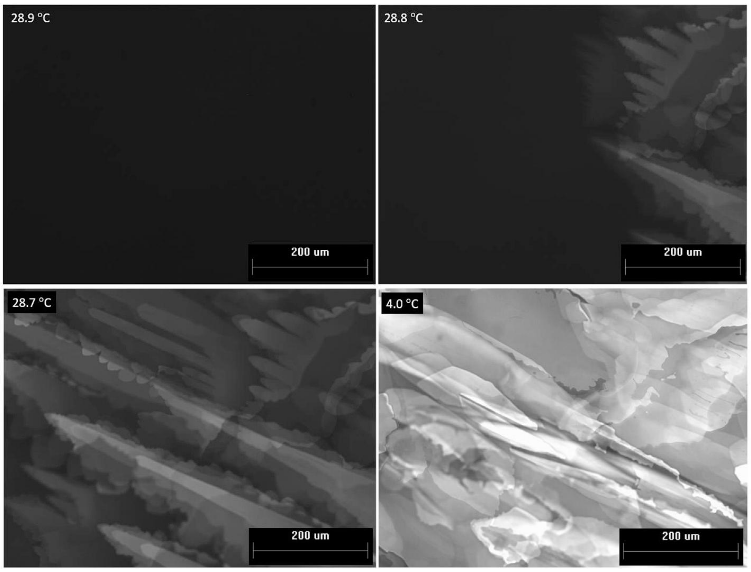

**Fig. 11.** CPM image series of 10 wt% octacosane in dodecane at different temperatures. A cooling rate of 0.5 °C/min was applied and the detected WAT is 28.8 °C.

displayed in Fig. 9, Fig. 10, and Fig. 11. As can be seen in Fig. 9, Fig. 10, and Fig. 11 wax crystallization starts with bright spots being visible on the image. These grow in size and number as the temperature further decreases and more wax crystallizes.

Apart from a few exceptions, the progression of WAT with cooling rate in Fig. 8 is of parabolic shape, facing concave upward. The DSC graph of octacosane progresses approximately linearly, and is coherent with other monodisperse wax in Fig. 12 of chapter 4.4. The crude oil condensate contains low amounts of a wax fraction that precipitates at about 10 °C higher than the major wax fraction. In CPM, this is observed as the occurrence of small wax crystals at approximately 35 °C with little to no change until around 25 to 20 °C. As a result, the DSC of crude oil condensate shows a jump in WAT of 15 °C between cooling rates 5 and 3 °C/min. This scenario is similar to the case presented in Fig. 7 of chapter 4.2, where WAT-detection is delayed at high cooling rates due to a precipitation onset that is not well pronounced. In Fig. 8, viscometry of macrocrystalline wax and light crude oil shows a progression of WAT with cooling rate that is either an approximate straight line, or a concave down parabola. This deviation from the general trend can be explained by the fact that the properties of waxy gels are a function of both thermal and shear history. At low cooling rates, the absolute amount of shearing done to the sample is greater than the shearing done at high cooling rates. Increased shearing can decrease wax crystal dimensions (Venkatesan et al., 2005), which can furthermore result in a lower viscosity change upon wax crystallization and thereby delayed WAT detection.

Comparing all techniques featured in Fig. 8, DSC accounted for the highest average WAT of medium crude oil and samples containing macrocrystalline wax. CPM showed the highest average WAT for both light crude oil and crude oil condensate. Viscometry detected the lowest average WAT for 5 out of the 6 samples, but this technique also detected the highest WAT for octacosane at low cooling rates. It can be concluded that no method is superior, since each method detected the highest WAT at certain conditions. Similar observations have been made by other authors in the past, and an explanation was given by the fact that different methods can have different sensitivities based on the waxy oil composition (Alcazar-Vara and Buenrostro-Gonzalez, 2011; Kok et al., 1996; Monger-McClure et al., 1999). The authors concluded that there should always be multiple methods used in comparison when testing WAT. As Fig. 8 also shows, the detected WAT for medium crude oil and octacosane samples was highest for DSC at high cooling rates, whereas other methods could detect higher WAT values at lower cooling rates. It appears that instrument sensitivity can also be cooling rate dependent. Testing a representative range of cooling rates in addition to testing multiple instruments could therefore be helpful in determining the worst-case-scenario when assessing WAT.

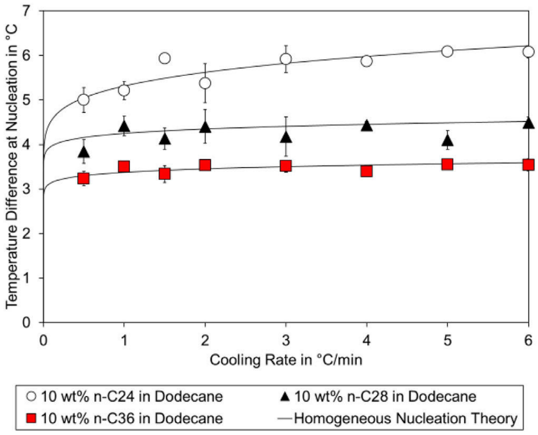

**Fig. 12.** Temperature difference at nucleation in relation to cooling rate for monodisperse paraffin waxes in dodecane. Each value is the average of three measurements, where error bars represent the according standard deviation. The solid lines represent fittings made via homogeneous nucleation theory.

### 4.4. Homogeneous nucleation theory

Paraffin wax solubility can be described using the van't Hoff relationship shown in equation (6), where the assumptions of ideal solubility behavior and negligible change in heat capacity upon crystallization are made (Ashbaugh et al., 2002). The term $x$ corresponds to the mole fraction of the dissolved paraffin waxes, $\Delta H_{diss}$ is the dissolution enthalpy, and $\Delta S_{diss}$ is the dissolution entropy.

$$\ln\left(\frac{1}{x}\right) = \frac{\Delta H_{diss}}{RT} - \frac{\Delta S_{diss}}{R} \tag{6}$$

According dissolution enthalpy and entropy values for paraffin waxes used in this study are listed in Table 4 together with calculated solubility temperatures for 10 wt% wax in dodecane, which corresponds to the theoretical WAT at given concentration.

**Table 4**
Dissolution enthalpy and entropy for different paraffin waxes in dodecane.

| Paraffin Wax Type | $\Delta H_{diss}$ | $\Delta S_{diss}$ | Calculated Cloud Point for 10 wt% Wax in Dodecane | Reference |
|---|---|---|---|---|
| | *kJ/ mole* | *J/ (mol•K)* | *°C* | |
| *n*-Tetracosane | 82.8 | 256.5 | 21.58 | (Brecevic and Garside, 1993) |
| *n*-Octacosane | 98.0 | 295 | 32.48 | (Madsen and Boistelle, 1979) |
| *n*-Hexatriacontane | 128.9 | 372 | 49.39 | (Madsen and Boistelle, 1979) |
| 5405 Sasol Wax (Macrocrystalline Wax) | 110.6 | 327 | 39.19 | (Paso et al., 2008) |
| 3971 Sasol Wax (Microcrystalline Wax) | 164.5 | 415 | 57.59 | (Paso et al., 2008) |

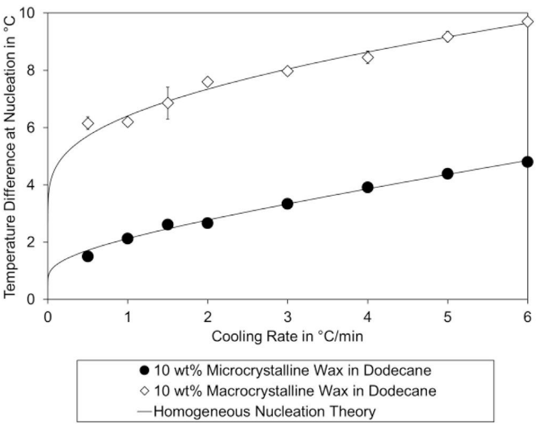

**Fig. 13.** Temperature difference at nucleation in relation to cooling rate for polydisperse paraffin waxes in dodecane. Each value is the average of three measurements, where error bars represent the according standard deviation. The solid lines represent fittings made via homogeneous nucleation theory.

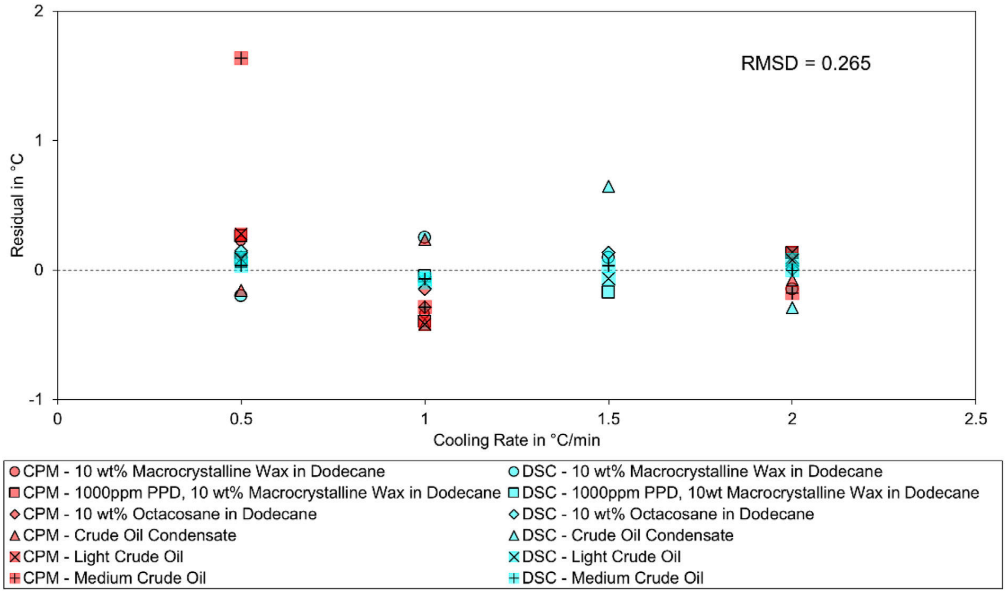

**Fig. 14.** Residual plot for linear regression of WAT within a cooling rate of 0.5–2 °C/min.

Paso showed that homogeneous nucleation theory can be used to describe the relationship between cooling rate and experimental WAT at low cooling rates (Paso, 2005). Using the concept of critical nuclei number density, the author established theoretical descriptions of supersaturation conditions and precipitation rate. Equation (7) shows the correlation between cooling rate and temperature difference at nucleation, which can be calculated as difference from equation (6) and WAT measurements. The term C* represents the cooling rate, ρ* is the critical nuclei density, A is a pre-exponential factor known as the collision factor, B is a material constant, and $\Delta T_{nuc}$ is the temperature difference at nucleation.

$$C^* = \left(\frac{A}{\rho^*}\right)\Delta T_{nuc}\left[\exp\left(-\frac{B}{\Delta T_{nuc}^2}\right) - \frac{\sqrt{B\pi}}{\Delta T_{nuc}}\,erfc\left(\frac{\sqrt{B}}{\Delta T_{nuc}}\right)\right] \tag{7}$$

Assuming one pseudo component, which contributes to the first precipitated fraction, this framework can also be applied to polydisperse waxes. The terms A/ρ* and B are varied as fitting parameters during least squares regression. Regression was done for DSC measurements of monodisperse and polydisperse waxes, and is shown in Figs. 13 and 14. According results for the fitting parameters are listed in Table 5.

Both mono- and polydisperse waxes are in good agreement with the model fit. As data scattering increases towards lower cooling rates, the deviation of model fit from experimental data is also more pronounced. As expressed by the model, the temperature difference at nucleation decreases as the cooling rate becomes smaller. This downward slope is more pronounced for polydisperse waxes than for monodisperse waxes. Another tendency is that the overall temperature difference at nucleation becomes smaller for paraffin waxes with higher (average) molecular weight. Model fitting was done for cooling rates of 6 °C/min and below, as cooling rates of up to 5 °C/min were used in the original work (Paso, 2005). Good overall fits could be obtained with the experimental data for cooling rates of up to 15 °C/min, but these scenarios yielded poor representation of the data at 1 °C/min and below. This confirms the initial assumption that only low cooling rates may be considered for modelling

**Table 5**
Fitting parameters for regression of homogeneous nucleation theory to DSC data of 10 wt% wax in dodecane.

| Paraffin Wax Type | $A/\rho^*$ | $B$ |
|---|---|---|
| Macrocrystalline | 4.42 | 67.09 |
| Microcrystalline | 2.27 | 2.29 |
| Tetracosane (n-C24) | 416.14 | 145.24 |
| Octacosane (n-C28) | 1.00E+7 | 255.26 |
| Hextriacontane (n-C36) | 1.00E+7 | 158.40 |

**Table 6**
WAT obtained via linear extrapolation from cooling rates of ≤2 °C/min to a zero cooling rate, and theoretical solubility limit calculated by equation (6).

| Method | Sample | Extrapolated WAT | Theoretical Solubility Limit | Difference |
|---|---|---|---|---|
| | | °C | °C | °C |
| DSC | 10 wt% Macrocrystalline Wax in Dodecane | 33.7 | 39.2 | 5.5 |
| CPM | 10 wt% Macrocrystalline Wax in Dodecane | 32.8 | 39.2 | 6.4 |
| DSC | 5 wt% Macrocrystalline Wax in Dodecane | 29.7 | 34.0 | 4.3 |
| DSC | 10 wt% Microcrystalline Wax in Dodecane | 56.4 | 57.6 | 1.2 |
| DSC | 5 wt% Microcrystalline Wax in Dodecane | 52.2 | 53.5 | 1.3 |
| DSC | 10 wt% Hexatricontane in Dodecane | 46.2 | 49.4 | 3.2 |
| DSC | 10 wt% Octacosane in Dodecane | 28.6 | 32.5 | 3.8 |
| CPM | 10 wt% Octacosane in Dodecane | 28.9 | 32.5 | 3.6 |
| Viscometry | 10 wt% Octacosane in Dodecane | 31.3 | 32.5 | 1.2 |
| DSC | 10 wt% Tetracosane in Dodecane | 16.7 | 21.6 | 4.9 |

with homogeneous nucleation theory. It has to be mentioned that the results indicate a considerable difference between measured and theoretical WAT, as the temperature difference at nucleation exhibited values of up to 10 °C and more. Lastly, it can be concluded that the results from the new WAT-detection algorithm are in good agreement with theoretical descriptions derived from homogeneous nucleation theory.

### 4.5. *WAT extrapolation*

The cooling rates imposed on crude oil during subsea production are typically low. A study that performed CPM measurements of live crude oils found cooling rates of 0.1 °C/min to be representative at 50 °C and below (Ravenscrof et al., 2008). This value is a feasible approximation, when considering that pipeline insulation is often designed for the crude oil to reach ambient temperatures after at least 24–36 h during production stop. Measuring at very low cooling rates therefore appears to be necessary. If this is not possible, an alternative is to extrapolate to lower cooling rates. Moreover, authors have previously attempted to obtain the thermodynamic solubility limit of hydrocarbons in organic solvents via linear extrapolation to an infinitely slow cooling rate (zero cooling rate) (LI Chuan-Xian et al., 2003; Young and Schall, 2001; Zhao et al., 2014). As has been demonstrated in chapter 4.2 and 4.3, linearity between WAT and cooling rate is often not the case. A better fit of the data was found by using second degree polynomials. Still, extrapolation with polynomials is not recommended as long as according equations are not based on the physical nature of the problem. Under consideration of homogeneous nucleation theory, a more correct description of the WAT to cooling rate dependency could be obtained via exponential or logarithmic equations. As can be seen in Figs. 12 and 13 of chapter 4.4, a strong change in function value would be needed when approaching zero cooling rate, which is a region that is not well defined by the experimental data. Using this type of extrapolation is therefore unreliable. Under consideration of the experimental data alone, a robust approach would be to limit linear extrapolation to cooling rates of 2 °C/min and lower. As depicted in the residual plot of Fig. 14, good agreement is found for a linear fit of DSC and CPM data in this region. The root mean square deviation (RMSD) was lowered from 1.903 to 0.265 when limiting linear regression to cooling rates of $\leq 2$ °C/min, as compared to using the whole range of data.

Linear extrapolation from data at 0.5 °C/min to 2 °C/min was exemplarily applied to a number of samples, and the results are listed in Table 6. The extrapolated WAT is not representative of the theoretical equilibrium, because the obtained values are within a range of 1–7 °C lower than the calculated solubility limit. Calculating the solubility limit, however, ideal solubility behavior was assumed. The difference between theoretical and measured WAT might therefore be smaller, if taking into account non-ideal behavior of the mixture and the fact that a certain amount of wax has to have crystallized to be detected. Another implication of Table 6 is that in order to account for the worst case scenario, methods predicting the WAT based on composition might provide a more conservative estimate. Still, the proposed extrapolation procedure can provide an outcome closer to the conditions in an actual pipeline. Moreover, it can be used as a method of comparison. Especially when measured WAT values are scattered, but available for several cooling rates, linear extrapolation of WAT at slow cooling rates can constitute a meaningful tool for averaging and comparing.

## 5. Conclusion

In this article, different WAT measuring techniques were assessed on a theoretical and practical level, where emphasis was put on the dependency of WAT on cooling rate. As a first step, a new algorithm for more accurate WAT detection was established. This algorithm was further tested with waxy model solutions and crude oil, for which measurements were conducted and compared with DSC, CPM, and viscometry. Modelling was done, and extrapolation methods for obtaining the WAT at an infinitely small cooling rate (zero cooling rate) were discussed.

The developed detection algorithm showed good reproducibility of experimental WAT at improved sensitivity. Good agreement was found between the experimental data and homogeneous nucleation theory. The progression of WAT with cooling rate was measured to be predominantly non-linear. A linear WAT to cooling rate relationship was true for only a few of the tested cases and therefore represents an oversimplification of a more complex picture. If WAT is to be extrapolated linearly to a zero cooling rate, it is recommended to limit the procedure to cooling rates between 0.5 °C/min and 2 °C/min, as this showed to be an approximately linear regime. However, the extrapolated WAT does not represent equilibrium conditions, and significant differences between the theoretical solubility limit and the measured or extrapolated WAT were found. Moreover, for some samples one method could be more sensitive at high cooling rates, whereas another method could be more sensitive at lower cooling rates. It is therefore recommended to not only test more than one measuring technique, but to assess a representative range of cooling rates as well when measuring the onset temperature of wax precipitation.

## Acknowledgements

This work was carried out as a part of SUBPRO, a Research-based Innovation Centre within Subsea Production and Processing. The authors gratefully acknowledge the financial support from SUBPRO, which is financed by the Research Council of Norway, major industry partners and NTNU. The authors would further like to thank Sebastien Simon and Jens Norrman for their support and helpful discussions.

## Acronyms

| | |
|---|---|
| CPM | Cross-polarized microscopy |
| CT | Computed tomography |
| DSC | Differential scanning calorimetry |
| FT-IR | Fourier-transform infrared |
| HPLC | High-performance liquid chromatography |
| NIR | Near-infrared |
| NMR | Nuclear magnetic resonance |
| PPD | Pour point depressant |
| RMSD | Root mean square deviation |
| WAT | wax appearance temperature |

*Symbols*

| | |
|---|---|
| $A$ | Pre-exponential factor (collision factor) |

| | |
|---|---|
| $B$ | Material constant |
| $CI$ | Confidence interval |
| $ci$ | Confidence interval factor (input parameter) |
| $c_{wax}$ | Wax content |
| $C^*$ | Cooling rate |
| $\Delta H_{diss}$ | Dissolution enthalpy |
| $\Delta S_{diss}$ | Dissolution entropy |
| $\Delta T_{nuc}$ | Temperature difference at nucleation |
| $E_A$ | Activation energy |
| $H$ | Signal intensity, corresponds to heat flow (DSC) or apparent viscosity (viscometry) |
| $\overline{H}_i$ | Averaged signal intensity |
| $i, j, k, m, n$ | Indexes |
| $\mu$ | Viscosity |
| $\mu_0$ | Pre-exponential factor |
| $Q_{oil}$ | Thermal effect |
| $R$ | Ideal gas constant |
| $\rho^*$ | Critical nuclei density |
| $\sigma$ | Standard deviation |
| $T$ | Temperature |
| $T_{int}$ | Temperature interval (input parameter) |
| $T_{start}$ | Starting temperature (input parameter) |
| $x$ | Mole fraction |

## References

Al-Zahrani, S.M., Al-Fariss, T.F., 1998. A general model for the viscosity of waxy oils. Chem. Eng. Process. Intensification 37 (5), 433–437.

Alcazar-Vara, L.A., Buenrostro-Gonzalez, E., 2011. Characterization of the wax precipitation in Mexican crude oils. Fuel Process. Technol. 92 (12), 2366–2374.

Amadi, S.U., et al., 2005. Measurement of the wax appearance temperature of gas-to-liquids products, Alaska north slope crude, and their blends. Energy Sources 27 (9), 831–838.

Ashbaugh, H.S., et al., 2002. Interaction of paraffin wax gels with random crystalline/amorphous hydrocarbon copolymers. Macromolecules 35 (18), 7044–7053.

Becker, J.R., 2001. Paraffin-Crystal-Modifier Studies in Field and Laboratory. Society of Petroleum Engineers.

Brecevic, L., Garside, J., 1993. Solubilities of tetracosane in hydrocarbon solvents. J. Chem. Eng. Data 38 (4), 598–601.

Chen, J., Zhang, J., Li, H., 2004. Determining the wax content of crude oils by using differential scanning calorimetry. Thermochim. Acta 410 (1–2), 23–26.

Chuan-Xian, Li, Z.C.-G, De-Jun, Sun, Jie, Sun, 2003. Physicochemical Research on effect of pour point depressant on wax precipitation and dissolution of waxy oil. Chem. J. Chin. Univ. 24 (8), 1451–1455.

Clarke, E.W., 1951. Crystal types of pure hydrocarbons in the paraffin wax range. Ind. Eng. Chem. 43 (11), 2526–2535.

Claudy, P., Létoffé, J.-M., Bonardi, B., Vassilakis, D., Damin, B., 1993. Interactions between n-alkanes and cloud point-cold filter plugging point depressants in a diesel fuel. A thermodynamic study. Fuel 72 (6), 821–827.

Coutinho, J.A.P., Daridon, J.-L., 2005. The limitations of the cloud point measurement techniques and the influence of the oil composition on its detection. Petrol. Sci. Technol. 23 (9–10), 1113–1128.

Dudek, M., Kancir, E., Øye, G., 2017. Influence of the crude oil and water compositions on the quality of synthetic produced water. Energy Fuel. 31 (4), 3708–3716.

Emanuele, V., et al., 2005. Wax crystallization and aggregation in a model crude oil. J. Phys. Condens. Matter 17 (45), S3651.

Erickson, D.D., Niesen, V.G., Brown, T.S., 1993. Thermodynamic Measurement and Prediction of Paraffin Precipitation in Crude Oil. Society of Petroleum Engineers.

Huang, Z., Zheng, S., Fogler, H.S., 2015. Wax Deposition: Experimental Characterizations, Theoretical Modeling, and Field Practices. CRC Press.

Japper-Jaafar, A., Bhaskoro, P.T., Mior, Z.S., 2016. A new perspective on the measurements of wax appearance temperature: comparison between DSC, thermomicroscopy and rheometry and the cooling rate effects. J. Petrol. Sci. Eng. 147, 672–681.

Karacan, C.Ö., Demiral, M.R.B., Kök, M.V., 2000. Application of x-ray ct imaging as an alternative tool for cloud point determination. Petrol. Sci. Technol. 18 (7–8), 835–849.

Kelland, M.A., 2014. Production Chemicals for the Oil and Gas Industry. CRC press.

Kok, M.V., et al., 1996. Comparison of wax appearance temperatures of crude oils by differential scanning calorimetry, thermomicroscopy and viscometry. Fuel 75 (7), 787–790.

Kök, M.V., Letoffe, J.M., Claudy, P., 1999. DSC and rheometry investigations of crude oils. J. Therm. Anal. Calorim. 56 (2), 959–965.

Kruka, V.R., Cadena, E.R., Long, T.E., 1995. Cloud-Point Determination for Crude Oils.

Létoffé, J.M., Claudy, P., Kok, M.V., Garcin, M., Volle, J.L., 1995. Crude oils: characterization of waxes precipitated on cooling by d.s.c. and thermomicroscopy. Fuel 74 (6), 810–817.

Machado, A.L.d.C., Lucas, E.F., 1999. Poly(Ethylene-co-Vinyl acetate) (EVA) copolymers as modifiers of oil wax crystallization. Petrol. Sci. Technol. 17 (9–10), 1029–1041.

Madsen, H.E.L., Boistelle, R., 1979. Solubility of octacosane and hexatriacontane in different n-alkane solvents. J. Chem. Soc. Faraday Trans. 1 Phys. Chem.Condens. Phases 75, 1254–1258.

Monger-McClure, T.G., Tackett, J.E., Merrill, L.S., 1999. Comparisons of Cloud Point Measurement and Paraffin Prediction Methods.

Oschmann, H.-J., 1998. Das Kristallisationsverhalten von Paraffinen in Abhängigkeit von ihrer Zusammensetzung sowie seine Beeinflussung durch Paraffininhibitoren, Technische Universität Clausthal, Papierflieger.

Paso, K.G., 2005. Paraffin Gelation Kinetics. University of Michigan.

Paso, K., Kompalla, T., Aske, N., Sjöblom, J., 2008. A quartz crystal microbalance characterization of metal-oil interfaces and interactions with wax molecules. J. Dispersion Sci. Technol. 29 (5), 775–782.

Paso, K., et al., 2009a. Wax Deposition Investigations with Thermal Gradient Quartz Crystal Microbalance, Handbook of Surface and Colloid Chemistry. CRC Press, pp. 567–584.

Paso, K., Kallevik, H., Sjoblom, J., 2009b. Measurement of wax appearance temperature using near-infrared (NIR) scattering. Energy Fuel. 23 (10), 4988–4994.

Paso, K., Kompalla, T., Oschmann, H.J., Sjöblom, J., 2009c. Rheological degradation of model wax-oil gels. J. Dispersion Sci. Technol. 30 (4), 472–480.

Ravenscrof, P.D., McCracken, I.R., Forsdyke, I., Chilcott, N., 2008. ‘Live’Wax appearance measurements-using ‘real Data’to strip out conservatism in pipeline design. In: 19th Oilfield Chemistry Symposium, Geilo, Norway.

Roehner, R.M., Hanson, F.V., 2001. Determination of wax precipitation temperature and amount of precipitated solid wax versus temperature for crude oils using FT-IR spectroscopy. Energy Fuel. 15 (3), 756–763.

Roenningsen, H.P., Bjoerndal, B., Baltzer Hansen, A., Batsberg Pedersen, W., 1991. Wax precipitation from North Sea crude oils: 1. Crystallization and dissolution temperatures, and Newtonian and non-Newtonian flow properties. Energy Fuel. 5 (6), 895–908.

Ronningsen, H.P., 1995. Correlations for Predicting Viscosity of W/O-emulsions Based on North Sea Crude Oils. Society of Petroleum Engineers.

Ruwoldt, J., Simon, S., Norrman, J., Oschmann, H.-J., Sjöblom, J., 2017. Wax-inhibitor interactions studied by isothermal titration calorimetry and effect of wax inhibitor on wax crystallization. Energy Fuel. 31 (7), 6838–6847.

Singh, P.V., Ramachandran, Fogler, H. Scott, Nagarajan, Nagi, 2000. Formation and aging of incipient thin film wax-oil gels. AIChE J. 45 (5), 1059–1074.

Venkatesan, R., 2004. The Deposition and Rheology of Organic gels.

Venkatesan, R., et al., 2005. The strength of paraffin gels formed under static and flow conditions. Chem. Eng. Sci. 60 (13), 3587–3598.

Yang, F., Zhao, Y., Sjöblom, J., Li, C., Paso, K.G., 2015. Polymeric wax inhibitors and pour point depressants for waxy crude oils: a critical review. J. Dispersion Sci. Technol. 36 (2), 213–225.

Young, P.H., Schall, C.A., 2001. Cycloalkane solubility determination through differential scanning calorimetry. Thermochim. Acta 367, 387–392.

Zhao, Y., Paso, K., Sjöblom, J., 2014. Thermal behavior and solid fraction dependent gel strength model of waxy oils. J. Therm. Anal. Calorim. 117 (1), 403–411.

# Publication II

## Isothermal Titration Calorimetry for Assessing Wax Inhibitors

# Isothermal Titration Calorimetry for Assessing Wax-Inhibitors

*Chemistry in the Oil Industry XV: Enabling Efficient Technologies Programme, Manchester, UK, 2017*

Jost Ruwoldt[1*], Sebastien Charles Simon[1], Hans-Jörg Oschmann[1], Johan Sjöblom[1]

[1]Ugelstad Laboratory, Department of Chemical Engineering, NTNU, N-7491 Trondheim, Norway

[*]Corresponding author e-mail: jost.ruwoldt@ntnu.no

Keywords: Flow Assurance, Wax Inhibitor, Pour Point Depressant, Isothermal Titration Calorimetry

## Abstract

Wax inhibitors and pour point depressants play an important role in managing wax related challenges in crude oil production. Co-precipitation of the inhibitor can alter crystal morphology, which can furthermore lead to delayed formation and decreased yield strength of a wax-oil gel [1]. Inhibitor effectiveness is often assessed by measuring the effect of inhibitor on Wax Appearance Temperature, crystal morphology, or gel breakage strength [2]. Testing inhibitor-wax interactions is a new approach that could additionally provide insights into the underlying reactions. In this work, isothermal titration calorimetry is applied to measure the interaction heat between wax inhibitors and macrocrystalline wax. The interaction heat is then compared to experiments performed on similar wax-inhibitor systems using differential scanning calorimetry, cross-polarized microscopy, and rheometry. All inhibitors tested show effects in one or more performance criteria. Findings suggest that there is a difference in the heat of interaction for particular inhibitors with the wax system, and that the affinity of inhibitor to solid wax is much stronger than to wax molecules that are in solution.

## 1. Introduction

Current trends in crude oil production are to explore deeper waters and harsher environments, which can aggravate challenges that arise from paraffin wax in the crude oil. As the crude oil is cooled down during pipeline-transport, paraffin waxes that were initially soluble due to high temperature and pressure in the reservoir can precipitate. Crystallized wax can cause challenges and issues both downhole and topside, which include [3]:

- Flow reduction or pipeline plugging due to wax deposition
- Increased fluid viscosity
- Restartability issues due to high wax gel strength
- Reduced operating efficiency
- Removal and disposal of wax

Wax deposition is managed by both prevention and remediation strategies. These can further be grouped into three categories, which are thermal measures, mechanical measures, and chemical measures [4]. Thermal prevention measures are applied to prevent the crude oil to cool below the Wax Appearance Temperature (WAT), for example via pipeline insulation or heating. The WAT or cloud point generally refers to the temperature, at which the onset of wax crystallization can be observed [5]. Thermal remediation measures consist of heating to melt and remove deposited waxes. A combination of thermal and chemical measures is provided by using hot solvents or water with surfactants. Mechanical measures remove wax deposition by scraping or cutting. Pigging is the most prominent form of mechanical wax removal [6], but other methods such as wireline cutters are documented as well [3]. During pigging, a cylindrical scraper is pushed through the pipeline to remove the wax deposit from the pipe walls. Preparing the pipeline with non-stick coating is also a measure taken by industry to prevent or reduce wax deposition [7]. Chemical prevention methods include the use of pour point depressants (PPDs), and dispersants/surfactants [8]. Pour point depressants are designed to lower the point at which crude oil forms a solid gel, which can maintain pumpability even after wax has crystallized. Surfactants and dispersants aim to reduce the adhesion of solid wax particles to each other or to the pipeline wall [9]. The term wax inhibitor (WI) will be used in this study as a common term describing substances, which can alleviate challenges due to paraffin wax via one or more functionalities. Technologies for wax control, which are not fully established in industry, include microwave heating, acoustic and ultrasonic treatment, microbial treatment [10], cold flow technology [11], and fused chemical reactions [12].

Wax crystallization is reported to take place in three stages, which are nucleation, growth, and agglomeration [4, 13]. Due to supersaturation, nucleation usually lags behind the thermodynamic equilibrium of a given waxy solution. Different geometrical shapes have been reported for wax crystals formed in organic solvents, which include plate shapes, needle shapes, and malcrystalline masses [14]. Based on crystal size, waxes can be categorized into macrocrystalline and microcrystalline wax. Macrocrystalline wax is reported to mainly consist of low molecular weight *n*-alkanes, whereas microcrystalline wax contains a significant amount of high molecular weight *iso*-alkanes and *cyclo*-alkanes [1]. When applying a constant cooling rate, crystallization happens almost instantaneously for single-component wax solutions, whereas in multi-component systems the crystal growth is a process that progresses over a certain time and temperature span. Consequently, the structure and strength of the resulting crystal network is not only depending on composition of the crude oil, but also on parameters such as cooling rate, shear conditions, thermal and shear history [6]. Moreover, the presence of crystal modifying substances plays an important role. Other compounds than paraffin wax may co-precipitate, which can alter and distort the structure of the formed wax crystals. This effect is the functioning mechanism of PPDs [15]. Macrocrystalline wax often has a high degree of three dimensional interlocking, which yields high gel strengths. In presence of the right PPD chemistries, this type of wax can crystallize as compact, dendrite-like or malcrystalline masses, yielding overall lower viscosity fluids and gels. Common PPD chemistries include poly(ethylene-vinyl acetate) (EVA), polyacrylate (PA), poly(ethylene-butene) (PEB), maleic anhydrides (MA), and even nano-hybrid materials [1, 16]. Generic chemical structures are shown in Fig. 1.

The WAT is usually considered as the first parameter to determine whether or not wax deposition may become an issue [5]. The most prominent methods to determine the WAT are cross-polarized microscopy (CPM), differential scanning calorimetry (DSC), viscometry, and visual inspection, which is also referred to as cloud point measurement. Alternative methods for measuring the WAT include FT-IR [17], NIR scattering [18], Filter-plugging [19], Sonic Testing [20], and NMR [21]. Apart from super cooling effects imposed by high cooling rates, a general criticism of WAT-measurements is that a certain amount of wax needs to precipitate, before it can be detected. This leads to a difference in sensitivity, which is instrument dependent [21]. The pour point is a well-established industrial standard for assessing when issues with the production of waxy crude oils might occur. The pour point is defined as the temperature, at which a given waxy solution loses its ability to flow freely. It can be determined via ASTM D97, D5849, or D5949 [22-24]. Also, the pour point is used for testing the effectiveness of wax inhibitors and pour point depressants. A comparable measure is the gelation point, which originates from characterization techniques of polymers. In the context of waxy crude oils, the gelation point is defined as the temperature, at which the storage modulus G' becomes larger than the loss modulus G" [25]. An alternative method was presented by applying a constant shear stress in a rotational rheometer, and defining the gelation point as the temperature, at which the shear rate drops to zero [26]. Rheometry is also applied for measuring gel breakage strength, which is fundamental to pipeline restart modelling [27]. Similar techniques have furthermore been applied to study the effect of wax inhibitors and other chemical additives onto gel breakage of model oil systems [28, 29]. For measuring the rate of wax deposition, cold finger or flow loop experiments are commonly applied [3, 30, 31]. The advantage of cold finger experiments is the smaller experiment setup und easier experiment conduct as compared to a flow loop rig. The advantage of flow loops is that this setup imitates the conditions found in a crude oil pipeline to the highest degree.

Isothermal titration calorimetry (ITC) is primarily used for measuring biochemical processes, such as the binding affinity of ligands for different proteins [32, 33]. The application of ITC to crude oil derived systems has predominantly focused on the characterization of asphaltenes. Merino-Garcia et al. performed experiments with asphaltene and resin solutions in toluene to determine the average number of sites in asphaltenes molecules, and the enthalpy of interaction between asphaltenes and resins [34]. The author furthermore investigated the interactions of asphaltenes with nonylphenol [35]. Wei et al. studied aggregation and self-association properties of tetrameric acid and asphaltenes, and the interactions of asphaltenes with asphaltene-inhibitors [36, 37]. This research was further expanded to asphaltene model compounds [38, 39]

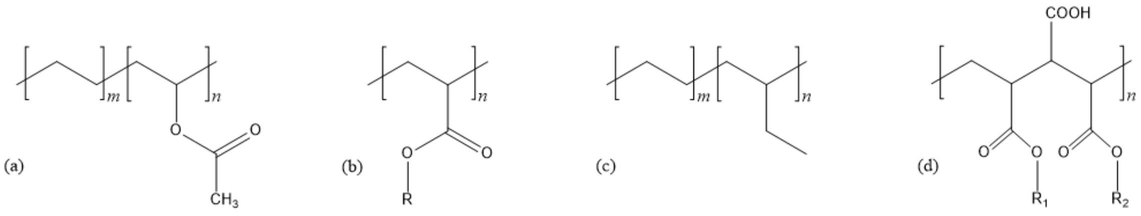

Fig. 1. Chemical structure of (a) poly(ethylene vinyl acetate) (EVA), (b) polyacrylate ester (PA), (c) poly(ethylene butene) (PEB), and (d) monoester of maleic anhydride acrylate ester copolymer [1, 16]

and asphaltenes, which had been fractionated via adsorption on calcium carbonate or stepwise precipitation [40]. Overall, research in this area provided a closer look onto the properties of asphaltenes and related components, and allowed for the identification of inhibitors with strong interaction enthalpy.

ITC has been applied to a model wax solutions in order to measure the interaction heat of certain WIs with macrocrystalline wax [41]. The results were then compared to performance characteristics, such as the inhibitors effect on WAT, gel breakage strength, and crystal morphology. It was shown that there are differences in interaction heat for different WIs, and that there is no correspondence between interaction heat and the selected performance characteristics. To expand these findings, this study investigates the interactions of selected WIs with macrocrystalline wax at temperatures above and below WAT. Complementary to that, the influence of WI onto wax crystallization is examined via DSC, CPM and rheometry. The goal is to determine the individual interaction heat contributions from both solubilized wax and solid wax crystals. This not only enables the calculation of binding affinities on a molecular level, but it furthermore sheds light onto the working mechanism of PPDs and WIs.

## 2. Experimental Section

### Materials and Sample Preparation

N-hexane (HPLC-grade, ≥97%) and a mixture of xylene isomers (reagent-grade, ≥98.5%) were obtained from VWR, Norway. Toluene (anhydrous, 99.8%) was purchased from Sigma-Aldrich, Norway. All solvent were used without further purification. A wax inhibitor (PPD $1_P$) based on polycarboxylate was provided by BASF, Germany, and further purified. Marcocrystalline wax was obtained as 5405 Sasolwax from Sasol Wax, Germany. Composition and characteristics of the wax are available in literature [42].

The wax inhibitor PPD 1 of the previous study [41] contained a percentage of petroleum distillate, so the polymer was further purified and correspondingly labeled as PPD $1_P$. The purification process consisted of repeatedly adding and removing toluene in a rotary evaporator at up to 90 °C and 200 mbar. The remaining substance was then filled into a petri dish and placed in an oven at 60 °C for 24 h under atmospheric conditions. The final yield was approximately 80 wt% of the original PPD weight, which is equal to the amount of active content as specified by the producer.

Asphaltenes were prepared via hexane precipitation from a light crude oil that originated from the Norwegian continental shelf. Prior to sampling, the crude oil was heated to 60 °C for at least 60 min and shaken thoroughly to ensure homogeneity of the sample. 8g of crude oil were mixed with 320 ml n-hexane and stirred for at least 24 h. The resulting mixture was filtered using a 0.45 µm HVLP-type Millipore filter membrane and afterwards rinsed with n-hexane until the filtrate was clear. The filter paper with asphaltenes was dried under nitrogen atmosphere for at least 24 h. The final yield of asphaltenes accounted for 2.2 wt% of the original crude oil.

All solutions were prepared by first weighing the solids and further adding the required amount of solvent. Solutions containing wax were placed in an oven at 60 °C for at least 30 min prior to usage, so ensure all wax was dissolved in the solvent.

### Isothermal Titration Calorimetry (ITC)

ITC experiments were conducted on a NANO ITC Standard Volume from TA Instruments. Calibration was performed by measuring the heat of reaction for defined titrations of Tris-base with HCl. The reference cell was filled with pure xylenes. Titration took place in 25 injections of 10 µl each, where both sample and reference cell have a volume of 1 ml. All experiments were carried out at a stirring rate of 250 rpm. The calorimeter was equilibrated to a baseline drift of less than 0.1 µW before each experiment, which took in between 30 and 120 min. Wax dispersions for ITC were prepared by quenching the hot waxy solvent at 20 °C for 60 min. Before injection into the sample chamber, the wax dispersion was thoroughly shaken for 5 s and then sonicated for 20 s. Solutions with only asphaltenes were prepared at least one day before usage, to ensure that the system had stabilized. Asphaltene solutions were sonicated for 30 min right after preparation and for 10 min right before usage in ITC. Solutions of PPD $1_P$ for ITC were prepared by heating to 80 °C for 10 min, mixing in a shaker for 10 min, and sonicating for 10 min. Pure solvents used in ITC were degassed via sonication for 30 min. Heat integration was carried out automatically in the NanoAnalyze software. For each experiment, the heat values of a blank injection with pure solvent were subtracted, to correct for the heat generated by friction in the syringe. All experiments were conducted two to four times, depending on reproducibility of the measurement. The interaction heat was calculated according to Wei et al. [37] as net enthalpy, where the heat of titrating inhibitor into toluene ($\Delta H_{Int}$) and the heat of titrating toluene into wax dispersion ($\Delta H_{Wax}$) is subtracted from the heat measured when titrating inhibitor into the wax dispersion ($\Delta H_{Total}$), as shown in equation (1). The resulting interaction heat error was calculated according to the propagation of error.

$$\Delta H_{Int} = \Delta H_{Total} - (\Delta H_{Inhibitor} + \Delta H_{Wax}) \quad (1)$$

### Differential Scanning Calorimetry (DSC)

DSC experiments were conducted on a Q2000 from TA Instruments with the samples contained in Tzero Hermetic Pans. The instrument was calibrated via the melting of indium. During each run, the sample was heated to 100 °C and kept isothermal for 2 min to ensure complete dissolution of all solids, before the measurement commenced and a cooling rate was applied. The sealed pans were weighed before and after the experiment to ensure that no sample loss had occurred. The WAT was determined as the earliest detectable thermal effect, similar to the previously published procedure [41]. In this procedure, the heat flow vs temperature graph is approximated by a straight line on a temperature interval of 15 °C and moved to lower temperatures incrementally while checking for WAT. The WAT is defined as the highest temperature at the lower end of the interval, for which three consecutive points are outside the 99.9 % confidence interval. This confidence interval is equivalent to 3.291 times the standard deviation of the approximated straight line, assuming normal distribution of the thermal noise.

### Cross Polarized Microscopy (CPM)

Microscope images were taken with a Nikon Eclipse microscope fitted with a CoolSnap-Pro camera by Media Cybernetics and cross-polarization filters. The sample temperature was controlled with a Linkham PE 94 and LTS-120E Peltier system. The samples were filled into glass capillaries with a cross section of 0.3 x 0.03 $mm^2$, sealed with glue and fixed in place on a microscope slide. For each measurement, the sample underwent the following temperature program: Heating to 60 °C, isothermal at 60 °C for 10 min, cooling to 30 °C at a rate of 20 °C/min, and then cooling to 4 °C at a rate of 1 °C/min. Upon reaching 4 °C, the temperature was kept constant and CPM images were shot within the time frame of 20 to 40 min after reaching 4 °C. During each temperature cycle, the sample cell was continuously flushed with nitrogen, to avoid condensation inside the sample cell.

### Rheometry and Gel Breakage Strength

Gel breakage was measured in an Anton Paar Physica 301, which was equipped with a 4 cm diameter 2° cone and plate geometry that had been sandblasted to provide additional roughness to prevent slippage. The rheometer used a gap size of 0.170 mm in each case. The procedure for measuring gel breakage represents an adapted version of the methods used and develop previously in our group [43, 44]. Before each experiment, the sample was placed on a heating plate kept at 120 °C for at least 5 min, and then injected into the measuring geometry of the rheometer, which was preheated to 35 °C. A cooling rate of 0.5 °C/min was applied down to 4 °C, and the sample was kept isothermal at 4 °C for 10 min, before shearing at a shear rate of 0.1 $s^{-1}$. The gel breakage strength is defined as the maximum shear force recorded.

## 3. Results and Discussion

### Previous Work: Correlation between Interaction Heat and Wax Inhibitor Performance

Previous investigations were subject to testing five polymeric PPDs, and asphaltenes to be able to compare three essentially different measures [41]: (i) heat of interaction between wax and WI, (ii) influence of WI on delayed wax crystallization, and (iii) effect of WI on the structure and strength of the resulting wax crystal network. Experimental procedures have been improved between the previous work and this study, which is why this section is different from the rest of this study in the following key elements: (a) Toluene was previously used as bulk solvent and has been replaced by a xylene isomer mixture, as this solvent has a lower vapor pressure and the influence of evaporation is therefore smaller. (b) Cooling rate for gel breakage and sample concentrations for all methods were adapted slightly to improve sensitivity of the measurements and comparability between different methods. (c) PPDs of the previous study contained petroleum distillate and have been purified for this study. The results of ITC experiments are shown in Fig. 2.

In each case, the absolute interaction heat first increases to a local maximum between injection two to five und subsequently decreases to asymptotically approach zero net heat towards the final injections. The highest interaction heat was measured for PPD 4, which is EVA with 25 % VA. Asphaltenes showed the lowest interaction heat. PPD 1, 2, and 5 represent the average and are similar within the standard deviation. To assess the performance of different WIs, measurements of WAT, gel breakage strength, and wax crystal morphology were made. The procedures for these methods are similar to this study, with the exception of previously mentioned changes, in particular a cooling rate of 1 °C/min used for gel breakage. A comparison of WI characteristics and final results is shown in Table 1.

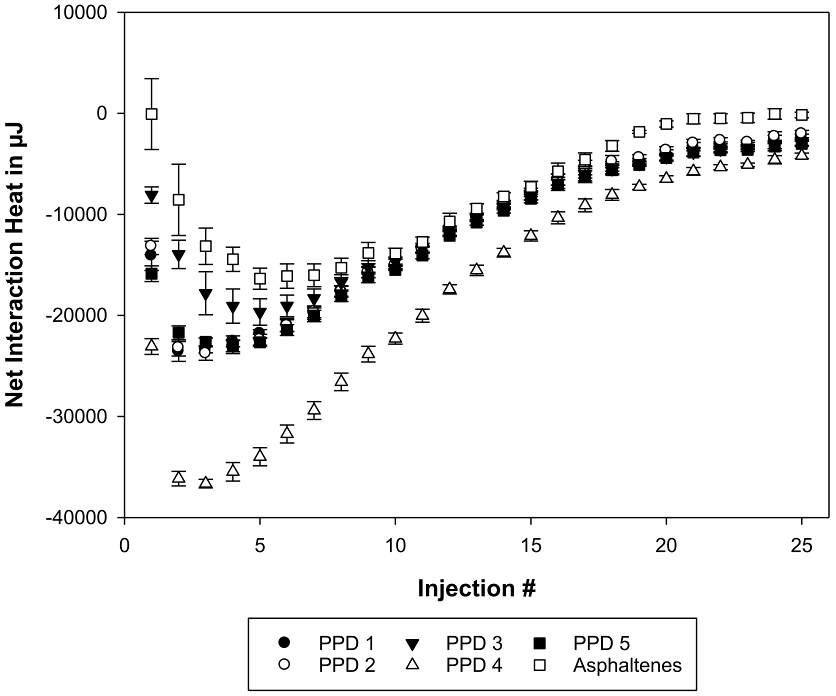

Fig. 2. Resulting interaction heat for 1 wt % active PPD or asphaltenes with 10 wt % macrocrystalline wax dispersion in toluene at 20 °C. Each injection accounts for 10 µL of titrant being added to 1 mL of wax dispersion. Error bars represent the standard deviation from the average of each measurement. Reprinted (adapted) with permission from Ruwoldt, J., et al., *Wax-Inhibitor Interactions Studied by Isothermal Titration Calorimetry and Effect of Wax Inhibitor on Wax Crystallization*. Energy & Fuels, 2017. Copyright 2017 American Chemical Society.

Table 1: Comparison of inhibitor properties and final results from ITC, DSC and rheometry. Reprinted (adapted) with permission from Ruwoldt, J., et al., *Wax-Inhibitor Interactions Studied by Isothermal Titration Calorimetry and Effect of Wax Inhibitor on Wax Crystallization*. Energy & Fuels, 2017. Copyright 2017 American Chemical Society.

| | **No Inhibitor** | **PPD 1** | **PPD 2** | **PPD 3** | **PPD 4** | **PPD 5** | **Asphaltenes** |
|---|---|---|---|---|---|---|---|
| Chemistry based on | | Poly-carboxylate | Poly-carboxylate, MA | PA, EVA | EVA, 25 % VA | Modified EVA | Hexane precipitated |
| Active content [%] | | 80 | 70 | 50 | 100 | 100 | 100 |
| Maximum interaction heat, ITC [mJ] | | -23.6 | -23.8 | -19.7 | -36.6 | -23.0 | -16.4 |
| WAT, DSC, 5 °C/min [°C] | 20.1 | 14.6 | 17.6 | 17.7 | 18.7 | 17.8 | 18.8 |
| WAT, Viscometry, 5 °C/min [°C] | 22.6 | 19.1 | 20.7 | 20.9 | 20.8 | 21.3 | 22.3 |
| Gel-breakage strength, Rheometry [Pa] | 401 | No Gel | No Gel | 120 | 295 | 362 | 71 |
| Crystal morphology, CPM | Needle and plate shape | Small, compact | Small, compact | Compact, round | Small and compact or big flakes | Needle and plate shape | Distorted, dendrite like |

The best performance can be attributed to PPD 1, which accounted for the greatest decrease in WAT as compared to the case without inhibitor, and which together with PPD 2 showed the greatest effect on crystal morphology and gel strength. Both PPD 1 and PPD 2 showed maximum interaction heat values, which are on the average of all 6 samples tested. Despite the fact that PPD 4 accounted for the highest interaction heat, this sample showed lower influence on WAT and gel breakage strength as compared to PPD 1 to 3. The reason for this was depicted by CPM imaging, as PPD 4 accounted for wax crystals that are either round and small crystals or assemblies of multiple plates joined together, which were larger in total size than the average plate shape crystals formed without inhibitor [41]. Larger geometries can lead to a higher degree of three dimensional interlocking, and hence the inhibitor performance of PPD 4 was lower.

In conclusion, no correlation was found between the interaction heat measured via ITC and performance characteristics, such as a high decrease in WAT or gel breakage strength. Affinity between paraffin wax and WI appears to be a necessity for co-precipitation of WI in the formed wax crystals, but the ability of the WI to change wax crystal morphology to smaller crystals with less propensity to interlock is a crucial property as well [41].

## Effect of Wax Inhibitors on Wax Crystallization

To characterize the effect of WIs used in this study onto wax crystallization, experiments using DSC, CPM and rheometry were conducted. PPD 1P and asphaltenes were selected as representative WI chemistries, because PPD 1 showed the best performance as depicted in Table *1*, and asphaltenes are a natural part of crude oil. DSC measurements are depicted in Fig. 3 together with average WAT values and standard deviation obtained from three measurements.

PPD 1P accounted for a decrease of approximately 1.6 °C as compared to the inhibitor free case and also changed the shape of the heat profile to sharper edges at the onset of wax crystallization, as well as a second local maximum at approximately 0 °C. The addition of asphaltenes accounted for no qualitative change of the DSC heat profile. Moreover, asphaltenes led to no detectable decrease in WAT, which can be explained by the fact that the asphaltenes to wax ratio is lower than in the previous study. Asphaltenes have been reported to serve as wax crystallization sites and therefore increase the cloud point [45, 46], which could be the reason for the on average higher WAT as compared to the inhibitor free case. Compared with experiments listed in Table *1*, the wax content was doubled to 10 wt% at a constant concentration of 1000 ppm WI to provide better comparability to gel breakage strength measurements. Also considering a change in bulk solvent, the obtained WAT values consequently are different from Table *1*, but show a similar trend. The results of gel breakage measurements are depicted in Fig. 4.

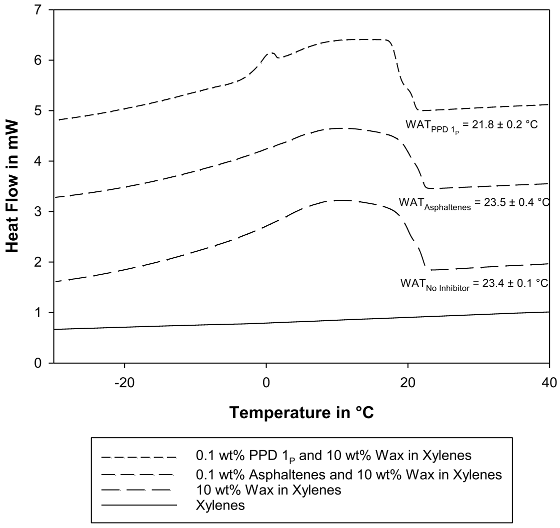

Fig. 3. DSC heat profiles and WAT average of three measurements with standard deviation at a cooling rate of 5 °C/min. Graphs were shifted on the y-axis for improved overview.

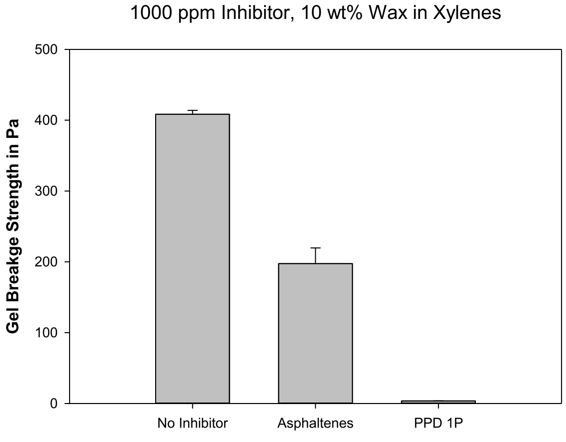

Fig. 4. Rheometric results for gel breakage strength at 4 °C. Each value is the average of two to four measurements with according standard deviation.

The addition of both WIs led to a decrease in gel breakage strength as compared to the case without inhibitor. In presence of asphaltenes, the gel breakage strength was about 50 % lower. Through the addition of PPD 1P, no gel formation could be observed at a temperature of 4 °C. Compared to Table 1, the gel breakage strength without inhibitor is similar in value for both solvents. PPD $1_P$ has the same effect as PPD 1. The additions of asphaltenes lead to a smaller decrease in gel breakage strength, which could be a result of the fact that the asphaltene to wax ratio is half. CPM images of the crystal structures formed at this temperature are depicted in Fig. 5 and Fig. 6.

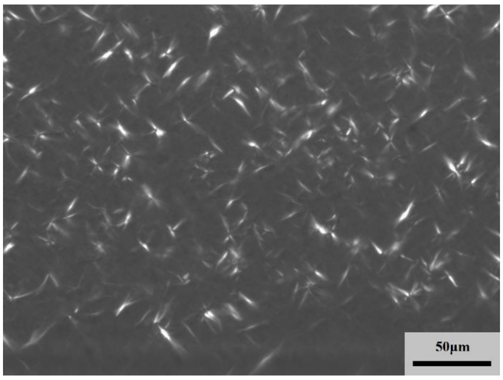

Fig. 5. CPM image of 10 wt% wax in xylenes at 4 °C.

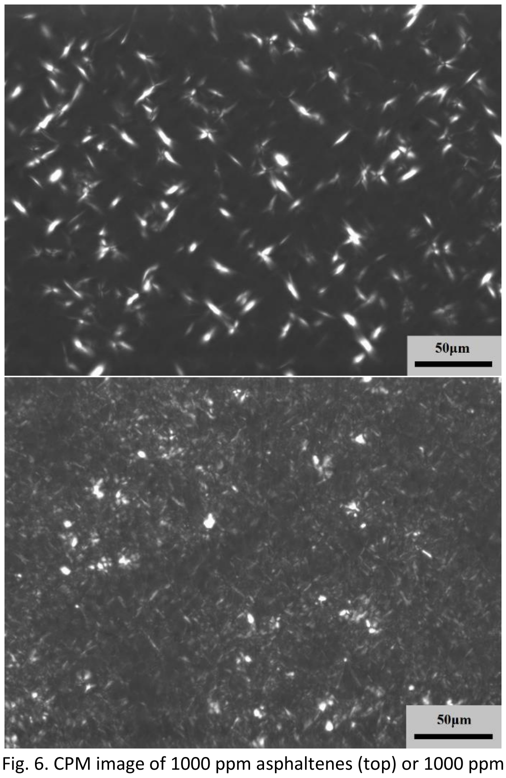

Fig. 6. CPM image of 1000 ppm asphaltenes (top) or 1000 ppm PPD $1_P$ (bottom) with 10 wt% wax in xylenes at 4 °C.

The macrocrystalline wax crystallizes in xylenes as predominantly plate shaped crystals, and some crystals appear to have stearic centers where several planes are linked together. Asphaltenes caused wax to crystallize in more round and dendrite like shapes, and PPD $1_P$ promoted the growth of predominantly round and compact crystal shapes that are considerably smaller. The results of CPM imaging is in agreement with both Table *1* and rheometric measurements, where asphaltenes showed some effect and PPD $1_P$ showed a great effect.

All in all, the documented effect of the two WIs is in agreement with previous results. Moreover, the purification of PPD 1 appears to not have changed the performance of this polymer for the macrocrystalline wax used.

### Inhibitor-Wax Interactions at Varying Temperatures

Two distinct temperatures were selected for ITC experiments. At 35 °C, the wax is fully solubilized in xylenes, as this temperature is above WAT. At 20 °C a certain amount of wax has precipitated, but the wax dispersion still remains fully fluid, which is a necessity to ensure complete mixing in ITC. As compared to the previous study, the asphaltene and PPD concentrations have been doubled to increase sensitivity of the measurements. The results for the interactions between PPD $1_P$ and macrocrystalline wax are presented in Fig. 7, to which the according heat profiles are listed as Fig. 10 and Fig. 11 in the appendix.

In the raw heat profiles of Fig. 10 and Fig. 11, all injection types show a local minimum right after each injection, after which the heat signal returns to the baseline. Only in case of injections of pure xylenes into 10 wt% wax in xylenes at 20 °C, the signal is not fully equilibrated at the end of each injection interval. In this case, an injection interval of 60 min was chosen, which represents the largest possible interval to limit experiment time and thereby the influence of solvent evaporation. Injections of PPD $1_P$ in xylenes into wax in xylenes at 20 °C were conducted in intervals of 60 min as well, and all other injection types were done using injection intervals of 5 to 10 min. The experiment time was made dimensionless by dividing by the total experiment duration in order to provide better comparability of the graphs. The integrated heat values in Fig. 7 show that at both temperatures, the largest heat contribution is due to the dilution or re-dissolution of macrocrystalline wax. This is to be expected as this component is present at the highest percentage. Injections of PPD $1_P$ into pure solvent have the lowest heat contribution for both temperatures. At 35 °C, the interaction heat is decreasing approximately linearly with injection number. At 20 °C, the interaction heat also follows a decreasing trend that asymptotically approaches zero net heat towards the final injections. Experiments where PPD $1_P$ is injected into wax showed on average 1.7 times higher heat values at 20 °C than at 35 °C. The final interaction heat at 20 °C, however, is on average 80 times greater than the interaction heat at 35 °C. The aggregate state of the wax therefore has crucial influence on the response of the system. Analogous measurements were made with asphaltenes and are displayed in Fig. 8. The according heat profiles are shown in the appendix as Fig. 12 and Fig. 13.

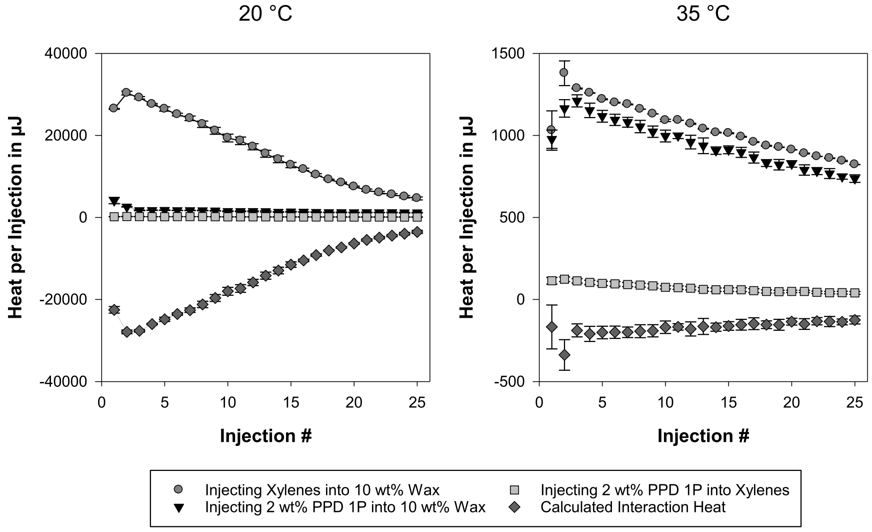

Fig. 7. ITC results: Heat per injection for determining the interaction heat of 2 wt% PPD $1_P$ in xylenes with 10 wt% wax in xylenes at temperatures 35 °C and 20 °C. Experiments consist of 25 injections of 10 µl substance into 1 ml sample cell with xylene isomer mixture as bulk solvent. Each measurement represents the average of two to four measurements with according standard deviation.

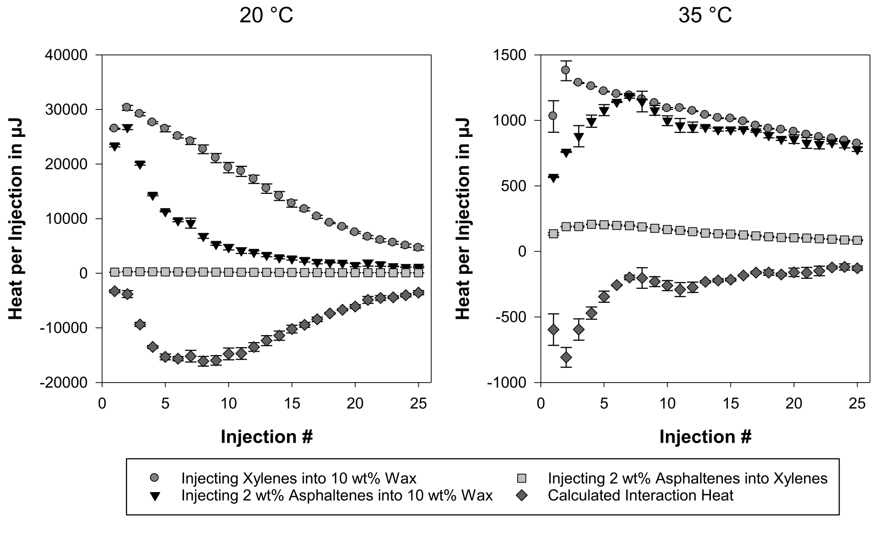

Fig. 8. ITC results: Heat per injection for determining the interaction heat of 2 wt% asphaltenes in xylenes with 10 wt% wax in xylenes at temperatures 35 °C and 20 °C. Experiments consist of 25 injections of 10 µl substance into 1 ml sample cell with xylenes isomer mixture as bulk solvent. Each measurement represents the average of two to four measurements with according standard deviation.

ITC raw heat profiles in Fig. 12 and Fig. 13 show similar characteristics for asphaltenes as compared to PPD $1_P$, where each injection is marked by a local minimum right after injection, and a subsequent return to the baseline. Injections with asphaltenes were mostly performed at injection intervals of 10 min, except for injections made into wax dispersions, which used injection intervals of 60 min. Fig. 8 shows that injecting asphaltenes into pure solvent has led to the smallest heat contribution. Injecting asphaltenes into wax at 20 °C showed heat values that are closer to the dilution or re-dissolution heat of the wax, which in turn resulted in lower interaction heat values than for PPD $1_P$. Injections of asphaltenes into wax at 35 °C displayed considerably lower heat per injection than the dilution of wax during the first five injections, which contributed to interaction heat values higher than for PPD $1_P$. The interaction heat at 35 °C is the largest for the second injection, and at 20 °C, the largest interaction heat stretches over a plateau that comprises approximately injections five to nine. These maxima are in both cases followed by an approximately asymptotic decrease in interaction heat.

The interaction heat for both PPD $1_P$, and Asphaltenes with dissolved or crystalline waxes is exothermic. Moreover, both substances display considerably larger interaction heat when there is solid wax present, which suggests that the largest contribution of the interaction heat is due to reactions of polymer or asphaltenes with the solid wax crystals. This further confirms the observations of the previous study, where PPD 4 was injected into a 1 wt% wax solution in a screening experiment at 20 °C [41]. The wax solution contained no solid wax and the resulting interaction heat was found to be lower by more than a factor of 1000, even though the wax content had been reduced by only a factor of 10. An explanation could be, that the affinity of wax inhibiting substances to solid paraffin wax is much greater than to the dissolved wax molecules, which would invoke co-precipitation even when the thermodynamic solubility limit of the WI has not been reached. This phase change could then lead to the release of a much greater interaction heat.

For experiments taking place at 35 °C, the interaction heat can be plotted versus the molar ratio of injected WI by wax in the sample cell. The molecular weight of asphaltenes was approximated by 750 g/mol, as this was found to be the average molecular weight measured by fluorescence depolarization [47]. The average molecular weight of the wax is calculated as molar average according to the composition of Sasolwax 5405 provided by Paso et al. [42]. A rough approximation of 150 g/mol as monomer weight is used for PPD $1_P$ and a uniform liquid density of 0.86 kg/l is assumed. The results are shown in Fig. 9.

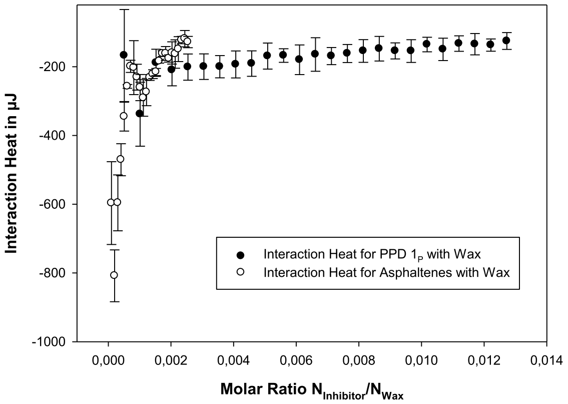

Fig. 9. Interaction heat measured at 35 °C and related to molar ratio in the titration cell

The decreasing trend in asphaltene-wax interaction heat shows that only a small fraction of asphaltenes are interacting with the wax. Moreover, the approximately linear decrease in interaction heat for PPD $1_P$ is a result of an excess of wax molecules in the experiment. Lower wax percentages or higher amounts of inhibitor would be needed to provide a better resolution. As a conclusion, the method presented is well capable of measuring binding affinities of inhibitor-wax systems in organic solvents. Careful experiment design is necessary, however, to be able to cover a range of relevant substances and concentrations.

## Experimental Effort

The experimental expenditure is one aspect to consider when choosing the appropriate type of analysis for a given problem. All expenditures can generally be converted to a monetary value, i.e. the hours worked by lab personnel, cost of instrument acquisition and maintenance or running costs such as solvent consumption and electricity. The time needed for experiment conduct, as well as amount of sample required will be discussed at this point, since ITC has only been applied on a research basis to study inhibitor-wax interactions.

In total, it took 10 to 12 working days to measure the interaction heat for both PPD $1_P$, and asphaltenes with wax at one temperature setting. At injection intervals of 5 to 10 min, two experiments can be conducted in one day, for injection intervals longer than 20 min, one experiment can be conducted at the most. The cleaning and preparation of one ITC experiment usually involves about 2 to 3 h of lab work, even though a number of tasks can be conducted in parallel. ITC experiments are very prone to contamination and established cleaning protocols are therefore extensive. In comparison to that, DSC, CPM and rheological measurements usually are finished within a few hours or less, which includes sample preparation, data processing, and experiment repetitions. The amount of inhibitor sample required is less for these measurements, since inhibitor is usually dosed on ppm-scale. In ITC, concentrations of 1 wt% and more are necessary. As a result, the experimental expenditures for measuring inhibitor-wax interactions in ITC are far greater than for other methods.

## 4. Summary and Conclusions

In this work, ITC was used to measure the interaction heat between a polymeric WI, and asphaltenes with macrocrystalline wax. As comparison, the influence of both substances on wax crystallization was investigated using DSC, CPM, and rheometry. Results were also discussed in respect to the experimental effort involved.

Both PPD $1_{P}$ and asphaltenes reduced the gel breakage strength and showed significant influence on the wax crystal morphology. DSC measurements showed a reduction in WAT through the addition of PPD $1_{P}$, but not for asphaltenes. In ITC, both WIs accounted for detectable interaction heat with solid wax as well as dissolved wax. Moreover, ITC experiments revealed interaction heat values, which are considerably higher for wax that is both solid and dissolved than for dissolved wax only.

In a previous study, no correspondence between good WI performance and high interaction heat values had been found [41], which is not in conflict with the findings of this work. The results of this study indicate however, that the major heat contribution is due to interactions between inhibitor and solid wax crystals. So even though ITC does not appear as a suitable tool for assessing the effectiveness of WIs, it can still be concluded that ITC can provide new information about binding affinity and working mechanism of WIs.

## 5. Acknowledgements

This work was carried out as a part of SUBPRO, a Research-based Innovation Centre within Subsea Production and Processing. The authors gratefully acknowledge the financial support from SUBPRO, which is financed by the Research Council of Norway, major industry partners and NTNU. The authors would further like to thank BASF for providing wax inhibitor samples and Sasol for providing the wax sample.

## 6. Acronyms

CPM = cross-polarized microscopy
DSC = differential scanning calorimetry
EVA = ethylene-vinyl acetate copolymer
FT-IR = Fourier-transform infrared (spectroscopy)
HPLC = high-performance liquid chromatography
ITC = isothermal titration calorimetry
MA = maleic anhydrides
NIR = near-infrared (spectroscopy)
NMR = nuclear magnetic resonance (spectroscopy)
PA = polyacrylate
PEB = poly(ethylene butene)
PPD = pour-point depressant
VA = vinyl acetate
WAT = wax appearance temperature
WI = wax inhibitor

## 7. References

1. Yang, F., et al., *Polymeric Wax Inhibitors and Pour Point Depressants for Waxy Crude Oils: A Critical Review.* Journal of Dispersion Science and Technology, 2015. **36**(2): p. 213-225.
2. Pedersen, K.S. and H.P. Rønningsen, *Influence of Wax Inhibitors on Wax Appearance Temperature, Pour Point, and Viscosity of Waxy Crude Oils.* Energy & Fuels, 2003. **17**(2): p. 321-328.
3. Kelland, M.A., *Production chemicals for the oil and gas industry*. 2014: CRC press.
4. Paso, K.G., *Paraffin gelation kinetics*. 2005: University of Michigan.
5. Huang, Z., S. Zheng, and H.S. Fogler, *Wax Deposition: Experimental Characterizations, Theoretical Modeling, and Field Practices*. 2015: CRC Press.
6. Venkatesan, R., et al., *The strength of paraffin gels formed under static and flow conditions.* Chemical Engineering Science, 2005. **60**(13): p. 3587-3598.
7. Guo, Y., et al., *An excellent non-wax-stick coating prepared by chemical conversion treatment.* Materials Letters, 2012. **72**: p. 125-127.
8. Bai, Y. and Q. Bai, *Subsea engineering handbook*. 2012: Gulf Professional Publishing.
9. Al-Yaari, M., *Paraffin Wax Deposition: Mitigation and Removal Techniques*. 2011, Society of Petroleum Engineers.
10. Aiyejina, A., et al., *Wax formation in oil pipelines: A critical review.* International Journal of Multiphase Flow, 2011. **37**(7): p. 671-694.
11. Jemmett, M.R., *Rheology and deposition of heterogeneous organic mixtures: An expansion of "cold flow" research*. 2012, The University of Utah.
12. Singh, P. and H.S. Fogler, *Fused Chemical Reactions: The Use of Dispersion To Delay Reaction Time in Tubular*

*Reactors.* Industrial & Engineering Chemistry Research, 1998. **37**(6): p. 2203-2207.

13. Machado, A.L.d.C. and E.F. Lucas, *Poly(Ethylene-co-Vinyl Acetate) (EVA) Copolymers as Modifiers of Oil Wax Crystallization.* Petroleum Science and Technology, 1999. **17**(9-10): p. 1029-1041.
14. Clarke, E.W., *Crystal Types of Pure Hydrocarbons in the Paraffin Wax Range.* Industrial & Engineering Chemistry, 1951. **43**(11): p. 2526-2535.
15. Oschmann, H.-J., *Das Kristallisationsverhalten von Paraffinen in Abhängigkeit von ihrer Zusammensetzung sowie seine Beeinflussung durch Paraffininhibitoren*, in *Fakultät für Bergbau, Hüttenwesen und Maschinenwesen*. 1998, Technisch Universität Clausthal: Papierflieger.
16. Wei, B., *Recent advances on mitigating wax problem using polymeric wax crystal modifier.* Journal of Petroleum Exploration and Production Technology, 2015. **5**(4): p. 391-401.
17. Roehner, R.M. and F.V. Hanson, *Determination of Wax Precipitation Temperature and Amount of Precipitated Solid Wax versus Temperature for Crude Oils Using FT-IR Spectroscopy.* Energy & Fuels, 2001. **15**(3): p. 756-763.
18. Paso, K., H. Kallevik, and J. Sjoblom, *Measurement of wax appearance temperature using near-infrared (NIR) scattering.* Energy & Fuels, 2009. **23**(10): p. 4988-4994.
19. Monger-McClure, T.G., J.E. Tackett, and L.S. Merrill, *Comparisons of Cloud Point Measurement and Paraffin Prediction Methods.* 1999.
20. Becker, J.R., *Paraffin-Crystal-Modifier Studies in Field and Laboratory*. 2001, Society of Petroleum Engineers.
21. Roenningsen, H.P., et al., *Wax precipitation from North Sea crude oils: 1. Crystallization and dissolution temperatures, and Newtonian and non-Newtonian flow properties.* Energy & Fuels, 1991. **5**(6): p. 895-908.
22. *Standard Test Method for Pour Point of Petroleum Products*. 2017, ASTM International.
23. *Standard Test Method for Pour Point of Crude Oils*. 2016, ASTM International.
24. *Standard Test Method for Pour Point of Petroleum Products (Automatic Pressure Pulsing Method)*. 2016, ASTM International.
25. Venkatesan, R., P. Singh, and H.S. Fogler, *Delineating the Pour Point and Gelation Temperature of Waxy Crude Oils.* 2004.
26. Zhao, Y., et al., *Controlled Shear Stress and Controlled Shear Rate Nonoscillatory Rheological Methodologies for Gelation Point Determination.* Energy & Fuels, 2013. **27**(4): p. 2025-2032.
27. Paso, K.G., *Comprehensive treatise on shut-in and restart of waxy oil pipelines.* Journal of Dispersion Science and Technology, 2014. **35**(8): p. 1060-1085.
28. Yang, F., et al., *Hydrophilic nanoparticles facilitate wax inhibition.* Energy & Fuels, 2015. **29**(3): p. 1368-1374.
29. Zhao, Y., et al., *Utilizing ionic liquids as additives for oil property modulation.* RSC Advances, 2014. **4**(13): p. 6463-6470.
30. Sarica, C. and E. Panacharoensawad, *Review of Paraffin Deposition Research under Multiphase Flow Conditions.* Energy & Fuels, 2012. **26**(7): p. 3968-3978.
31. Jennings, D.W. and K. Weispfennig, *Effects of Shear and Temperature on Wax Deposition: Coldfinger Investigation with a Gulf of Mexico Crude Oil†.* Energy & Fuels, 2005. **19**(4): p. 1376-1386.
32. Feig, A.L., *Applications of isothermal titration calorimetry in RNA biochemistry and biophysics.* Biopolymers, 2007. **87**(5-6): p. 293-301.
33. Saboury, A.A., *A review on the ligand binding studies by isothermal titration calorimetry.* Journal of the Iranian Chemical Society, 2006. **3**(1): p. 1-21.
34. Merino-Garcia, D. and S.I. Andersen, *Thermodynamic Characterization of Asphaltene−Resin Interaction by Microcalorimetry.* Langmuir, 2004. **20**(11): p. 4559-4565.
35. Merino-Garcia, D. and S.I. Andersen, *Interaction of Asphaltenes with Nonylphenol by Microcalorimetry.* Langmuir, 2004. **20**(4): p. 1473-1480.
36. Wei, D., et al., *Interactions between asphaltenes and alkylbenzene-derived inhibitors investigated by isothermal titration calorimetry.* Journal of Thermal Analysis and Calorimetry, 2015. **120**(3): p. 1835-1846.
37. Wei, D., et al., *Aggregation of tetrameric acid in xylene and its interaction with asphaltenes by isothermal titration calorimetry.* Journal of Thermal Analysis and Calorimetry, 2015. **122**(1): p. 463-471.
38. Wei, D., et al., *An ITC study of interaction and complexation of asphaltene model compounds in apolar solvent II: Interactions with asphaltene inhibitors.* Colloids and Surfaces A: Physicochemical and Engineering Aspects, 2016. **495**: p. 87-99.
39. Simon, S., et al., *An ITC and NMR study of interaction and complexation of asphaltene model compounds in apolar solvent I: Self-association pattern.* Colloids and Surfaces A: Physicochemical and Engineering Aspects, 2016. **494**: p. 108-115.
40. Subramanian, S., et al., *Asphaltene fractionation based on adsorption onto calcium carbonate: Part 2. Self-association and aggregation properties.* Colloids and Surfaces A: Physicochemical and Engineering Aspects, 2017. **514**: p. 79-90.
41. Ruwoldt, J., et al., *Wax-Inhibitor Interactions Studied by Isothermal Titration Calorimetry and Effect of Wax Inhibitor on Wax Crystallization.* Energy & Fuels, 2017.
42. Birdi, K., *Handbook of surface and colloid chemistry*. 2015: CRC Press.
43. Yao, B., et al., *Organically modified nano-clay facilitates pour point depressing activity of polyoctadecylacrylate.* Fuel, 2016. **166**: p. 96-105.
44. Zhao, Y., et al., *Gelation and Breakage Behavior of Model Wax–Oil Systems: Rheological Properties and Model Development.* Industrial & Engineering Chemistry Research, 2012. **51**(23): p. 8123-8133.
45. García, M.d.C. and L. Carbognani, *Asphaltene−Paraffin Structural Interactions. Effect on Crude Oil Stability.* Energy & Fuels, 2001. **15**(5): p. 1021-1027.
46. García, M.d.C., *Crude Oil Wax Crystallization. The Effect of Heavy n-Paraffins and Flocculated Asphaltenes.* Energy & Fuels, 2000. **14**(5): p. 1043-1048.

47. Groenzin, H. and O.C. Mullins, *Molecular Size and Structure of Asphaltenes from Various Sources.* Energy & Fuels, 2000. **14**(3): p. 677-684.

## 8. Appendix

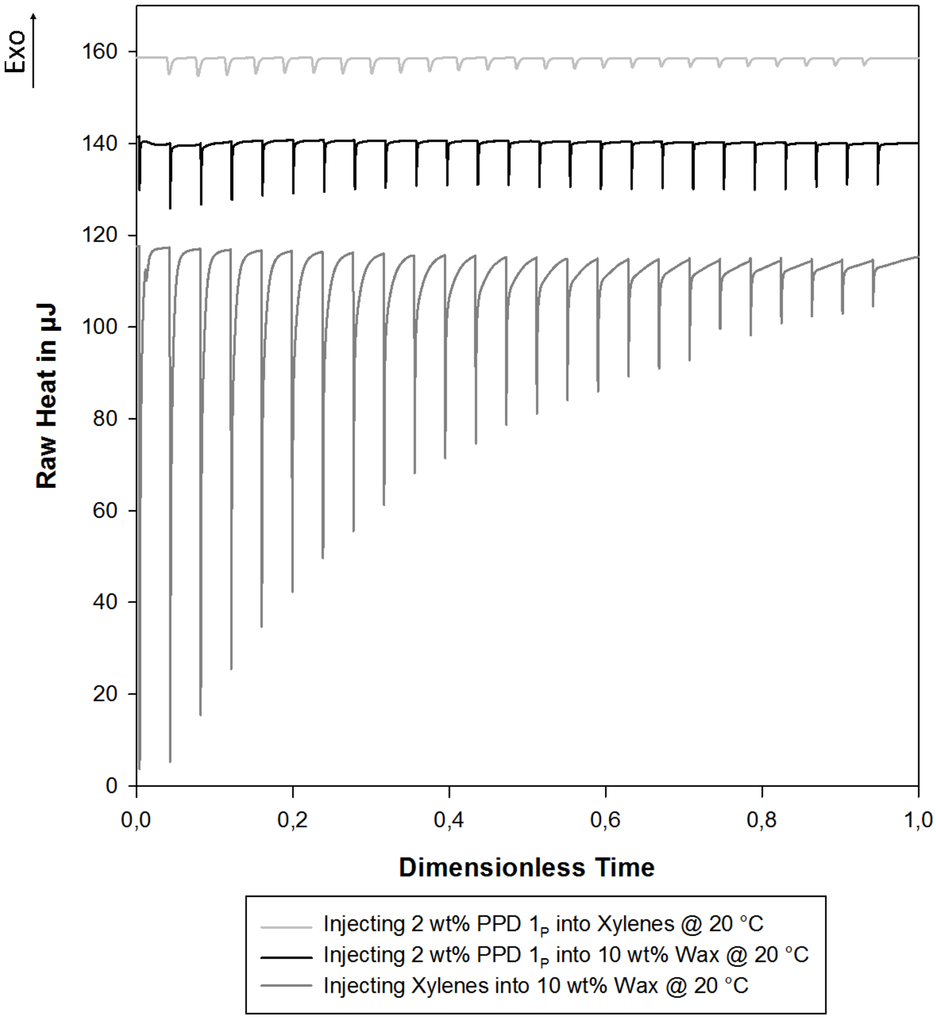

Fig. 10. ITC raw heat profiles for determining the interaction heat of PPD $1_P$ with macrocrystalline wax in xylenes at 20 °C. Experiments consist of 25 injections of 10 µl substance into 1 ml sample cell with xylene isomer mixture as bulk solvent. Raw heat profiles were shifted on the y-axis, and made dimensionless on the x-axis by dividing by the total experiment duration for improved overview.

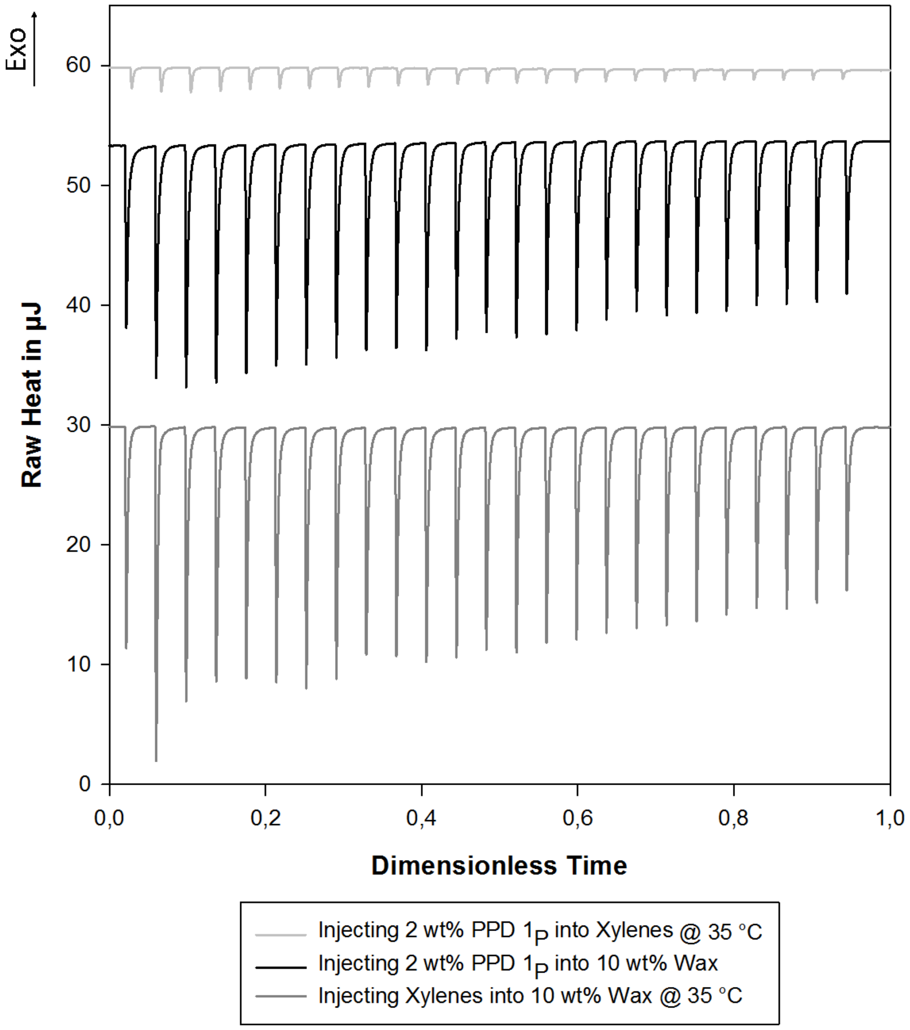

Fig. 11. ITC raw heat profiles for determining the interaction heat of PPD $1_P$ with macrocrystalline wax in xylenes at 35 °C. Experiments consist of 25 injections of 10 µl substance into 1 ml sample cell with xylene isomer mixture as bulk solvent. Raw heat profiles were shifted on the y-axis, and made dimensionless on the x-axis by dividing by the total experiment duration for improved overview.

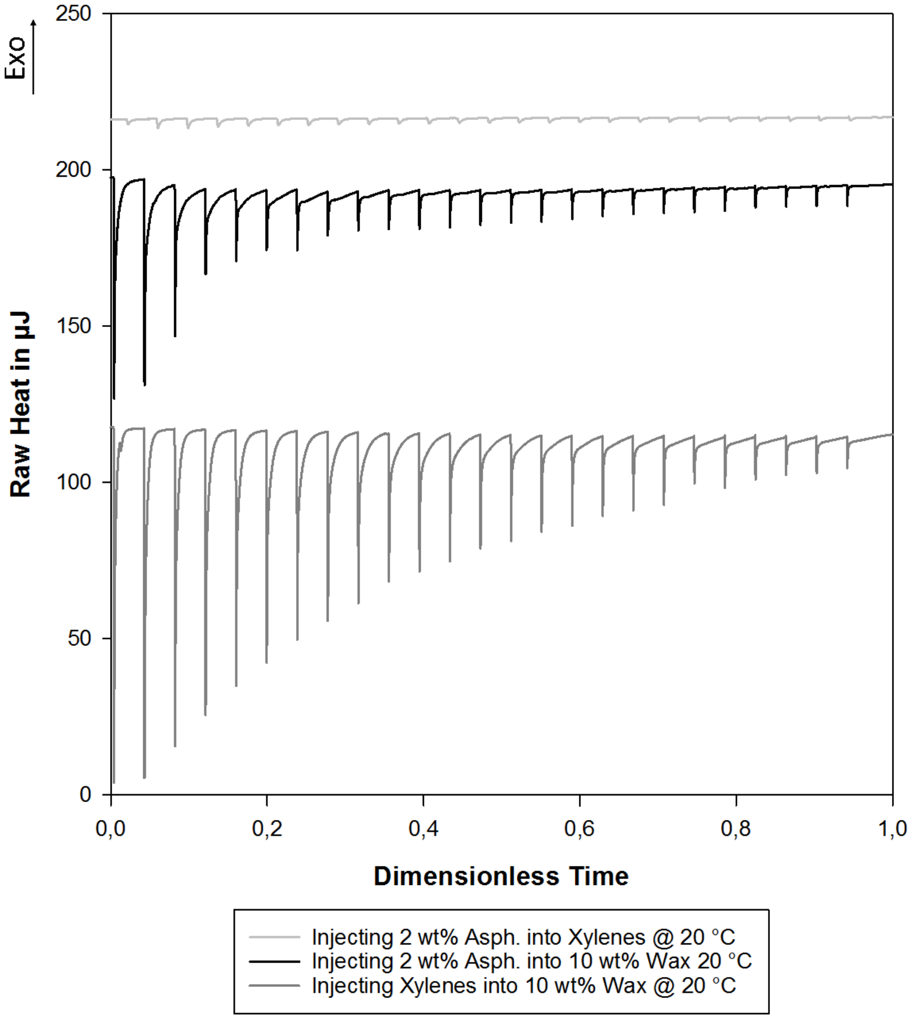

Fig. 12. ITC raw heat profiles for determining the interaction heat of asphaltenes with macrocrystalline wax in xylenes at 20 °C. Experiments consist of 25 injections of 10 µl substance into 1 ml sample cell with xylene isomer mixture as bulk solvent. Raw heat profiles were shifted on the y-axis, and made dimensionless on the x-axis by dividing by the total experiment duration for improved overview.

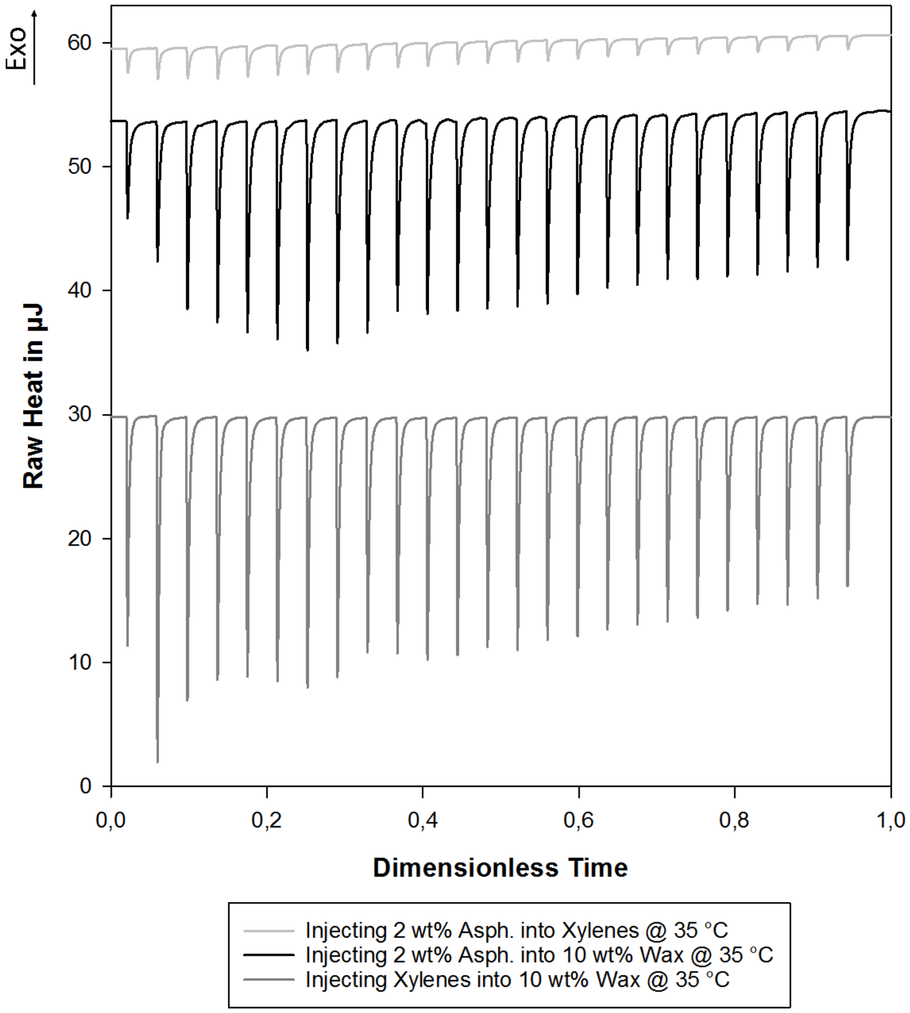

Fig. 13. ITC raw heat profiles for determining the interaction heat of asphaltenes with macrocrystalline wax in xylenes at 35 °C. Experiments consist of 25 injections of 10 µl substance into 1 ml sample cell with xylene isomer mixture as bulk solvent. Raw heat profiles were shifted on the y-axis, and made dimensionless on the x-axis by dividing by the total experiment duration for improved overview.

# Publication III

## Wax-Inhibitor Interactions Studied by Isothermal Titration Calorimetry and Effect of Wax Inhibitor on Wax Crystallization

energy&fuels

Article

pubs.acs.org/EF

# Wax-Inhibitor Interactions Studied by Isothermal Titration Calorimetry and Effect of Wax Inhibitor on Wax Crystallization

Jost Ruwoldt,*,† Sebastien Simon,† Jens Norrman,† Hans-Jörg Oschmann,† and Johan Sjöblom†

†Ugelstad Laboratory, Department of Chemical Engineering, Norwegian University of Science and Technology (NTNU), Sem Sælandsvei 4, N-7491 Trondheim, Norway

*Supporting Information*

**ABSTRACT:** Isothermal titration calorimetry is applied to investigate the interactions of polymeric pour-point depressants (PPDs) or asphaltenes with macrocrystalline wax in a model oil system. This represents a novel approach to measure and compare the heat of interaction for solid wax crystals with different wax inhibitors (WIs). In addition, the PPDs were characterized via size-exclusion chromatography and differential scanning calorimetry (DSC), and the effect of PPDs or asphaltenes onto the wax appearance temperature (WAT) and the formed wax-oil gel was investigated using DSC, cross-polarized microscopy (CPM), and rheometry. The results show that there is detectable interaction heat with wax crystals for all PPDs and asphaltenes. DSC and viscometry show a decrease in observed WAT for all WIs as compared to the additive-free blank case. CPM imaging shows differences in structure, shape, and size of the wax crystals formed in the presence of particular PPDs or asphaltenes, which is also seen as a decrease in gel-breakage strength. Overall, there is no direct correlation between interaction heat and WI performance characteristics, such as a high decrease in WAT or gel strength. Ethylene-vinyl acetate copolymer (EVA) with 25% vinyl actetate accounts for the highest interaction heat measured but shows effective decrease in wax crystals size for only part of the crystals while acting as a flocculate to others, which resulted in a low effect on gel strength. Commercial PPDs based on polycarboxylate have the best performance for the model oil system used but show only overage interaction heat values. The interaction heat of asphaltenes with wax is measurable but lower than for the PPDs tested. The presence of asphaltenes significantly lowered the gel strength and changed the wax crystal morphology to rounder and dendrite-like shapes. These findings suggest that asphaltene compounds are incorporated into the wax crystals, changing the structure and shape of the crystals.

## 1. INTRODUCTION

In the production of waxy crude oil, paraffin wax poses challenges when the oil is cooled below wax appearance temperature (WAT), due to the formation of solid wax crystals. Problems related to wax in crude oils include the formation of a wax deposition layer and gel formation during pipeline shut-in.[1] The worst case is a plugged pipeline, which can cause sever costs for replacement and downtime.[2] Strategies employed to manage and prevent problems associated with waxy crude oils can be grouped into thermal, chemical, and mechanical measures.[3] Thermal measures seek to heat or maintain the oil above WAT, whereas mechanical measures remove the deposit by scraping or cutting the deposit. Pigging is the most prominent form of mechanical wax removal.[4] Research has been done on nonwax-stick coating,[5] fused chemical reactions,[6] microwave heating, as well as acoustic and ultrasonic treatment.[7] Polymeric type wax inhibitors (WIs) and pour-point depressants (PPDs) are among the most commonly applied chemical measures to prevent gelling and high viscosity fluids that would obstruct crude oil production.[8] The terms WI and PPD are used as synonyms, even though there is a slight difference in etymology and meaning.[9] Generally speaking, WIs are substances that are used to prevent or alleviate problems associated with the crystallization of wax, whereas PPDs are substances that reduce the pour-point of a given waxy solution. The pour-point is defined as the temperature at which the liquid loses its ability to flow freely and can be determined using ASTM D97, D5849, or D5949.[10−12] In this study, the term PPD is used for the commercial and noncommercial polymers that were investigated, whereas WI is used in a general context describing substances that can influence wax crystallization in an advantageous manner.

Wax crystallization takes place in three stages, which are nucleation, growth, and agglomeration.[8,13] Nucleation usually lags behind the thermodynamic equilibrium, as a result of supersaturation, which has been verified by DSC measurements.[14] Different geometrical shapes have been reported for wax particles that crystallize from organic solvents, including plate shapes, needle shapes, and malcrystalline masses.[15] The size and shape of wax particles are reported to depend on factors such as molecular weight and melting point of the waxes, solvent−solute ratio, and the composition of the solution.[16,17] Depending on the size and shape of the formed crystals, wax types are also categorized into macrocrystalline and microcrystalline wax. Macrocrystalline wax is mainly composed of low molecular weight *n*-alkanes ($C_{16}$−$C_{40}$), whereas microcrystalline wax holds significant amounts of high molecular weight *iso*-alkanes and *cyclo*-alkanes.[8] Consequently, macrocrystalline wax tends to form relatively large crystals with high aspect ratios, while microcrystalline wax in

**Received:** March 14, 2017
**Revised:** May 24, 2017
**Published:** May 26, 2017

DOI: 10.1021/acs.energyfuels.7b00749
Energy Fuels 2017, 31, 6838−6847

comparison, tends to form smaller crystals. Both wax types generally differ in WAT, gelation temperature, and tensile strength of the formed gel, where macrocrystalline is reported to lead to the formation of strong gels and microcrystalline wax to weak gels.[18]

The precise mechanisms of action of WIs and PPDs are unknown, but it is generally assumed that PPDs are included in the growing wax crystals by cocrystallization to modify their size and shape.[9] The resulting crystal morphology is disordered to an extent, where three-dimensional interlocking of the wax crystals is reduced. Also, the incorporated molecules can prevent particle−particle interactions from forming aggregates or volume spanning networks.[19] The use of PPDs therefore leads to lower gelation temperatures and lower viscosity of the formed wax-oil gel, which in turn maintains favorable flow properties and pumpability. Ethylene copolymers are reported as commonly used PPDs.[8,20,21] These include chemistries such as poly(ethylene-co-vinyl acetate) (EVA), polyethylene, poly(ethylene-propylene), and poly(ethylene-butene). Additionally poly(maleic anhydride amide co-α-olefin) or coated nanoparticles are mentioned as effective WIs and PPDs.[8,22,23]

Asphaltenes are defined as a substance group originating from petroleum, coal, or shale oil, which is soluble in benzene, but insoluble in low molecular weight n-alkanes.[24] Asphaltene molecules are of high molecular weight and contain polycondensed aromatic rings with aliphatic chains attached.[25] Heteroatoms, such as oxygen, nitrogen, sulfur, or trace metals, are found in asphaltenes as well. The effect of asphaltenes on wax precipitation is discussed controversially in literature.[16] It has been reported that the presence of asphaltenes decreases pour point and tensile strength of the formed wax-oil gel.[26−29] These results are contradicted by authors stating no synergistic interactions between asphaltenes and wax.[30] Others reported that asphaltenes act as crystallization sites, increasing the WAT and pour point.[31,32] Also, an influence of asphaltenes on the efficiency of PPDs is suggested,[17,33] and the dispersion degree of asphaltenes is pointed out as an influence on wax crystallization.[34]

Isothermal titration calorimetry (ITC) is a technique predominantly used for the study of proteins, ligand binding to proteins and RNA folding,[35] to determine, for example, the number of binding sites, equilibrium constants, Gibbs free energy of binding processes, enthalpy, or entropy of binding.[36] The method has recently also been applied to petroleum-based systems. Wei et al. studied the self-association of asphaltene model compounds,[37] the aggregation of tetrameric acid, as well as their interactions with asphaltenes.[38−40] Moreover, Subramanian et al. studied the aggregation of different asphaltene fractions obtained via stepwise precipitation with n-hexane or by adsorption and desorption on calcium carbonate.[41] These experiments allowed the study of component characteristics and properties, the quantification of interaction strength between asphaltenes and inhibitor, and the identification of similarities and differences of certain asphaltene fractions.

The goal of this study is to investigate the effect of different WIs and PPDs on wax crystallization and the mechanisms involved, where ITC is used as a novel technique to measure the heat of interaction between paraffin wax and PPDs or asphaltenes, respectively. Size-exclusion chromatography (SEC) and differential scanning calorimetry (DSC) are used to study the polymeric PPDs. DSC, cross-polarized microscopy (CPM), and rheometry are applied to examine the influence of PPDs or asphaltenes on WAT, crystal morphology, and strength of the formed wax-oil gel. The results allow the comparison of three essentially different measures: (i) heat of interaction between solid wax and WI, (ii) influence of WI on delayed wax crystallization, and (iii) effect of WI on changing the structure and strength of the resulting wax crystal network.

## 2. EXPERIMENTAL SECTION

**2.1. Materials.** HPLC-grade toluene (≥99.9%), n-hexane (≥99.7%), and tetrahydrofuran (THF, ≥ 99.7%) were obtained from VWR and used without further purification. PPD 1, 2, and 3 are commercial samples containing petroleum distillate, and PPD 5 is a noncommercial PPD, all provided by BASF. PPD 4 was purchased from Sigma Aldrich. PPD chemistries are listed in Table 1. All PPDs were used without any further treatment. Macrocrystalline wax was obtained as 5405 Sasowax from Sasol Wax Germany.

Table 1. Pour-Point Depressants

| alias | chemistry based on | active content (%) |
|---|---|---|
| PPD 1 | polycarboxylate | 80 |
| PPD 2 | polycarboxylate, maleic acid | 70 |
| PPD 3 | polyacrylate, EVA | 50 |
| PPD 4 | EVA, 25% vinyl acetate | 100 |
| PPD 5 | modified EVA | 100 |

**2.2. Sample Preparation.** PPDs, asphaltenes, and wax solutions were prepared by first weighing the solids and then adding the required amount of solvent. All mass-percentages were prepared to a deviation of ≤0.1 wt %. Prior to use in experiments, complete dissolution of all solids was ensured by heating to at least 20 °C above WAT for at least 30 min. Overall, PPD dosages were designed in excess to ensure a response of the system.

Asphaltenes were precipitated from a crude oil that originated from the Norwegian continental shelf. Prior to preparation, the crude oil was heated to 60 °C for at least 1 h and shaken thoroughly to ensure homogeneity of the sample. 160 mL n-Hexane was added to 4 g of crude oil and stirred for a duration of 24 h. The resulting mixture was filtered through a 0.45 μm HVLP-type Millipore filter membrane and subsequently rinsed with hexane until the filtrate was entirely clear. The filter cake was dried for at least 24 h under nitrogen atmosphere. The final yield of asphaltenes accounted for approximately 2.1 wt % of the original crude oil.

**2.3. Size-Exclusion Chromatography (SEC).** The molecular weight distribution was determined via HPLC with a Shodex KF-803 packed bed column and a Shimadzu SPD-20A UV-detector measuring at a wavelength of 220 and 254 nm. THF was used as bulk solvent at a flow rate of 1 mL/min, and calibration was performed using four and six Shodex SM-105 polystyrene (PS) standards, ranging from 1.22 to 124 kDa, which allowed calculating the relationship between retention time and molecular weight. Injections of 90 μL were done with a sample concentration of 2 g/L and a calibration standard concentration of 1 g/L.

**2.4. Differential Scanning Calorimetry (DSC).** DSC experiments were conducted on a Q2000 from TA Instruments. The instrument was calibrated by measuring the melting of indium and deionized water. During experiments, the temperature program consisted of heating the sample to 90 °C and keeping this temperature for 2 min to ensure complete dissolution of the solids before cooling at a constant temperature gradient. The standard samples were weighed before and after each experiment to check that no sample loss had occurred. Sample concentrations of 5 wt % macrocrystalline wax and 1000 ppm PPD or asphaltenes in toluene were used.

To determine the WAT, an algorithm was developed in analogy to Kok et al., who defined the deviation of a thermal effect under consideration of the thermal noise.[42] In this algorithm, the WAT is defined as the highest temperature, at which three consecutive data points are outside the 99.9% confidence interval. In doing so, the assumptions of a linear temperature-heat relationship above WAT and normal distribution of the thermal noise were made. The confidence interval is calculated as 3.291 times the standard deviation of the heat signal, where the temperature-heat curve is approximated by least-squares approximation. The temperature interval is set to 15 °C and moved from higher-to-lower temperatures for each data point incrementally, while checking for WAT at the lowest temperature of the interval. A schematic of the algorithm is shown in Figure 1.

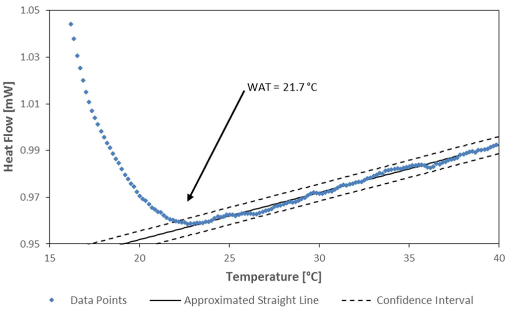

**Figure 1.** Schematic of WAT algorithm for DSC of 5 wt % macrocrystalline wax in toluene at a cooling rate of 2 °C/min.

**2.5. Rheological Experiments.** Rheological experiments were performed on an Anton Paar Physica 301 equipped with a 4 cm in diameter 2° cone and plate geometry, which had been sandblasted to provide additional roughness and to prevent slippage. A gap size of 0.170 mm was used in each case. In the method development, previously applied experiment procedures were adapted to the model oil system used in this study.[43,44] For both experiment types, fast temperature programs were used in order to minimize evaporation of the toluene and ensure reproducibility. In comparison to DSC and CPM, the concentrations of wax, PPD, and asphaltenes were doubled, to improve the instrument response.

*2.5.1. Gel-Breakage Strength.* The sample was loaded into the rheometer, which was preheated to 30 °C. Cooling took place at a rate of 20 °C/min to 20 °C and subsequently at 1 °C/min to 4 °C. The temperature was held at 4 °C for 2 min before shearing occurred at a rate of 0.1 $s^{-1}$. The gel-breakage strength was defined as the maximum shear stress recorded. Experiments with a ratio of standard deviation to mean value of less than 5% were conducted twice, all other experiments were conducted at least three times.

*2.5.2. Viscometry.* The sample was loaded into the rheometer, which was preheated to 35 °C. A cooling rate of 5 °C/min was applied, while constant shearing at 0.1 $s^{-1}$ occurred. The WAT was determined from the temperature-viscosity curve similar as for DSC but with a temperature interval of 5 °C. Each experiment was conducted at least three times.

**2.6. Cross-Polarized Microscope (CPM).** CPM images were taken with a Nikon Eclipse ME600 microscope fitted with a CoolSNAP-Pro camera by Media Cybernetics and cross-polarization filters. Scaling was done using a stage micrometer. Temperature control of the sample was done with a Linkham PE 94 and LTS-120E Peltier system. Concentrations of 5 wt % macrocrystalline wax and 1000 ppm PPD or asphaltenes in toluene were prepared, filled into capillaries with a cross section of 0.3 × 0.03 mm, and sealed with glue. The temperature program consisted of heating to 60 °C and keeping at 60 °C for 5 min, cooling at 20 °C/min to 30 °C with subsequent cooling at 1 °C/min to 4 °C and keeping at that temperature. Pictures were taken in the time frame from 30 to 40 min after the sample had reached a temperature of 4 °C. During the temperature cycles, the sample cell was continuously flushed with nitrogen, to avoid the influence of water condensing.

**2.7. Isothermal titration Calorimetry (ITC).** Isothermal titration was performed on a NANO ITC Standard volume from TA Instruments. The apparatus was calibrated by measuring the heat of reaction for defined titrations of Tris-base with HCl. The reference cell was filled with toluene. All experiments were carried out at a temperature of 20 °C and a stirring rate of 250 rpm. Both sample and reference cells have a volume of 1 mL. Titration took place with a 250 $\mu$L syringe in 25 injections, amounting to 10 $\mu$L of titrant being added to the sample cell during each injection. The calorimeter was equilibrated to a baseline drift of less than 0.1 $\mu$W before each experiment started, which took approximately 30 min for pure solvent in the titration chamber or several hours in case of a wax dispersion. Additionally, 300 s of baseline were recorded before and after each experiment. Data analysis took place in the NanoAnalyze software of TA Instruments. Regions for heat integration were set as the injection instants. For each experiment, the heat generated by frictional losses of the injection was corrected by subtracting reference toluene into toluene injections. All experiments were conducted at least twice to show reproducibility and improve statistical significance.

Solvents and solutions used in ITC were degassed by sonicating for 30 min before use. In addition, PPD, and asphaltene solutions for ITC were prepared 1 day in advance and stored at room temperature, to ensure complete dissolution and equilibration of the samples. Moreover, these solutions were prepared to 1 wt % of active content, to ensure comparability and counteract the amount of petroleum distillate contained in the sample. Referencing the amount of active content is a different approach than referencing the total PPD weight as for DSC, CPM, and rheometry. This approach was chosen because the active content presumably is the interacting fraction in ITC, and PPDs were simply added in excess for the other experiment setups. The wax dispersion used in ITC was prepared by heating 10 wt % macrocrystalline wax in toluene to 100 °C for at least 30 min and subsequent quenching by immersion in a water bath held at constant 20 °C. After a duration of 1 h, the mixture was removed from the water bath, shaken vigorously for 5 s, and sonicated for 5 s before being filled into the ITC chamber.

## 3. RESULTS AND DISCUSSION

**3.1. PPD Characterization.** The molecular weight distributions of PPD 1 to 5 are shown in Figure 2. The presence of multiple peaks for each sample suggests distinct populations and that PPD 1 to 5 are all polydispersed. PPD 4 and PPD 5 show concurring peaks and similar curve patterns, which is coherent with similarities in their respective chemistries. Analogously, these similarities can also be observed for PPD 1 and PPD 2. For all PPDs, there is a considerable amount with a molecular weight below 1000 g/mol equivalent to PS detected, which can be explained as unreacted monomer, polymer with a low degree of polymerization or petroleum

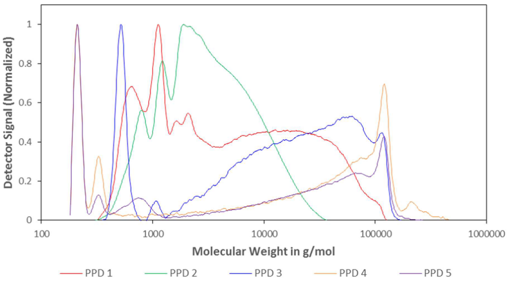

**Figure 2.** Molecular weight distribution equivalent to PS measured by size-exclusion chromatography for all polymer samples; detector signal at 220 nm (normalized to the highest peak).

distillate contained in the commercial samples. The average molecular weights were calculated by integration using the trapezoid rule and are listed in Table 2. It is to be mentioned that the molecules greater than 100 000 g/mol equivalent to PS were not separated by the column. Moreover, the assumption is made that molecular weight and absorbance at 220 nm are proportional and that the confirmation of each sample is the same as for the PS standard. Because of this and due to the presence of monomers, the computed molecular weights in Table 2 are not to be taken as absolute values but as a measure of comparison within this study.

**Table 2. Mass and Number Average Equivalent to PS Calculated by Integration via Trapezoidal Rule for All Polymer Samples**

| | PPD 1 | PPD 2 | PPD 3 | PPD 4 | PPD 5 |
|---|---|---|---|---|---|
| number-average (kDa) | 41.5 | 9.2 | 67.3 | 117.7 | 90.6 |
| mass average (kDa) | 61.9 | 14.1 | 86.8 | 156.9 | 118.4 |

The DSC profiles show distinct crystallization peaks for the different PPDs (Figure 3). The according crystallization heat is listed in Table 3 and was determined by integrating from crystallization onset to −50 °C with a linear baseline for each sample. At −50 °C, all samples except for PPD 5 showed a qualitative return to the reference profile of pure toluene, so the heat value of PPD 5 has to be considered with caution. The difference in measured heat is approximately within the same range for PPD 1 to 5 when related to active content but 3 to 6 times lower than for an equivalent wax solution. The crystallization onset was determined using the same algorithm as for the WAT described in section 2.4. The crystallization onset is approximately the same for all PPDs except for PPD 4, which is higher. PPD 1, 2, and 3 show two local maxima, which can either be due to the petroleum distillate contained in the samples or due to polymer fractions of different molecular weight.

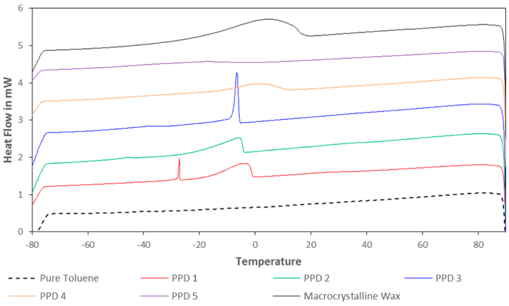

**Figure 3.** DSC profiles of 5 wt % substance in toluene at a cooling rate of 5 °C/min.

**Table 3. Crystallization Heat and Crystallization Onset for Different PPDs in Comparison to Macrocrystalline Wax Measured at a Cooling Rate of 5 °C/min**[a]

| substance | crystallization heat (J/g) | crystallization onset (°C) |
|---|---|---|
| 5 wt % PPD 1 | 4.2 | 0.1 |
| 5 wt % PPD 2 | 3.1 | −3.7 |
| 5 wt % PPD 3 | 2.4 | −5.0 |
| 5 wt % PPD 4 | 4.1 | 13.5 |
| 5 wt % PPD 5 | 2.0 | −1.9 |
| 5 wt % macrocrystalline wax | 12.6 | 20.1 |

[a] All samples use toluene as bulk solvent.

Overall, the DSC results are coherent with SEC observations because multi component mixtures are characterized by a broad crystallization peak in DSC as shown in Figure 3. Moreover, PPD 1 has a higher crystallization onset temperature than PPD 2, and PPD 4 has a higher onset temperature than PPD 5, which confirms that a higher-average molecular weight accounts for a higher onset temperature for polymers of similar chemistries.

**3.2. Wax Inhibitor Performance.** *3.2.1. Wax Appearance Temperature.* The qualitative progression of the DSC heat curve follows a linear decrease with temperature, until the WAT is reached and a broad peak with considerable tailing is measured, as shown in Figure 4. The addition of PPD 1 and 2 caused both delay and sharpening of the peaks at precipitation onset, as reported in similar studies.[45,46] The WAT was computed for a variety of cooling rates in DSC and is shown in Figure 5. The overall trend is that WAT increases with decreasing cooling rates for all samples. PPD 1 to 5 and asphaltenes lower the WAT as compared to the blank sample without WI. The highest decrease is measured for PPD 1, which decreases the WAT by about 6 °C for all cooling rates. Asphaltenes show the lowest decrease for cooling rates of 10 °C/min and lower, and PPD 4 has the second lowest decrease for cooling rates in between 8 and 3 °C/min. Determining an overall ranking is difficult, as for example PPD 5 shows the lowest decrease in WAT at 20 °C/min, but the second largest decrease at 1 °C/min as compared to the WI-free blank sample. The fact that the WAT-cooling rate curves have different slopes and shapes implies that there are differences in the kinetics involved for causing the nucleation lag.

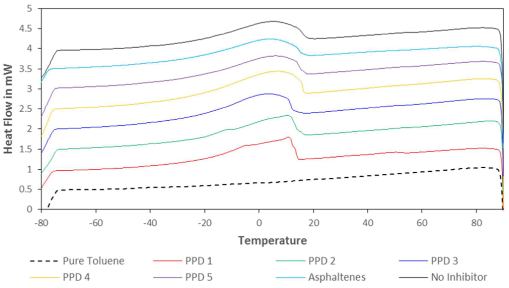

**Figure 4.** DSC profiles for 5 wt % macrocrystalline wax and 1000 ppm PPD or asphaltenes in toluene at a cooling rate of 5 °C/min.

The standard deviation for the DSC results is the greatest at the lowest and highest cooling rates, respectively. High cooling rates, such as 20 °C/min, have a considerably lower resolution due to a fixed data sampling rate at 0.1 $s^{-1}$, which leads to less accurate determinations of the WAT. In contrast to that, low cooling rates have a high resolution but a lower signal-to-noise ratio, since the heat signal is approximately proportional to the

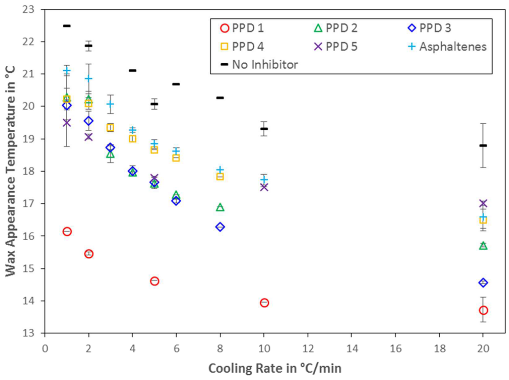

**Figure 5.** WAT values of 5 wt % macrocrystalline wax with and without 1000 ppm PPD or asphaltenes measured at different cooling rates using DSC; error bars represent the standard deviation from the average of each measurement.

cooling rate. The result of this can be seen by the increase in standard deviation at lower cooling rates.

The WAT measurements via viscometry are displayed in Figure 6 and have a similar trend as comparable DSC results at the same cooling rate. In both cases, PPD 1 accounts for the highest and asphaltenes for the lowest decrease in WAT. All PPDs and asphaltenes show a lower WAT than the WI-free blank sample. PPD 2, 3, 4, and 5 are within the standard deviation similar in value. The model oil contained twice the amount of wax as compared to DSC measurements, in order to increase the sensitivity of the measurement. To ensure comparability, the ratio of PPD or asphaltenes to wax was kept constant.

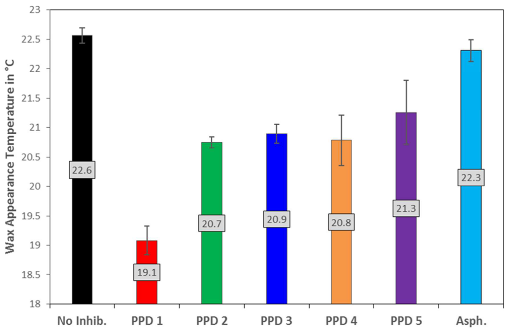

**Figure 6.** Wax appearance temperatures of 10 wt % macrocrystalline wax with and without 2000 ppm PPD or asphaltenes measured at a cooling rate of 5 °C/min using viscometry; error bars represent the standard deviation from the average of each measurement.

Both DSC and viscometry show a decrease in WAT for the addition of PPD 1 to 5 or asphaltenes. Such a decrease can be attributed to the change in solubility equilibrium as a result of the formation of solute complexes.[47] This will lead to favorable conditions during crude oil production, where wax deposition may not be a problem as the crude oil temperature does not drop below the WAT. Still, so-called thermodynamic wax inhibitors (TWI) are required in high volumes, which can cause these to be uneconomical.[48] The use of crystal modifying WIs is therefore favorable to TWIs because these are used in concentrations as low as parts per million. In conclusion, investigating the effect of WI on WAT contains valuable information, but the effect on the strength of the formed gel has to be taking into account as well to fully assess the WI performance.

### 3.2.2. Cross-Polarized Microscopy (CPM).

Wax crystals are made visible in CPM images as white spots, whereas the dark background can be attributed to bulk solvent or crystal geometries and orientations, where the polarized light is not sufficiently depolarized. In Figure 7, the influence of different PPDs or asphaltenes onto the wax crystal morphology is shown and compared to the blank case with no WI. Wax crystals formed without additives show plate and needlelike structures similar to CPM images reported in other studies.[49−51] The intensity and amount of white spots in an image can also provide ground for the estimation of the amount of wax precipitated.[49] Addition of PPD 1 and PPD 2 therefore suggests the lowest amount of wax precipitated, which shows as crystals of a few micrometer or less in diameter, which are smaller than

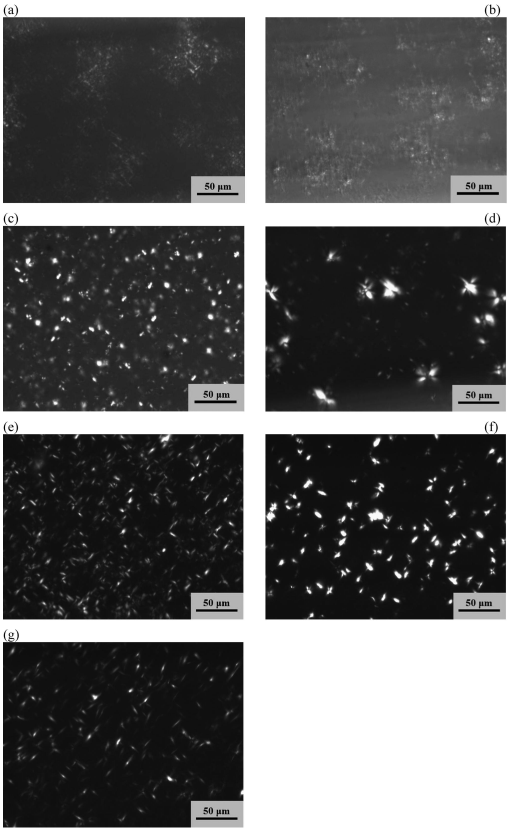

**Figure 7.** CPM images for 5 wt % macrocrystalline wax and 1000 ppm PPD or asphaltenes in toluene @ 4 °C, where (a) PPD 1, (b) PPD 2, (c) PPD 3, (d) PPD 4, (e) PPD 5, (f) asphaltenes, and (g) no WI.

for the other samples tested. PPD 3 and asphaltenes show a morphological change to more compact, round-, and dendrite-shaped crystals as compared to the plate or needle shapes observed for the case with no WI. PPD 5 shows no qualitative change in morphology. As good functioning pour-point depressants are changing the morphology to preferably smaller crystals with lower propensity to overlap, a ranking can be made based on the CPM images in which PPD 1 and 2 are the best working WIs, and PPD 3 and asphaltenes are working WIs with a lower performance than the first two. Investigating the effect of PPD 4 onto wax crystallization, two groups of crystals with distinct morphologies were found. The first group is composed of structures that are smaller and more compact than crystals formed without WI. The second group displays shapes with a stearic center and several branches, which can be described as plates or flakes joined together. These crystals are greater in size than crystals observed in case of no added WI. Similar crystal aggregates are reported for PPD-treated crude oils[17,50] and are also observed for crystals formed in the presence of asphaltenes but smaller in size. PPD 4 therefore seems to achieve the desired effect for part of the crystals and act as a flocculent to others. This can for example be explained by premature consumption of the polymer through cocrystallization, since PPD 4 displayed the highest temperature for the crystallization onset as shown in the DSC profile of Figure 3. Another explanation would be to assume that the polymer is able to act as a steric hindrance as well as a steric connector to wax crystals.

*3.2.3. Gel-Breakage Strength.* The results of the gel-strength measurements in Figure 8 show the influence of the different PPDs and asphaltenes on the strength of the wax-crystal structure formed. The shape of the stress−strain curve showed an initial linear response, followed by a maximum with subsequent decrease in shear stress as shearing continues, which is in agreement with reports on similar investigations.[44,45,52] The best performance is attributed with PPD 1 and 2, as the waxy model oil remained free-flowing even at 4 °C. The lowest gel-strength was measured for asphaltenes, but also PPD 3 lowered the gel-strength to less than one-third of the WI-free case. These results are in agreement with the results from CPM imaging. Adding PPD 4 to change the crystal morphology to many small and a few big crystals yielded a decrease to around 75% of the gel strength without additives. The flocculated crystals therefore seem to interlock, forming a gel of considerable strength. No qualitative change in crystal morphology for PPD 5 is confirmed by the least influence on lowering the gel-strength from the WI-free blank case.

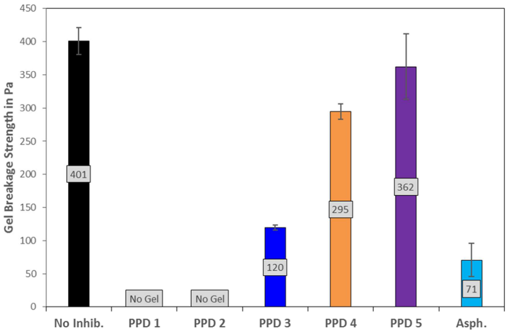

**Figure 8.** Gel breakage strength of 10 wt % macrocrystalline wax with and without 2000 ppm PPD or asphaltenes measured at 4 °C; error bars represent the standard deviation from the average of each measurement.

### 3.3. Inhibitor-Wax Interactions.

PPD solutions of different concentrations were prepared prior to ITC analysis to determine the solubility limit. At a ratio of 1 wt % active PPD in toluene, none of the samples showed precipitated solids after a duration of more than 10 days.

*3.3.1. Wax Inhibitor Dilution and Dissociation.* The ITC results displayed in Figure 9 show that injections of PPD or asphaltenes into toluene can follow three distinct patterns. The titration heat for injecting asphaltenes in toluene into toluene is similar to the dissociation of asphaltenes aggregates reported in earlier works.[39] After subtracting the heat values of the reference toluene in toluene injection, the heat calculated for each injection of PPD 4 or PPD 5 in toluene into toluene is below the detection limit. PPD 1, 2, and 3 all follow a trend in which the dilution is exothermic in the beginning but becomes endothermic at injection 2 or 3 with absolute heat values decreasing toward later injections. This pattern could be interpreted as an indication that PPD 1, 2, and 3 associate in toluene. When the solution of PPD in toluene is injected into pure toluene, the associates formed are dissociating, giving an endothermic signal. Another explanation would be that the injection of PPD 1, 2, and 3 shows the dilution heat of the petroleum distillate contained in these samples.

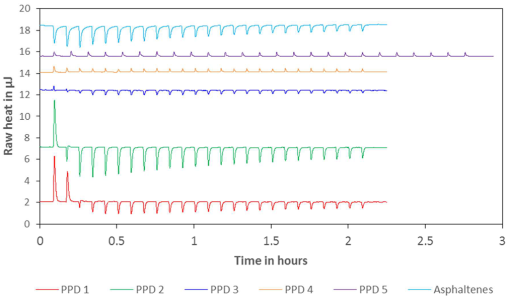

**Figure 9.** Heat signals for injections of 1 wt % active PPD or asphaltenes in toluene into pure toluene.

*3.3.2. Injections into Wax Dispersion.* A CPM image of the wax dispersion as used in ITC experiments is shown in Figure 10. The image shows the typical morphology of macrocrystalline wax with predominantly plate and needle-shaped crystals. It is to be noted that this sample was not filled in a capillary like the other samples but directly injected onto a microscope slide kept at 20 °C.

The injection interval required for wax dispersions is longer than for injections into toluene, as redissolution of wax is a kinetically slower process. Too long injection intervals aggravate the influence of solvent evaporation, so the decision is a trade-off. At injection intervals of 30 min, initial injections did not fully equilibrate for PPD 3 and 5, but toward later injections, PPD 1 to 5 had equilibrated before the next injection, as can be seen in Figure 11. Injections of pure toluene and of asphaltenes in toluene into the wax dispersion were set to an interval span of 60 min, which is shown in Figure 12.

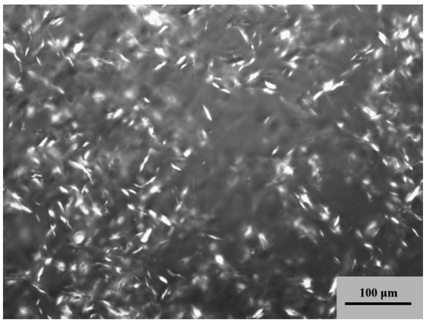

**Figure 10.** CPM image of 10 wt % macrocrystalline wax dispersion prepared for ITC experiments at 20 °C.

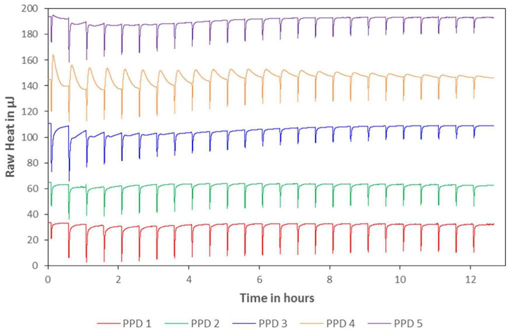

**Figure 11.** Heat signals for injections of 1 wt % active PPD in toluene into 10 wt % macrocrystalline wax dispersion in toluene.

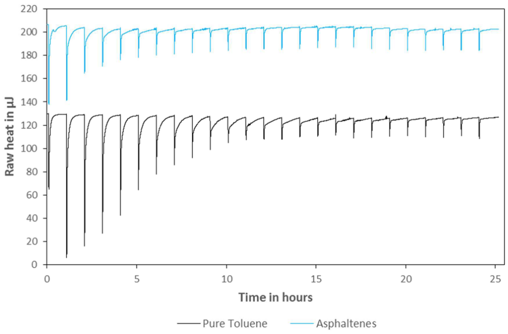

**Figure 12.** Heat signals for injections of 1 wt % asphaltenes in toluene or pure toluene into 10 wt % macrocrystalline wax dispersion in toluene.

With this setting, the transferred heat did not reach a steady value for all injections, but the overall baseline drift was negligibly small, obtained values were reproducible, and the recovered cell volume was approximately the same as the input.

Injections of PPD 1, PPD 2, or asphaltenes in toluene into the wax dispersion are qualitatively similar to the injection of pure toluene into the wax dispersion. Injections of PPD 3 and 5 show two local minima for injections 2 to 6, of which the first minimum is the direct response to the injection and the second minimum is a delayed exothermic process. During these injections, equilibrium is not reached at the end of each interval, so a part of the interaction heat is expected to not be attributed correctly. Still the injection intervals were kept at 30 min for better comparability. The injection of PPD 4 is different from the other samples because the initial endothermic response right after injection is followed by an exothermic peak for every injection. Similar as for PPD 3 and 5, this indicates two phenomena happening at different kinetic rates. The heat signals for PPD 1 and PPD 2 show only one local minimum during each injection interval. For PPD 1 to 5, the heat signal equilibrates within a fraction of the injection interval toward the end of the experiment, which is different for the injection of pure toluene into the wax dispersion. This indicates that either the heat released from inhibitor-wax interactions is canceling out with the heat required for redissolution or the polymer is inhibiting solid wax from redissolving.

### 3.3.3. *Interaction Heat.*

The heat of interaction was calculated as net enthalpy in analogy to Wei et al.,[38] where the heat of titrating inhibitor into toluene ($\Delta H_{\mathrm{int}}$) and the heat of titrating toluene into wax dispersion ($\Delta H_{\mathrm{wax}}$) is subtracted from the heat measured when titrating inhibitor into the wax dispersion ($\Delta H_{\mathrm{total}}$), as shown in eq 1.

$$\Delta H_{\mathrm{Int}} = \Delta H_{\mathrm{total}} - (\Delta H_{\mathrm{Inhibitor}} + \Delta H_{\mathrm{wax}}) \quad (1)$$

The calculated interaction heat for all PPDs or asphaltenes with wax is exothermic. Figure 13 shows the average values with their standard deviation. The resulting standard deviation is calculated according to the propagation of error. The first injection is generally disregarded, as diffusion into the syringe tip during equilibration skews the result of the first injection. The highest interaction heat was measured for PPD 4 and the lowest heat values are attributed with asphaltenes. PPD 1, 2, and 5 are within the standard deviation similar, and PPD 3 is on average lower than these until injection 10. The maximum interaction enthalpy would be expected to occur at injection 2 because of the highest abundance of unreacted reagent in the reaction chamber. Still the highest interaction enthalpy is measured later than at injection 2 for all PPDs and asphaltenes except for PPD 1. This supports the idea that reaction kinetics

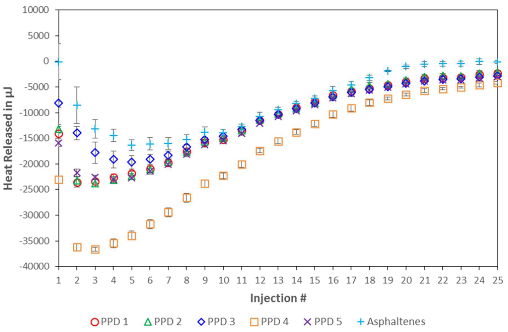

**Figure 13.** Resulting interaction heat for 1 wt % active PPD or asphaltenes with 10 wt % macrocrystalline wax dispersion in toluene; each injection accounts for 10 $\mu$L of titrant being added to 1 mL of wax dispersion; error bars represent the standard deviation from the average of each measurement.

**Table 4. Comparison of the Final Results from ITC, DSC, and Rheometry**

| | no inhibitor | PPD 1 | PPD 2 | PPD 3 | PPD 4 | PPD 5 | asphaltenes |
|---|---|---|---|---|---|---|---|
| ITC, maximum interaction heat (mJ) | | −23.6 | −23.8 | −19.7 | −36.6 | −23.0 | −16.4 |
| WAT, DSC, 5 °C/min (°C) | 20.1 | 14.6 | 17.6 | 17.7 | 18.7 | 17.8 | 18.8 |
| WAT, viscometry, 5 °C/min (°C) | 22.6 | 19.1 | 20.7 | 20.9 | 20.8 | 21.3 | 22.3 |
| gel-breakage strength (Pa) | 401 | no gel | no gel | 120 | 295 | 362 | 71 |
| CPM, crystal morphology | needle and plate shape | small, compact | small, compact | compact, round | small and compact or big flakes | needle and plate shape | distorted, dendrite-like |

are as slow as that during the first two to five injections, part of the interaction enthalpy is released after consecutive injections. All samples are approaching zero net heat in the final injections, but only asphaltenes have zero interaction heat with wax within the margin of error at the end.

A screening experiment was conducted to determine the interaction heat of 1 wt % PPD 4 in toluene with a 1 wt % macrocrystalline wax in toluene solution, which contained no precipitated wax as the WAT is below 20 °C. The interaction heat was measured to be 9.6 $\mu$J per injection averaged over all 25 injections. In comparison to that, the average interaction heat for PPD 4 with a 10 wt % wax dispersion is approximately 17800 $\mu$J per injection. This indicates that the interaction heat measured for PPD 4 with macrocrystalline wax is predominantly due to the interactions of polymer with solid wax.

**3.4. Comparison of the Different Methods.** The interaction enthalpy highest in magnitude was determined for each sample in ITC and is listed together with comparative numerical results of DSC and rheological measurements in Table 4. PPD 1 and 2 have the highest influence on lowering gel-strength and WAT and the greatest effect on changing crystal morphology, but both PPDs show interaction heat values at the average of all six samples. The highest interaction heat is attributed with PPD 4, which ranks among the last three for all other experiments as shown in Table 4. The data therefore suggests that for the model oil system used, there is no correspondence between the heat of interaction measured in ITC and WI performance characteristics, such as lowering the WAT or gel strength. This further implies that it is not the ability of the WI to react with the solid wax crystals but characteristics such as changing the morphology to smaller and more compact crystals with low tendency to interlock, which make up an effective WI or PPD.

It is to be noted that asphaltenes were shown to interact with the wax. This and the changes in crystal morphology then suggest that asphaltenes influence the formation of wax crystals by being attached to or incorporporated into the wax crystals. In addition to that, aggregated or dispersed asphaltenes may be present in the liquid, distorting the wax crystal growth to more branched structures without actively being incorporated into the crystals. This would explain the high efficiency of asphaltenes in lowering gel-breakage strength, in contrast to a lower interaction heat compared to PPD 1 to 5.

## 4. SUMMARY AND CONCLUSION

In this work, five commercial and noncommercial PPDs as well as asphaltenes were investigated in their interactions with solid wax and their effect on wax crystallization in a model oil system made up of macrocrystalline wax in toluene. PPD characterization was done using SEC and DSC. The influence of PPD or asphaltenes onto WAT, wax-crystal morphology, and strength of the formed wax-oil gel was measured via DSC, CPM, and rheometry. The interaction heat of PPD or asphaltenes with solid wax was measured by ITC.

The polymeric PPDs were found to have a polydispersed molecular weight distribution. The ITC measurements showed detectable interaction heat with macrocrystalline wax for all samples. The highest interaction heat was measured for PPD 4, which is EVA copolymer with 25% vinyl-acetate, and the lowest interaction heat was found for asphaltenes. DSC and viscometry showed the ability of all PPDs and asphaltenes to lower the WAT. PPD 1, which is a polycarboxylate-based polymer, accounted for the highest decrease in WAT, and asphaltenes showed the lowest effect. The influence of additives on lowering the gel-breakage strength was coherent with CPM imaging. PPD 1 and 2 showed the greatest decrease in wax crystal size, which lead to the formation of a suspension with no detectable gel strength at 4 °C. Asphaltenes accounted for a change in crystal morphology to rounder- and dendrite-like shapes, which lead to the gel strength being decreased to less than 20% of the gel strength without additives. This and the fact that there was measurable interaction heat for asphaltenes imply that asphaltenes are attached to or incorporated into the wax crystals. The EVA-based samples, PPD 4 and 5, reduced the gel strength by 25% or less, which is coherent with CPM imaging. This suggests that PPD 4 is not a good working WI for the model oil system used, despite the fact that this polymer showed the highest interaction heat.

In conclusion, no direct correspondence was found between the interaction heat of PPD or asphaltenes with solid wax and the WI performance, measured as the impact on lowering WAT or strength of the formed wax-oil gel. The ability of WI to cocrystallize with wax is a necessity, but other characteristics, such as changing the wax crystal morphology to smaller crystals with less propensity to interlock, are crucial properties as well.

## ■ ASSOCIATED CONTENT

### Ⓢ Supporting Information

The Supporting Information is available free of charge on the ACS Publications website at DOI: 10.1021/acs.energyfuels.7b00749.

Stress-strain diagrams (PDF)

## ■ AUTHOR INFORMATION

### Corresponding Author

*E-mail: jost.ruwoldt@ntnu.no.

### ORCID

Jost Ruwoldt: 0000-0002-0583-224X

### Notes

The authors declare no competing financial interest.

## ■ ACKNOWLEDGMENTS

This work was carried out as a part of SUBPRO, a Research-Based Innovation Centre within Subsea Production and Processing. The authors gratefully acknowledge the financial support from SUBPRO, which is financed by the Research Council of Norway, major industry partners and NTNU. The authors would further like to thank BASF for providing PPD samples and Sasol for providing the wax sample. The authors thank Kristofer Paso for contributions in the initiation phase and for helpful discussions of the results.

## ■ ACRONYMS

CPM = cross-polarized microscopy
DSC = differential scanning calorimetry
EVA = ethylene-vinyl acetate copolymer
HPLC = high-performance liquid chromatography
ITC = isothermal titration calorimetry
PPD = pour-point depressant
PS = polystyrene
SEC = size-exclusion chromatography
THF = tetrahydrofuan
WAT = wax appearance temperature
WI = wax inhibitor

## ■ REFERENCES

(1) Aiyejina, A.; et al. Wax formation in oil pipelines: A critical review. *Int. J. Multiphase Flow* **2011**, *37* (7), 671−694.

(2) Huang, Z.; et al. A fundamental model of wax deposition in subsea oil pipelines. *AIChE J.* **2011**, *57* (11), 2955−2964.

(3) Paso, K. G. *Paraffin Gelation Kinetics*; University of Michigan, 2005.

(4) Venkatesan, R.; et al. The strength of paraffin gels formed under static and flow conditions. *Chem. Eng. Sci.* **2005**, *60* (13), 3587−3598.

(5) Guo, Y.; et al. An excellent non-wax-stick coating prepared by chemical conversion treatment. *Mater. Lett.* **2012**, *72*, 125−127.

(6) Singh, P.; Fogler, H. S. Fused Chemical Reactions: The Use of Dispersion To Delay Reaction Time in Tubular Reactors. *Ind. Eng. Chem. Res.* **1998**, *37* (6), 2203−2207.

(7) Jemmett, M. R. *Rheology and Deposition of Heterogeneous Organic Mixtures: An Expansion of "Cold Flow" Research*; The University of Utah, 2012.

(8) Yang, F.; et al. Polymeric Wax Inhibitors and Pour Point Depressants for Waxy Crude Oils: A Critical Review. *J. Dispersion Sci. Technol.* **2015**, *36* (2), 213−225.

(9) Oschmann, H.-J., Das Kristallisationsverhalten von Paraffinen in Abhängigkeit von ihrer Zusammensetzung sowie seine Beeinflussung durch Paraffininhibitoren. In *Fakultät für Bergbau, Hüttenwesen und Maschinenwesen*; Technisch Universität Clausthal: Papierflieger, 1998.

(10) *Standard Test Method for Pour Point of Petroleum Products*; ASTM International, 2017.

(11) *Standard Test Method for Pour Point of Crude Oils*; ASTM International, 2016.

(12) *Standard Test Method for Pour Point of Petroleum Products (Automatic Pressure Pulsing Method)*; ASTM International, 2016.

(13) Machado, A.L.d.C.; Lucas, E. F. Poly(Ethylene-co-Vinyl Acetate) (EVA) Copolymers as Modifiers of Oil Wax Crystallization. *Pet. Sci. Technol.* **1999**, *17* (9−10), 1029−1041.

(14) Paso, K.; et al. Paraffin Polydispersity Facilitates Mechanical Gelation. *Ind. Eng. Chem. Res.* **2005**, *44* (18), 7242−7254.

(15) Clarke, E. W. Crystal Types of Pure Hydrocarbons in the Paraffin Wax Range. *Ind. Eng. Chem.* **1951**, *43* (11), 2526−2535.

(16) Ariza-León, E.; Molina-Velasco, D.-R.; Chaves-Guerrero, A. Review of Studies on Asphaltene - Wax Interaction and the Effect thereof on Crystallization. *CT&F - Ciencia, Tecnología y Futuro* **2014**, *5*, 39−53.

(17) Yi, S.; Zhang, J. Relationship between Waxy Crude Oil Composition and Change in the Morphology and Structure of Wax Crystals Induced by Pour-Point-Depressant Beneficiation. *Energy Fuels* **2011**, *25* (4), 1686−1696.

(18) Zhao, Y. *Shut in and Restart of Waxy Crude Oil Pipelines: Gelation, Rheology Model Development, and Application of Polymer/Ionic Liquid Based Additive*. Ph.D. Thesis, NTNU, 2013.

(19) Al-Yaari, M. Paraffin Wax Deposition: Mitigation and Removal Techniques. *SPE Saudi Arabia section Young Professionals Technical Symposium*, March 14−16, Dhahran, Saudi Arabia; Society of Petroleum Engineers: Richardson, TX, 2011.

(20) Wei, B. Recent advances on mitigating wax problem using polymeric wax crystal modifier. *J. Pet. Explor. Prod. Technol.* **2015**, *5* (4), 391−401.

(21) Guo, X.; et al. Effect of Cooling Rate on Crystallization of Model Waxy Oils with Microcrystalline Poly(ethylene butene). *Energy Fuels* **2006**, *20* (1), 250−256.

(22) Yang, F.; et al. Hydrophilic nanoparticles facilitate wax inhibition. *Energy Fuels* **2015**, *29* (3), 1368−1374.

(23) Li, L.; et al. Improvement of oil flowability by assembly of comb-type copolymers with paraffin and asphaltene. *AIChE J.* **2012**, *58* (7), 2254−2261.

(24) Kokal, S. L.; Sayegh, S.G. Asphaltenes: The Cholesterol of Petroleum; *Middle East Oil Show*, March 11−14, Bahrain; Society of Petroleum Engineers: Richardson, TX, 1995; 29787.

(25) Ghosh, A. K.; et al. Review on aggregation of asphaltene vis-a-vis spectroscopic studies. *Fuel* **2016**, *185*, 541−554.

(26) Alcazar-Vara, L. A.; Garcia-Martinez, J. A.; Buenrostro-Gonzalez, E. Effect of asphaltenes on equilibrium and rheological properties of waxy model systems. *Fuel* **2012**, *93*, 200−212.

(27) Tinsley, J. F.; et al. Waxy Gels with Asphaltenes 1: Characterization of Precipitation, Gelation, Yield Stress, and Morphology. *Energy Fuels* **2009**, *23* (4), 2056−2064.

(28) Oliveira, G. E.; et al. The Effect of Asphaltenes, Naphthenic Acids, and Polymeric Inhibitors on the Pour Point of Paraffins Solutions. *J. Dispersion Sci. Technol.* **2007**, *28* (3), 349−356.

(29) Venkatesan, R.; et al. The Effect of Asphaltenes on the Gelation of Waxy Oils. *Energy Fuels* **2003**, *17* (6), 1630−1640.

(30) Yang, X.; Kilpatrick, P. Asphaltenes and Waxes Do Not Interact Synergistically and Coprecipitate in Solid Organic Deposits. *Energy Fuels* **2005**, *19* (4), 1360−1375.

(31) García, M.d.C.; Carbognani, L. Asphaltene−Paraffin Structural Interactions. Effect on Crude Oil Stability. *Energy Fuels* **2001**, *15* (5), 1021−1027.

(32) García, M.d.C. Crude Oil Wax Crystallization. The Effect of Heavy n-Paraffins and Flocculated Asphaltenes. *Energy Fuels* **2000**, *14* (5), 1043−1048.

(33) Tinsley, J. F.; et al. Waxy Gels with Asphaltenes 2: Use of Wax Control Polymers. *Energy Fuels* **2009**, *23* (4), 2065−2074.

(34) Lei, Y.; Han, S.; Zhang, J. Effect of the dispersion degree of asphaltene on wax deposition in crude oil under static conditions. *Fuel Process. Technol.* **2016**, *146*, 20−28.

(35) Feig, A. L. Applications of isothermal titration calorimetry in RNA biochemistry and biophysics. *Biopolymers* **2007**, *87* (5−6), 293−301.

(36) Saboury, A. A. A review on the ligand binding studies by isothermal titration calorimetry. *J. Iran. Chem. Soc.* **2006**, *3* (1), 1−21.

(37) Simon, S.; et al. An ITC and NMR study of interaction and complexation of asphaltene model compounds in apolar solvent I: Self-association pattern. *Colloids Surf., A* **2016**, *494*, 108−115.

(38) Wei, D.; et al. An ITC study of interaction and complexation of asphaltene model compounds in apolar solvent II: Interactions with asphaltene inhibitors. *Colloids Surf., A* **2016**, *495*, 87−99.

(39) Wei, D.; et al. Interactions between asphaltenes and alkylbenzene-derived inhibitors investigated by isothermal titration calorimetry. *J. Therm. Anal. Calorim.* **2015**, *120* (3), 1835−1846.

(40) Wei, D.; et al. Aggregation of tetrameric acid in xylene and its interaction with asphaltenes by isothermal titration calorimetry. *J. Therm. Anal. Calorim.* **2015**, *122* (1), 463−471.

DOI: 10.1021/acs.energyfuels.7b00749
*Energy Fuels* 2017, 31, 6838−6847

(41) Subramanian, S.; et al. Asphaltene fractionation based on adsorption onto calcium carbonate: Part 2. Self-association and aggregation properties. *Colloids Surf., A* **2017**, *514*, 79−90.

(42) Kok, M. V.; et al. Comparison of wax appearance temperatures of crude oils by differential scanning calorimetry, thermomicroscopy and viscometry. *Fuel* **1996**, *75* (7), 787−790.

(43) Yao, B.; et al. Organically modified nano-clay facilitates pour point depressing activity of polyoctadecylacrylate. *Fuel* **2016**, *166*, 96−105.

(44) Zhao, Y.; et al. Gelation and Breakage Behavior of Model Wax−Oil Systems: Rheological Properties and Model Development. *Ind. Eng. Chem. Res.* **2012**, *51* (23), 8123−8133.

(45) Jung, T.; Kim, J.-N.; Kang, S.-P. Influence of polymeric additives on paraffin wax crystallization in model oils. *Korean J. Chem. Eng.* **2016**, *33* (6), 1813−1822.

(46) Zhao, Y.; et al. Utilization of DSC, NIR, and NMR for wax appearance temperature and chemical additive performance characterization. *J. Therm. Anal. Calorim.* **2015**, *120* (2), 1427−1433.

(47) Claudy, P.; et al. Interactions between n-alkanes and cloud point-cold filter plugging point depressants in a diesel fuel. A thermodynamic study. *Fuel* **1993**, *72* (6), 821−827.

(48) Bai, Y.; Bai, Q. *Subsea Engineering Handbook*; Gulf Professional Publishing, 2012.

(49) Paso, K. G.; et al. PPD architecture development via polymer−crystal interaction assessment. *J. Pet. Sci. Eng.* **2014**, *115*, 38−49.

(50) Wu, Y.; et al. Modified Maleic Anhydride Co-polymers as Pour-Point Depressants and Their Effects on Waxy Crude Oil Rheology. *Energy Fuels* **2012**, *26* (2), 995−1001.

(51) Vignati, E.; Piazza, R.; Visintin, R. F. G.; Lapasin, R.; D'Antona, P.; Lockhart, T. P.; et al. Wax crystallization and aggregation in a model crude oil. *J. Phys.: Condens. Matter* **2005**, *17* (45), S3651.

(52) Paso, K. G. Comprehensive treatise on shut-in and restart of waxy oil pipelines. *J. Dispersion Sci. Technol.* **2014**, *35* (8), 1060−1085.

# Publication IV

## Inhibitor-wax interactions and PPD effect on wax crystallization: New approaches for GC/MS and NMR, and comparison with DSC, CPM, and rheometry

# Inhibitor-wax interactions and PPD effect on wax crystallization: New approaches for GC/MS and NMR, and comparison with DSC, CPM, and rheometry

Jost Ruwoldt[1*], Geir Humborstad Sørland[1], Sébastien Simon[1], Hans-Jörg Oschmann[1], Johan Sjöblom[1]

[1]Ugelstad Laboratory, Department of Chemical Engineering, NTNU, N-7491 Trondheim, Norway

[*]Corresponding author e-mail: jost.ruwoldt@ntnu.no

## Abstract

Three pour point depressants (PPDs) with different chemistries, and extracted asphaltenes were studied in their influence on wax crystallization in a model system. A new procedure for nuclear magnetic resonance (NMR) was developed to monitor changes in liquid phase as wax precipitated. Similar experiments were used to study *n*-alkane depletion during precipitation via the use of GC/MS. Additive performance was furthermore evaluated via differential scanning calorimetry (DSC), rheometry, and cross-polarized microscopy (CPM). All additives induced morphological changes to wax crystals, which also affected apparent viscosity and waxy gelling. Some additives improved flow-ability of the waxy model oil significantly, while others showed less pronounced or even adverse effects. Following DSC and NMR results, PPDs with good wax inhibition could delay both the onset of wax crystallization and reduce the amount of precipitated wax. In accordance with that, GC/MS showed additives to delay certain stages in compositional change during wax precipitation. Moreover, efficient PPDs could suppress interactions between liquid and solid waxes that showed in the NMR $T_2$-distribution. It appears that PPD beneficiation greatly influences the mobility of dissolved wax molecules, which would also entail an effect on interactions at the solid-liquid interface of wax crystals. In conclusion, experimental procedures for NMR and GC/MS were extended to study PPD-wax interactions more in-depth, and experimental results show potential for improving the knowledge of wax inhibition.

## 1. Introduction

Paraffin wax crystallization is one of the major challenges during crude oil production [1]. As the crude oil is transported through subsea pipelines, cooling of the oil induces wax crystallization once the wax appearance temperature (WAT) is reached. Issues associated with wax crystallization include increased fluid viscosity, formation of a wax deposition layer, pipeline restart issues due to waxy gelation, and reduced separation efficiency due to the formation of pickering emulsion [2]. Managing wax related issues entails significant costs, but if these issues are not addressed properly they can lead to production stop and even the loss of equipment [3-5]. Wax inhibitors play a central role in wax control, as these can ensure low fluid viscosity and prevent gelling. Even though the effect of these additives is well documented, the exact working mechanism remains still unknown [6, 7].

Wax crystallization as crystallization in general is reported to take place in three stages, which are (i) nucleation, (ii) growth, and (iii) agglomeration [8]. Stage (i) is usually delayed by a nucleation lag, which is cooling rate dependent [9]. The observed WAT or cloud point is therefore generally lower than the thermodynamic solubility limit of the wax. Wax crystal size increases during stage (ii), spawning crystal morphologies such as plates, needles, and malcrystalline masses [10]. Three dimensional interlocking can take place, marking wax crystal agglomeration of stage (iii). A solid like gel can be formed at a solid wax content as low as 1 – 2 % [11]. Upon shearing, this gel displays yielding behavior after an initial Hookean response, which is followed by gel breakage and degradation [12]. Gel yield strength is subject to thermal and shear histories [13], but also to the type of wax composition.

Macrocrystalline wax is reported to form high yield strength gels, whereas microcrystalline wax forms weak gels due to smaller and more compact crystal structures [14]. Macrocrystalline wax is mostly composed of low molecular weight *n*-alkanes ($C_{16}$-$C_{40}$), and microcrystalline wax contains large amounts of high molecular weight (~$C_{40}$ and above) *iso*-alkanes and *cyclo*-alkanes [6].

Wax inhibitors include thermodynamic wax inhibitors, dispersants and surfactants, as well as pour point depressants (PPDs) [15]. Thermodynamic wax inhibitors are solvents or crude oil distillates that decrease WAT, but are deemed uneconomic due to a high volume required. Dispersants and surfactants act on the wax crystal surface, reducing particle-particle or particle-wall adhesion [15]. PPDs lower the pour point, which is defined as the temperature, at which the waxy oil loses its ability to flow freely [16]. PPDs are considered to predominantly act as crystal modifiers [7]. Crystal modifying substances alter wax crystal morphology via co-crystallization. During continued crystal growth, the incorporated PPD molecule can impose spatial hindrances to wax molecules that further precipitate on the crystal, leading to crystal distortion. This is often realised by polar moieties in the otherwise hydrocarbon-like polymer [17]. The hydrodynamic radius of wax crystals can thereby be reduced, as well as the propensity to overlap and form volume spanning networks. PPD polymers have also been reported to improve the thermodynamic solubility of wax via solute complexes [18]. Natural constituents of the crude oil can also act as PPD active substances. Asphaltenes have been confirmed as such by many authors [19-25]. It has been suggested that asphaltenes serve as nucleation site for wax crystallization, leading to more finely dispersed wax crystals [23, 24]. Moreover, co-precipitation mechanism for asphaltenes on wax crystals has been stated [21, 24, 26, 27]. Resins have also been mentioned as natural PPDs [28]. In addition, a recent study found that increasing the paraffin isomer content can affect wax crystallization in a beneficial way [29].

Industrial PPDs have been categorized into copolymers, comb polymers, and nanohybrid PPDs [6]. Copolymers usually consists of a polyethylene (PE) backbone that contains amorphous moieties with possibly higher polarity. Such chemistries include ethylene-propylene (PE-PEP), ethylene-butene (PE-PEB), poly(maleic anhydride amide co-a-olefin) (MAC), and ethylene-vinyl actetate copolymer (EVA) [30-33]. Comb polymers can be based on these, but additionally include pendant alkyl chains [6]. Ideally, such alkyl chains should match the average carbon number of the crude oil waxes [34]. Pendant alkyl chains and polar moieties can promote polymer interactions with wax and more polar components of the crude oil, such as asphaltenes [30, 34-37]. Nanoparticles and nanoparticle-polymer composites have been subject to recent studies, due to their ability to improve pour point beneficiation [38-45]. Such particles were stated to function as wax nucleation sites, which can lead to the formation of larger aggregates that are more compact and amorphous in structure [41, 43].

Aim and approach of this study are twofold. Firstly, improved procedures for NMR and GC/MS were presented to study PPD effect on wax crystallization in liquid phase. Similar approaches had been made by other authors in the past [46, 47], but involved procedures and techniques have been refined and extended since then. Secondly, experimental results from NMR and GC/MS technique were compared to established techniques, such as differential scanning calorimetry (DSC), rheometry, and cross-polarized microscopy (CPM). In addition, a comparison of wax precipitation curves (WPC) obtained by different techniques was made to better assess PPD effect on wax precipitation. Subject to the investigation were three polymeric PPDs and asphaltenes in a waxy model system. The goal was to evaluate the potential of new procedures for studying PPD-wax interactions and extend the knowledge about wax inhibition.

## 2. Experimental section

### 2.1. Materials

Solvents were obtained as toluene (anhydrous, 99.8%), deuterated toluene (anhydrous, 99.6 atom % Deut.), and *n*-heptane (anhydrous, 99%) from Sigmaaldrich, Norway. Asphaltenes were precipitated from a heavy crude oil (API 19°) originating from the Norwegian shelf by using *n*-hexane (HPLC grade, ≥97%) supplied by VWR, Norway. Characteristics and properties of these asphaltenes have been previously published [48-50]. Pour point depressants featured in this study are listed in Table 1. Macrocrystalline wax was obtained as 5405 Sasolwax from Sasol, Germany. A chromatogram of the wax is shown in Fig. 1. The wax consisted of mostly *n*-alkanes, where 84.6 wt% were in the range of *n*-$C_{20}$ to *n*-$C_{40}$ and 0.9 wt% were extrapolated to be *n*-$C_{41}$ and higher. *Iso*-alkanes are visible as peaks in between larger *n*-alkane peaks, and the total isomer content was approximately 12 - 15 wt%. Standards for GC-analysis were purchased as heptadecane (analytical standard), and alkane standard mixture ($C_{10}$-$C_{40}$, even carbon numbers, 50 mg/l each in heptane) from Sigmaaldrich, Norway.

Table 1. Chemical additives

| Alias | Chemistry based on | Supplied by |
|---|---|---|
| PPD A | polycarboxilate (proprietary) | BASF, Germany |
| PPD B | polyacrylate, EVA (proprietary) | BASF, Germany |
| PPD C | EVA, 40% vinyl acetate | DuPont, Germany |
| Asphaltenes | Asphaltenes from hexane precipitation of a heavy crude oil | - |

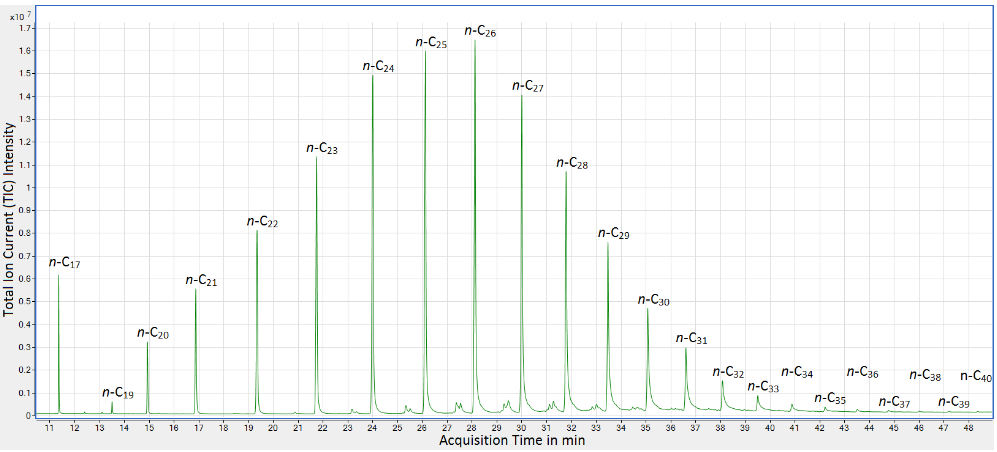

Fig. 1. TIC chromatogram of splitless injection of wax (Sasolwax 5405) in heptane with heptadecane (*n*-$C_{17}$) standard.

### 2.2. Sample preparation

The crude oil was heated to 60 °C for 1 h and shaken thoroughly before use, to ensure homogeneity of the sample. Asphaltenes were precipitated by diluting the crude oil sample with 40 ml *n*-hexane per gram crude oil and stirring overnight. The resulting mixture was then filtered through a 0.45 μm HVLP-type Millipore filter membrane and afterwards rinsed with *n*-hexane until the filtrate was clear. The yield of asphaltenes accounted for 2.3 wt% of the crude oil.

The samples PPD A and PPD B originally contained different petroleum cuts, yielding 80 % and 50 % active content, respectively. The polymers were solvent purified by repeated addition and removal of toluene in a rotary evaporator at up to 90 °C and 200 mbar. The remaining substance was subsequently dried in an oven at 60 °C for 24 h under atmospheric pressure. The amount of remaining solvent was estimated in a Q600 thermogravimetric analyzer (TGA). Heating the solid sample from 60 to 200 °C at a rate of 10 °C/min, the total weight loss amounted to 2.5 wt% for PPD A and 4.0 wt% for PPD B. Above 200 °C the weight loss increased rapidly as the polymer started to disintegrate.

Waxy samples, also referred to as model waxy oils, were prepared by first weighing the solids (PPD/asphaltenes and wax) and then adding the required amount of toluene. Wax was dissolved by heating to at least 20 °C above WAT for at least 30 min. PPD and asphaltene containing solutions were additionally sonicated prior to use. Sample concentrations of 1000 ppm PPD or asphaltenes and 5 wt% wax in toluene were consistently used for all types of experiments.

### 2.3. Differential scanning calorimetry (DSC)

DSC experiments were conducted on a Q2000 from TA Instruments. The instrument was calibrated by measuring the melting heat and temperature of pure indium. For each experiment, 20 – 25 mg sample was loaded into Tzero Hermetic Aluminum Pans, which were sealed hermetically. The pans were weighed before and after the experiment, to ensure that no solvent loss had occurred. During each experiment run, the sample was first heated to 90 °C and then held isothermally for 10 min. A constant cooling rate of 0.2 °C/min was subsequently applied and data recording commenced. This heating program was repeated multiple times, as the reheating period showed to remove all thermal history.

WAT determination was conducted based on a previously published procedure [51]. In this procedure, the DSC heat flow with temperature is approximated by a straight line before wax crystallization onset. A confidence interval is calculated as 1.92 times the standard deviation of data from the straight line approximation. The WAT is then defined as the highest temperature, at which three consecutive points are outside of the confidence interval.

The WPC was computed from the excess heat, which is the difference of heat signal and interpolated baseline as shown in Fig. 2. The baseline was approximated as second degree polynomial of the specific heat capacity, as suggested by Coto et al [52]. This baseline approximation used data on a 10 K interval starting 5 °C above WAT, as well as data between -55 to -70 °C. The conversion between heat flow and specific heat capacity was done via equation (1), where $c_p$ is the specific heat capacity, $\dot{Q}$ is the heat flow, $C_r$ is the cooling rate, and $K$ is an instrument calibration constant.

$$\dot{Q} = \frac{c_p C_r}{K} \tag{1}$$

The cumulative sum of excess heat (heat signal baseline subtracted from actual heat signal) could then be used to compute the amount of precipitated wax by dividing through the total sum of excess heat. The assumption of athermal behavior of the wax was thereby made, which implies that specific crystallization heat does not change with temperature. An example is given in Fig. 2. As can be seen, below -55 °C the heat signal has returned to a stable baseline. This intrinsic procedure was favored over procedures employing extrinsic properties, as the specific crystallization heat of wax was strongly affected by PPD addition.

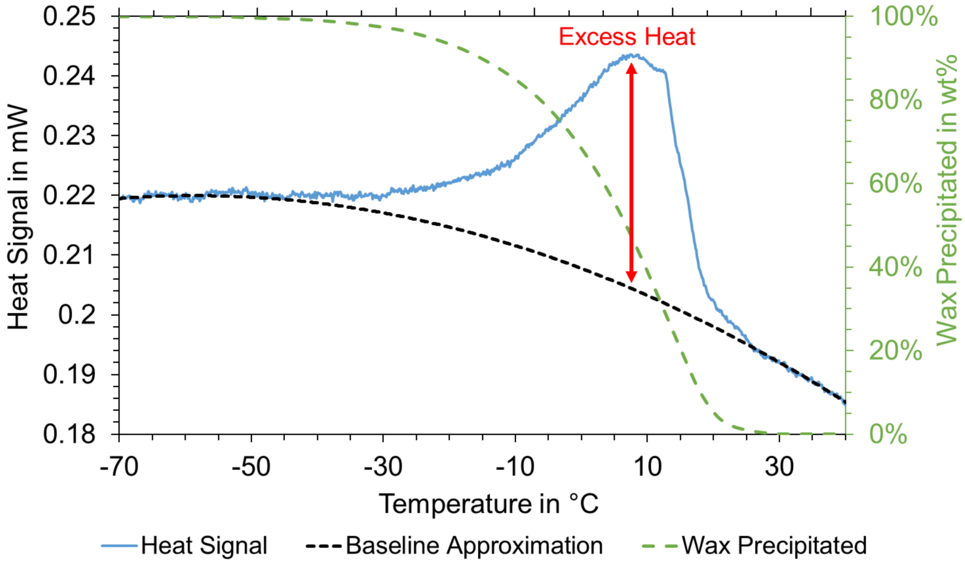

Fig. 2. WPC computation from DSC data of 5 wt% wax in toluene at a cooling rate of 0.2 °C/min. The heat flow represents the average of 4 measurements for improved signal to noise ratio at low cooling rates. The baseline was approximated by a 2nd degree polynomial.

### 2.4. Rheometry

Rheometric experiments were conducted on an Anton Paar Physica 301. The rheometer was equipped with a 4 cm diameter 2° cone and plate geometry, which had been sandblasted on both sides to provide additional roughness and to prevent slippage. The gap size was 0.170 mm. A solvent trap filled with toluene was used to prevent evaporation of the sample. The sample was loaded into the geometry, which had been preheated at 5 – 10 °C above WAT, after which cooling at a rate of 0.2 °C/min commenced.

In viscometry measurements a constant shear rate of 0.1 $s^{-1}$ was applied. This shear rate is an order of magnitude lower than previous procedures used for WAT determination [51, 53, 54]. This was done, because the focus was not on WAT determination, but on monitoring viscosity changes due to wax crystallization. Higher shear rates and a consequently higher amount of total strain would have caused a higher degree of gel degradation, and thus lower measurement sensitivity.

Gel yield strength was measured by quiescently cooling to -2 °C, holding isothermally for 30 min, and then ramping the shearing from $10^{-4}$ – 1 $s^{-1}$ logarithmically for 10 min. The yield strength was defined as the maximum shear stress recorded in the flow curve.

### 2.5. Cross polarized microscopy (CPM)

CPM imaging was done on a Nikon Eclipse ME600 microscope, which was fitted with cross-polarization filter and a CoolSNAP-Pro camera by Media Cybernetics. Temperature control was handled by a Linkham PE 94 and LTS-120E Peltier system. The preheated samples were filled into glass capillaries with a cross section of 0.3 x 0.03 mm, which were sealed on both ends using 3 M Scotch cyanoacrylate glue and fixed in place on microscope slides. To prevent sample contamination, an air bubble was kept on both ends of the capillary. During measurements, the temperature was first ramped to 60 °C, kept isothermally for 15 min, cooled to 30 °C at a rate of 10 °C/min, and then cooled to -2 °C at a rate of 0.2 °C/min. The temperature was held constant at -2 °C and imaging was done within the time frame of 30 – 60 min of the isothermal period.

### 2.6. Nuclear Magnetic Resonance (NMR)

NMR Experiments were conducted on a low field (21 MHz) NMR spectrometer without frequency resolution, which was supplied by Anvendt Teknologi AS, Norway. The sequence applied was the standard Carr-Purcell-Meiboom-Gill (CPMG) sequence for acquiring the transverse relaxation time ($T_2$) decay [55]. The inter echo spacing ($2\tau$) used was 300 μs and the number of echoes acquired was set to 12000. To produce the $T_2$-distributions from the multi-exponentially decaying curve, the one-dimensional Inverse Laplace Transform was made use of [56]. $T_2$-distributions were used as a qualitative and quantitative measure, as solids are known to display short $T_2$, whereas substances in the liquid state show long $T_2$. To quantify substances in the liquid state, a signal intensity was computed as sum over $T_2 > 3 \bullet 10^{-3}$ s by convention.

All experiments used a constant sample weight of 3 g. Deuterated toluene was used as bulk solvent to obtain $T_2$-distributions that reflect only the dissolved components. The molecular weight of deuterated toluene was taken into account in the weighing procedure, to mimic the same mole fraction of experiments with 5 wt% wax in non-deuterated toluene. The temperature ramping started with an isothermal segment at 45 °C in the beginning, and then cooling at a rate of 0.2 °C/min took place. Sample temperature was controlled with preheated or precooled air that continuously flushed the vial from bottom to top. The flow of air was held constant throughout all experiments by applying constant inlet pressure. As determining the actual sample temperature inside the NMR is difficult, an apparent temperature was computed from comparing dynamic and static experiments with 5 wt% hexadecane in deuterated toluene. Dynamic experiments refer to applying a constant cooling rate of 0.2 °C/min, whereas in static experiments the sample was equilibrated isothermally for 60 min before data acquisition. The data was then used to compute a temperature correction function, as shown in Fig. 3. This was done by fitting static and dynamic data with a polynomial function each, and computing the difference. The obtained function accounts for the gap between setpoint temperature and actual temperature in the sample. Assuming that the influence of exothermic wax crystallization is negligibly small at a cooling rate of 0.2 °C/min, this conversion was also applied to wax containing samples.

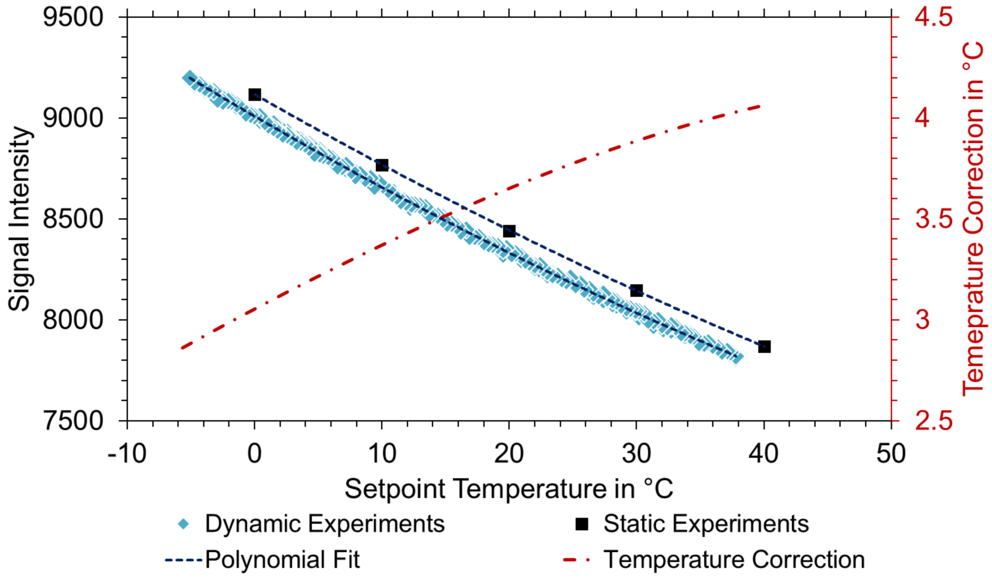

Fig. 3. Dynamic and static experiments for temperature calibration of NMR data with 5 wt% hexadecane in deuterated toluene.

Moreover, hexadecane did not precipitate over the entire temperature range tested. Experiments in Fig. 3 were therefore used to correct for the signal change with temperature due to the Boltzmann factor [57], which accounts for repartition of hydrogen atoms between the different energy levels. To do so, the signal intensity of solubilized wax $S_{wax}$ was divided by the polynomial fit of dynamic experiments with 5 wt% hexadecane in deuterated toluene $\bar{S}_{hexadecane}$, yielding the corrected signal intensity $S_{corr,i}$ as shown in equation (2). The corrected signal was constant for temperatures above WAT, but unequal to 1 due to the difference in atomic ratio of hydrogen atoms of hexadecane and wax. As stated in equation (3), the corrected signal intensity was therefore normalized by dividing through the average signal intensity $\bar{S}_{corr}$ between setpoint temperatures 28 – 38 °C. This provided a measure for the total fraction of dissolved wax $c_{liquid}$, which is equal to 1 above WAT. From mass balancing, the apparent solid wax $c_{solid}$ is implicitly given by equation (4). Due to the normalization procedure, additives were treated as part of the wax. This simplification is in analogy to DSC experiments, where the WPC is also measured in respect to the sum of precipitating components.

$$S_{corr,i} = \frac{S_{wax,i}}{\bar{S}_{hexadecane}(T_i)} \tag{2}$$

$$c_{liquid} = \frac{S_{corr,i}}{\bar{S}_{corr}} \tag{3}$$

$$c_{solid} = 1 - c_{liquid} \tag{4}$$

### 2.7. Filtration experiments and GC/MS

Changes in liquid phase composition were investigated after inducing wax crystallization through cooling and subsequent liquid phase recovery by filtration. Experiments were conducted with a 250 ml jacketed glass vessel, which was temperature controlled using a Julabo external Pt 100 sensor coupled to a Julabo F-32 HE water bath filled with a 20/80 (vol/vol) mixture of ethyleneglycol in water. The sensor was directly immersed into the bulk sample, which was continuously stirred with a magnetic stirrer. A schematic of the setup is shown in Fig. 4. In experimentation, 150 ml of waxy solvent were filled into the vessel, both heated at 40 - 60 °C. The sample was allowed to equilibrate at 35 °C, after which cooling at a rate of 0.2 °C/min was applied. Sampling took place by piercing the PTFE/silicon septum at the bottom of the vessel with a needle and withdrawing 2 ml of sample, which was then filtered through a 0.45 µm PTFE filter membrane. Syringe needles, syringes, and filters were preconditioned isothermally at the target sampling temperature before sample withdrawal. The filtered sample was weighed and subsequently diluted with 85 g/g *n*-heptane, which also contained 4 mg/l heptadecane as internal standard for GC/MS analysis.

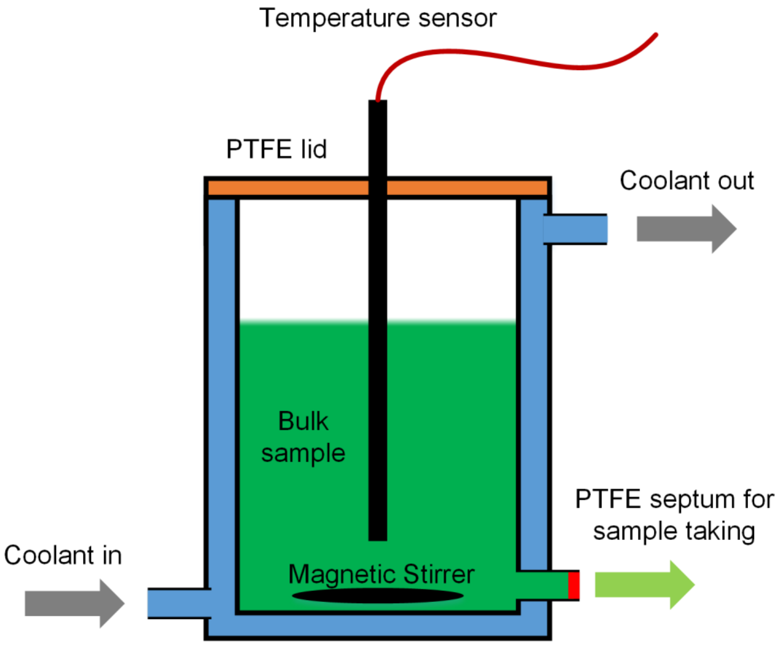

Fig. 4. Schematic of wax crystallization vessel

GC/MS analysis was performed on an Agilent 7890B with split/splitless inlet and a 7693A injection tower. A DB-1HT capillary column with 30 m length, 0.25 mm diameter, and 0.1 µm film thickness was used for separation. The GC was coupled to a 5977B mass spectrometer detector (MSD), which was set at 150 °C quad, 230 °C source, and 330 °C transfer line temperature. The MSD was set to a scanning range of 10 to 620 g/mol at a frequency of 4.6 scans per second, a step size of 0.1 m/z, and 6.5 min solvent delay. The inlet temperature was set at 330 °C. To quantify alkanes with a carbon number of $\leq C_{35}$, the inlet was operated in split mode at a split ratio of 1:20 and 2 µl sample injection. To measure alkanes with a carbon number of $\geq C_{30}$, the inlet was operated in splitless mode with 0.5 µl sample injection. Both modes had identical settings for oven program and flow of helium carrier gas. The oven temperature started at 50 °C, was first ramped to 90 °C at 20 °C/min, then to 180 °C at 10 °C/min, and lastly at 4 °C/min to 340 °C, where the temperature was held for 2 min. The flow of helium carrier gas was set to 1.2 ml/min with a holding period of 30 min, then ramped to 1.6 ml/min at a rate of 0.02 ml/min per minute and subsequently held constant.

Integration of elution peaks was done via MassHunter on the total ion chromatogram (TIC), excluding characteristic m/z values for molecules typically found in air. For quantification, the integrated peaks were divided by the peak are of heptadecane internal standard. The detector response was nonlinear for all $n$-alkanes. Measurements were therefore done as interpolation from a calibration function, which had been fitted by nonlinear regression to four (split injection) or five (splitless injection) known dilutions of wax plus alkane standard mixture. This way, both the ratio of regarded $n$-alkanes in wax was determined, as well as a calibration function. Involved terms are shown in equations (5), (6), and (7), where $a$, $b$, $c$, $a^*$, $b^*$, and $c^*$ are calibration constants, $f_x$ is the ratio of a specific $n$-alkane in the wax, $\mathrm{C_x}$ is the $n$-alkane concentration (analyte) with according peak area $\mathrm{A_x}$, and $C_{IS}$ is the internal standard (heptadecane) concentration with peak area $\mathrm{A_{IS}}$.

$$y(x) = \left(a\sqrt{x} + bx + cx^2\right)f_x = a^*\sqrt{x} + b^*x + c^*x^2\text{, where} \tag{5}$$

$$y(x) = \frac{\mathrm{C_x}}{C_{IS}} = f_x\,\frac{\mathrm{C_{wax}}}{C_{IS}} \tag{6}$$

$$x = \frac{\mathrm{A_x}}{\mathrm{A_{IS}}} \tag{7}$$

As the standard mixture contained only even numbered $n$-alkanes, the response of uneven carbon numbers was obtained via polynomial interpolation. Two fittings are exemplarily shown in Fig. 5. The advantage of this procedure is that comparably few injections are needed for calibrating with sufficient resolution over a broad concentration range. This was deemed necessary, as the MSD response for $n$-alkanes showed variation during long injection series. The order of injections was also optimized to compensate for this drift. At first, a calibration series was run, then followed by sample injections pertaining to one wax crystallization experiment. Right after that, these injections were repeated in reversed order, followed directly by a second calibration run. Calibration was hence performed as average over two calibration series, which were run before and after each measurement series. Wax crystallization experiments were conducted in doubles, providing four measurement points in total per component.

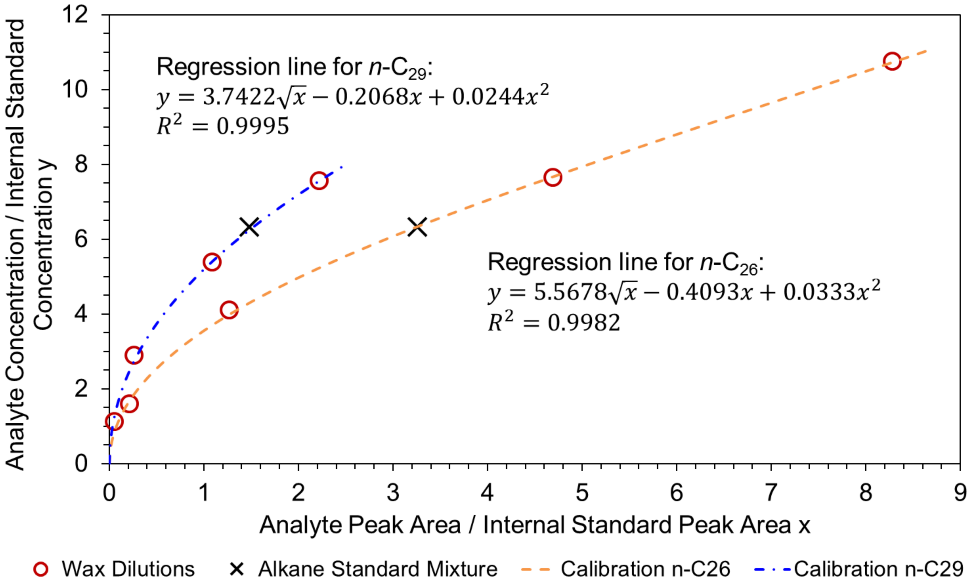

Fig. 5. Exemplary regression lines for calibration of $n$-C26 and $n$-C29 for GC/MS analysis.

## 3. Results and discussion

To provide a complete picture, PPD precipitation and effect on wax crystallization is first discussed as studied by established techniques such as DSC, rheometry, and CPM. Secondly, the main advancement of this study is presented and discussed, which comprises PPD-wax interactions in liquid phase studied by NMR and GC/MS, and additionally a WPC method comparison. Sample concentrations of 1000 ppm PPD and 5 wt% wax in toluene were used consistently throughout all experiments. The concentration of PPD is thereby higher than usual in petroleum production, which was deemed necessary to obtain well-quantifiable differences between the additives.

## 3.1. PPD characterization and effect on wax crystallization

### 3.1.1. PPD precipitation in pure solvent

The precipitation behavior of different PPD chemistries was first observed in DSC, using 5 wt% PPD in toluene without the addition of wax. As shown in Fig. 6, each PPD has one or two characteristic precipitation peaks. The precipitation onset temperature was determined with the same procedure as the WAT. For all PPDs, the precipitation onset was detected before the main peak. The peak shape of PPD B is narrower than that of PPD A, which suggests a lower degree of polydispersity. Also, PPD A and PPD B show one main peak between 0 and -10 °C, and a smaller peak between -25 and -40 °C. This secondary peak could be explained by unreacted monomer or remaining solvent in the sample. The crystallization temperature as well as total heat released by PPD C is lower than for PPD A and PPD B, indicating a lower tendency to crystallize in toluene solvent. Experiments in Fig. 6 show data with a cooling rate of 5 °C/min, because this provides a better illustration of the polymer precipitation profile. PPDs were also measured at a cooling rate of 0.2 °C/min and the characteristic peaks followed the same trends.

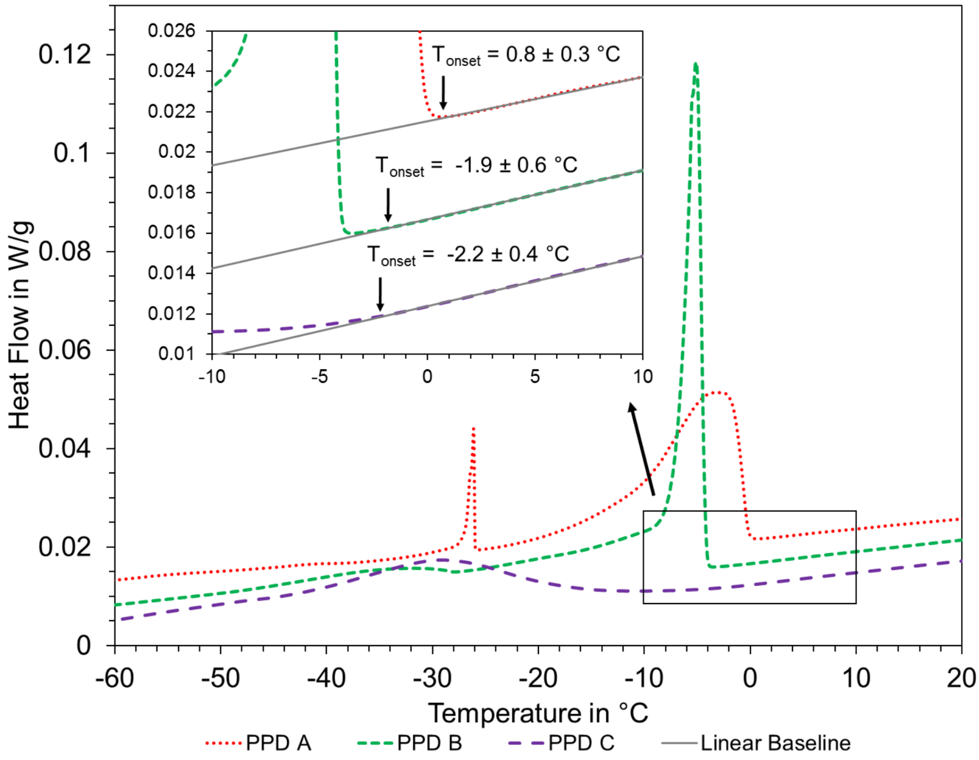

Fig. 6. DSC heat flow of 5 wt% PPD in toluene at a cooling rate of 5 °C/min. Graphs were shifted on the y-axis for better overview.

### 3.1.2. Wax precipitation in DSC

To ensure comparability with other experiments, DSC employed a cooling rate of 0.2 °C/min. This cooling rate is low compared to the usual operating settings for DSC. To improve the signal to noise ratio, at least four repetitions of identical measurements were run and the final graph was averaged over these. Fig. 7 shows the noise improved results for DSC measurements of different additives with 5 wt% wax in toluene. Data was reproducible within a certain margin of error, as indicated by the standard deviation. According WAT values are listed in Table 2, which were computed as the heat flow exceeding the linear baseline prior to wax precipitation. Addition of PPD A amounted to the largest decrease in WAT, which can also be seen in Fig. 7 as shift in the main peak to lower temperatures. For all samples, a strong increase in heat flow was observed between 18 – 20 °C, marking the onset of the main peak. For all samples except PPD A, the WAT was measured 1 – 4 °C higher than the onset of this main peak. The WAT is visible as slightly scattered, but distinct change in slope of the heat flow. WAT determination via exceeding the linear baseline was chosen over the tangent intersection procedure, as this provides a more sensitive estimate of the WAT [51]. The peak shape for PPD C, asphaltenes, and no PPD is similar. Other authors also found asphaltenes to decrease WAT with little impact on the shape of the wax crystallization peak [21]. For PPD A and PPD B it appears that two additional peaks are superimposed onto the main crystallization peak. In particular, PPD B shows such an imposed peak between the temperatures 0 – 5 °C. These peaks are likely to be the result of the bimodal crystallization peaks shown in Fig. 6 for PPDs in pure solvent. However, the intensity change per mass of polymer is higher than for pure PPD solutions of Fig. 6, which would suggest co-crystallization of wax at these temperatures, also.

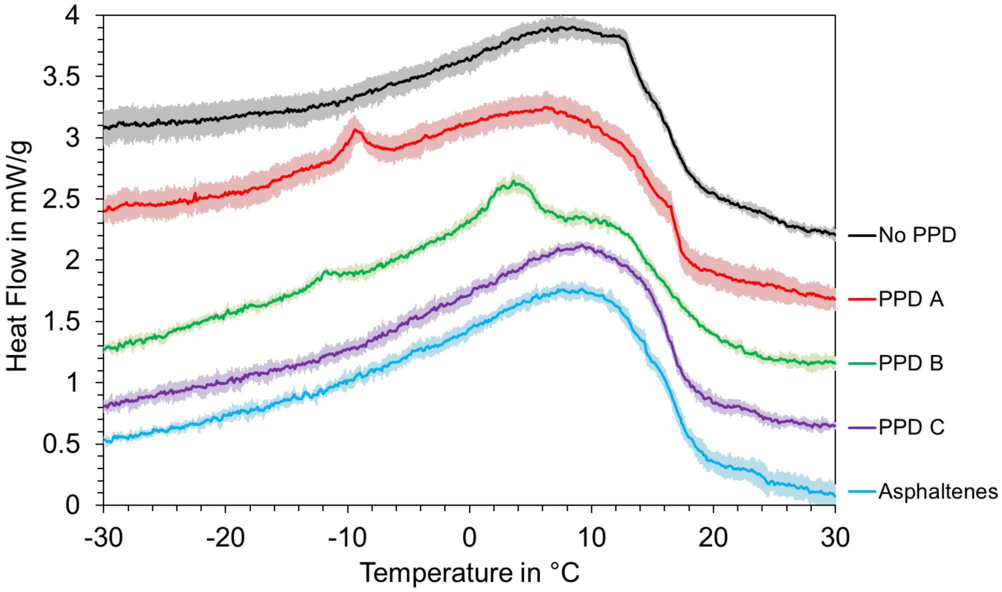

Fig. 7. DSC heat flow for 1000 ppm PPD or asphaltenes and 5 wt% wax in toluene. Each graph represents the average over at least four identical measurements to improve signal to noise ratio, where the shaded area marks the standard deviation. Graphs were shifted on the y-axis for better overview.

Table 2. Computed WAT from DSC data.

| Sample | WAT in °C |
|---|---|
| 5 wt% wax in toluene | 25.2 |
| 1000ppm PPD A and 5 wt% wax in toluene | 18.5 |
| 1000ppm PPD B and 5 wt% wax in toluene | 22.5 |
| 1000ppm PPD C and 5 wt% wax in toluene | 23.7 |
| 1000ppm asphaltenes and 5 wt% wax in toluene | 23.9 |

### 3.1.3. Wax crystallization during continuous shearing (viscometry)

The efficiency of PPDs and asphaltenes for improving flow-ability of the waxy model oil was tested by rheometry and CPM. Viscometry measurements in Fig. 8 show three distinctive regions of precipitation. At temperatures above Region 1, no wax crystallization was observed by viscometry, which is in part due to the low shear rate imposed. Region 1 then marks the crystallization onset, where an increase in apparent viscosity by several orders of magnitude was recorded for all additives except for PPD A. In region 2 the apparent viscosity further increases due to continued wax crystal growth. In region 3 the crystal growth continues, but gel degradation effects due to continuous shearing lead to an apparent viscosity decrease for all additives except in presence of PPD A. For no PPD and PPD A, the apparent viscosity increased continuously as cooling progressed. It has to be noted that for all samples except for PPD A, the minimum torque required for reliable measurement was reached 1 – 4 °C below the WAT listed in Table 2.

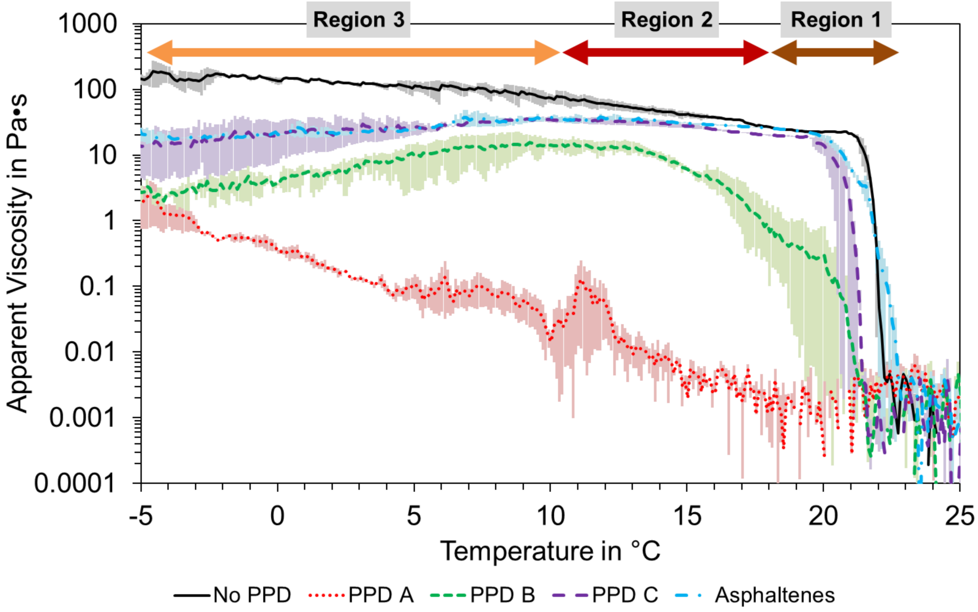

Fig. 8. Viscometry results for 1000ppm PPD and 5 wt% macrocrystalline wax in toluene at a shear rate of 0.1 $s^{-1}$. A cooling rate of 0.2 °C/min was applied and the graphs represent the average of two to three measurements. Error bars mark minimum and maximum values. Three different regions can be distinguished: Region 1 (Wax crystallization onset), Region 2 (wax crystal growth), and Region 3 (continued crystal growth and gel degradation).

#### 3.1.4. Wax crystallization during quiescent cooling

The effect of PPD or asphaltene addition on wax crystallization under quiescent conditions is illustrated in Fig. 9. The additive free case showed wax crystallization with co-joined structures in the size range of 50 µm and more. Clustering of multiple layers around a stearic center can be observed, and the individual branches are mostly straight. Such structures can be interpreted as needle-shaped crystals that are cross-linked to form 3D structures. Alternatively, the observed geometries could represent plate shaped crystals that are skewed with respect to the plane of observation. Addition of PPD A and PPD B both resulted in the formation of distorted and smaller crystals with the lowest yield strength. PPD A led to the formation of small and finely dispersed wax crystals. PPD B addition resulted in roundly shaped crystal clusters. Both PPD C and asphaltenes also showed the formation of more finely dispersed wax crystals. In case of PPD C, the CPM image appears to contradict yield strength measurements, since crystal dimensions were shown to be smaller than without additive. However, the crystal network appeared denser, which could explain that the resulting yield strength was higher. Asphaltene addition significantly lowered gel yield strength and the crystal network is also less dense than for PPD C.

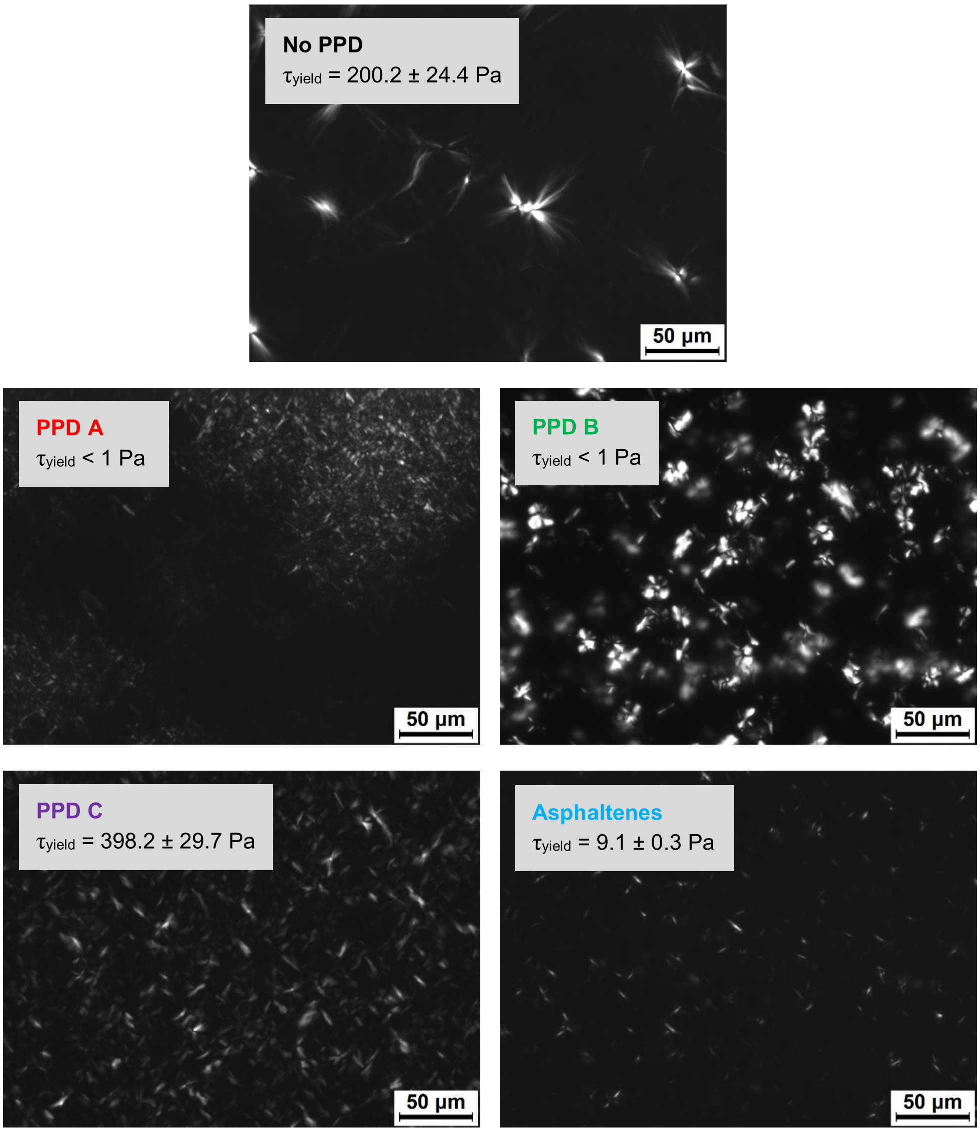

Fig. 9. CPM images of 1000 ppm PPD and 5 wt% macrocrystalline wax in toluene at -2 °C. The according gel yield strength as averaged over two to four rheometry experiments is shown as well.

Comparing the results of viscometry and gel yield strength, there appears to be a difference in additive effect depending on the shear conditions during wax crystallization. It has been pointed out by other authors that increased shearing can result in the reduction of gel yield strength due to the rupture of crystal-crystal linkages [13, 58]. As a result, at -2 °C both asphaltenes and no PPD show shear stresses that are approximately two orders of magnitude lower after continuous shearing than the yield stresses after quiescent cooling. Also, a significant improvement of flow-ability was made by addition of PPD C as shown in Fig. 8, whereas in Fig. 9 the gel yield strength was higher compared to the additive free case. Shearing therefore can improve the effect certain PPDs have on waxy gelation. All in all, the results are in agreement with other studies published on the effect of PPD or asphaltene on wax crystallization and gelling [30, 35, 47, 59-62]. Moreover, it can be concluded that PPD A and PPD B are efficient wax inhibitors for the waxy model oil. Asphaltenes also showed beneficial influence on wax crystallization, but PPD C exhibited poor wax inhibition efficiency for the tested system.

## 3.2. Inhibitor-wax interactions studied in liquid phase

### 3.2.1. Wax precipitation studied by NMR

The $T_2$-distributions from NMR measurements are displayed in Fig. 10 for qualitative comparison. Each sample produced a characteristic and reproducible distribution. The data is presented in raw form without correction for the temperature lag in the sample. Experiments with a monodisperse, non-crystallizing alkane (hexadecane) in deuterated toluene resulted in a single peak. This peak shifted towards shorter $T_2$ with decreasing temperature due to increasing viscosity, hence a reduction in diffusion coefficient and therefore $C_{16}$ mobility. Artifacts at $T_2$ of $10^{-3}$ s and shorter appear in all distributions, but are more pronounced when additives were added and after solid wax had formed.

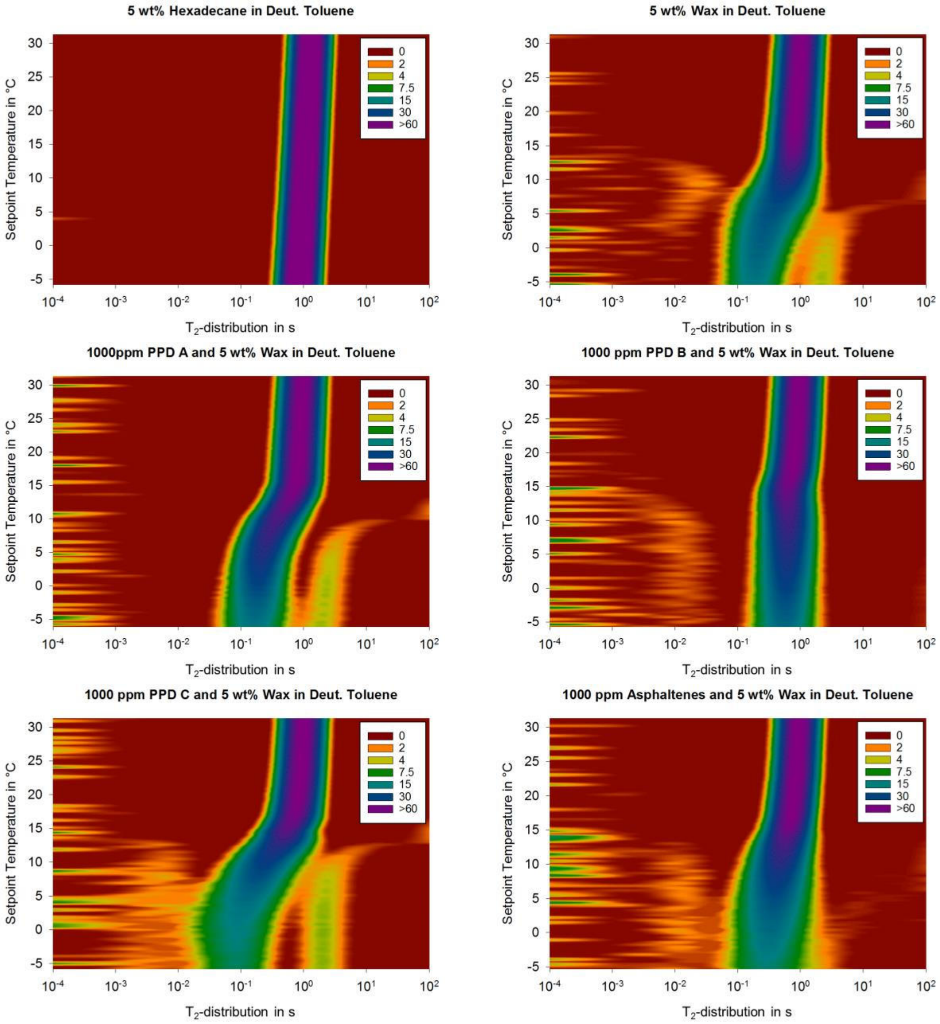

Fig. 10. NMR $T_2$-distribution in dependence of (uncorrected) setpoint temperature. Each measurement was made on 3 g solution of 5 wt% alkanes in deuterated toluene with and without 1000 ppm PPD.

Analogous to the hexadecane sample, the main peak in the $T_2$-distribution of 5 wt% wax in deuterated toluene shows a shift to lower $T_2$ with decreasing temperature. Below 15 °C setpoint temperature, wax crystallization is visible as broadening of the main peak and signal intensity decrease. This intensity decrease is due to the precipitation of dissolved wax molecules, which invokes $T_2$ decreases below $10^{-3}$ $s^{-1}$ for the affected molecules. In other words, the phase change is reflected by affecting the mobility of wax. Moreover, two secondary peaks can be observed. One secondary peak is at $T_2$ of $10^{-2}$ s and above, the other one appears at $10^0 – 10^1$ s.

Secondary peaks at shorter $T_2$ are the results of spatial hindrances imposed on the bulk fluid by particles in the dispersion [63]. The growing wax crystals therefore act to partially decrease liquid wax mobility. Such a decrease is the result of liquid wax molecules that are 'bond' by the proximity to solid wax crystals [64]. Interestingly, PPD A showed a suppression of the regarded peak. PPD C and asphaltenes resulted in an enhancement of the secondary peak at low $T_2$. Additives therefore appear to influence interactions at the solid-liquid interface and can possibly suppress intermediate states.

The secondary peak at long $T_2$ ($10^0 – 10^1$ $s^{-1}$) appears counterintuitive at first, but has been detected for the additive free sample, PPD A, and PPD C. An increase in liquid wax mobility is inconsistent with the idea of an imposing solid crystal structure. Moreover, no physical meaning can be attributed with $T_2$ larger than $10^1$ $s^{-1}$. The most likely explanation is that the inverse Laplace routine is splitting a single peak into two, as this routine is mathematically ill posed. Depending on the smoothing factor, the secondary peak with the longest $T_2$ was observed to change position and intensity. The secondary peak occurring at $T_2$ of approximately $10^{-2}$, however, was less or not at all affected by the smoothing factor, which indicates significands of this peak.

All in all, efficient additives (PPD A and PPD B) resulted in more defined states, whereas PPD C with poor inhibition performance led to a broadening of the $T_2$ distribution, which could indicate a blurring of the solid-liquid transition. A previous study reported similar results, i.e. a shift towards shorter $T_2$ with lower signal intensity during wax crystallization in deuterated solvent [46]. PPD additives were also found to delay wax crystallization and reduce the amount of apparent solid wax, but the occurrence of secondary peaks in $T_2$-distribution had not yet been considered.

### 3.2.2. Wax precipitation studied by GC/MS

Based on the results of previously discussed experiments, liquid phase sampling was conducted at 18 °C down to -2 °C in 4 °C intervals. The induced shear of the magnetic stirrer (850 RPM) was sufficiently large, so that the wax dispersion remained free flowing. Gelling could be observed close to surface level, but never in the bottom two thirds of the sample bulk. CPM was used to screen the filtration procedure at a sampling temperature of 6 °C. None of the tested samples showed solids remaining in the filtrate.

Fig. 11 shows the absolute concentration of *n*-alkanes from $C_{22}$ to $C_{40}$ of the additive free sample. As the temperature is cooled down, the liquid phase contains less *n*-alkanes. Data was reproducible within a certain margin of error. With decreasing sampling temperature, the carbon number of affected *n*-alkanes shifted from higher to lower molecular weight. The study of compositional change was limited to *n*-alkanes with carbon numbers of $C_{20}$ to $C_{40}$ for several reasons. Firstly, the largest change in concentration was observed for *n*-alkanes in the range of $C_{22}$ to $C_{40}$. Secondly, *n*-alkanes with a higher molecular weight than $C_{40}$ were excluded, as accurate quantification was made difficult by a low response of the MSD detector for high boiling point substances. Thirdly, quantification of *iso*-alkanes was not accurate enough. This was due to low intensity peaks with broad spanning elution times.

Moreover, the detector response could not be calibrated for *iso*-alkanes, due to a lack of structural information and hence an appropriate calibration standard.

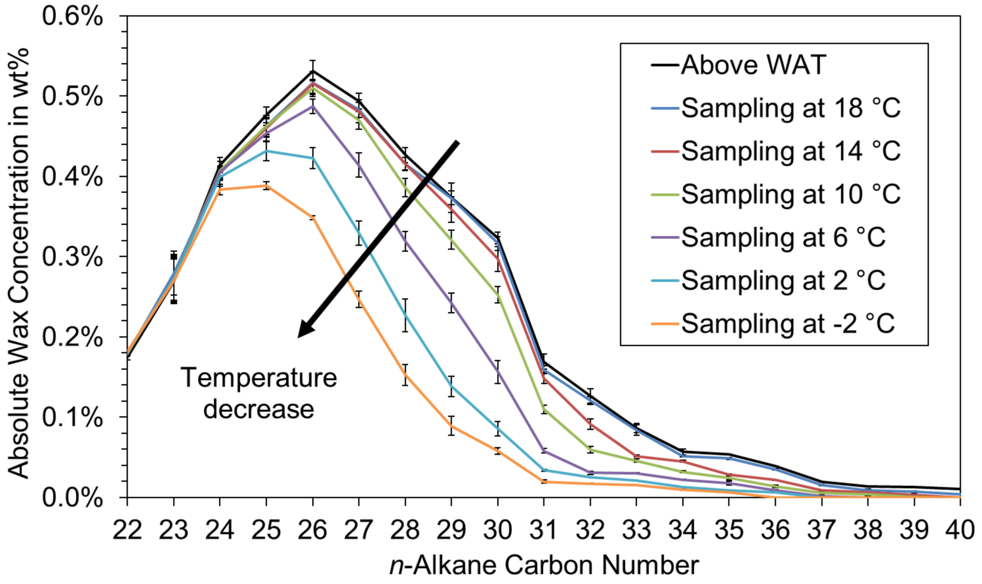

Fig. 11. Composition of *n*-alkanes between $C_{22}$ and $C_{40}$ for 5 wt% wax in toluene at different temperatures of sample taking. Error bars represent the standard deviation from the average of four measurements.

### 3.2.3. Liquid Phase Compositional Change

To compare the influence of different additives on wax crystallization, the change in composition was considered rather than absolute concentrations. An advantage is that this approach provides a more sensitive estimate of affected molecular weight regimes. A disadvantage is that subtracting two similar values amplifies the relative error. As a result, the compositional changes illustrated in Fig. 12 should be interpreted in terms of general trends, i.e. multiple component trends rather than individual concentration changes. Still, as can be seen in Fig. 11 the standard deviation of individual concentrations is significant for the majority of measurements. In particular, at sampling temperatures between 14 °C and -2 °C, almost all changes in concentration differ by a multiple of the respective standard deviation. The depicted trends are therefore statistically significant. The wax concentration decrease in Fig. 12 was calculated as difference of two subsequent measurements, i.e. the decrease at 14 °C yields the composition 18 °C minus the composition at 14 °C and so forth. All systems show similar trends, which followed three distinct steps:

| | |
|---|---|
| Step (i) | Right after wax crystallization onset, *n*-alkanes are depleted on a broad range of molecular weights (above WAT to 18 °C). |
| Step (ii) | As wax precipitation continues, the affected range of wax molecular weight is shifted to a narrower region of *n*-alkanes, which bears similarities to a Gaussian bell curve (18 °C to 10 °C). |
| Step (iii) | As sampling temperatures decreases even further, the bell-shaped curve is shifted to affect lower molecular weight *n*-alkanes (10 °C and below). This is due to depletion of higher molecular weight alkanes and due to temperature induced precipitation of lower molecular weight alkanes. |

The results are in agreement with the view that lower temperatures can induce wax crystallization of lower molecular weight alkanes, also. The addition of PPD A shows lower and narrower *n*-alkane decreases during step (i) and (ii). PPD B addition delayed step (i) down to 14 °C, which was observed for other samples until 18 °C only. The overall sum of component loss during step (i) appears to be the lowest for asphaltenes. However, higher molecular weight components are depleted to a larger extent between 14 °C and 2 °C than this is the case for other samples. This indicates that asphaltenes do not necessarily delay wax precipitation, but favor the depletion of low molecular weight components first. A similar observation was made by Chen et al. after addition of poly alkyl methcrylate or alkyl naphthalene copolymer [65]. In contrast to that, PPD A displays prolonged depletion of high molecular weight components. This can be seen e.g. in a lower decrease of $C_{36}$ to $C_{38}$ at 18 – 14 °C, but an above average decrease of these components at 10 °C and lower. For PPD A and PPD B, the general shape of the concentration decrease appears narrower at sampling temperatures of 6 °C and 2 °C than for PPD C.

In a previous study, Paso et al. published similar results on *n*-alkane depletion during wax crystallization [47]. Temperature decrease was also found to lead to the depletion of higher molecular weight alkanes during later stages of wax crystallization. However, depletion *n*-alkanes on a broad range of molecular weight (step (i)) was found to stretch over a larger temperature regime (up to 30 °C) than as the results in Fig. 12. Moreover, the current study showed *n*-alkane depletion to take place more progressively, i.e. less rapid changes in total wax content with decreasing temperature. Still, such phenomena are governed by the initial wax composition. The Fischer-Tropsch waxes used by Paso et al. had lower molecular weight and lower isomer content than the wax used in this study [47]. Also, the previous study featured equilibrated systems, whereas a constant cooling rate was applied in this study. The results were therefore not found to be contradicting.

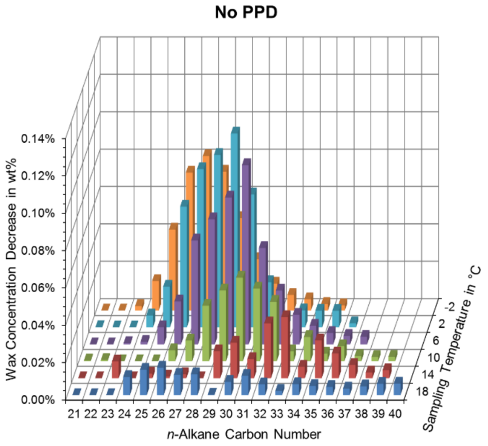
**No PPD**

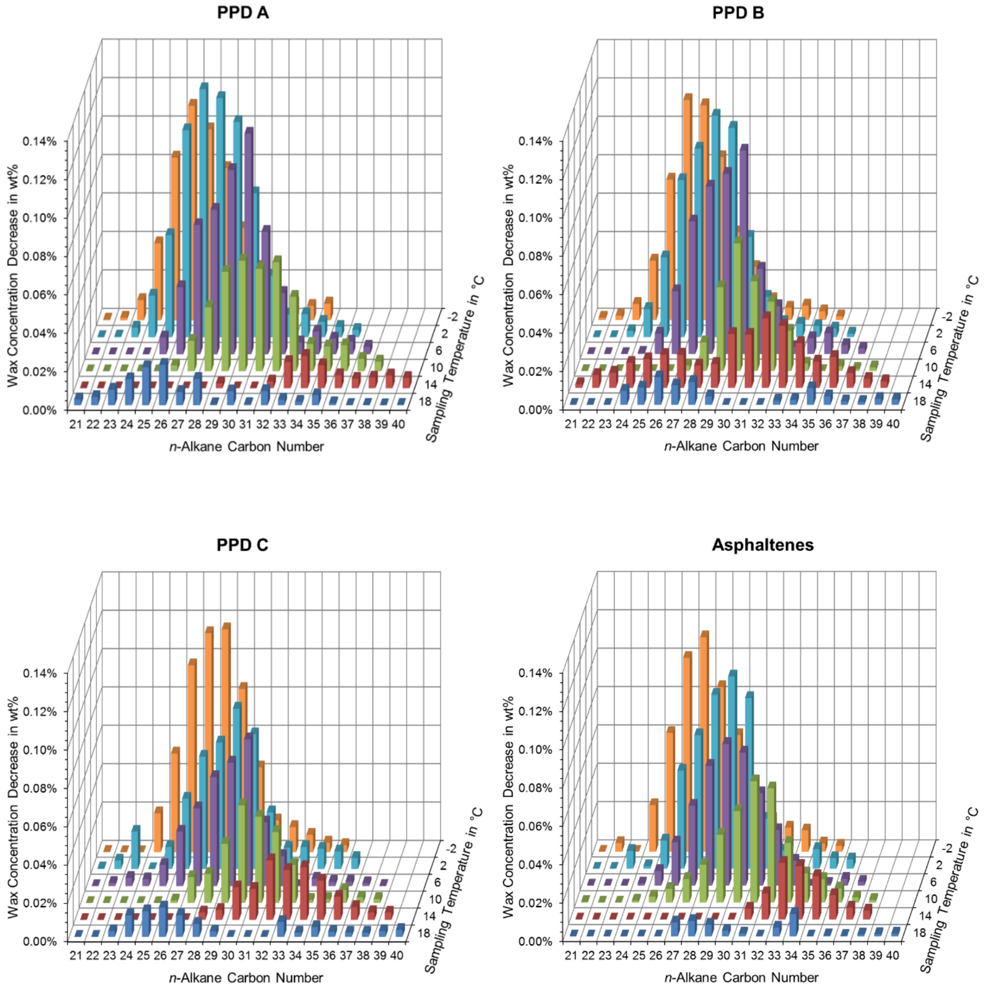

Fig. 12. Changes of *n*-alkane content in liquid phase as measured by GC/MS. Each sample consisted of 1000 ppm PPD or asphaltenes and 5 wt% wax in toluene. The wax concentration decrease was computed by subtracting each alkane concentration from the next higher temperature concentration.

## 3.3. Wax Precipitation Curve (WPC)

### 3.3.1. WPC measured by DSC

The data of Fig. 7 was converted into the WPC via the procedure described in section 2.3 and results are displayed Fig. 13. All PPDs induced temperature depression of the WPC, but not asphaltenes. For PPD A, the WPC depression is similar to translating the WPC of additive free experiments by 2 – 3 °C. In other words, the curves are almost parallel on the temperature interval between 15 °C and -5 °C. For PPD B there is approximately no reduction in precipitated wax until 15 °C. After that the WPC depression surpassed even PPD A. PPD C yielded notable reduction in precipitated wax only below 10 °C. The trends for WPD depression correspond with the order of polymer precipitation of Fig. 6, i.e. PPDs with a higher precipitation onset temperature also started to decrease the amount of precipitated wax in Fig. 13 at higher temperatures. Asphaltenes did not induce WPC depression that was statistically significant. The WPC curves of no PPD and asphaltenes are almost identical.

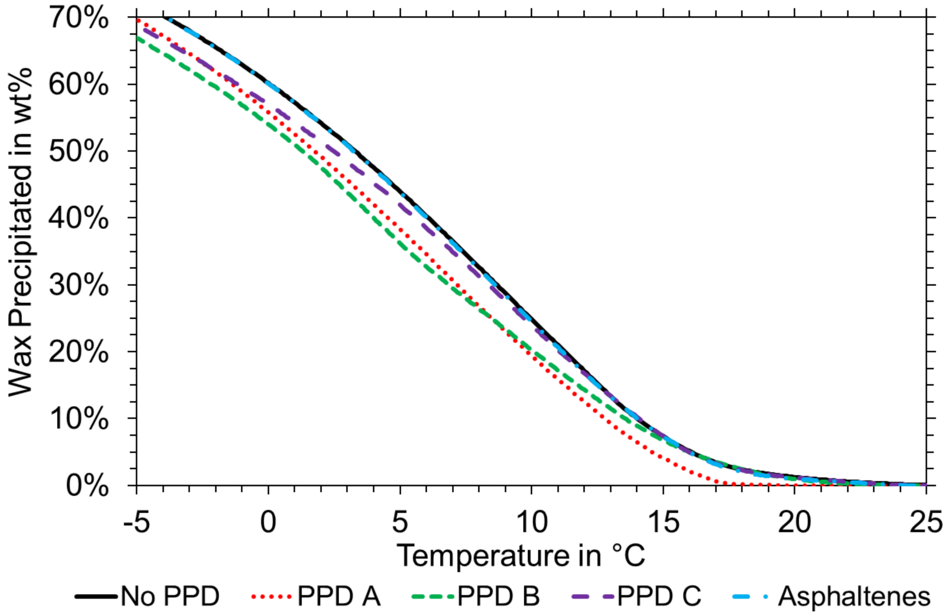

Fig. 13. DSC Wax precipitation curve (WPC) for 1000 ppm PPD or asphaltenes and 5 wt% wax in toluene. Percentages were calculated with respect to the total amount of precipitated wax. Lower temperatures were omitted from the plot for better overview.

### 3.3.2. WPC measured by NMR

The $T_2$-distributions in Fig. 10 were converted into WPCs via the in section 2.6 described procedure. As can be seen in Fig. 14, the apparent solid wax started increasing at approximately 25 °C for all samples except for the sample containing PPD A. As in DSC experiments, PPD A induced the largest crystallization lag. The WPC depression induced by PPD B starts to be statistically significant below 15 °C. On average, asphaltenes accounted for higher apparent solid wax than samples containing PPD A or PPD B. However, some differences can be notices for comparing WPC of NMR and DSC. In NMR, asphaltenes reduced the amount of precipitated wax in comparison to the additive free case, which was not the case in DSC. The presence of PPD C even increased the apparent solid wax in NMR. The amount of data scattering is largest for PPD C, which is due to the blurring of solid and liquid phase contributions in the $T_2$-distribution at around $10^{-3}$ s.

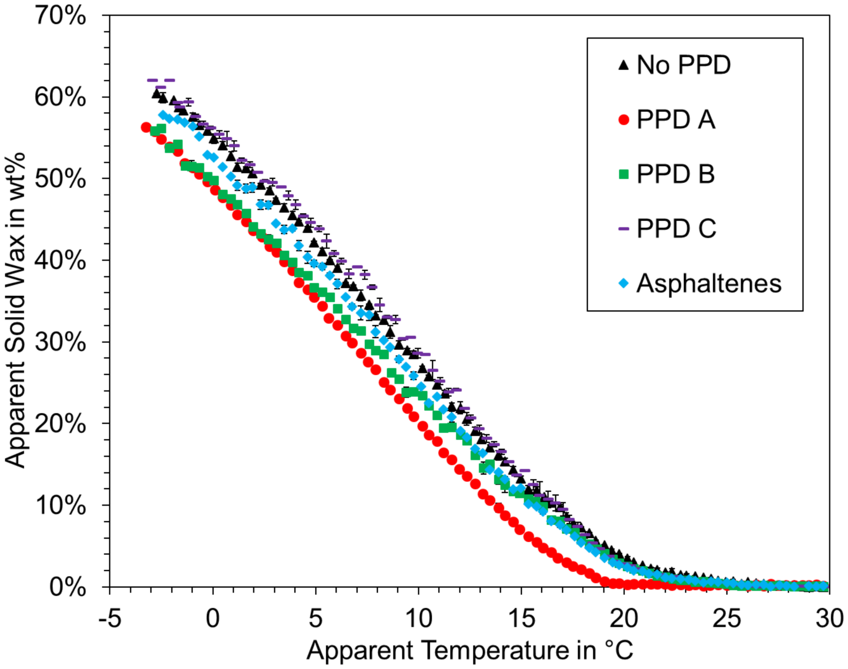

Fig. 14. Wax precipitation curve measured in NMR of 5 wt% wax in deuterated toluene with and without 1000 ppm PPD or asphaltenes. Graphs represent the average of two identical measurements with maximum and minimum as error bars.

### 3.3.3. *N*-alkane depletion measured by GC/MS

To approximate the WPC by given data from GC analysis, the relative decrease $p_{\%}$ in $C_{20}$ to $C_{40}$ *n*-alkane was computed. Following equation (8), this decrease was calculated as the sum of *n*-alkanes at a certain sampling temperature $c_i(T_{sample})$ divided by the sum of all measured *n*-alkanes $c_i(T_{above\ WAT})$. This percentage is only an approximation of the actual WPC, especially as not all precipitating components are included.

$$p_{\%}(T_{sample}) = 100\% - \frac{\sum_{i=20}^{40} c_i(T_{sample})}{\sum_{i=20}^{40} c_i(T_{above\ WAT})} \qquad (8)$$

As can be seen in Fig. 15, the *n*-alkane decrease increases for all samples as the sampling temperature is lowered. The relative error was computed according to the propagation of uncertainty, but is not visible in Fig. 15 due to low values. The depicted differences therefore carry a high statistical significance. For PPD C and asphaltenes, the *n*-alkane decrease is lower than the additive free sample at temperatures of 2 – 14 °C. For PPD A and PPD B, the relative decrease is higher than the additive free case at 6 °C and below. These results are counter intuitive due to a reversed trend as compared to WPCs obtained by DSC (Fig. 13) and NMR (Fig. 14). Since two other techniques show a lower total amount of precipitated wax with PPD A and PPD B, it appears that these additives promote precipitation of $C_{20}$ to $C_{40}$ *n*-alkanes over other components. Such an observation makes sense from the viewpoint that industrial PPDs, especially comb polymers, are often tailored to chemically match the wax molecules responsible for gelling [6, 34]. A possible explanation is therefore that PPD A and PPD B increase selectivity for precipitation of *n*-alkanes over *iso*-alkanes, which were quantified in DSC and NMR, but not in GC/MS. However, more data is needed to confirm this influence on selective wax precipitation.

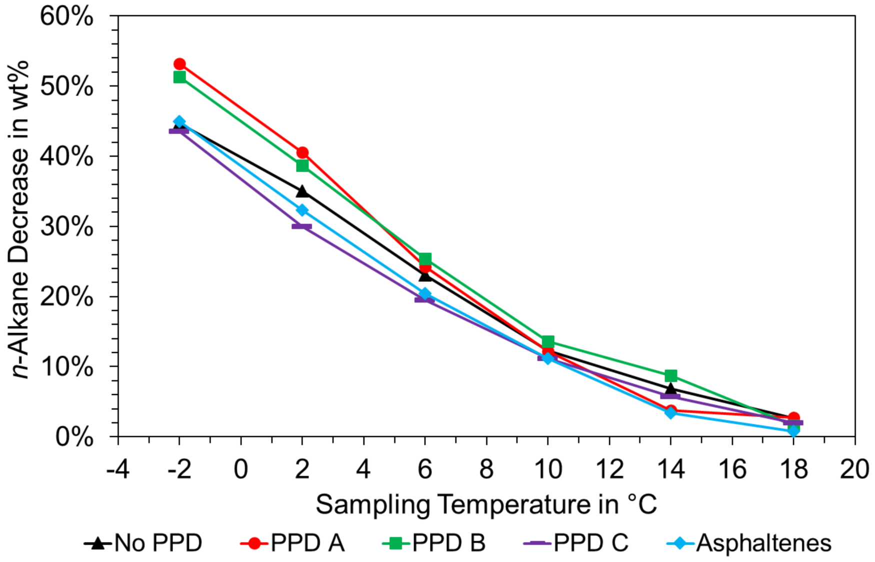

Fig. 15. Percentage of *n*-alkane decrease as measured by GC/MS.

### 3.3.4. Comparison

To compare the different techniques employed for WPC determination, results of DSC, NMR, and GC/MS are plotted together in Fig. 16. No PPD and PPD A were selected to represent the base case and one additive with strong effect on wax precipitation. As can be seen, the techniques do not superimpose, but the depicted tendencies are the same. Regarding GC/MS results, the graphs are naturally different from DSC and NMR, as only 84.6 wt% of the total wax was considered. NMR technique shows an earlier onset of wax precipitation than DSC for both samples. In fact, the $T_2$ in NMR is decreased by several orders of magnitudes, whereas the relative change in DSC heat flow is comparatively low when wax crystallizes, which implies that NMR could be more sensitive. The fact that DSC measured a higher solid wax content than NMR below 8 °C could be due to the temperature correction function, as this does not account for exothermic wax crystallization. On the other hand, WPC computation in DSC involved a polynomial baseline fitting to calculate the excess heat. This baseline might not fully represent the involved physics, as heat capacity changes as a function of the total solids content. Moreover, the difference in molecular weight of deuterated and non-deuterated toluene could influence solubility of the wax. Interestingly, the temperature lag induced by PPD A remains almost constant for both NMR and DSC results, which in turn suggests good comparability of these techniques.

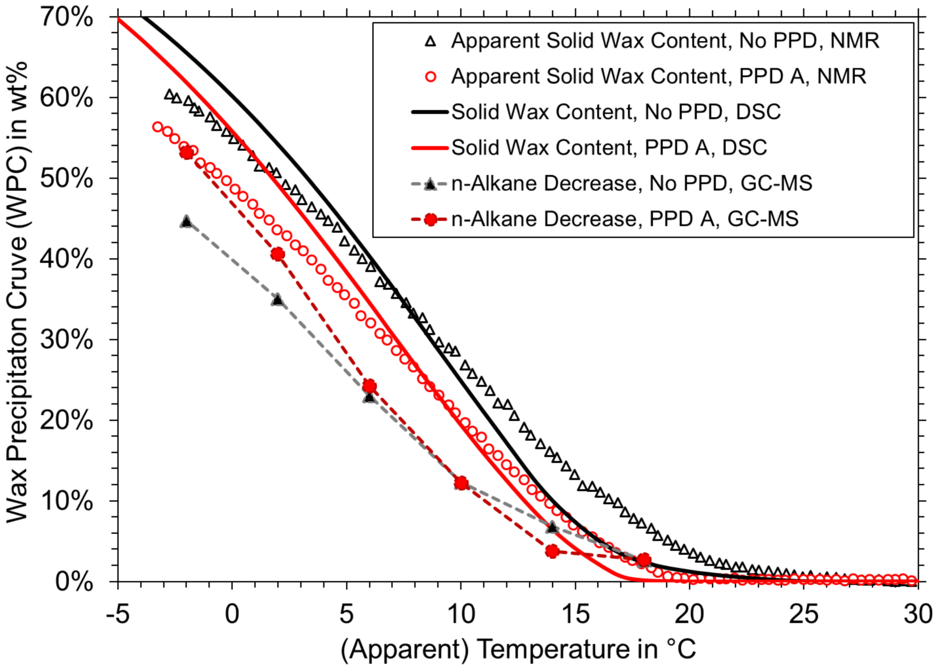

Fig. 16. Comparison of WPC determined by different techniques for samples of 5 wt% wax in toluene with and without 1000 ppm PPD A.

## 4. Conclusion

In this article, the effect of chemical additives on wax crystallization was studied in a waxy model system using both established techniques and new approaches. Firstly, additive efficiency was characterized by the use of DSC, rheometry, and CPM. Secondly, PPD-wax interactions in liquid phase were mapped via new approaches in NMR and GC/MS. In addition, a comparison of WPC among different techniques was made. Main results and conclusions are summarized below.

1. The chemical additives showed different effect on apparent viscosity, gel yield strength, and crystal morphology as determined by rheometry and CPM. Efficient wax inhibition was attributed with PPD A and PPD B, leading to a change in wax crystal morphology towards smaller and more compact crystals with lower propensity to overlap, which further reduced apparent viscosity of the waxy dispersion, and gel yield strength. Asphaltenes induced similar, but less pronounced effects, and PPD C could both improve as well as aggravate waxy oil flow-ability.
2. The $T_2$-distribution of NMR experiments indicated the formation of intermediate states during solid-liquid transition, where dissolved wax molecules displayed increased as well as reduced mobility. Most likely, these intermediate states represent dissolved wax 'bond' by the proximity to solid wax crystals [64]. Efficient inhibitors (PPD A and PPD B) could suppress certain states, whereas PPD C led to a blurring of the solid-liquid transition in the NMR $T_2$ distribution.
3. Following wax crystallization experiments with liquid phase extraction, GC/MS component analysis revealed *n*-alkane depletion to happen in three distinct steps. Wax precipitation started with the reduction of *n*-alkanes on a broad range of molecular weight (step i). At lower temperatures, the concentration decrease would affect narrower *n*-alkane regions (step ii),

which would decrease in average molecular weight at even lower temperatures (step iii). Chemical additives could affect compositional changes during wax crystallization and efficient inhibitors were shown to delay step i and step ii.

4. Both DSC and NMR showed delayed crystallization onset and a reduction in the amount of precipitated wax for efficient additives (PPD A and PPD B). Combining these techniques with results from GC/MS suggested that additives with efficient wax inhibition may at the same time increase selectivity for *n*-alkane precipitation. All in all, the different approaches for WPC determination did not superimpose, but general trends were similar.

In conclusion, new procedures for studying PPD-wax interactions by the use of NMR and GC/MS technique were presented. Testing shows potential for these to investigate wax inhibition phenomena more closely. Moreover, the link to additive characteristics with importance to flow assurance was made. Comparison indicated that additives with efficient wax inhibition as determined by DSC, CPM, and rheometry also showed characteristic behavior in NMR and GC/MS, such as the suppression of secondary $T_2$ peaks, delay of characteristic *n*-alkane decrease, and increased *n*-alkane selectivity.

## 5. Acknowledgements

This work was carried out as a part of SUBPRO, a Research-based Innovation Centre within Subsea Production and Processing. The authors gratefully acknowledge the financial support from SUBPRO, which is financed by the Research Council of Norway, major industry partners and NTNU.

## 6. Acronyms

CPM = cross-polarized microscopy

DSC = differential scanning calorimetry

EVA = ethylene vinyl-acetate copolymer

GC/MS = gas chromatography coupled mass spectrometry

HPLC = high-performance liquid chromatography

HVLP = high volume low pressure

MAC = poly(maleic anhydride amide co-a-olefin)

MSD = mass spectrometer detector

NMR = nuclear magnetic resonance

PPD = pour point depressant

PE = polyethylene

PE-PEP = polyethylene poly(ethylene-propylene)

PE-PEB = polyethylene poly(ethylene-butene)

PTFE = polytetrafluoroethylene

TIC = total ion chromatogram

TGA = thermogravimetric analyzer

WAT = wax appearance temperature

WPC = wax precipitation curve

## 7. References

1. Huang, Z., S. Zheng, and H.S. Fogler, *Wax Deposition: Experimental Characterizations, Theoretical Modeling, and Field Practices*. 2015, Boca Raton (FL), USA: CRC Press.
2. Kelland, M.A., *Wax (Paraffin) Control*, in *Production Chemicals for the Oil and Gas Industry*. 2009, CRC Press.
3. Venkatesan, R., *The deposition and rheology of organic gels*. 2004, University of Michigan.
4. Sarica, C. and M. Volk, *Tulsa University Paraffin Deposition Projects*. 2004, The University of Tulsa (US). p. 130.
5. Singh, P.V., Ramachandran; Fogler, H. Scott; Nagarajan, Nagi, *Formation and aging of incipient thin film wax-oil gels.* AIChE Journal 2000. **45**(5): p. 1059-1074.
6. Yang, F., et al., *Polymeric Wax Inhibitors and Pour Point Depressants for Waxy Crude Oils: A Critical Review.* Journal of Dispersion Science and Technology, 2015. **36**(2): p. 213-225.
7. Oschmann, H.-J., *Das Kristallisationsverhalten von Paraffinen in Abhängigkeit von ihrer Zusammensetzung sowie seine Beeinflussung durch Paraffininhibitoren*, in *Fakultät für Bergbau, Hüttenwesen und Maschinenwesen*. 1998, Technische Universität Clausthal: Papierflieger.
8. Machado, A.L.d.C. and E.F. Lucas, *Poly(Ethylene-co-Vinyl Acetate) (EVA) Copolymers as Modifiers of Oil Wax Crystallization.* Petroleum Science and Technology, 1999. **17**(9-10): p. 1029-1041.
9. Paso, K., et al., *Paraffin Polydispersity Facilitates Mechanical Gelation.* Industrial & Engineering Chemistry Research, 2005. **44**(18): p. 7242-7254.
10. Clarke, E.W., *Crystal Types of Pure Hydrocarbons in the Paraffin Wax Range.* Industrial & Engineering Chemistry, 1951. **43**(11): p. 2526-2535.
11. Kané, M., et al., *Morphology of paraffin crystals in waxy crude oils cooled in quiescent conditions and under flow.* Fuel, 2003. **82**(2): p. 127-135.
12. Paso, K.G., *Comprehensive treatise on shut-in and restart of waxy oil pipelines.* Journal of Dispersion Science and Technology, 2014. **35**(8): p. 1060-1085.
13. Venkatesan, R., et al., *The strength of paraffin gels formed under static and flow conditions.* Chemical Engineering Science, 2005. **60**(13): p. 3587-3598.
14. Zhao, Y., *Shut in and Restart of Waxy Crude Oil Pipelines: Gelation, Rheology Model Development, and Application of Polymer/Ionic Liquid Based Additive*. 2013, Norges teknisk-naturvitenskapelige universitet (NTNU): Tondheim, Norway.
15. Bai, Y. and Q. Bai, *Subsea engineering handbook*. 2012, Waltham (MA), USA: Gulf Professional Publishing (Elsevier).
16. *Standard Test Method for Pour Point of Petroleum Products*, in *D97*. 2017: ASTM International.
17. Wei, B., *Recent advances on mitigating wax problem using polymeric wax crystal modifier.* Journal of Petroleum Exploration and Production Technology, 2015. **5**(4): p. 391-401.
18. Claudy, P., et al., *Interactions between n-alkanes and cloud point-cold filter plugging point depressants in a diesel fuel. A thermodynamic study.* Fuel, 1993. **72**(6): p. 821-827.
19. Li, Y., et al., *Influence of Asphaltene Polarity on Crystallization and Gelation of Waxy Oils.* Energy & Fuels, 2018. **32**(2): p. 1491-1497.
20. Lei, Y., S. Han, and J. Zhang, *Effect of the dispersion degree of asphaltene on wax deposition in crude oil under static conditions.* Fuel Processing Technology, 2016. **146**: p. 20-28.
21. Alcazar-Vara, L.A., J.A. Garcia-Martinez, and E. Buenrostro-Gonzalez, *Effect of asphaltenes on equilibrium and rheological properties of waxy model systems.* Fuel, 2012. **93**: p. 200-212.
22. Tinsley, J.F., et al., *Waxy Gels with Asphaltenes 1: Characterization of Precipitation, Gelation, Yield Stress, and Morphology.* Energy & Fuels, 2009. **23**(4): p. 2056-2064.

23. Oliveira, G.E., et al., *The Effect of Asphaltenes, Naphthenic Acids, and Polymeric Inhibitors on the Pour Point of Paraffins Solutions.* Journal of Dispersion Science and Technology, 2007. **28**(3): p. 349-356.
24. Venkatesan, R., et al., *The Effect of Asphaltenes on the Gelation of Waxy Oils.* Energy & Fuels, 2003. **17**(6): p. 1630-1640.
25. Prahl, U., *Isolierung erdölstämmiger Pour Point Depressants und Untersuchung ihrer Wirkungsweise in paraffinhaltigen Fluiden*, in *Fakultät für Bergbau, Hüttenwesen und Maschinenwesen*. 2001, Technische Universität Clausthal: Papierflieger.
26. Ariza-León, E., D.-R. Molina-Velasco, and A. Chaves-Guerrero, *Review of Studies on Asphaltene - Wax Interaction and the Effect thereof on Crystallization.* CT&F - Ciencia, Tecnología y Futuro, 2014. **5**: p. 39-53.
27. Kriz, P. and S.I. Andersen, *Effect of Asphaltenes on Crude Oil Wax Crystallization.* Energy & Fuels, 2005. **19**(3): p. 948-953.
28. Smith, P.B. and R.M.J. Ramsden, *The Prediction Of Oil Gelation In Submarine Pipelines And The Pressure Required For Restarting Flow*, in *SPE European Petroleum Conference*. 1978, Society of Petroleum Engineers: London, United Kingdom.
29. Kurniawan, M., et al., *Influence of Microcrystalline Wax on the Properties of Model Wax-Oil Gels.* Energy & Fuels, 2018. **32**(5): p. 5857-5867.
30. Tinsley, J.F., et al., *Waxy Gels with Asphaltenes 2: Use of Wax Control Polymers.* Energy & Fuels, 2009. **23**(4): p. 2065-2074.
31. Guo, X., et al., *Effect of Cooling Rate on Crystallization of Model Waxy Oils with Microcrystalline Poly(ethylene butene).* Energy & Fuels, 2006. **20**(1): p. 250-256.
32. Schwahn, D., et al., *Self-Assembling Behavior in Decane Solution of Potential Wax Crystal Nucleators Based on Poly(co-olefins).* Macromolecules, 2002. **35**(3): p. 861-870.
33. Machado, A.L.C. and E.F. Lucas, *Influence of ethylene-co-vinyl acetate copolymers on the flow properties of wax synthetic systems.* Journal of Applied Polymer Science, 2002. **85**(6): p. 1337-1348.
34. Chen, Z., et al., *A Study on the Interaction of Crude Oil Waxes With Polyacrylate Pour Point Depressants by Monte Carlo Simulation.* Petroleum Science and Technology, 2014. **32**(17): p. 2151-2157.
35. Wu, Y., et al., *Modified Maleic Anhydride Co-polymers as Pour-Point Depressants and Their Effects on Waxy Crude Oil Rheology.* Energy & Fuels, 2012. **26**(2): p. 995-1001.
36. Li, L., et al., *Improvement of oil flowability by assembly of comb-type copolymers with paraffin and asphaltene.* AIChE Journal, 2012. **58**(7): p. 2254-2261.
37. Wu, C., et al., *Molecular dynamics simulation guiding the improvement of EVA-type pour point depressant.* Fuel, 2005. **84**(16): p. 2039-2047.
38. Zhao, Z., et al., *A new kind of nanohybrid poly(tetradecyl methyl-acrylate)-graphene oxide as pour point depressant to evaluate the cold flow properties and exhaust gas emissions of diesel fuels.* Fuel, 2018. **216**: p. 818-825.
39. Yao, B., et al., *Performance improvement of the ethylene-vinyl acetate copolymer (EVA) pour point depressant by small dosage of the amino-functionalized polymethylsilsesquioxane (PAMSQ) microsphere.* Fuel, 2018. **220**: p. 167-176.
40. Jing, G., et al., *Influence of Different Vinyl Acetate Contents on the Properties of the Copolymer of Ethylene and Vinyl Acetate/Modified Nano-SiO2 Composite Pour-Point Depressant.* Energy & Fuels, 2017. **31**(6): p. 5854-5859.
41. Yao, B., et al., *Organically modified nano-clay facilitates pour point depressing activity of polyoctadecylacrylate.* Fuel, 2016. **166**: p. 96-105.
42. Song, X., et al., *Effect of SiO2 Nanoparticles on Wax Crystallization and Flow Behavior of Model Crude Oil.* Industrial & Engineering Chemistry Research, 2016. **55**(23): p. 6563-6568.
43. Norrman, J., et al., *Nanoparticles for Waxy Crudes: Effect of Polymer Coverage and the Effect on Wax Crystallization.* Energy & Fuels, 2016. **30**(6): p. 5108-5114.

44. Yang, F., et al., *Hydrophilic nanoparticles facilitate wax inhibition.* Energy & Fuels, 2015. **29**(3): p. 1368-1374.

45. Zhang, D., et al., *Application of Nano-Material Based Hybrid Pour-Point Depressant for Long-Distance Waxy Crude Pipeline.* 2012(45127): p. 459-466.

46. Zhao, Y., et al., *Utilization of DSC, NIR, and NMR for wax appearance temperature and chemical additive performance characterization.* Journal of Thermal Analysis and Calorimetry, 2015. **120**(2): p. 1427-1433.

47. Paso, K.G., et al., *PPD architecture development via polymer–crystal interaction assessment.* Journal of Petroleum Science and Engineering, 2014. **115**: p. 38-49.

48. Subramanian, S., et al., *Asphaltene fractionation based on adsorption onto calcium carbonate: Part 2. Self-association and aggregation properties.* Colloids and Surfaces A: Physicochemical and Engineering Aspects, 2017. **514**: p. 79-90.

49. Pinto, F.E., et al., *Fractionation of asphaltenes in n-hexane and on adsorption onto CaCO3 and characterization by ESI(+)FT-ICR MS: Part I.* Fuel, 2017. **210**: p. 790-802.

50. Subramanian, S., et al., *Asphaltene fractionation based on adsorption onto calcium carbonate: Part 1. Characterization of sub-fractions and QCM-D measurements.* Colloids and Surfaces A: Physicochemical and Engineering Aspects, 2016. **495**: p. 136-148.

51. Ruwoldt, J., M. Kurniawan, and H.-J. Oschmann, *Non-linear dependency of wax appearance temperature on cooling rate.* Journal of Petroleum Science and Engineering, 2018. **165**: p. 114-126.

52. Coto, B., et al., *Analysis of paraffin precipitation from petroleum mixtures by means of DSC: Iterative procedure considering solid–liquid equilibrium equations.* Fuel, 2010. **89**(5): p. 1087-1094.

53. Kruka, V.R., E.R. Cadena, and T.E. Long, *Cloud-Point Determination for Crude Oils.* Journal of Petroleum Technology, 1995. **47**(08): p. 681-687.

54. Roenningsen, H.P., et al., *Wax precipitation from North Sea crude oils: 1. Crystallization and dissolution temperatures, and Newtonian and non-Newtonian flow properties.* Energy & Fuels, 1991. **5**(6): p. 895-908.

55. Meiboom, S. and D. Gill, *Modified Spin-Echo Method for Measuring Nuclear Relaxation Times.* Review of Scientific Instruments, 1958. **29**(8): p. 688-691.

56. Provencher, S.W., *A constrained regularization method for inverting data represented by linear algebraic or integral equations.* Computer Physics Communications, 1982. **27**(3): p. 213-227.

57. Slichter, C.P., *Principles of magnetic resonance*. Vol. 1. 2013, Springer-Verlag Berlin Heidelberg: Springer Science & Business Media.

58. Zhao, Y., et al., *Gelation and Breakage Behavior of Model Wax–Oil Systems: Rheological Properties and Model Development.* Industrial & Engineering Chemistry Research, 2012. **51**(23): p. 8123-8133.

59. Ruwoldt, J., et al., *Asphaltene fractionation based on adsorption onto calcium carbonate: Part 3. Effect of asphaltenes on wax crystallization.* Colloids and Surfaces A: Physicochemical and Engineering Aspects, 2018. **554**: p. 129-141.

60. Jung, T., J.-N. Kim, and S.-P. Kang, *Influence of polymeric additives on paraffin wax crystallization in model oils.* Korean Journal of Chemical Engineering, 2016. **33**(6): p. 1813-1822.

61. Yi, S. and J. Zhang, *Relationship between Waxy Crude Oil Composition and Change in the Morphology and Structure of Wax Crystals Induced by Pour-Point-Depressant Beneficiation.* Energy & Fuels, 2011. **25**(4): p. 1686-1696.

62. Pedersen, K.S. and H.P. Rønningsen, *Influence of Wax Inhibitors on Wax Appearance Temperature, Pour Point, and Viscosity of Waxy Crude Oils.* Energy & Fuels, 2003. **17**(2): p. 321-328.

63. Jestin, J. and L. Barré, *Application of NMR Solvent Relaxation and SAXS to Asphaltenes Solutions Characterization.* Journal of Dispersion Science and Technology, 2004. **25**(3): p. 341-347.
64. Duval, F.P., et al., *An NMR Investigation of Water Self-Diffusion and Relaxation Rates in Controlled Ionic Strength Laponite Sols and Gels.* Journal of Colloid and Interface Science, 2001. **242**(2): p. 319-326.
65. Chen, W., Z. Zhao, and C. Yin, *The interaction of waxes with pour point depressants.* Fuel, 2010. **89**(5): p. 1127-1132.

# Publication V

## Influence of Wax Inhibitor Molecular Weight: Part 1. Fractionation and Effect on Crystallization of Polydisperse Waxes.

# Publication VI

## Asphaltene fractionation based on adsorption onto calcium carbonate: Part 3. Effect of asphaltenes on wax crystallization

Colloids and Surfaces A 554 (2018) 129–141

Contents lists available at ScienceDirect

Colloids and Surfaces A

journal homepage: www.elsevier.com/locate/colsurfa

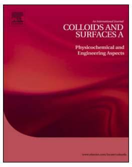

# Asphaltene fractionation based on adsorption onto calcium carbonate: Part 3. Effect of asphaltenes on wax crystallization

Jost Ruwoldt*, Sreedhar Subramanian, Sébastien Simon, HansJörg Oschmann, Johan Sjöblom

*Ugelstad Laboratory, Department of Chemical Engineering, NTNU, N-7491 Trondheim, Norway*

## GRAPHICAL ABSTRACT

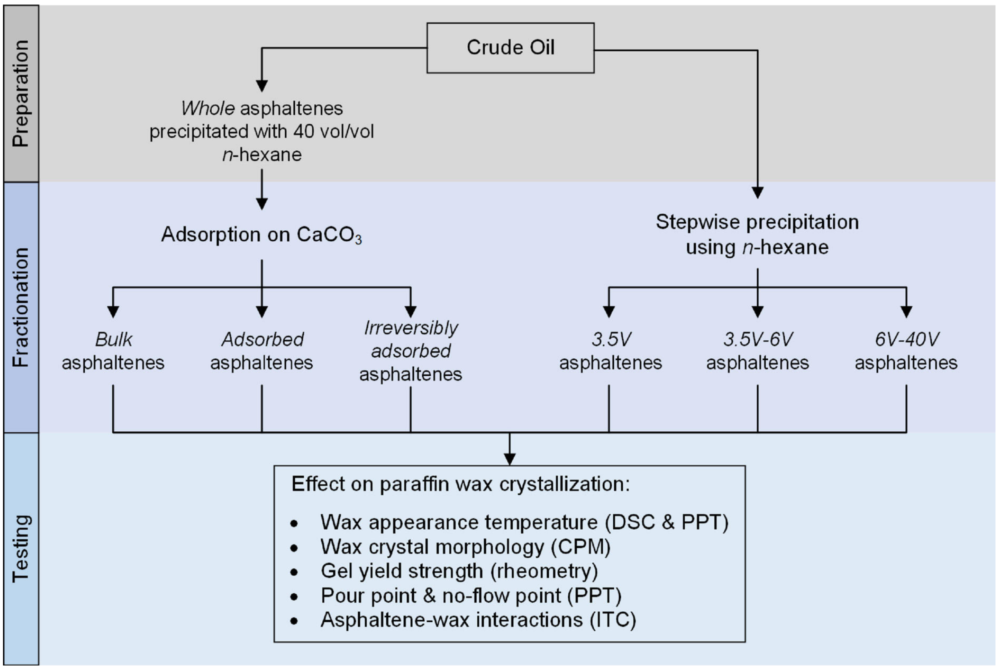

## ARTICLE INFO

*Keywords:*
Asphaltene fractionation

## ABSTRACT

Asphaltenes fractionation procedures were developed and tested in two preceding articles (doi: https://doi.org/10.1016/j.colsurfa.2016.02.011, doi: https://doi.org/10.1016/j.colsurfa.2016.11.035), and asphaltene fractions

---

*Abbreviations:* CPM, cross-polarized microscopy; DCM, dichloromethane; DSC, differential scanning calorimetry; FTIR, Fourier-transformed infrared spectrometry; ITC, isothermal titration calorimetry; MAC, maleic anhydride co-polymer; NIR, near-infrared spectroscopy; PEB, poly(ethylene-butene); PPD, pour point depressant; PPT, pour point tester; QCM, quartz crystal microbalance; THF, tetrahydrofuran; WAT, wax appearance temperature; WI, wax inhibitor

* Corresponding author.

*E-mail address:* jost.ruwoldt@ntnu.no (J. Ruwoldt).

https://doi.org/10.1016/j.colsurfa.2018.06.025
Received 19 April 2018; Received in revised form 28 May 2018; Accepted 8 June 2018

Paraffin wax
Wax crystallization
Isothermal titration calorimetry (ITC)
Cross polarized microscopy (CPM)
Differential scanning calorimetry (DSC)

were characterized in terms of composition, adsorption and self-aggregation properties. In this article, the effect of asphaltene fraction on wax crystallization was studied. Asphaltene fractionation on calcium carbonate was developed further to a column separation procedure, which yielded asphaltene fractions with even larger differences according to FTIR analysis. Wax crystallization was studied using differential scanning calorimetry (DSC), cross-polarized microscopy (CPM), rheometry, and pour point tests (PPT). Asphaltenes were found to change wax crystal morphology and decrease gel yield strength with increasing concentration. The effect on wax appearance temperature (WAT) was generally less. The greatest effect on WAT and pour point was made by *bulk* asphaltenes, which is the lowest polarity fraction from separation on calcium carbonate. *Irreversibly adsorbed* asphaltenes, containing significant amounts of carbonyl, carboxylic or derivative groups, induced the largest changes in wax crystal morphology. Still, high pour point and gel yield strength indicated low performance for this fraction. Overall, wax inhibition performance tended to be best for asphaltene fractions with low solubility and mixed functional groups. In isothermal titration calorimetry (ITC), unfractionated *whole* asphaltenes interacted more strongly with crystallized wax than asphaltene fractions *bulk* and *irreversibly adsorbed*. The findings indicate that wax crystallization is influenced the most by an ensemble of asphaltenes with different functional groups, rather than groups with more distinct properties.

## 1. Introduction

Current trends in crude oil production are towards higher depths, harsher environments, and increased field complexity. These trends can aggravate flow assurance challenges imposed by paraffin wax in the crude oil. Crystallized wax can cause issues both downhole and topside, which include flow reduction or plugging due to wax deposition, increased fluid viscosity, and restartability issues because of the formation of high strength waxoil gels [1]. Different thermal, mechanical, and chemical methods are usually taken for wax control, in particular the use of chemical additives such as wax inhibitors (WI) and pour point depressants (PPD) [2,3]. As new PPDs, the use of fractionated asphaltenes has been suggested [4]. A positive influence on gelation and gel yield strength of waxy crude oils has been attributed to asphaltenes [4–6]. Moreover, several patents exist for the use of asphaltenes as pour point depressants for shale oil [7–9]. In two preceding publications, asphaltenes were fractionated via newly developed procedures that involved asphaltene adsorption on calcium carbonate, as well as stepwise precipitation from bulk [10,11]. This article is a continuation of previous work, where the fractionation on calcium carbonate was developed further to a column separation procedure that yields asphaltene fractions with even larger property differences. The primary objective was to study the influence of various asphaltene fractions on a model waxy oil. This allows cross referencing of asphaltene properties from current and previous characterizations with their effect on wax crystallization. The goal is to determine which asphaltene characteristics are most crucial during wax crystallization, and hence improve the understanding of asphaltene-wax interactions.

Paraffin wax is a natural constituent of crude oil, which is defined as mostly straight, ring formed, and branched alkanes with 18 or more carbon atoms [1]. Wax crystallization is reported to take place in three steps, which are (i) nucleation, (ii) growth, and (iii) agglomeration [12]. The wax appearance temperature (WAT) is defined as the highest temperature, at which the crystallization of wax can be observed [13]. As the wax crystals grow in size, three dimensional interlocking of the crystals facilitates the formation of a solid like gel [14]. Paraffin wax crystals formed in organic solvents can exhibit plate shapes, needle shapes, and malcrystalline or dendrite like masses [15,16]. The waxes can be grouped into macrocrystalline and microcrystalline waxes, depending on the crystal shape [17]. Macrocrystalline wax has been reported to largely consist of low molecular weight *n*-alkanes that form predominantly plate shaped crystals with large hydrodynamic radii. Microcrystalline wax is considered to contain significant amounts of high molecular weight *iso*-alkanes and *cyclo*alkanes, leading to compact and round crystal morphologies with smaller diameters. As a consequence, macrocrystalline wax generally leads to the formation of strong gels, whereas microcrystalline wax accounts for in comparison weak gels [18].

The temperature at which a liquid loses its ability to freely flow due increasing amounts of precipitated wax is referred to as pour point, as defined by ATSM D97 [19]. A pour point depressant (PPD) consequently refers to chemical additives, which can decrease the pour point. The term wax inhibitor (WI) will be used in a more general context in this study. It refers to chemical additives that can alleviate challenges associated with paraffin wax crystallization via one or more functionalities. PPDs function as crystal modifying substances through coprecipitation with the wax [20–22]. PPD polymers provide spatial hindrances during continued crystals growth, leading to the formation of distorted and more compact crystal shapes with lower hydrodynamic radius. This can further result in particle dispersions with lower viscosity, waxoil gels of lower yield strength, and prevention or delay of the formation of a solid like gel, a process also referred to as pour point depression. Asphaltenes have been noted to predominantly interact with the more polar or aromatic groups of a PPD [17]. In waxy crude oils, the presence of asphaltenes has been reported to enhance as well as diminish the effect of WIs and PPDs [23,24]. For example, synergistic effects between asphaltenes and maleic anhydride co-polymers (MAC) as well as ethylenevinyl acetate copolymer (EVA) have been reported [25–27].

Asphaltenes have been reported to be natural PPDs by many authors [5,6,23,25–34]. Still, the effect of asphaltenes has been discussed contradictorily [35]. Some authors state no synergistic interactions between wax and asphaltenes [36], and other authors report asphaltenes aggravating issues associated with paraffin wax [24,37]. Asphaltenes are defined via solvent properties, being insoluble in low molecular weight *n*-alkane solvents [38]. Due to this definition, asphaltenes can have greatly varying composition and properties depending on the crude oil of origin, which would in turn account for the contradicting reports. However, most reports agree on the following effects that asphaltenes can have on paraffin wax crystallization:

1 Asphaltenes can serve as nucleation sites for wax crystals, which can increase WAT [37], but also lead to more finely dispersed wax crystals [6,23].
2 Asphaltenes can cocrystallize with wax, which can alter crystal morphology and improve crude oil rheology [6,29,35,39].
3 It is mainly the aliphatic part of asphaltenes, which interacts with paraffin wax [29,39,40].
4 The dispersion degree of asphaltenes plays a crucial role during wax crystallization [5,30,31].

Several authors have investigated the effect of asphaltene properties on wax crystallization by using either asphaltenes originating from different crude oils [24,29] or fractionated asphaltenes [4,6,34]. In two of these cases, asphaltene fractionation has been conducted by dissolving asphaltenes in dichloromethane (DCM) and inducing stepwise precipitation with pentane [34,41]. In one case, asphaltenes were fractionated on silica gel and via reverse phase chromatography [4].

The authors concluded that low polarity asphaltenes and the abundance of alkyl chains accounted for better pour point depression [4,6,29,34]. High polarity asphaltenes were reported to have less of an effect on wax crystallization.

## 2. Experimental section

### 2.1. Materials

An additive free crude oil from the Norwegian continental shelf was used for asphaltene precipitation, which is identical to the crude oil used in the two preceding studies [10,11]. Macrocrystalline wax was acquired as 5405 Sasolwax from Sasol, Germany. Composition and properties of the wax can be found in literature [42]. Solvents for model oil systems were obtained as xylene isomer blend (VWR, ≥98.5%, reagent grade) and *p*-xylene (Sigmaaldrich, 99%, ReagentPlus®). Asphaltenes were extracted with *n*hexane (VWR, ≥97%, HPLCgrade). Asphaltene fractionation was performed with precipitated calcium carbonate (Speciality Minerals Inc., USA), chloroform (VWR, 99.0–99.4%, analytical reagent), toluene (Sigmaaldrich, 99.8%, anhydrous), dichloromethane (DCM) (Sigmaaldrich, 99.8%, anhydrous, 40–150 ppm amylene as stabilizer), hydrochloric acid (Merck, 37%), and milli-Q water.

### 2.2. Sample preparation

Solutions containing paraffin wax, also referred to as waxy model oils or model system, were prepared by first weighing the solid(s), and then adding the required amount of liquid solvent. After preparation, the solution was heated to at least 20 °C above WAT for at least 30 min prior to use, to ensure complete dissolution of all solids. Samples containing asphaltenes were sonicated for at least 30 min before use. Crude oil was heated at 60 °C for 1 h, and shaken thoroughly before sampling to ensure homogeneity of the sample.

### 2.3. Asphaltene extraction

Asphaltenes, termed *whole* asphaltenes, were obtained by mixing the crude oil with 40 vol/g *n*-hexane and stirring for at least 24 h at ambient conditions. The resulting mixture was filtered with 0.45 *μ*m HVLP-type Millipore filter membrane and the filter cake was rinsed with *n*-hexane until the filtrate was entirely clear. Filter plus *whole* asphaltenes were then dried under nitrogen atmosphere for at least 24 h. The final yield accounted for 2.5 ± 0.1 wt% of the original crude oil.

### 2.4. Asphaltene fractionation

#### 2.4.1. Fractionation based on bulk precipitation

The detailed procedure for asphaltene fractionation via bulk precipitation is described in a preceding publication [11]. In short, *n*hexane was added to crude oil in three steps, following a dilution of 3.5, 6, and 40 volumes of *n*-hexane per gram crude oil. After each step, asphaltenes were recovered via filtration with a 0.45 *μ*m Millipore filter. The filtrate was washed with 50 ml *n*-hexane and dried under nitrogen atmosphere. The fractions *3.5 V*, *3.5–6 V*, and *6–40 V* asphaltenes were obtained by this procedure, where the prefix refers to the dilution ratio of crude oil with *n*-hexane in vol/g.

#### 2.4.2. Fractionation based on adsorption on calcium carbonate

The fractionation on calcium carbonate was based on the previous work done by Subramanian et al. [10]. Minor adjustments to the fractionation procedure were made by using a fixed bed column, and using chloroform instead of tetrahydrofuran (THF) to obtain *adsorbed* asphaltenes. The reason for a change in solvent was that retention times were considerably higher using a column than the original batch procedure, and THF was found to oxidize the asphaltenes after long exposure.

A flow diagram of the column separation procedure is shown in Fig. 1. Asphaltene solution was prepared as 4 g/l *whole* asphaltenes in toluene. The solution was sonicated for 30 min and then stirred overnight. The next day, the asphaltene solution was filtered through a

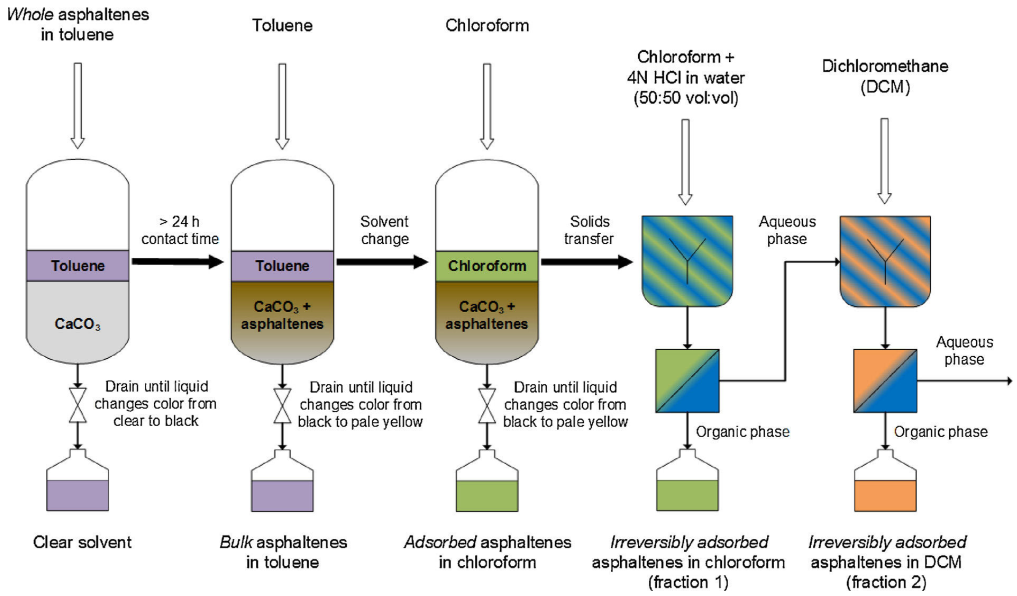

**Fig. 1.** Flow diagram of asphaltene fractionation of calcium carbonate.

0.45 µm HVLP filter before transferring it to the packed bed column consisting of calcium carbonate (mean particle size = 0.7 µm, BET area = 14.7 $m^2$/ mg). A ratio of at least 130 g/g calcium carbonate per *whole* asphaltenes was used to provide sufficient surface area for adsorption.

The asphaltene solution was allowed to flow through the column, and dropwise eluted by using a drain valve, thereby allowing sufficient time for contact between the asphaltenes and the calcium carbonate packing. Fresh toluene was added to the column at periodic intervals to ensure that the column did not become dry. Once the solvent drained at the bottom of the column changed color from black to pale yellow as shown in Fig. 2, the end of the first elution step was marked. All asphaltene in toluene solution collected until this point was labelled as bulk asphaltene solution. In the next stage, chloroform was used as the solvent for extraction of asphaltenes from the packed column. The same procedure as for *bulk* asphaltenes was repeated. The column was replenished with chloroform and drained at the bottom until the drained solvent color again changed from black to pale yellow. The collected asphaltene solution in chloroform is labelled as *adsorbed* asphaltene solution. The remaining asphaltenes present in the column were extracted by dissolving it in an equivolume mixture of chloroform and 4 N HCl solution. The organic and aqueous phases were separated. The organic layer containing asphaltenes was thus labelled *irreversibly-adsorbed* asphaltenes (fraction 1). Some asphaltenes were found to remain in the aqueous layer, and this was further extracted using DCM. This fraction was labelled as irreversibly adsorbed asphaltenes (fraction 2). Fraction 1 and fraction 2 of *irreversibly adsorbed* asphaltenes were treated individually during characterization, but mixed together as one fraction to study the effect on wax crystallization. All asphaltene solutions were filtered separately using a 0.45 µm filter, before being concentrated in a rotary evaporator followed by drying under nitrogen stream at up to 70 °C using a block heater (Grant UBR).

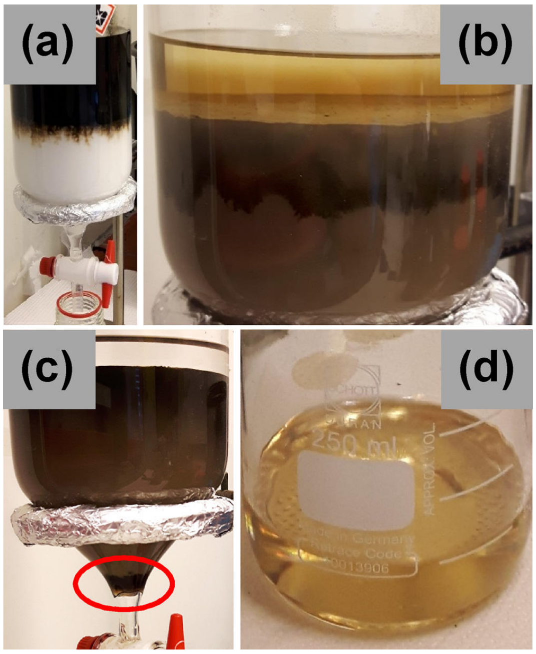

**Fig. 2.** Asphaltene fractionation on calcium carbonate: (a) Introduction of whole asphaltenes in toluene onto the column, (b) column during the elution with chloroform, (c) column after removal of adsorbed asphaltenes (contrast and brightness adjusted), where the glass wool is encircled in red, and (d) pale yellow eluate that marks the end of an elution step (For interpretation of the references to colour in this figure legend, the reader is referred to the web version of this article).

### 2.4.3. Asphaltene characteristics

Extensive characterization of asphaltenes fractionated by both adsorption on calcium carbonate and bulk precipitation has been performed earlier [10,11]. These characterization techniques include the use of elementary analysis, Fourier-transformed infrared spectrometry (FTIR), precipitation onset measured with near-infrared spectroscopy (NIR), adsorption on stainless steel via quartz crystal microbalance (QCM), and self-association in isothermal titration calorimetry (ITC). Among the bulk precipitated asphaltene fractions, the *asphaltene 3.5 V* sub-fraction was found to contain higher amount of oxygen compared to fractions *3.5 V–6 V* and *6 V–40 V* [11]. Other properties of asphaltene sub-fractions described in previous work include higher self-association (ITC, NMR) and lower solubility characteristics (NIR) among *irreversibly-adsorbed* asphaltenes, along with a significantly higher ability to adsorb on stainless steel [10,11]. Extended work on the more detailed composition of all sub fractions was also done based on NMR and mass spectrometry techniques [43].

In this work, elemental composition (C, H, N, O, S) and metal content (Fe, Ni, V, Ca, Na, K) for the asphaltene subfractions obtained from the modified column method described in section 2.4.2 was determined by Laboratory SGS Multilab (Evry, France) [10]. Similarly, the FTIR spectra of column separated asphaltene sub-fractions was recorded using a Tensor 27 spectrometer (Bruker Optics) equipped with a Bruker Golden Gate diamond Attenuated Total Reflection (ATR) cell.

### 2.5. Differential scanning calorimetry (DSC)

Experiments were conducted on a DSC Q2000 from TA Instruments. Instrument calibration was done by measuring the melting of indium. Prior to experiment, 10 to 20 mg sample were loaded in the sample pans and sealed hermetically. Before and after each experiment, the sample pans were weighed to ensure that no sample loss due to evaporation had occurred. Before each measurement, the sample was heated to at least 40 °C above WAT for at least 2 min, to erase the thermal history. The WAT was determined according to a previously published procedure [44]. In this procedure, the baseline is approximated by linear least squares and the WAT is defined as exceeding a threshold value, set as 3.291 times the standard deviation of experiment data from the linear approximation. Four measurements were done for each cooling rate and sample. Extrapolation to a zero cooling rate was done from WAT data with cooling rates of 2 to 0.5 °C/min.

### 2.6. Rheometry and gel breakage

Gel breakage measurements were conducted on an Anton Paar Physica 301. The rheometer was equipped with a 4 cm diameter 2° cone and plate geometry, which had been sandblasted for providing additional roughness and preventing slippage. A gap size of 0.170 mm was used. Experimental procedures consisted of preheating the sample to more than 20 °C above WAT, and loading it into the rheometer geometry set at 35 °C. Cooling at a rate of 1 °C/min was done until 4 °C, and then kept isothermal for 10 min. The sample was subsequently sheared at a shear rate of 0.1 $s^{-1}$ and the development of shear stress with total strain was recorded. The gel breakage strength was defined as the maximum shear stress, which appeared right after the linear elastic regime. Each measurement was repeated four to six times.

### 2.7. Crosspolarized microscopy (CPM)

To observe changes in wax crystal morphology, cross polarized microscopy (CPM) was applied. A Nikon Eclipse ME600 microscope fitted with a CoolSNAP-Pro camera by Media Cybernetics and

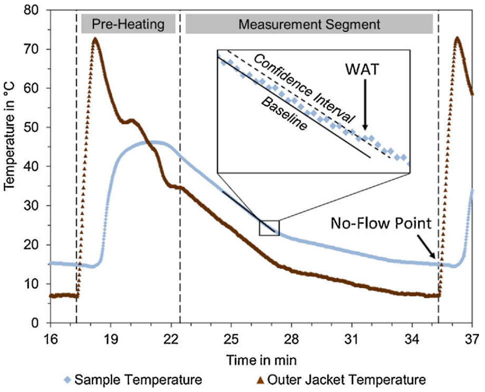

**Fig. 3.** Exemplary PPT data for 1000 ppm whole asphaltenes and 10 wt% macrocrystalline wax in p-xylene. The no-flow point marks the end of each measurement segment. The noflow point is determined according to ASTM D5985 as deflection of a piston in the rotating sample beaker [45]. The WAT is determined as exceeding the confidence interval around the linear baseline approximation.

crosspolarization filters were used for CPM imaging. A stage micrometer was taken for scaling. The temperature was controlled via a Linkham PE 94 and LTS-120E Peltier system. The samples were filled into glass capillaries with a cross section of 0.3 x 0.03 mm, which were fixated on microscope slides and sealed on both ends with 3 M Scotch cyanoacrylate base glue. An air bubble was kept between glue and sample to prevent contamination. The temperature program consisted of heating to 60 °C, keeping isothermal for 15 min, and subsequent cooling at a rate of 1 °C/min to 4 °C. The sample was then kept isothermal, and images were taken within the time frame of 20–40 min after reaching 4 °C.

### 2.8. *Pour point tester (PPT)*

Pour point analyses were done according to ASTM D5985 [45], using a pour point tester (PPT) 45150 from PSL Systemtechnik, Germany. The noflow point is measured as deflection of the piston located in the sample cell rotating at 0.1 rpm. The pour point can be computed from the noflow point by rounding up to the nearest multiple of 3 °C. In Fig. 3, the temperature changes during a measurement cycle are exemplarly shown. The wax was redissolved by heating to 45 °C between each measurement. The WAT was determined analogous to DSC experiments in Section 2.5, i.e. the sample temperature was approximated linearly and the WAT was defined as exceeding the confidence interval (as 3.291 times the standard deviation) around the baseline on a 10 °C interval. The slope of the baseline resembles the applied cooling rate and was 3.9 °C/min on average when detecting WAT.

### 2.9. *Isothermal titration calorimetry (ITC)*

ITC experiments were performed on a NANO ITC Standard volume from TA Instruments. Both sample and reference cell have a volume of 1 ml. The reference cell was filled with bulk solvent of xylene isomer blend. The instrument was calibrated via measuring the reaction heat for defined titrations of Trisbase with HCl. Before each experiment, the instrument was equilibrated to a baseline drift of less than 0.1 μW, which took approximately 30 to 60 min. Titrations were done in 25 injections of 10 μl using a 250 μl syringe and stirring at 250 rpm. Injection intervals were set to match the time needed for the heat signal to return to the baseline. Experiments conducted at 35 °C used injection intervals of 5 to 15 min, and experiments conducted at 20 °C involving paraffin wax had injection intervals of 60 min. Data evaluation was done in the NanoAnalyze software of TA Instruments with automated heat integration of each injection. The interaction heat was calculated as net enthalpy $\Delta H_{Int}$, which is the difference of the measured heat values for the dissociation of asphaltenes $\Delta H_{Asph}$, the dilution or redissolution heat of wax $\Delta H_{Wax}$, and combined effects of titrating asphaltenes into wax $\Delta H_{Total}$. The latter three quantities are measured in separate experiments. For each, the heat generated due to friction in the syringe was subtracted, which was obtained from blank xylene into xylene injections. The net enthalpy $\Delta H_{Int}$ is then computed via Eq. (1), in analogy to Wei et al. [46].

$$\Delta H_{Int} = \Delta H_{Total} - (\Delta H_{Asph} + \Delta H_{Wax}) \tag{1}$$

Solvents and solutions for ITC were degassed by sonicating for at least 30 min. Asphaltene solutions were prepared at least one day in advance and stored at room temperature, to ensure that the solutions had stabilized. Wax dispersions were prepared by quenching the hot waxy solution at 20 °C in a temperature controlled bath. As part of the quenching, the dispersion was kept in the bath for a duration of 1 h, shaken vigorously for 5 s after removal, and sonicated for 20–30 s before being filled into the ITC sample chamber.

## 3. Results and discussion

### 3.1. *Characterization of asphaltene fractions*

#### 3.1.1. *Fractionation yields*

The average yield in percentages from asphaltene fractionation are listed in Table 1. Each value is the average of two to five batches with according standard deviation. The bulk precipitation procedure yielded values close to the target of 20%, 30%, and 50% for the fractions *3.5 V*, *3.5 V – 6 V*, and *6 V – 40 V* asphaltenes, respectively [11]. The fractionation on calcium carbonate produced yields that are significantly lower for *bulk* and *irreversibly adsorbed* asphaltenes, and higher for *adsorbed* asphaltenes than previously reported [10]. However, the order of magnitude for each fraction yield is very similar. Differences can be explained by changing the procedure from batch to column, and by the substitution of THF with chloroform. Also, a lower percentage of asphaltenes was recovered at the end. One factor contributing to the loss of material is due to glass wool that is used to keep the calcium carbonate in place. Asphaltenes would adsorb on the glass wool, which could not be retrieved in subsequent steps.

#### 3.1.2. *Elemental analysis*

The elemental and metal composition of the asphaltene sub-fractions obtained from column fractionation method is given in Table 2. The calcium content in all the sub-fractions (*bulk*, *adsorbed* and *irreversibly adsorbed*) is lower than the whole (filtered) asphaltenes, thereby indicating that the samples are not contaminated by $CaCO_3$. The H/C ratio varied over a broader ranger (1.15–1.29), with the *irreversibly adsorbed* asphaltene sub-fractions (both 1 and 2) exhibiting a higher aliphatic nature, which is in agreement with previous results [10]. There is a noticeable variation in the oxygen content among the sub-fractions, with *irreversibly adsorbed* asphaltenes exhibiting a much higher content of oxygen. The oxygen content in *irreversibly adsorbed* fractions (4.48% and 3.79%) obtained in the present column fractionation method is comparable with the data reported by Subramanian et al. [10], who obtained an oxygen content of 4.22% in the *irreversibly adsorbed* asphaltene sub-fraction. The *bulk* asphaltenes in column method show the least content of oxygen atoms (1.44%), followed by adsorbed asphaltenes with 2.28%. The *adsorbed* asphaltenes have been enriched in nitrogen and sulfur heteroatoms, as well as metals Ni and V. In conclusion, an evolution of elemental composition from *bulk* to *irreversibly adsorbed* asphaltenes can be seen in terms of H/C ratio and oxygen content.

**Table 1**
Average yields of asphaltene fractionation with according standard deviation. The fractionation on calcium carbonate was conducted three times, and the fractionation via bulk precipitation was conducted five times.

| Procedure | Fraction and Yield with Standard Deviation *[wt%]* | | | | Total Recovered |
|---|---|---|---|---|---|
| Fractionation on calcium carbonate | *Bulk*<br>38.8 ± 6.8 % | *Adsorbed*<br>42.7 ± 4.1 % | *Irreversibly Adsorbed*<br>12.4 ± 0.3 % | | 93.9 ± 2.8 % |
| | | | Fraction 1<br>9.2 ± 1.1 % | Fraction 2<br>3.4 ± 1.0 % | |
| Fractionation via bulk precipitation | | *3.5 V*<br>18.2 ± 0.5 % | *3.5 V-6 V*<br>34.3 ± 0.1 % | *6 V-40 V*<br>47.5 ± 0.1 % | ~100% |

**Table 2**
Elemental and metal composition of asphaltene subfractions obtained by column fractionation. The mass balance is indicated by a percentage in gain (positive) and loss (negative), and is calculated with respect to whole asphaltenes as reported earlier [10].

| Element | Asphaltenes | | | | | Percentage loss or gain |
|---|---|---|---|---|---|---|
| | *Whole* (filtered) | *Bulk* | *Adsorbed* | *Irreversibly adsorbed* | | |
| | | | | Fraction 1 | Fraction 2 | |
| C *[wt%]* | 86,1 | 86,1 | 84,2 | 81,4 | 82,9 | −4,2 |
| H *[wt%]* | 8,40 | 8,28 | 8,31 | 8,39 | 8,88 | −3,6 |
| N *[wt%]* | 1,40 | 1,21 | 1,52 | 1,30 | 1,10 | −7,6 |
| O *[wt%]* | 1,83 | 1,44 | 2,28 | 4,48 | 3,77 | 12,6 |
| S *[wt%]* | 2,26 | 1,80 | 2,30 | 1,92 | 1,94 | −13,7 |
| Total *[wt%]* | 99,99 | 98,83 | 98,61 | 97,49 | 98,59 | – |
| H/C Ratio *[-]* | 1,171 | 1,154 | 1,184 | 1,237 | 1,285 | – |
| Fe *[ppm]* | < 42 | < 24 | < 29 | 626 | < 63 | – |
| Ni *[ppm]* | 67 | 59 | 81 | < 65 | 64 | – |
| V *[ppm]* | 223 | 248 | 278 | 166 | 172 | 8,6 |
| K *[ppm]* | < 420 | < 240 | < 290 | < 650 | < 630 | – |
| Na *[ppm]* | < 420 | < 240 | < 290 | < 650 | < 630 | – |
| Ca *[ppm]* | 987 | 242 | < 290 | < 650 | < 630 | – |

### 3.1.3. FTIR spectroscopy

The FTIR spectra of column fractionated asphaltenes and *whole* asphaltenes are shown in Fig. 4 All asphaltene sub-fractions show similar absorption bands at 2950 $\text{cm}^{-1}$ and 2830 $\text{cm}^{-1}$, thereby indicating similar alkyl groups across the fractions. Only the *irreversibly adsorbed* asphaltenes (fractions 1 and 2) show significant absorption at 1700 $\text{cm}^{-1}$, which corresponds to presence of carbonyl, carboxylic or derivative groups. Thus, the IR spectra and elemental analysis indicates that the column procedure has resulted in obtaining asphaltene sub-fractions with more distinct differences, especially in *bulk* and *adsorbed* asphaltenes. The composition of *irreversibly adsorbed* asphaltenes appears to be similar as reported earlier [10,11].

## 3.2. Effect of asphaltene concentration on wax crystallization

The influence of *whole* asphaltene dosing was tested on model oil solutions of 10 wt% macrocrystalline wax in xylene with different amounts of asphaltenes. Gel breakage strength, WAT, and pour point were taken as representative performance criteria for the ability of asphaltenes to act as WIs and PPDs.

It has been demonstrated that the gel breakage strength is independent of shear rate, as long as the shear rate is sufficiently low [47]. As depicted in Fig. 5, deviation from the target shear rate could occur in the beginning, but the shear rate was sufficiently close to the target value of 0.1 $\text{s}^{-1}$ when gel breakage occurred. Adding *whole* asphaltenes not only decreased the gel breakage strength, but also resulted in gel breakage at lower levels of strain. Also, adhesive breakage can be observed for the sample containing no asphaltenes, which is visible as oscillations of shear stress and shear rate at a strain of 50% and more. Ideal adhesive breakage is marked by a stickslip behavior of

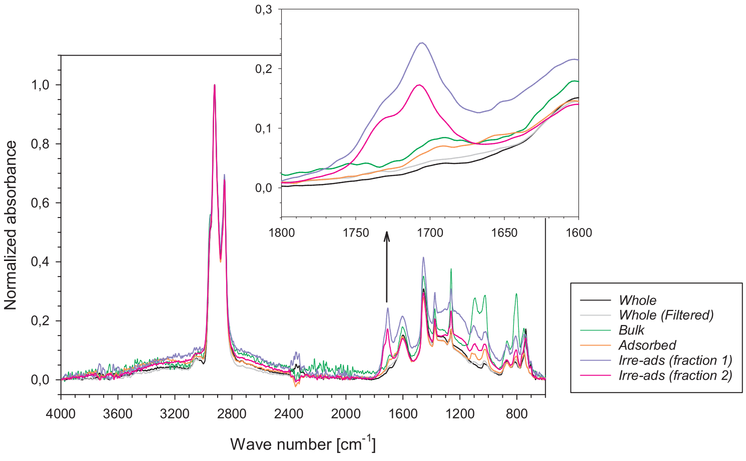

**Fig. 4.** FTIR spectra of asphaltene sub-fractions.

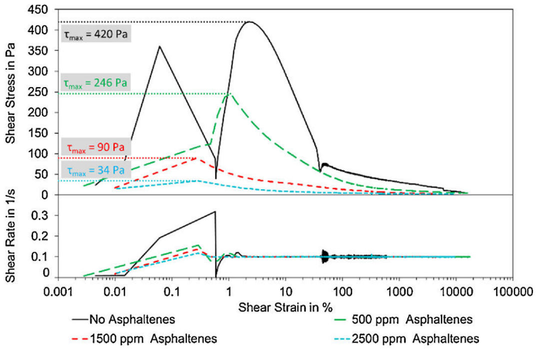

**Fig. 5.** Stressstrain diagram showing the influence of different amounts of whole asphaltenes on gel yield stength of 10 wt% macrocrystalline wax in xylene isomer blend at 4 °C.

the gel, which shows as oscillations of the shear stress during continuous shearing [48]. The fact that adhesive breakage has not been observed for samples containing asphaltenes indicates different gel properties and a different gel degradation mechanism.

Exemplary results of WAT values from DSC experiments are plotted in Fig. 6. The development of WAT with cooling rate can be best described as quadratic parabola, which faces concave upward. However, for cooling rates between 0.5 °C/min and 2 °C/min, the progression of WAT is approximately linear. This cooling rate regime was therefore used for linear extrapolation to an infinitely small cooling rate denoted as $WAT_0$. Another reason for this extrapolation is that data scattering makes comparison at a single, low cooling rate difficult. Fig. 6 also indicates a decrease in WAT with the addition of more *whole* asphaltenes. As can be seen in Fig. 7, the $WAT_0$ would decrease until a concentration of 2000 ppm was reached, and increase thereafter. The addition of *whole* asphaltenes therefore appears to improve the solubility of macrocrystalline wax only until a certain point, but not further. In comparison, gel breakage strength decreased for each concentration increase over the entire range tested in Fig. 7.

The effect of *whole* asphaltene addition on crystal morphology was investigated via CPM, and results are presented in Fig. 8. CPM imaging of 10 wt% macrocrystalline wax in xylene isomer blend shows lines of different thickness, which are oriented either in parallel and orthogonal to each other, or branched around a common center. These structures account for needle and plate shaped crystals. As the amount of asphaltenes increases, the observed shapes become on average smaller, more compact, and more branched, which indicates whole asphaltenes to act as a crystal modifier. Considering the reduction in gel breakage strength induced by *whole* asphaltene addition in Fig. 7, the morphological changes appear to also reduce the three dimensional interlocking of wax particles. Moreover, the amount of visible wax particles in Fig. 8 increases with increasing asphaltene concentration. In CPM imaging, only the portion of crystals can be seen, which have an orientation that allows for the depolarization of light. The increase in observable wax crystals consequently does not imply an increase in solid wax content, but a diversification of crystal geometry and orientation.

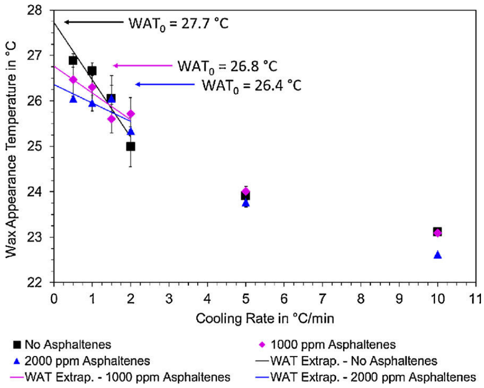

**Fig. 6.** DSC results for WAT progression with cooling rate for different amounts of whole asphaltenes, and 10 wt% macrocrystalline wax in xylene isomer blend. The solid straight lines mark extrapolation to $WAT_0$ at zero cooling rate. Each point represents the average of four measurements with according standard deviation.

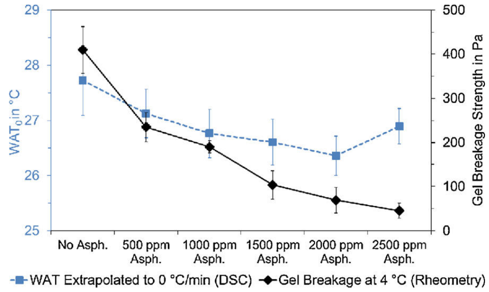

**Fig. 7.** Influence of amounts of whole asphaltene on $WAT_0$ and gel breakage in a waxy model oil. Measurements were done with whole asphaltenes and 10 wt % macrocrystalline wax in xylene isomer blend. The $WAT_0$ was obtained via linear extrapolation from cooling rates between 0.5 °C/min and 2 °C/min with four measurements per cooling rate, yielding 16 measurements per $WAT_0$. Gel breakage strength was calculated as the maximum yield stress recorded during gel breakage with four measurements per sample. Error bars represent the standard deviation of each value.

Fig. 9 shows that the addition of *whole* asphaltenes could decrease the WAT for all samples tested. Still, the WAT decrease became statistically significant only at concentrations of 5000 ppm and more. In comparison to DSC measurements, the scattering of WAT is more pronounced. Also, the WAT obtained from PPT measurements is slightly lower than in DSC of Fig. 7. This is a consequence of the faster cooling rate employed and the fact that the PPT is not designed for WAT determination. Also presented in Fig. 9 is the influence of *whole* asphaltenes on no-flow point, which exhibits better reproducibility than WAT measurements. The No-Flow Point represents an estimate of the pour point with a higher temperature resolution. It increased at 500 ppm *whole* asphaltenes compared to the case with no asphaltenes. For higher asphaltene concentrations, the noflow point followed a decreasing trend, except for increasing the concentration to 2 wt% *whole* asphaltenes. This shows that the addition of *whole* asphaltenes can have positive as well as adverse effects on the flow-ability of the waxy model oil. The largest reduction in noflow point from the blank case was 1.5 °C, which is comparably low. Pour point decreases of 30 °C and more are often needed to ensure unobstructed flow in subsea pipelines. It has been stated that high paraffin wax percentages may diminish the possible effect of PPDs [22]. A reduction in wax percentage in the waxy model oils could have improved the sensitivity of noflow point to asphaltene addition. Still, the wax amount was kept constant at 10 wt% for better comparison between all techniques.

### 3.3. *Effect of asphaltene fraction on wax crystallization*

Asphaltene fractions were tested in model waxy oils with 1500 ppm asphaltenes and 10 wt% wax in xylene. Experiments were set up in such a way, to have all asphaltene fractions present as stable nano-

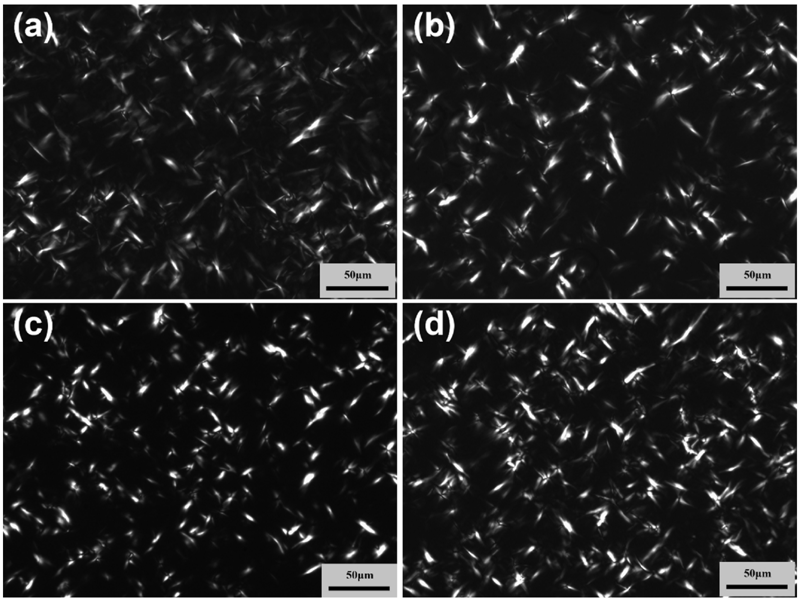

**Fig. 8.** CPM images of 10 wt% macrocrystalline wax in xylene isomer blend with (a) no additive, (b) 500 ppm, (c) 1500 ppm, and (d) 2500 ppm whole asphaltenes.

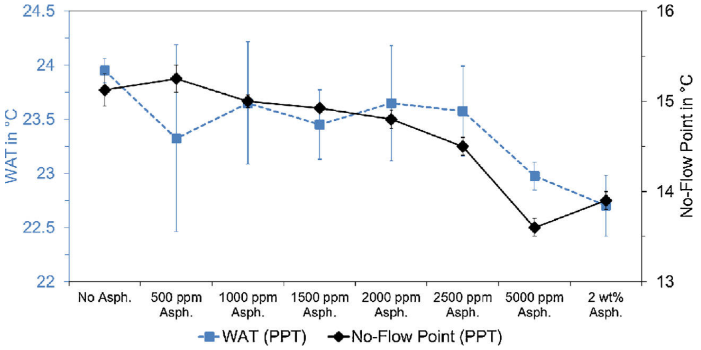

**Fig. 9.** Influence of different amounts of whole asphaltene on WAT and No-Flow Point. Measurements were done with whole asphaltenes and 10 wt% macrocrystalline wax in pxylene using a pour point tester (PPT). Each value represents the average of 2–4 measurements with according standard deviation as error bars.

aggregates. This was confirmed by random screening of the mixtures using a microscope and at no point were asphaltene flocculates found. Xylene represents only the aromatic fraction of crude oil neglecting the major constituent, which is saturated and aliphatic in nature. This deviation from real world systems was deemed necessary, because using an aliphatic solvent would result in asphaltene flocculation. These flocculates can be different in properties and quantity depending on asphaltene fraction used, so the conducted experiments would be less comparable. The presented data can therefore be interpreted as the effect of dispersed asphaltenes on wax crystallization.

In DSC analysis, the qualitative shape of the exothermic peak due to wax crystallization was similar for all samples. As depicted in Fig. 10, the main difference between the samples is crystallization onset at a different temperature. Shifts could also occur at a later stage of crystallization, such as the heat profile of *bulk* asphaltenes. There, the heat flow in comparison to other samples appears higher between 20 and 0 °C, and lower after 0 °C. Paraffin wax crystallization consequently can be affected during all stages of crystallization.

As shown in Fig. 11, the effect on $WAT_0$ was the greatest for *bulk* asphaltenes, which is in agreement with other reports [6,29,34]. *Irreversibly adsorbed* asphaltenes accounted for no measurable change in $WAT_0$. This indicates that there is either no effect or that positive and negative effects are cancelling out. The second lowest effect on $WAT_0$ was displayed by *3.5 V* asphaltenes. These two fractions have poor solubility and a higher oxygen content in common. Gel breakage strength was lowered the most by *whole*, *3.5 V*, and *3.5 V–6 V* asphaltenes. Fractionation on calcium carbonate yielded asphaltene groups, which all had less or no effect on gel breakage.

The influence of four selected asphaltene fractions on crystal morphology is shown in Fig. 12. *Bulk* asphaltenes had less effect on crystal size than *whole* asphaltenes. The addition of *3.5 V–6 V* asphaltenes increased crystal distortion considerably. The effect of *3.5 V* asphaltenes was similar to *3.5 V–6 V* asphaltenes. Other fractions not shown in Fig. 12 were also tested in CPM, but did not yield notable changes in crystal morphology as compared to *whole* asphaltenes. *Irreversibly adsorbed* asphaltenes changed crystal morphology the most. The resulting

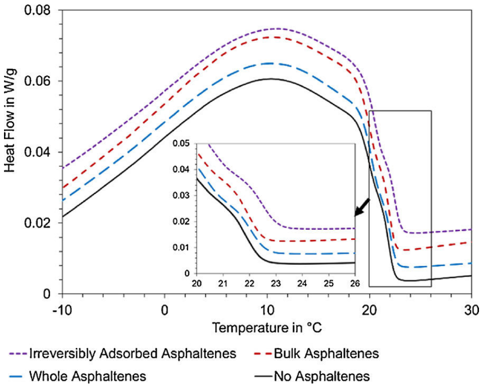

**Fig. 10.** DSC heat flow versus temperature at a cooling rate of 5 °C/min for four selected samples of 1500 ppm asphaltenes and 10 wt% macrocrystalline wax in xylene isomer blend. Graphs were shifted on the y-axis for better overview.

gel contained smaller, and more finely dispersed wax particles. Still, this change was not beneficial as the gel strength of *irreversibly adsorbed* asphaltenes was highest of all fractions. It has been suggested that asphaltenes act as connectors between wax crystals [30]. This could explain the comparably high gel strength for *irreversibly adsorbed* asphaltenes, since reduction of wax crystal size usually leads to a decrease in gel strength. These asphaltenes might be incorporated into the wax crystals via co-precipitation, while the polar sections could act as connectors between the crystals. This could then form an interconnected and volume spanning network of higher strength.

WAT and pour point are both measures that describe particular instances during wax crystallization. Asphaltenes can delay certain aspects of wax crystallization based on their composition. As a result, decreases in WAT and pour point follow a similar trend for each asphaltene fraction. Fig. 13 reveals that *bulk* asphaltenes had the greatest influence on both measures. *Irreversibly adsorbed* asphaltenes showed no detectable change in WAT and pour point compared to no asphaltenes. The remaining asphaltene fractions all accounted for decreases in WAT and pour point, and were within the standard deviation similar to the effect of *whole* asphaltenes.

Separation via adsorption on calcium carbonate also represents a separation based on polarity, due to the polar nature of adsorbent, and eluents with different polarities. As a consequence, *bulk* asphaltenes can be considered less polar, and *irreversibly adsorbed* asphaltenes can be considered more polar than *whole* asphaltenes. Overall, this separation did not yield a product with improved wax inhibition performance. *Bulk* asphaltenes showed the best results in terms of WAT and pour point. Still, this fraction had less effect on gel breakage strength and crystal morphology than *whole* asphaltenes. Averaged over all five parameters, *3.5 V*, and *3.5 V–6 V* asphaltenes showed the best effect. Both fractions had a higher impact on gel breakage strength and crystal morphology than *whole* asphaltenes, and accounted for similar or better pour point depression. Only the effect on WAT was similar to or poorer than that of *whole* asphaltenes. Low solubility therefore could be advantageous. This complies with research suggesting that less soluble asphaltenes are often found in wax deposits [32]. Also, low solubility could facilitate co-precipitation with wax, which is a requirement for crystal modifiers. Morphological changes in the wax crystal could further be induced by polar functional groups in the asphaltene molecules. As CPM imaging showed, the degree of crystal distortion is highest for *irreversibly adsorbed* asphaltenes and lowest for *bulk* asphaltenes. Still, crystal distortion and gel strength did not correlate. Regarding gel strength, the best results were obtained from the second fraction, respectively, *adsorbed* and *3.5 V–6 V* asphaltenes. A counter intuitive trend is given by the development of H/C ratio with inhibition performance for asphaltenes from bulk precipitation. Lower solubility fractions, i.e. *3.5 V* asphaltenes, have higher H/C ratios, which indicates more aromatic and less aliphatic systems. The aliphatic part of an asphaltene molecule is considered responsible for asphaltene-wax interactions. Still the products from bulk fractionation showed better effect on wax crystal morphology and gel yield strength for fractions with supposedly higher aromaticity. An explanation could be that other effects, such as the influence of asphaltene solubility, are counteracting the change in aliphatic content.

At the bottom line, none of the fractionation procedures isolated asphaltenes that could be an alternative to polymeric PPDs. The fractions from adsorption on calcium carbonate even showed on average lower performance than the original material, *whole* asphaltenes. This indicates that asphaltenes of different properties and functional groups might need to act synergistically to have a good effect on wax crystallization. Another explanation would be that the chemical composition of the asphaltenes has been altered, which is supported e.g. by the increase in oxygen content in Table 2. All in all, the results indicate that low solubility and intermediate polarity have the most favorable effect on wax crystallization.

### 3.4. Asphaltene-wax interactions

Asphaltenewax interactions were measured via ITC using solutions of 2 wt% asphaltenes in xylene isomer blend. This concentration was considered high enough for good signal response, but low enough to prevent asphaltene precipitation in the syringe. ITC experiments were made with *bulk* and *irreversibly adsorbed* asphaltenes to include fractions of the highest and lowest polarity. *Whole* asphaltenes were also tested to compare with the original material. Injections were made into a 10 wt% macrocrystalline wax in xylene isomer blend. Random checks were performed with a microscope on asphaltene solutions. At no point were

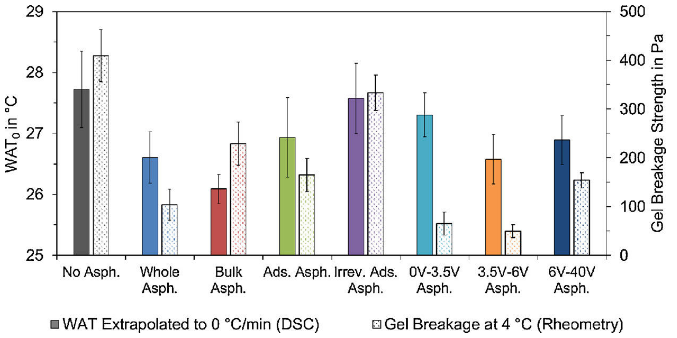

**Fig. 11.** Influence of different asphaltene fractions on $WAT_0$ and gel breakage. Measurements were done with 1500 ppm asphaltenes and 10 wt% macrocrystalline wax in xylene isomer blend. The $WAT_0$ was obtained via linear extrapolation from cooling rates between 0.5 °C/min and 2 °C/min with four measurements per cooling rate, yielding 16 measurements per $WAT_0$. Gel breakage strength was calculated as the maximum yield stress recorded during gel breakage with four to six measurements per sample. Error bars represent the standard deviation of each value.

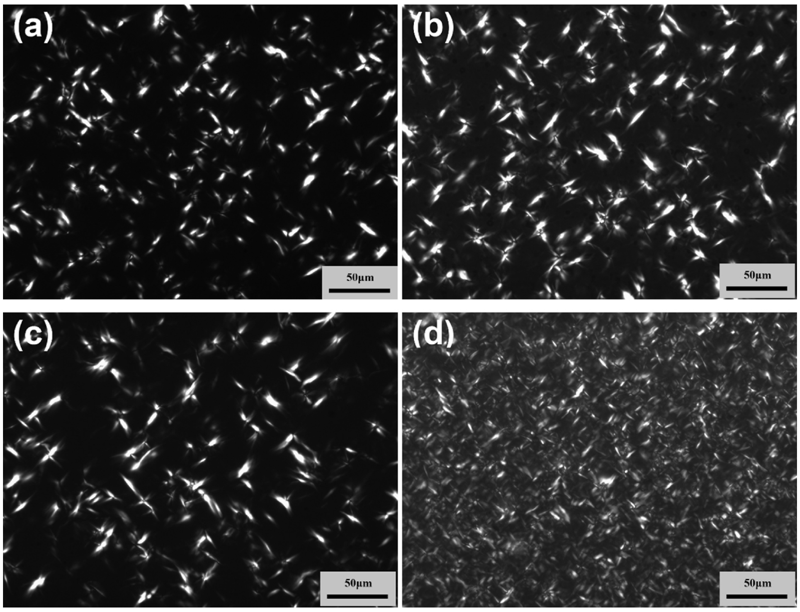

**Fig. 12.** CPM images of 10 wt% macrocrystalline wax in xylene isomer blend with (a) 1500 ppm whole asphaltenes, (b) 1500 ppm 3.5 V–6 V asphalenes, (c) 1500 ppm bulk asphaltenes, and (d) 1500 ppm irreversibly adsorbed asphaltenes.

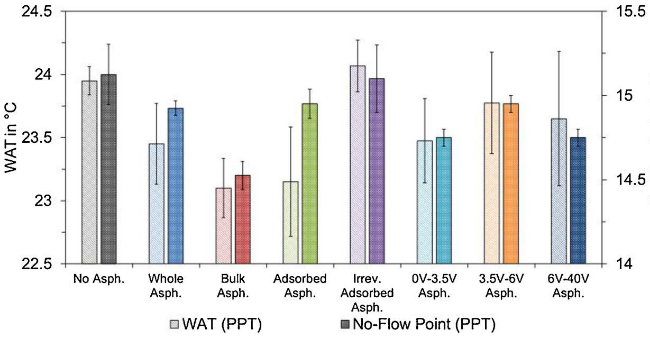

**Fig. 13.** Influence of different asphaltene fractions on WAT and No-Flow Point. Measurements were done with 1500 ppm asphaltenes and 10 wt% macrocrystalline wax in pxylene using a pour point tester (PPT). Each value represents the average of 2–4 measurements with according standard deviation as error bars.

particle flocculates found. The presented data therefore accounts for interactions of dispersed asphaltenes, i.e. most likely nanoaggregates, with wax. ITC experiments conducted at 35 °C contained solubilized wax only, and typical results are shown in Fig. 14. The precipitation onset of the waxy solution was measured to be $WAT_0 = 27.7\,^{\circ}C$. At 20 °C, a fraction of macrocrystalline wax had therefore precipitated. Results of ITC experiments conducted at 20 °C are plotted in Fig. 15.

The heat profile of every injection shows a large minimum and subsequent return to the baseline. Secondary effects can be observed for *whole* and *irreversibly adsorbed* asphaltenes in Fig. 14, where local extrema on a scale of less than 1% of the large minimum are visible in the heat profile approximately 5–10 min after each injection. It appears that multiple processes are taking place, which have different kinetics. Similarly, local minima or inflection points can be observed that follow the minimum right after each injection in Fig. 15. At both temperatures, the largest heat contributor is the dilution or redissolution of wax. This process as well as asphaltene dissociation are endothermic reactions. Consequently, as the heat released is lower in presence of asphaltenes, an exothermic reaction between asphaltenes and wax can be observed in Figs. 14 and 15. Also visible is the difference in time scale. Experiments at 35 °C showed a comparably fast return to the baseline after each injection. The injection interval could therefore be set at 15 min and less. Experiments at 20 °C accounted for a slower return to the baseline. It appears that the involved redissolution processes of solid wax are rate limiting. Injection intervals were set at 60 min. Complete equilibration at the end of each injection interval is not the case. Still, the experiments showed good reproducibility, little to no baseline drift, and equilibration during early injections. Because of that, the injection interval was not increased. Too long injection intervals promote the influence of solvent evaporation and diffusion into the syringe tip, so this decision is always a tradeoff.

The heat released during each titration is computed by integration. For this, a linear baseline is fitted between each injection point. The calculated interaction heat for *whole*, *bulk*, and *irreversibly adsorbed* asphaltenes with macrocrystalline wax is plotted in Figs. 16 and 17. The contributions $\Delta H_{Total}$, $\Delta H_{Asph}$, and $\Delta H_{Wax}$ are the average of two to four

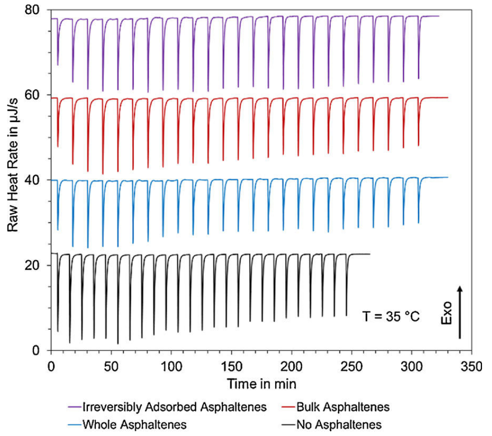

**Fig. 14.** ITC heat profiles for 25 injections of 2 wt% asphaltenes into 10 wt% macrocrystalline wax in xylene isomer blend at 35 °C. Graphs have been shifted on the y-axis for better overview.

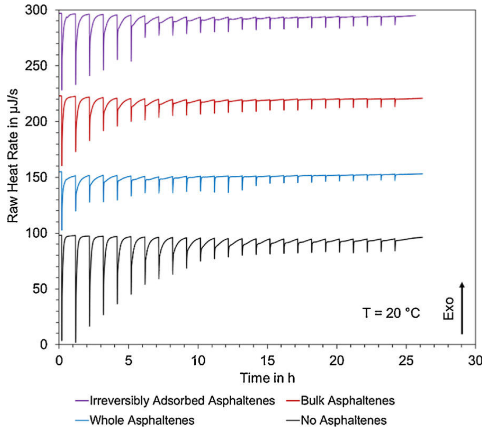

**Fig. 15.** ITC heat profiles for 25 injections of 2 wt% asphaltenes into 10 wt% macrocrystalline wax in xylene isomer blend at 20 °C. Graphs have been shifted on y-axis for better overview.

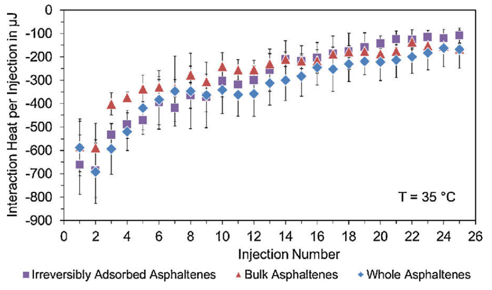

**Fig. 16.** Interaction heat for 2 wt% asphaltenes with 10 wt% macrocrystalline wax in xylene isomer blend at 35 °C. The wax is fully in solutions, as $WAT_0$ = 27.7. Error bars represent the standard deviation.

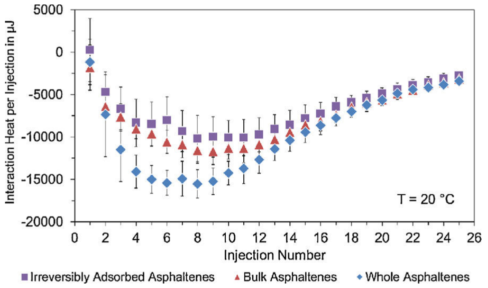

**Fig. 17.** Interaction heat for 2 wt% asphaltenes with 10 wt% macrocrystalline wax in xylene isomer blend at 20 °C. The wax is partially crystallized, as $WAT_0$ = 27.7 °C. Error bars represent the standard deviation.

measurements, depending on reproducibility of the individual value. Results for *whole* asphaltenes have been published previously [49], but were measured two additional times to provide higher statistical significance.

For experiments conducted at 35 °C in Fig. 16, the resulting interaction heat is almost identical. All samples show maximum interaction heat at the second injection. Subsequent injections decrease in interaction heat and asymptotically approach zero interaction heat towards the final injections. *Bulk* asphaltenes are on average lower than *whole* and *irreversibly adsorbed* asphaltenes. Still, only during injection 3–5 this difference is large enough to be statistically valid.

For experiments at 20 °C in Fig. 17, the interaction heat per injection is by a factor of 10–45 higher than at 35 °C. Interactions of asphaltenes with solid wax appear to be stronger than with dissolved wax. *Bulk* and *irreversibly adsorbed* asphaltenes are within the standard deviation similar in interaction heat at 20 °C. *Whole* asphaltenes are considerably higher in interaction heat during injection 3–10. All samples have a global maximum at either injection 8 or 9. Towards the final injections all samples are converging and asymptotically approach zero interaction heat. This could be explained by a diminishing of reaction sites at the end. Interactions with both dissolved and solid wax are exothermic, as the interaction heat attained negative heat values.

It can be concluded that separation on calcium carbonate did not produce a fraction with increased interaction heat. On the contrary, interactions with solid wax were highest for unfractionated *whole* asphaltenes. Interactions with solubilized wax did not show significant difference between the tested samples. Neither the most polar *irreversibly adsorbed* asphaltenes, nor the least polar *bulk* asphaltenes interact more strongly with macrocrystalline wax. Instead, *whole* asphaltenes with intermediate polarity accounted for the strongest interactions with solid wax. It appears that the sum of all functional groups contribute more to asphaltenewax interactions than one group with more distinct properties. These results are concurring with Section 3.3, where the best effects on crystal morphology and waxy gel strength were achieved by asphaltenes with a mixed range of functional groups.

## 4. Conclusion

This article investigated the effect of fractionated asphaltenes on wax crystallization. Asphaltenes were separated into groups with more distinct properties via adsorption on calcium carbonate or stepwise precipitation with *n*-hexane. A waxy model oil containing macrocrystalline wax in xylene was used to study the effect of asphaltenes on wax crystallization. The performance of asphaltenes to act as WIs was investigated via DSC, rheometry, CPM, and PPT. Asphaltene-wax interactions were measured in ITC. Key results are summarized as follows.

1 In experiment design, asphaltene concentrations and solvent were chosen to provide stable asphaltene nano-aggregates without flocculation. According to FTIR spectra, all asphaltene fractions displayed abundance of aliphatic groups, which can facilitate co-crystallization with wax.

2. Increasing the concentration of *whole* asphaltenes facilitated changes to wax crystal morphology and decreased gel yield strength. Regarding WAT and pour point, a concentration increase did not always yield an improvement.
3. Fractionation on calcium carbonate resulted in asphaltene groups with the largest differences in composition and properties. Yet, the overall inhibition performance and interaction strength of each group with wax did not improve as compared to unfractionated *whole* asphaltenes.
4. *Bulk* asphaltenes from fractionation on calcium carbonate induced the largest WAT and pour point decreases. Still, the effect on gel yield strength and crystal morphology was less pronounced. This group had lower polarity and the lowest H/C ratio indicating higher amounts of aromatic structures.
5. *Irreversibly adsorbed* asphaltenes accounted for the largest changes in crystal morphology, forming smaller and finely dispersed wax crystals. Still, wax inhibition performance was poor in terms of pour point and waxy gel strength. This fraction contained increased quantities of carbonyl, carboxylic or derivative groups, making it the highest polarity group.
6. Solvent fractionation resulted in the fractions *3.5 V, 3.5 V–6 V*, and *6 V–40 V* asphaltenes, which differed in solubility, but had more similar composition and functional groups than asphaltenes from fractionation on calcium carbonate. The groups *3.5 V* and *3.5 V–6 V* asphaltenes showed the best effect on waxy gel strength and similar or better pour point depression as compared to *whole* asphaltenes.

Overall, asphaltene fractionation did not yield a product equivalent to polymeric PPDs. Wax inhibition performance tended to be best for asphaltene fractions with low solubility and a mixed range of functional groups. Wax crystallization is therefore influenced by an ensemble of asphaltenes with different properties. It is suggested that asphaltenes with different chemical compositions might form synergies when acting on wax crystallization. These synergies could be explained by bi-functional colloids: Less polar asphaltenes interact with wax i.e. by facilitating co-crystallization, whereas more polar asphaltenes impose spatial interferences during wax crystal growth. This would result in the formation of more distorted wax crystals with less propensity to interlock. Still, additional data is needed to support this hypothesis, e.g. the precise structure and composition of individual asphaltene molecules.

## Acknowledgements

This work was carried out as a part of SUBPRO, a Research-based Innovation Centre within Subsea Production and Processing. The authors gratefully acknowledge the financial support from SUBPRO, which is financed by the Research Council of Norway, major industry partners and NTNU.

## References

[1] M.A. Kelland, Production Chemicals for the Oil and Gas Industry, second ed., CRC press, Boca Raton, 2014.

[2] A. Aiyejina, et al., Wax formation in oil pipelines: a critical review, Int. J. Multiphase Flow 37 (7) (2011) 671–694.

[3] K.G. Paso, Paraffin Gelation Kinetics, University of Michigan, 2005.

[4] U. Prahl, Isolierung Erdölstämmiger Pour Point Depressants Und Untersuchung Ihrer Wirkungsweise in Paraffinhaltigen Fluiden, in Fakultät Für Bergbau, Hüttenwesen Und Maschinenwesen, Technische Universität Clausthal, Papierflieger, 2001.

[5] J.F. Tinsley, et al., Waxy gels with asphaltenes 1: characterization of precipitation, gelation, yield stress, and morphology, Energy Fuel 23 (4) (2009) 2056–2064.

[6] R. Venkatesan, et al., The effect of asphaltenes on the gelation of waxy oils, Energy Fuel 17 (6) (2003) 1630–1640.

[7] H.P. Jensen, Pour Point Depressant Made from the Asphaltene Component of Thermally Treated Shale Oil, U.S.P.a.T. Office, Editor, Chevron Research Company, San Francisco, Calif., USA, 1980.

[8] D.K. Wunderlich, J.H. Frankovich, Pour Point Depressant Made by Hydrovisbreaking and Deasphalting a Shale Oil, U.S.P. Office, Editor, Sinclair Oil Corporation, New York, USA, 1970.

[9] G.B. Irving, E. Knapp, Process for Reducing the Pour Point of Shale Oil, U.S.P. Office, Editor, Esso Research and Engineering Company, USA, 1970.

[10] S. Subramanian, et al., Asphaltene fractionation based on adsorption onto calcium carbonate: part 1. Characterization of sub-fractions and QCM-D measurements, Colloids Surf. A: Physicochem. Eng. Aspects 495 (2016) 136–148.

[11] S. Subramanian, et al., Asphaltene fractionation based on adsorption onto calcium carbonate: part 2. Self-association and aggregation properties, Colloids Surf. A: Physicochem. Eng. Aspects 514 (2017) 79–90.

[12] A.Ld.C. Machado, E.F. Lucas, Poly(ethylene-co-vinyl acetate) (EVA) copolymers as modifiers of oil wax crystallization, Pet. Sci. Technol. 17 (9–10) (1999) 1029–1041.

[13] Z. Huang, S. Zheng, H.S. Fogler, And Field practices, Wax Deposition: Experimental Characterizations, Theoretical Modeling, CRC Press, Boca Raton, 2015.

[14] K. Paso, et al., Paraffin polydispersity facilitates mechanical gelation, Ind. Eng. Chem. Res. 44 (18) (2005) 7242–7254.

[15] I. Rahimian, H. Laux, H.-J. Oschmann, Trübungs-und stockpunktabhängigkeiten in erdölen, Erdöl, Erdgas, Kohle 113 (2) (1997) 80–83.

[16] E.W. Clarke, Crystal types of pure hydrocarbons in the paraffin wax range, Ind. Eng. Chem. 43 (11) (1951) 2526–2535.

[17] F. Yang, et al., Polymeric wax inhibitors and pour Point depressants for waxy crude oils: a critical review, J. Dispersion Sci. Technol. 36 (2) (2015) 213–225.

[18] Y. Zhao, Shut in and Restart of Waxy Crude Oil Pipelines: Gelation, Rheology Model Development, and Application of Polymer/Ionic Liquid Based Additive, Norges teknisk-naturvitenskapelige universitet (NTNU), Tondheim, Norway, 2013.

[19] A. International, Standard Test Method for Pour Point of Petroleum Products, D97 (2017).

[20] B. Wei, Recent advances on mitigating wax problem using polymeric wax crystal modifier, J. Pet. Explor. Prod. Technol. 5 (4) (2015) 391–401.

[21] A.L.C. Machado, E.F. Lucas, Influence of ethylene-co-vinyl acetate copolymers on the flow properties of wax synthetic systems, J. Appl. Polym. Sci. 85 (6) (2002) 1337–1348.

[22] H.-J. Oschmann, Das Kristallisationsverhalten Von Paraffinen in Abhängigkeit Von Ihrer Zusammensetzung Sowie Seine Beeinflussung Durch Paraffininhibitoren, in Fakultät Für Bergbau, Hüttenwesen Und Maschinenwesen, Technische Universität Clausthal, Papierflieger, 1998.

[23] G.E. Oliveira, et al., The effect of asphaltenes, naphthenic acids, and polymeric inhibitors on the pour Point of paraffins solutions, J. Dispersion Sci. Technol. 28 (3) (2007) 349–356.

[24] Md.C. García, L. Carbognani, Asphaltene − Paraffin structural interactions. effect on crude oil stability, Energy Fuel 15 (5) (2001) 1021–1027.

[25] J.F. Tinsley, et al., waxy gels with asphaltenes 2: use of wax control polymers, Energy Fuel 23 (4) (2009) 2065–2074.

[26] B. Yao, et al., Ethylene–Vinyl acetate copolymer and resin-stabilized asphaltenes synergistically improve the flow behavior of model waxy oils. 2. Effect of asphaltene content, Energy Fuel (2018).

[27] B. Yao, et al., Ethylene–Vinyl acetate copolymer and resin-stabilized asphaltenes synergistically improve the Flow behavior of model waxy oils. 1. Effect of wax content and the synergistic mechanism, Energy Fuel 32 (2) (2018) 1567–1578.

[28] K. Oh, M. Deo, Characteristics of wax gel formation in the presence of asphaltenes, Energy Fuel 23 (3) (2009) 1289–1293.

[29] L.A. Alcazar-Vara, J.A. Garcia-Martinez, E. Buenrostro-Gonzalez, Effect of asphaltenes on equilibrium and rheological properties of waxy model systems, Fuel 93 (2012) 200–212.

[30] Y. Lei, et al., Study on the effect of dispersed and aggregated asphaltene on wax crystallization, gelation, and flow behavior of crude oil, Energy Fuel 28 (4) (2014) 2314–2321.

[31] Y. Lei, S. Han, J. Zhang, Effect of the dispersion degree of asphaltene on wax deposition in crude oil under static conditions, Fuel Process. Technol. 146 (2016) 20–28.

[32] E. Rogel, et al., Asphaltene characterization of paraffinic crude oils, Fuel 178 (Supplement C) (2016) 71–76.

[33] X. Song, et al., Effect of SiO2 nanoparticles on wax crystallization and flow behavior of model crude oil, Ind. Eng. Chem. Res. 55 (23) (2016) 6563–6568.

[34] Y. Li, et al., Influence of asphaltene polarity on crystallization and gelation of waxy oils, Energy Fuel 32 (2) (2018) 1491–1497.

[35] E. Ariza-León, D.-R. Molina-Velasco, A. Chaves-Guerrero, Review of studies on asphaltene - wax interaction and the effect thereof on crystallization, CT&F - Ciencia, Tecnología y Futuro 5 (2014) 39–53.

[36] X. Yang, P. Kilpatrick, Asphaltenes and waxes Do not interact synergistically and coprecipitate in solid organic deposits, Energy Fuel 19 (4) (2005) 1360–1375.

[37] Md.C. García, Crude oil wax crystallization. The effect of heavy n-paraffins and flocculated asphaltenes, Energy Fuel 14 (5) (2000) 1043–1048.

[38] S.L. Kokal, S.G. Sayegh, Asphaltenes: The Cholesterol Of Petroleum, in Middle East Oil Show, Society of Petroleum Engineers, Bahrain, 1995.

[39] P. Kriz, S.I. Andersen, Effect of asphaltenes on crude oil wax crystallization, Energy Fuel 19 (3) (2005) 948–953.

[40] M. Orea, et al., Retention of alkane compounds on asphaltenes. Insights about the nature of Asphaltene–Alkane interactions, Energy Fuel 30 (10) (2016) 8098–8113.

[41] T.J. Kaminski, et al., Classification of asphaltenes via fractionation and the effect of heteroatom content on dissolution kinetics, Energy Fuel 14 (1) (2000) 25–30.

[42] K. Paso, et al., Wax deposition investigations with thermal gradient quartz crystal microbalance, Handbook of Surface and Colloid Chemistry, CRC Press, 2009, pp. 567–584.

[43] F.E. Pinto, et al., Fractionation of asphaltenes in n-hexane and on adsorption onto CaCO3 and characterization by ESI(+)FT-ICR MS: part i, Fuel 210 (2017) 790–802.

[44] J. Ruwoldt, M. Kurniawan, H.-J. Oschmann, Non-linear dependency of wax appearance temperature on cooling rate, J. Pet. Sci. Eng. 165 (2018) 114–126.

[45] A. International, Standard Test Method for Pour Point of Petroleum Products (Rotational Method), D5985 (2014).
[46] D. Wei, et al., Aggregation of tetrameric acid in xylene and its interaction with asphaltenes by isothermal titration calorimetry, J. Therm. Anal. Calorim. 122 (1) (2015) 463–471.
[47] Y. Zhao, et al., Gelation and breakage behavior of model Wax–Oil systems: rheological properties and model development, Ind. Eng. Chem. Res. 51 (23) (2012) 8123–8133.
[48] K.G. Paso, Comprehensive treatise on shut-in and restart of waxy oil pipelines, J. Dispersion Sci. Technol. 35 (8) (2014) 1060–1085.
[49] J. Ruwoldt, et al., Isothermal titration calorimetry for assessing wax-inhibitors, Chemistry in the Oil Industry XV: Enabling Efficient Technologies Programme, (2017) Manchester (UK).